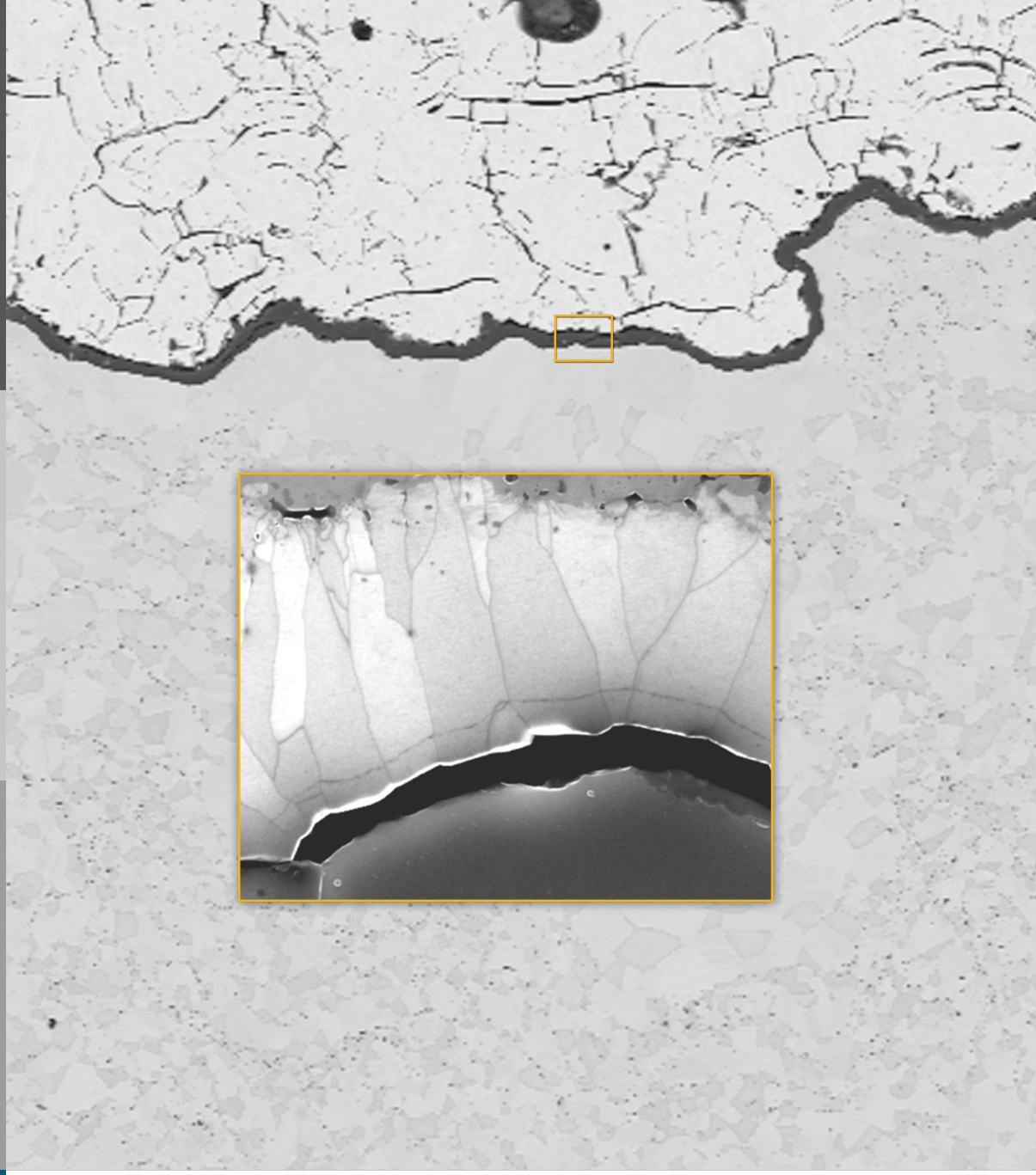

Influence of Material and Testing Parameters on the Lifetime of TBC Systems with MCrAlY and NiPtAl Bondcoats

Peng Song

Mitglied der Helmholtz-Gemeinschaft

JÜLICH
FORSCHUNGSZENTRUM

Schriften des Forschungszentrums Jülich
Reihe Energie & Umwelt / Energy & Environment Band / Volume 137

Forschungszentrum Jülich GmbH
Institute of Energy and Climate Research (IEK)
Microstructure and Properties of Materials (IEK-2)

Influence of Material and Testing Parameters on the Lifetime of TBC Systems with MCrAlY and NiPtAl Bondcoats

Peng Song

Schriften des Forschungszentrums Jülich
Reihe Energie & Umwelt / Energy & Environment Band / Volume 137

ISSN 1866-1793 ISBN 978-3-89336-783-2

Bibliographic information published by the Deutsche Nationalbibliothek.
The Deutsche Nationalbibliothek lists this publication in the Deutsche Nationalbibliografie; detailed bibliographic data are available in the Internet at http://dnb.d-nb.de.

Publisher and Distributor:	Forschungszentrum Jülich GmbH Zentralbibliothek 52425 Jülich Phone +49 (0) 24 61 61-53 68 · Fax +49 (0) 24 61 61-61 03 e-mail: zb-publikation@fz-juelich.de Internet: http://www.fz-juelich.de/zb
Cover Design:	Grafische Medien, Forschungszentrum Jülich GmbH
Printer:	Grafische Medien, Forschungszentrum Jülich GmbH
Copyright:	Forschungszentrum Jülich 2012

Schriften des Forschungszentrums Jülich
Reihe Energie & Umwelt / Energy & Environment Band / Volume 137

D 82 (Diss., RWTH Aachen University, 2011)

ISSN 1866-1793
ISBN 978-3-89336-783-2

The complete volume is freely available on the Internet on the Jülicher Open Access Server (JUWEL) at http://www.fz-juelich.de/zb/juwel

Abstract

The oxidation behavior of the bond coat is an important factor determining the lifetime of thermal barrier coatings (TBC) in the advanced gas turbine components. In the present work, the effect of various testing parameters, such as hot/cold dwell time, heating/cooling rate, atmosphere composition on the bondcoat oxidation and associated TBC lifetime has been investigated. The range of coating systems included Electron Beam - Physical Vapor Deposited (EB-PVD) and Air Plasma Sprayed (APS) TBC´s with MCrAlY (M = Ni, Co) and NiPtAl- bondcoats of various compositions.

The effect of the testing parameters strongly depended on the type and properties of the studied system. The lifetime of EB-PVD TBC systems with conventional MCrAlY and NiPtAl bondcoats forming uniform, flat alumina scales was found to be limited by critical scale thickness, upon which a rapid crack propagation at the scale/bondcoat interface results in macroscopic failure. The lifetime of such systems was found to be affected by factors, which influence the scale growth rate and adherence (in particular by oxygen partial pressure (pO_2) and water vapor content in the test gas in the case of MCrAlY), whereas the temperature cyclic frequency showed no significant effect. NiPtAl bondcoats showed a superior behavior than the conventional MCrAlY-bondcoats due to slower scale growth rate and better scale adherence. For EB-PVD TBC systems with Zr-doped MCrAlY-bondcoats the lifetime is mainly determined by the crack growth rate in the inhomogeneous inwardly growing oxide scales, whereas the lifetime is not dependent on the pO_2 but rather on the cyclic frequency.

For APS TBC systems the bondcoat oxidation is only one of several factors determining the ceramic topcoat lifetime. Therefore the oxide scale adherence is of less importance for lifetime of APS TBCs as compared to EB-PVD TBCs. For the former systems, the cracks initiated at the convex asperities of the rough oxide scale / bondcoat interface need to propagate through the TBC to cause macroscopic failure. The rate of crack propagation in the TBC is a critical step, which depends substantially on its microstructural properties. In addition to the TBC-porosity the bondcoat roughness profile is shown to be an important parameter, which to a large extent determines the rate of crack initiation and propagation. Higher Co-content in the bondcoat was found to stabilize its microstructure thereby lowering the CTE-mismatch stress in the ceramic topcoat thus extending the TBC-lifetime. The major drawback of high Co-contents was that such bondcoats are prone to form fast-growing spinel oxides. This effect, which was especially pronounced on rough surfaces could be suppressed by only a minor (few microns) enrichment of Al on the bondcoat surface prior to TBC-deposition produced by heat-treatment in high vacuum. With respect to the effects of experimental parameters it was found that contrary to EB-PVD TBC systems a higher cycle frequency leads to shortening of the APS TBC lifetime, whereas higher water vapor content had no significant influence.

The results of the present work indicate that the lifetime of the TBC systems with MCrAlY bondcoats would be shorter than that required for long-term operation (25 000 hours) at the envisaged operating temperature of 1000°C. Under such circumstances using NiPtAl-type of bondcoats or perhaps Pt-modified MCrAlY-bondcoats would be an option to obtain the necessary lifetime extension, which can even justify the high cost of metallic Pt.

Kurzfassung

Das Oxidationsverhalten von Haftvermittlerschichten ist ein wichtiger Faktor, der die Lebensdauer der Wärmedämmschichten auf Komponenten in modernen Gasturbinen bestimmt. In der vorliegenden Arbeit wurden die Einflüsse von Versuchsparametern, wie Hoch- und Raumtemperaturhaltezeit, Aufheiz- und Abkühlrate, Zusammensetzung der Atmosphäre, auf die Oxidation der Haftvermittlerschichten und die damit verbundene Lebensdauer der Wärmedämmschichten untersucht. Eine Reihe von Schichtsystemen wurde getestet, u.a. Electron Beam - Physical Vapor Deposited (EB-PVD) and Air Plasma Sprayed (APS) Wärmedämmschichten (WDS) mit MCrAlY (M = Ni, Co) und NiPtAl Haftvermittlerschichten unterschiedlicher Zusammensetzungen.

Der Einfluss der Versuchsparameter hängt stark vom Typ und den Eigenschaften der untersuchten Schichtsysteme ab. Die Lebensdauer der EB-PVD WDS Systeme mit konventionellen MCrAlY und NiPtAl Haftvermittlerschichten, die während der Oxidation eine homogene, flache Al-Oxidschicht bilden, ist durch eine kritische Oxidschichtdicke begrenzt. Nach dem Erreichen der kritischen Oxidschichtdicke erfolgt eine schnelle Rissbildung bzw. ausbreitung an der Grenzfläche Oxidschicht/Haftvermittlerschicht, die zu einem makroskopischen Versagen der Wärmedämmschicht führt. Als Folge von diesem Versagensmechanismus wird die Lebensdauer von den obengenannten Systemen sehr stark von Faktoren beeinflusst, die die Oxidschichtwachstumsrate und/oder Oxidschichthaftung bestimmen, insbesondere vom Sauerstoffpartialdruck in der Versuchsatmosphäre sowie dem Wasserdampfgehalt, wobei das thermische Zyklieren von Proben keinen wesentlichen Einfluss hat. Durch eine niedrigere Wachstumsrate sowie eine bessere Oxidschichthaftung zeigten sich die NiPtAl Haftvermittlerschichten den konventionellen MCrAlY Schichten überlegen. Die Lebensdauer von EB-PVD Wärmedämmschichten mit Zr-dotierten MCrAlY-Haftvermittlerschichten ist hauptsächlich durch die Geschwindigkeit der Rissausbreitung in inhomogenen, stark nach innen wachsenden Oxidschichten bestimmt und damit nicht durch den Sauerstoffpartialdruck, sondern durch das thermische Zyklieren beeinflusst.

Für die APS Wärmedämmschichten ist die Oxidation der Haftvermittlerschicht nur eine von mehreren lebensdauerbestimmenden Einflussgrößen. Deswegen ist die Oxidschichthaftung für die Lebensdauer der APS WDS, im Vergleich zu den EB-PVD WDS weniger bedeutend. In den APS WDS Systemen müssen sich die Risse, die sich in den konvexen Bereichen der rauen Haftvermittlerschichtoberflächen bilden, durch die keramische Wärmedämmschicht ausbreiten, um zu einem makroskopischen Versagen zu führen. Die Rissausbreitungsrate in der WDS ist ein kritischer Schritt, der signifikant von den mikrostrukturellen Eigenschaften der WDS abhängt. Zusätzlich zur WDS-Porosität scheint das Rauhigkeitsprofil der Haftvermittlerschicht ein wichtiger Parameter zu sein, das die Rissbildung bzw. –ausbreitung bestimmt. Außerdem wurde festgestellt, dass der höhere Co-Gehalt in der Haftvermittlerschicht deren Gefüge stabilisiert und damit die Abkühlspannungen durch die Unterschiede in thermischen Ausdehnungskoeffizienten zwischen der Oxidschicht bzw. WDS und Metallkomponenten reduziert, was zu einer Lebensdauerverlängerung der WDS führt. Der Nachteil der Co-reichen Haftvermittlerschichten ist, dass sie zur Bildung von schnellwachsenden Oxidschichten (Ni/Co-Spinell) neigen. Dieser negative Effekt, der speziell auf den rauen Haftvermittlerschichten beobachtet wurde, konnte mit einer geringen (wenige µm) Oberflächenanreicherung von Al durch die Wärmebehandlung in Hochvakuum vor dem Spritzen der APS WDS unterdrückt werden. Im Bezug auf die

experimentellen Parameter, wurde im Gegensatz zu EB-PVD WDS beobachtet, dass das thermische Zyklieren der APS-WDS zu einer Lebensdauerverkürzung führt und der Wasserdampfgehalt in der Testatmosphäre keinen großen Einfluss auf die Lebensdauer der APS WDS hat.

Die Ergebnisse der vorliegenden Arbeit deuten darauf hin, dass die Lebensdauer der EB-PVD sowie APS WDS Systeme mit MCrAlY Haftvermittlerschichten bei den zu erwarteten Betriebstemperaturen von 1000°C kürzer sein wird, als die von der Industrie gewünschte Lebensdauer von 25 000 Stunden. Unter diesen Bedingungen wird die Anwendung von NiPtAl oder überplatinierten MCrAlY Haftvermittlerschichten eine Option sein, um die erforderliche Lebensdauerverlängerung der WDS zu erzielen, die sogar die relativ hohen Kosten des Pt-Metalls rechtfertigen könnte.

Index

1. Introduction

1.1 Energy demand and requirements of environmental protection

Increasing of world population and world economy results in a growing energy consumption. The global primary energy demand is projected to increase by 1.5% per year between 2007 and 2030 [1]. Fossil fuel fired power plants will in the near future provide a large fraction of the total electricity supplies, which will still account for about 70% of electricity generated worldwide in 2030 (see Fig 1.1). The conversion of coal, oil and natural gas into electrical power is going to increase to 2.2×10^{14}kWh in 2030, which is around 75% more compared to 2007. Unfortunately, environment pollution and CO_2 emissions are expected to increase with increasing use of fossil fuel. Since power plants account for one third of the total CO_2 emissions [2], improvements in their efficiency can greatly contribute to the reduction of overall CO_2 emissions and also delay the time to exhaustion of conventional fossil fuels.

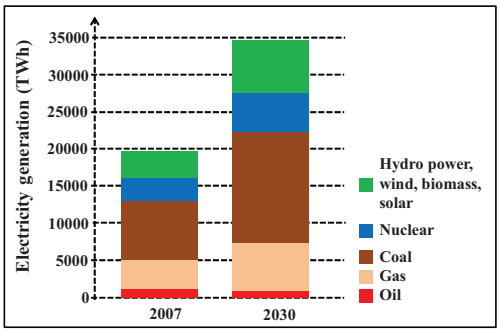

Fig. 1.1 Expected growth in electricity generation in 10^9 kWh worldwide [3]

Natural gas mainly consisting of methane is available from underground gas fields, or sometimes as a byproduct of oil drilling. Natural gas burns cleanly, which basically eliminates the emissions of sulphur oxides and particulates, two of the most serious atmospheric pollutants. Easy transportation using pipelines is another advantage of natural gas as a fuel versus coal. In addition, from all fossil fuels natural gas has the lowest CO_2 output per kWh produced in the operating power plants [3]. According to the data from the International Energy Agency (IEA), the use of natural gas in the power generation sector is expected to almost triple from 2002 to 2030 [1]. Considering the economic and environmental factors, high-efficiency turbines using natural gas appear to show a number of advantages in the power generation sector. Gas turbines can be particularly efficient, up to 60%, when waste heat from the turbine is recovered in a steam generator to drive a conventional steam turbine in a combined cycle configuration. As a result, the world natural gas consumption is projected to more than double over the next three decades, rising from 23% to 28% of world total primary energy

demand by 2030 and surpassing coal as the world's number two energy source and potentially overtaking oil's share in many large industrialized economies [1].

To simultaneously satisfy the increasing energy demand and greenhouse gases reduction, CO_2 capture technologies in recent years for fossil fuel firing power plants are being developed, as shown in Fig 1.2. However, the efficiency of gas turbines operating in such a power plant configuration will be decreased due to energy consumption by the CO_2-capture processes. Higher turbine operating temperatures could be one of strategies to compensate the efficiency penalties of CO_2-capture. Integrated Gasification Combined Cycle (IGCC) power plants with pre-combustion CO_2-separation shown in Fig 1.2, are considered to be implemented on an industrial scale in the near future [2]. In these advanced power plants a high-efficiency gas turbine will be operating under the conditions of increased water vapor content compared to combustion gas produced by burning natural gas.

In addition gas turbines are often used to compensate daily peaks in electricity consumption as well as fluctuations in power output from renewable energy sources (wind, solar etc). Therefore, a new generation of gas turbines should be able to operate under such conditions: higher operating temperatures, more H_2O-rich atmosphere and more frequent start-ups. This imposes increased requirements on the gas turbine materials, as will be discussed in the next chapter.

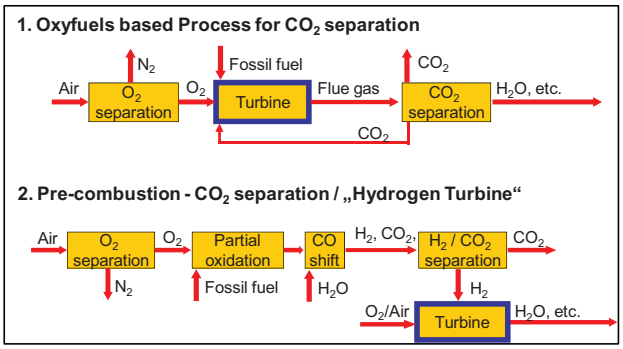

Fig. 1.2 Schematics for CO_2 Capture Technologies [2]

1.2 Gas turbine materials

A typical gas turbine used in a modern power plant is showed in Fig 1.3. Gas turbines operate thermodynamically according to the Brayton cycle, whereby the fuel gas mixed with air undergoes three main processes: compression, combustion and expansion. Air compressed to high-pressure in a multi-stage compressor enters the combustion chamber. Fuel and high-pressure air are combusted to form high-pressure exhaust gas, which is then released into the expansion stage (turbine). Through a series of rotating blades on a shaft in the turbine the exhaust gas drives an electrical generator. The temperature of the exhaust gas entering the turbine (turbine inlet temperature) can be as high as

1200°C~1400°C. Finally, the hot exhaust gas leaving the gas-turbine can be recovered to steam production to power a conventional steam turbine, thereby improving the efficiency of the power plant.

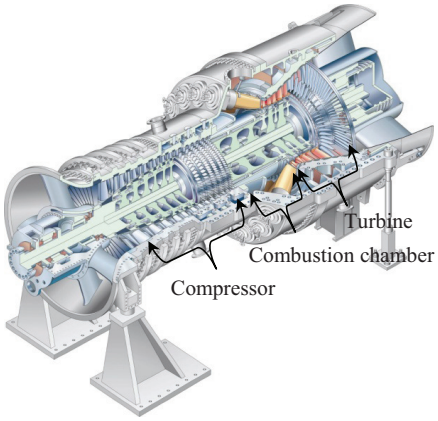

Fig. 1.3 Gas turbine - SIEMENS SGT5-8000H (340MW)

The elevated turbine inlet temperature directly affects the materials in the hottest sections of the gas-turbine, i.e. combustion chamber, vanes and blades, which should fulfill a number of requirements: high creep strength, suitable ductility at low temperatures, and high oxidation (corrosion) resistance. Most of these requirements are fulfilled nowadays by the so-called superalloys. The developments of new superalloy compositions and processing routes in the recent years allowed an increase of the turbine inlet temperature (Fig 1.4), thereby substantively contributing to the increase of the net efficiency of gas-turbines.

Superalloys are nickel-, iron-nickel-, and cobalt-base alloys generally used at temperatures above 800°C. From Fig 1.4 it can be seen that modern superalloys operate at temperatures which are relatively near to the alloy melting temperature. Many alloy compositions have been developed over the past decades [4]. The superalloy creep properties at high temperature are improved by the reduction of grain boundaries as a source of weakness for the mechanical properties. This resulted in development of directionally-solidified as well as single-crystal superalloys. The advanced single-crystal alloys now allow operating temperatures up to about 1100°C compared to 750°C for the first wrought superalloys developed in the 1940s [5].

A Ni-base superalloy typically consists mainly of a γ-Ni matrix and γ′-Ni_3Al strengthening precipitates. In the nickel-base alloys, chromium, as a strong γ phase and carbide stabilizer, is incompatible with the very high creep resistance alloys which contain high γ′ fraction. Excess Cr content also impairs the alloy microstructure stability by promoting formation of brittle TCP phases, such as σ-(Co, Cr) intermetallic. However, the high Cr content in superalloy is preferred to obtain high

hot corrosion resistance in harsh operating environments, whereas a high aluminum content of the alloys increased and chromium content decreased in order to reduce the negative Cr-effect on the creep properties of superalloys, especially at high temperatures (greater or 1000°C). Therefore, an optimum composition of the superalloys should be considered to maintain a balance of various properties. Newer generations of superalloys contain higher amounts of Al (5-6 wt%) and lower amounts of Cr (6-8 wt%) compared to alloys of earlier generations, which typically contained 3-4% Al and 12-16% Cr. This change in the alloy chemistry allowed an increase in the volume fraction of γ′ precipitates and consequently improved the alloy creep strength.

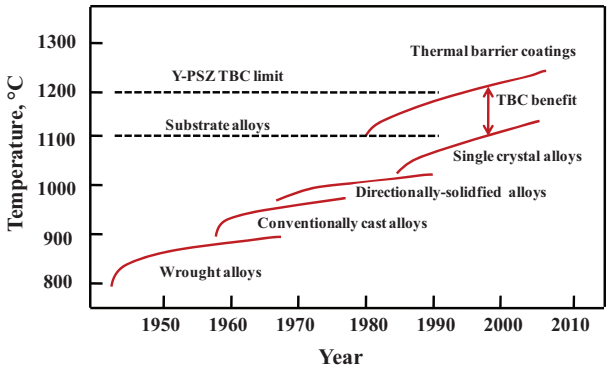

Fig. 1.4 Alloys and coatings development for gas turbine blades [6]

In modern gas turbines the turbine inlet temperatures increased to values exceeding the capabilities of superalloys with respect to mechanical strength and environmental stability. Therefore a superalloy component in the hottest sections of a gas turbine has to be coated. Aluminum rich thermally sprayed MCrAlY (M=Ni, Co) and/or aluminized coatings are applied on the surface of superalloys due to their ability to form a protective Al-oxide surface layer during exposure. Furthermore, the advanced gas turbine components are nowadays internally cooled, which reduces significantly the surface temperatures. The cooling efficiency can be greatly improved by using a ceramic thermal barrier coating (TBC) (Fig 1.4). Details of TBC composition, properties, manufacturing and operation are discussed in the next chapter.

2 TBC Systems

Thermal barrier coating (TBC) systems [7-10] consist of a ceramic top coat, most commonly yttria-stablized zirconia (YSZ), and an underlaying metallic bondcoat (BC) which are applied onto a superalloy component in the gas turbine. The ceramic top coat should have a low thermal conductivity, thereby reducing the heat transfer from hot gases (over 1200°C) to the structural superalloy component, a coefficient of thermal expansion (CTE) similar to that of the superalloy and a high strain tolerance. The metallic bond coating located between the ceramic layer and superalloy should have a sufficiently high aluminum content to form a protective thermally grown oxide (TGO) mainly consisting of α-Al_2O_3, and a CTE similar to the TBC and superalloy as well as good chemical compatibility with the base material (minor interdiffusion, possibly no brittle phase formation). Fig 2.1 shows macro photos of a TBC coated, internally cooled turbine blade and a schematic curve of the temperature distribution across the TBC-system.

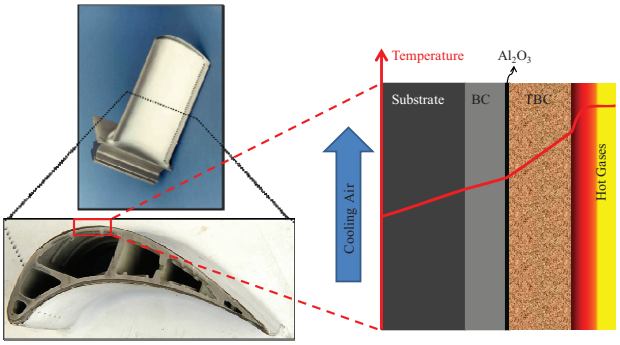

Fig 2.1 Cross-section of a TBC-coated turbine blade and schematic of temperature gradient in TBC cross-section

2.1 Ceramic Top coat

The ceramic top coat material directly exposed to the high temperature combustion gases should possess a high melting temperature, a high thermal reflectivity, good oxidation and corrosion resistance, low thermal conductivity, high coefficient of thermal expansion, and chemical stability. Based on the above requirements, ZrO_2 ceramics stabilized with 6-8% wt% Y_2O_3 are commonly applied for TBC top coats. Under equilibrium conditions, yttria at this level enters the zirconia solid solution and stabilizes its tetragonal crystal structure (t-YSZ) above about 1050°C. Numerous studies [7, 11] have shown that 6-8% wt.% Y_2O_3-stablized ZrO_2 is very suitable for TBC applications due to its average coefficient of thermal expansion (CTE, 9-11.5×$10^{-6}K^{-1}$) being close to that of the superalloys (12-14×$10^{-6}K^{-1}$). It also possesses a low thermal conductivity at elevated temperature (e.g., ~2.3 $W{\cdot}m^{-1}K^{-1}$ at 1000°C for compact polycrystalline ceramic) which is more than an order of magnitude below those of Ni-base superalloys and many other ceramics.

Up to now, alternative ceramic materials for the advanced next generation ceramic top coatings have been searched in numerous investigations. A number of zirconates (e.g. $La_2Zr_2O_7$, $Gd_2Zr_2O_7$, $SrZrO_3$) [12-13], Hafnates and Cenates (e.g. $La_2Hf_2O_7$, $La_2Ce_2O_7$) [14-15] as well as rare earth base compounds (e.g. $LaYbO_3$) [15] are of special interest. Some of them exhibit only a single phase from room temperature up to the melting temperature, which is higher than 2200°C [15]. However, no single material was found, which satisfies all the above requirements better than YSZ. Some materials with high temperature stability and lower thermal conductivity were developed, however, they have a lower coefficient of thermal expansion and lower fracture toughness which often leads to a reduced TBC lifetime under thermal cycling conditions. Therefore, ZrO_2 ceramics stabilized with 6-8% wt% Y_2O_3 are still applied in most state-of-the-art TBCs due to high strength, fracture toughness, and chemical stability as well as a relatively low Young's modulus.

Processing technologies to deposit ceramic topcoats [16-17] include Air Plasma Spraying (APS) [18-19] and Electron-Beam Physical Vapor Deposition (EB-PVD) [20-21]. With the EB-PVD process, the coating is obtained by condensation of a vapor on the substrate. The vapor can be produced by heating the anode material through a focused electron beam under high vacuum. The EB-PVD processing has already shown large scale industrial application for the TBC systems due to a high deposition rate (several micrometers per minute) and a high strain tolerance as well as good surface finish of the coating. However, EB-PVD is a line-of-sight deposition process, thereby it cannot be used to coat the inner surface of complex geometries.

The columnar microstructure is a specific characteristic of EB-PVD TBC's, which clearly differs from that produced by APS process (Fig 2.2). The inter-columnar spacing significantly contributes to a high level of strain compliance of EB-PVD TBC's. In contrast, the APS process is based on melting and accelerating YSZ powder in a plasma jet, which is generated by ionization of a gas such as Ar. The molten particles are directed at high velocity onto the substrate. Upon impact with the substrate, the molten particles flatten and solidify very rapidly. Therefore, the adhesion between the molten particles and substrate is primarily mechanical. This sprayed coating will typically include voids (10-20% porosity), as shown in Fig 2.2b, which reduce the thermal conductivity and increase the strain-

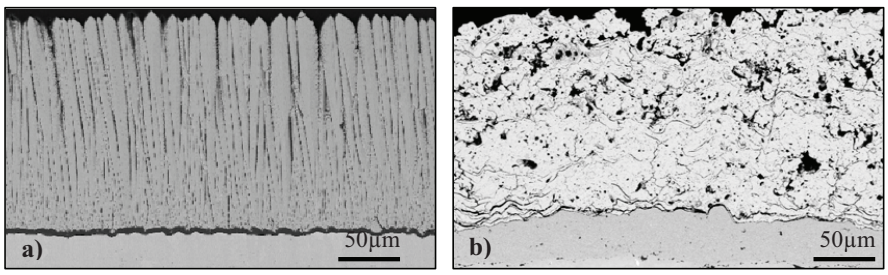

Fig 2.2 Microstructures of yttria stabilized zirconia TBC's deposited by a) EB-PVD, b) APS (SEM cross-sections)

tolerance. EB-PVD deposited coatings are comparatively smoother than APS coatings, which could increase the erosion resistance. Adhesion of EB-PVD coatings to the metallic bondcoat is generally much higher (around 400MPa) than that of APS coatings, which only is about 20-40MPa [22]. However, an advantage of APS is the wide range of processing temperatures, which enables use of materials and compounds with different melting characteristic, as well as much lower process costs compared to EB-PVD.

The YSZ microstructure has a large influence on the coefficient of thermal conductivity of the coating [23], whereby the defects resulting from APS processing such as cracks and pores typically reduce it compared to the comparatively dense YSZ produced by EB-PVD. The thermal conductivities of EB-PVD YSZ are in the order of 1.5-1.9 $W \cdot m^{-1}K^{-1}$, which is about a factor of two larger than the 0.8-1.1$W \cdot m^{-1}K^{-1}$ range found for APS YSZ coatings [24]. The columnar microstructure of the EB-PVD YSZ top coat allows an increased phonon and photon penetration compared to the APS top coat containing defects such as micro-cracks and pores parallel to the coating surface.

2.2 Metallic Bond coats

2.2.1 General Remarks

If the Al concentration in a metallic high temperature alloy is below the critical content necessary to form a continuous protective alumina scale, fast growing Ni and Cr-rich oxide scales form on the surface of the alloy (Fig 2.3a and b). This is a typical situation of an uncoated superalloy, whereby spallation of the non-protective oxides scales leads to fast metal consumption (Fig 2.3c). The TBC directly (without bondcoat) deposited on a superalloy would result in severe oxidation of the base material, which is typically followed by rapid spallation of the ceramic topcoat [25]. It should be mentioned that, due to the high oxygen permeability of YSZ, the ceramic topcoat cannot prevent or reduce the substrate oxidation.

To improve the oxidation resistance of the TBC coated superalloy, a metallic bond coat is deposited between ceramic top coat and superalloy component. The bondcoat oxidation resistance, chemical stability and mechanical properties influence the lifetime of the whole TBC system. Therefore, a number of requirements for the bond coat have to be fulfilled, such as formation of a slow growing and adherent TGO, a small CTE difference between TBC and superalloy, and chemical compatibilitywith the superalloy i.e. possibly a small interdiffusion rate and no brittle phase formation. In addition to the above mentioned properties the bondcoat provides in APS-TBC systems a rough surface necessary for a good mechanical keying of the TBC.

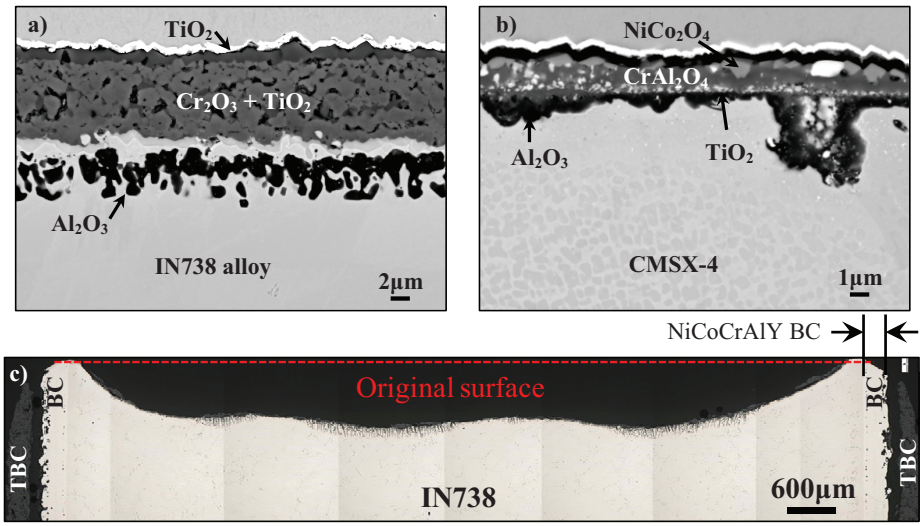

Fig. 2.3 Cross-sections of Ni-base superalloys a) IN738 and b) CMSX-4 after exposure in air for 24h at 1050°C; c) Cross-section of superalloy IN738 partially coated with TBC system with NiCoCrAlY bondcoat after oxidation for 2835h in air at 1050°C

The bond coats provide oxidation protection to the underlying superalloy by formation of a protective alumina scale [26-27]. In order to obtain formation of a continuous layer of α-Al_2O_3 during longer oxidation times a large aluminum reservoir in the bondcoat is required. For this purpose, two types of bond coats for TBC systems are presently commonly applied to a superalloy component: MCrAlY (M=Ni, Co) [28-30] and diffusion aluminide [31-33] coatings.

2.2.2 MCrAlY coatings

The MCrAlY coatings developed until now can be classified into NiCrAlY, CoCrAlY and NiCoCrAlY [34] which have differences in high temperature corrosion and oxidation resistance. The MCrAlY bond coat composition affects the TGO composition, growth rate, adherence and failure mechanisms. Therefore, optimized NiCoCrAlY bond coat compositions may be a useful approach to extend the TBC systems lifetime. CoCrAlY coatings are claimed to have better hot corrosion resistance and poorer oxidation resistance than NiCrAlY coatings. The main composition in the coatings can affect their thermal stability [35] and oxidation resistance. The NiCoCrAlY or CoNiCrAlY coatings provide a balance of oxidation and hot corrosion resistance. Figure 2.4 shows schematically corrosion and oxidation resistance properties of different kinds of MCrAlY bond coats.

High Cr and Al contents in MCrAlY bond coats are beneficial from the viewpoint of corrosion and oxidation resistance [36], however, a negative effect is observed simultaneously on the coating

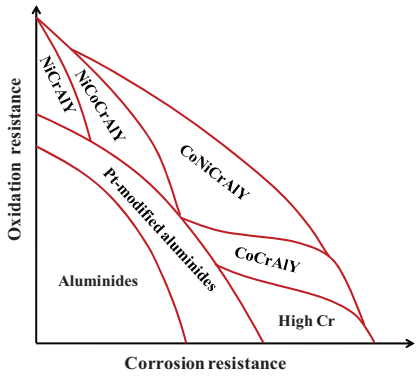

Fig 2.4 Schematic comparison of oxidation and corrosion resistance for different bondcoats [37]

ductility. Therefore, the Al and Cr contents in the bond coats should be optimized in order to balance a high fatigue resistance with a sufficiently high Al reservoir to form a continuous and compact α-Al_2O_3 layer even after long term high temperature exposure.

At high temperatures (above 1000°C) the NiCoCrAlY bond coats mainly consist of two phases [35]: γ-Ni solid solution (with Co, Cr, Mo and Re et al) and β-NiAl intermetallic compound. During high temperature oxidation, Al is constantly consumed from the coating due to growth of the α-Al_2O_3 scale and because of interdiffusion with the superalloy substrate. This will induce a phase transformation from β-NiAl to γ-Ni. With decreasing temperature, however, the MCrAlY coating microstructure is commonly more complex than the two phase γ + β structure. For ternary NiCrAl coatings it was shown [38] that the γ phase transforms at lower temperatures, e.g. 900°C, to γ′ and α-Cr.

Additions of rhenium, tantalum, and silicon to some MCrAlY coatings were found to affect the oxidation resistance and in particular the oxide scale adherence. Re promotes the presence of σ and α-Cr phases which can influence the thermo-mechanical fatigue resistance [39]. Ta was found to improve the yield strength and oxidation resistance of MCrAlY coatings [40].

Additions of so-called reactive elements (e.g. Y, Hf, La, Ce, Zr) have a substantial influence on the oxidation resistance of MCrAlY coatings and in particular greatly improve the alumina scale adherence. The details of reactive element effect (REE) will be discussed in chapter 3.2.2. Additions of Ce [41] and Hf [7, 42] apparent to have a beneficial effect on the high temperature oxidation resistance and mechanical properties of MCrAlY coating.

The MCrAlY coatings are manufactured by different processes such as electron-beam physical vapor deposition (EB-PVD) [43], low pressure plasma spraying (LPPS) [44], atmospheric plasma spraying (APS) [45], vacuum plasma spraying (VPS) [46] or high velocity oxy-fuel spraying (HVOF) [47]. The

EB-PVD process is able to produce comparable clean bondcoat compared to APS, however, the cost of bondcoat production by EB-PVD is higher than others industrial processing such as LPPS and HVOF, which were developed in recent decades.

2.2.3 NiPtAl coatings

Platinum-modified β-NiAl diffusion coatings are commonly applied to high-pressure turbine blades and nozzles in aero engines. Pt is applied by electroplating a 6~9 μm platinum layer onto the Ni-base superalloy prior to diffusion aluminizing via pack cementation, which is a modified chemical vapor deposition process. In the pack cementation process [48-49], the superalloy components (Fig 2.5) to be coated are embedded in a reactor filled with a powder mixture including an Al-rich alloy, an activator (halide salt), and an inert filler material such as Al_2O_3. Upon heating up the container, a volatile Al-containing halide will be generated and transport to the component surface. A chemical reaction between halides and substrate alloy occurs, which the Al-containing halide will be decomposed on the substrate surface resulting a metal deposition followed by associated diffusion process within the substrate alloy. In case of Al-rich alloys, β-NiAl will be formed as a consequence of Al-deposition and diffusion into the substrate, which results the formation of an aluminide coating on the surface of the components. Depending on the processing conditions, Pt is included within the coating as single phase solid solution Ni(Pt)Al or two phases $PtAl_2$ and solid solution Ni(Pt)Al. Pack cementation is a relatively cheap process which allowing to coat many components at the same time.

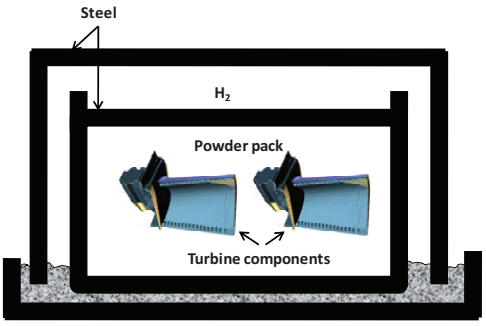

Fig 2.5 Schematic for pack cementation set up

There are two types of diffusion (platinum modified) aluminide coatings. The first type (high-a_{Al} coating) is formed at T≤1000°C by predominant inward diffusion of aluminum due to a sufficiently high aluminum activity. The second type (low-a_{Al} coating) is formed by predominant outward diffusion of nickel from the substrate alloy to react with aluminum to form a β-NiAl coating.

Pt exists as solute in the β-NiAl matrix or as a $PtAl_2$ compound in the coating. The NiPtAl coatings are currently used as bond coats only for EB-PVD TBC's, commonly deposited on commercial single-crystal Ni-base superalloys such as CMSX-4 and Rene N5. The TBC systems with NiPtAl bondcoats

were observed to have good performance in thermal cyclic testing at high temperature. The performance of β-NiPtAl and/or $PtAl_2$ aluminide coatings is limited by oxide scale rumpling, which was proposed to be associated with thermally induced stress, with β to γ′ phase transformation [50-51] as well as martensitic transformation [52]. A new class of diffusion Pt-modified aluminide coatings based on the γ-Ni + γ′-Ni_3Al system, has been recently developed by Gleeson [53]. The Pt-modified γ-Ni + γ′-Ni_3Al coatings showed excellent oxidation resistance and elimination of surface rumpling [32, 54], however it was observed to have a faster oxide scale growth rate than β-NiPtAl coatings [55].

3 Oxidation of Bondcoats in TBC systems

3.1 Oxidation of metals

The reaction between a metal and oxygen may lead to formation of an oxide. This reaction can for the simplest case of oxide MO_2 be expressed as:

$$M + O_2 = MO_2 \tag{3.1}$$

For constant temperature and pressure, the driving force (the Gibbs free energy) for the above reaction (3.1) is given by:

$$\Delta G = \Delta G_0 + RT \ln\left(\frac{a_{MO_2}}{a_M pO_2}\right) \tag{3.2}$$

Where, pO_2 is the oxygen partial pressure, a_M and a_{MO_2} are the activities of metal and oxide, respectively.

For the case of thermodynamic equilibrium, ΔG is equal to zero. The standard Gibbs free energy (ΔG_0) per mole of oxygen can be used to compare the stability of different oxides.

$$\Delta G_0 = -RT \ln\left(\frac{a_{MO_2}}{a_M pO_2}\right) \tag{3.3}$$

For unit metal and oxide activities, corresponding to pure metal and oxide, Equation 3.3 can be plotted in the form of a so-called Ellingham diagram, as shown in Fig 3.1. The values of the dissociation pressures for selected metal oxides can be obtained from Fig 3.1, which also includes the values of H_2/H_2O and CO/CO_2 pressure ratios corresponding to a given pO_2.

$$pO_2 = \exp\left(\frac{\Delta G_0}{RT}\right) \tag{3.4}$$

As can be observed from the Ellingham diagram, a lower (more negative) standard free-energy change for an oxide formation corresponds to a higher thermodynamic oxide stability and lower dissociation pressure.

The standard Gibbs free energies (ΔG^0) and oxide dissociation pressures derived from Fig 3.1 at 1000°C are summarized in Table 3.1 for oxides of a number of common alloying elements in MCrAlY and NiAl coatings. It can be seen that Al has the highest O-affinity, which is a prerequisite for formation of selective Al oxidation.

For protective oxide scale formation, another factor, called the Pilling-Bedworth ratio (*PBR*) also has to be considered. The *PBR* is the ratio between the volume of oxide formed and the volume of metal consumed to form the oxide. Continuous oxide scales can be expected only on metals for which the *PBR* is larger than 1, e.g. *PBR* (Al)=1.28; *PBR* (Cr)=2.07; and *PBR* (Fe)=2.10 [36]. For a number of metals such as W or Mo the *PBR* is much larger than two leading to high growth stresses in the respective oxide scale, which results in oxide scale spallation.

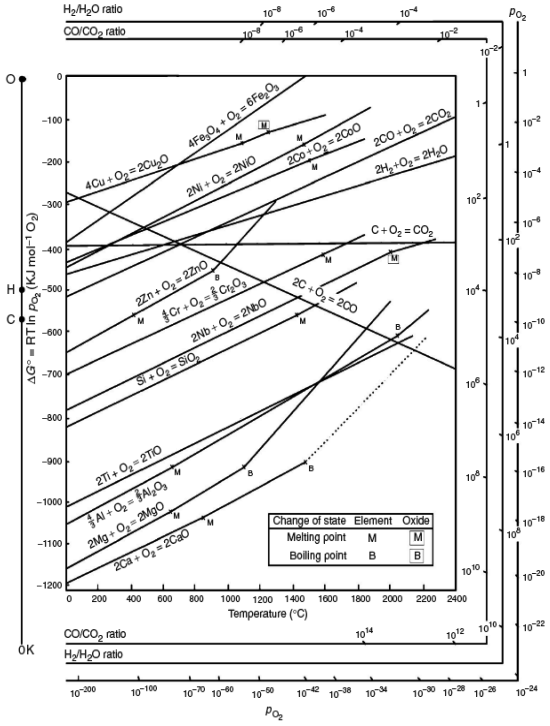

Fig 3.1 Ellingham-Richardson diagram for standard free energy of oxide formation per mole of oxygen [36]

Table 3.1 ΔG^0, pO_2 for the oxide formation of pure elements in MCrAlY coatings, 1000°C, 10^5Pa

	NiO	CoO	Cr_2O_3	Al_2O_3	SiO_2
ΔG^0 of oxide formation, kJ/mol O_2, 1000°C, 10^5Pa	-127	-144	-264	-403	-341
Oxygen pressure for oxide dissociation, bar	3.7E-11	1.5E-12	2.1E-22	8.3E-34	1.1E-28

If a continuous compact oxide layer forms on the alloy surface the reaction rate is commonly limited by diffusion of the reactants through the scale. The oxide scale growth by diffusion was first described by Wagner [36]. Thermodynamic equilibrium at the metal/oxide and oxide/gas interface is assumed to be established (as showed in Fig 3.2), which results in metal and oxygen activity gradients across the

oxide scale in opposite directions. The activity gradients will induce metal and oxygen ions to migrate across the scale.

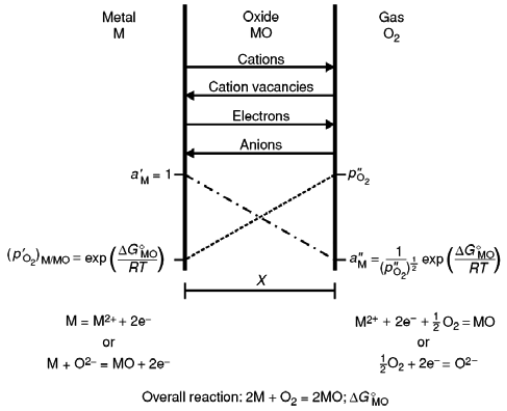

Fig 3.2 Schematic of oxide scale formation based on Wagner's model [36]

According to Wagner theory the scale growth obeys a parabolic rate law, i.e $X^2 = K \cdot t$, Where X is the oxide scale thickness, t is exposure time, and K is parabolic rate constant. For the cases of α-Al_2O_3 formation on MCrAlY and NiPtAl coatings, the growth of protective α-Al_2O_3 often follows a sub-parabolic time dependence:

$$X = K' \cdot t^n \tag{3.5}$$

where, n is constant ($0.33 \leq n \leq 0.5$).

The reason for deviation from the parabolic law is that scale growth occurs not via lattice diffusion but rather over grain boundaries, whereas the grain boundary density was observed to decrease with increasing scale thickness due to the columnar oxide microstructure. This effect was demonstrated earlier for FeCrAl ODS alloys [56], NiAl-alloys [57] and recently for FeCrAlY alloys [58].

3.2 Formation of TGO in TBC systems

A slow growing and adherent oxide scale forming on the bondcoats is a critical factor for the lifetime of TBC systems. From this viewpoint, Al_2O_3 and Cr_2O_3 as well as SiO_2 are typically considered as protective oxide layers on high temperature materials. However, SiO_2 is unstable at low pO_2 and/or high pH_2O atmospheres due to the formation of SiO and/or $SiO(OH)_2$. In addition, a high Si-content in the coatings would result in deterioration of its mechanical properties, especially ductility. Since the turbine component operating temperatures are higher than 1000°C Al_2O_3 scales are preferred compared to Cr_2O_3 scales because the latter show faster growth rates and are prone to volatilization [59] at high pO_2.

Although α-Al_2O_3 is a slowly growing oxide, alumina can also exist in other metastable crystal structures, which include cubic-spinel γ-Al_2O_3, tetragonal δ-Al_2O_3, and monoclinic θ-Al_2O_3. These transient metastable aluminas grow significantly faster (see Fig 3.3) than α-Al_2O_3 due to rapid outward cation transport, which results in typical scale morphologies containing whiskers/needles. The transformation of metastable alumina into stable α-Al_2O_3 produces tensile stresses due to a considerable volume reduction, which can influence the durability of a TBC system. Recently, some researchers found that reactive elements such as Hf [60], can suppress the metastable alumina growth and that Pt [33] hinders the θ to α-Al_2O_3 phase transformation.

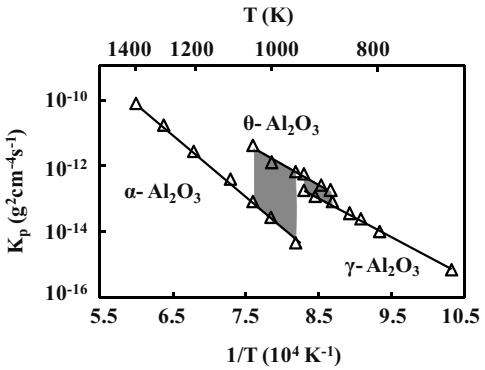

Fig 3.3 Arrhenius plot of parabolic rate constant (*Kp*) for the oxidation of pure NiAl [61]

After the transient oxidation stages, the α-Al_2O_3 formation plays an important role in the long term integrity of TBC systems with MCrAlY and NiPtAl coatings. Failure of TBC has been associated with the formation, growth and failure of alumina, which is affected by the aluminum reservoir in the coating, bondcoat composition, operating temperature, atmospheres and cyclic conditions as well as interdiffusion with the superalloys.

3.2.1 Effect of main coating composition on TGO formation

For the NiCrAl alloys with different contents of Al and Cr, three types of oxidation behavior based on empirical data were found (Fig 3.4):

(1) NiO external scale + Al_2O_3 /Cr_2O_3 sub-surface internal oxides for coating with low Al and Cr content
(2) Cr_2O_3 external scale + Al_2O_3 sub-surface internal oxides for coating with high Cr content
(3) only Al_2O_3 scale, especially for coating with high Al content

The Cr addition to Ni-Al alloys results in Cr-rich oxides formation during transient oxidation, which reduces the inward flux of oxygen thereby promoting exclusive Al_2O_3 formation. The effect of Cr on

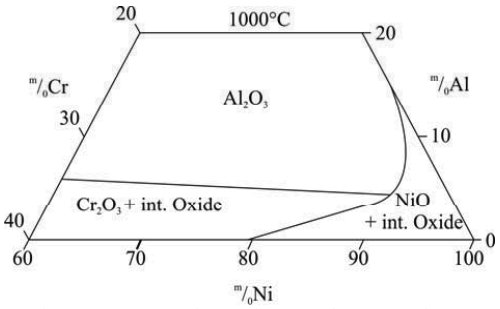

Fig 3.4 Schematic map for the oxide formed in NiCrAl system at 1000°C [62]

decreasing the critical Al content for external scale formation alloys can be described by the Wagner's formula for the transition from internal to external Al oxidation [36]:

$$N_{Al}^{(O)} > \left[\frac{\pi \cdot g^*}{2\nu} N_O^{(S)} \frac{D_O V_m}{D_{Al} V_{OX}} \right]^{1/2} \tag{3.6}$$

where D_O and D_{Al} are the diffusion coefficients of oxygen and aluminum in the alloy respectively, $N_O^{(s)}$ is the oxygen solubility in the alloy, ν is the valence of the metal in the oxide per mole metal, and V_{OX} and V_m are the molar volume of oxide and metal, respectively. The parameter g^* is the critical value for the volume fraction of oxide, $g=f(V_{OX}/V_m)$, for transition from internal to external scale formation to occur, and is commonly amount to be approximately 0.3.

Equation 3.6 shows that the critical Al-content for external alumina scale formation can be reduced if N_O and D_O are decreased and/or D_{Al} is increased. One of these factors is responsible for the effect of Cr promoting external oxidation of Al. For example, from Table 3.1 it follows that the dissociation pressure of Cr_2O_3 is significantly lower than that for NiO. Therefore alloying with Cr will reduce the oxygen solubility in the Ni matrix.

Cobalt additions in the MCrAlY coatings stabilize the γ and β phases within a large temperature range thereby suppressing the γ′-Ni_3Al phase formation which is formed from γ at temperatures below 1000°C in ternary NiCrAl alloy [38]. This transformation was shown to be associated with an increase of the boundcoat CTE [35]. Fig 3.5 shows a comparison of CTEs for the MCrAlY, NiPtAl, a superalloy and YSZ.

3.2.2 Effect of reactive elements (RE) additions in the coating on TGO formation

Small additions of reactive elements such as yttrium are typically present in MCrAlY coatings with a concentration of about 0.1 to 1 wt% to improve the alumina scale adherence. Yttrium, however, added in higher concentrations was observed to increase the oxide scale growth rate due to the fact that RE-

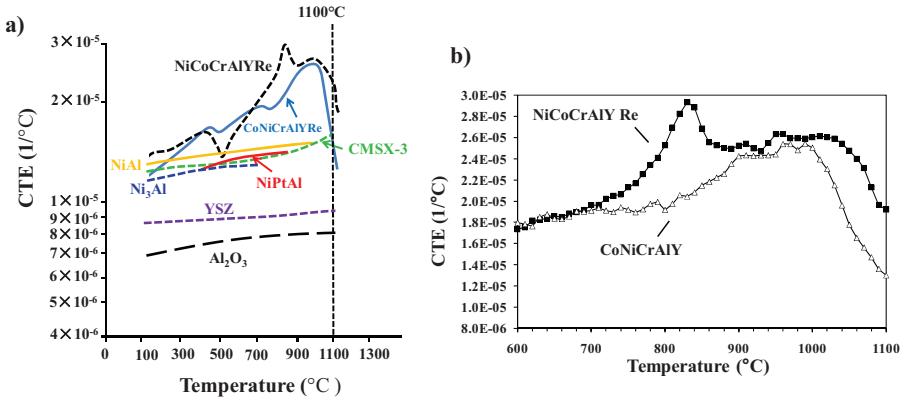

Fig. 3.5 Physical CTE as a function of temperature a) for the MCrAlY and NiPtAl coatings, NiAl and Ni_3Al, Al_2O_3 and YSZ as well as superalloy CMSX-3 [63-64], b) Detailed physical CTE as a function of temperature for the NiCoCrAlYRe and CoNiCrAlYcoatings [35]

oxide particles incorporated into the scale provide short-circuit paths for the inward oxygen transport [65]. Quadakkers [66] et al found that an increase of the yttria content in FeCrAl ODS alloy increases the scale growth rate. He explained that yttria-containing compounds enhance the oxygen transport via oxide grain boundaries or decrease the oxide scale grain size. A similar phenomenon of the oxygen inward transport being promoted by RE's such as Y, Y+Hf and Y+Zr, in NiCoCrAl coatings were also observed in Ref. [67]. The high Y-content can result in the formation of different mixed Y-Al oxide precipitates at the grain boundaries of the oxide scale such as $Y_3Al_5O_{12}$ (YAG: yttrium-aluminum-garnet) and $YAlO_3$ (YAP: yttrium-aluminum-perovskite) [68]. Some results indicated that these yttrium aluminates are detrimental to the oxide scale adhesion under certain circumstances [69] because of the different CTE's of Al_2O_3 and the yttrium aluminates. Other authors [70] found, in contrast, a beneficial effect of mixed Y-Al oxide pegs on the scale adhesion. Consequently, the proper concentration of yttrium in the coating is a very important factor for protective scale formation. However, the concentration of "free" yttrium in the MCrAlY coatings is difficult to control due to variations in the coating manufacturing parameters [67]. The commercial bond coat alloys commonly contain higher Y concentrations than would be necessary for ideal scale doping; this is to compensate the fact that part of the Y reacts with oxygen impurities during the thermal spraying process.

Several mechanisms [71-72] have been proposed to explain the RE effect, however, there is still no general agreement in the literature on their validity. These mechanisms include segregation or enrichment of RE to the metal/oxide interface to improve the adherence of oxide [72], change of the scale growth mechanism [73-74], hindering sulfur enrichment at the oxide/metal interface thereby preventing void formation [75]. The mechanisms, which got the largest amount of experimental evidence are:

- Changing the Al_2O_3 growth mechanism from simultaneous diffusion of metal and oxygen ions to nearly exclusive oxygen inward diffusion via oxide grain boundaries [66, 76]. Exclusive inward diffusion via TGO grain boundaries can effectively prevent vacancy condensation at the oxide/metal interface thereby improving the scale adherence.
- Improving the adherence of α-Al_2O_3 to the bond coat by gettering deleterious sulphur impurities, which can otherwise facilitate void growth [77]; gettering thus suppresses delamination at the TGO/bondcoat interface [75, 78-80].

3.2.3 Effect of Pt on oxide scale formation

To achieve a long TBC system lifetime, Pt-modified aluminide bondcoats are considered as coatings with a high potential because of their lower coefficient of thermal expansion (~$1.3\times10^{-5}K^{-1}$ within 400°C-900°C [63]) compared to MCrAlY coatings (~$1.8\text{-}2.6\times10^{-5}K^{-1}$ between 600°C-1000°C [35]), which is more comparable with the CTE of Al_2O_3 (~$0.7\text{-}0.8\times10^{-5}K^{-1}$ between 200°C-1200°C [63]).

For NiAl diffusion coatings Pt additions were shown to prolong significantly the coating lifetime. Several mechanisms have been proposed to explain the positive role of Pt addition on the coating performance as compared that of the conventional aluminides:

- Improving oxide adherence by preventing void formation at the oxide/coating interface [42], or mitigating the effects of sulphur in the alloy and coating [81-82].
- Promoting selective oxidation of Al, thereby promoting formation of a purer oxide, which in turn decreases the oxide growth rate and thus delays the onset of oxide spallation [83].
- Increasing the diffusivity of Al and decreasing the diffusivity of other elements, thereby promoting a rapid formation of alumina scales, also at lower Al concentration [84].
- To lower the rate at which β-NiAl transforms to the γ'-Ni_3Al phase beneath the oxide scale [85]. It is, however, not clear whether that occurs by stabilization of β-NiAl or whether it is a diffusion related mechanism. Pt increases slightly the isothermal oxide scale growth rate and slows down the transformation of transient to thermodynamically stable α-Al_2O_3 [33].

Attempts were made to use the Pt effect in TBC systems with MCrAlY bondcoats [86]. The lifetimes measured in cyclic oxidation test at 1000°C appeared to be well reproducible and longer than when using conventional bondcoats without Pt.

3.3 Failure of TBC systems

Although in some cases the TBC failure has been associated with the sintering of the TBC [87] and foreign object damage (FOD) [88] in most of the cases TBC-failure has been related to bondcoat

oxidation. It is important to mention that the TBC failure mechanisms for EB-PVD system differ from those for APS TBC coating.

3.3.1 Failure mechanisms for EB-PVD TBC systems

The failure of EB-PVD TBC's typically occurs at the TGO/bondcoat interface indicating that the TGO formation is a critical issue in the durability of the TBC systems. TGO buckling (Fig 3.6a) and subsequent spallation is a commonly observed failure mode for the EB-PVD coatings under residual compressive stress in the TBC and the oxide scale. The stress is induced by the thermal expansion misfit between TBC, TGO and underlying metallic components (MCrAlY or NiPtAl bond coats and superalloy) upon cooling. Buckling of a thin, flat and isotropic film under compression will occur, if the stress exceeds a critical value, which can be calculated using the following equation [89]:

$$\sigma / E = 4.8\left(\frac{h}{d_b}\right)^2 \tag{3.7}$$

Here h is the oxide scale thickness, and d_b is the critical radius of decohesion for an unbounded region at the oxide scale/bond coat interface. The residual compressive stress in the TGO can presently be measured by luminescence piezospectroscopy, which is a non-destructive method [90]. For typical values of the measured residual stress (3-5GPa) and a typical scale thickness (10μm) it can be shown using equation 3.7 that very large delaminations (d_b) are required to produce a buckle (of a few millimeters). Equation 3.7 also indicates that for a given defect size and thermal stress a critical TGO thickness for buckling should exist.

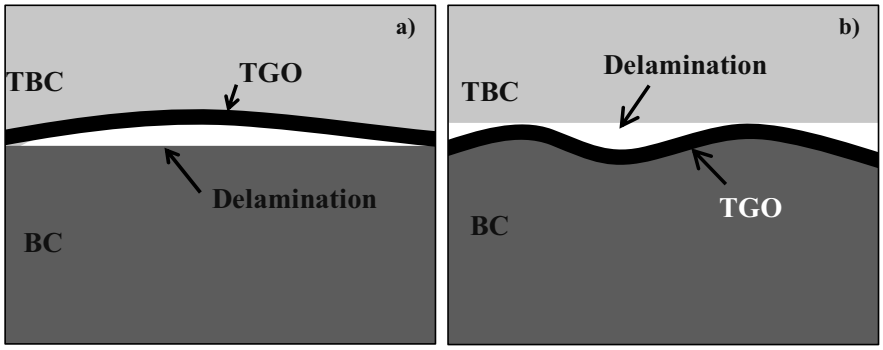

Fig. 3.6 Schematic of EB-PVD-TBC failure by a) buckling and b) TGO rumpling

The above described failure mode is typical for TBC's with MCrAlY bondcoats. The coalescence of interface separations around imperfections such as oxide Y_2O_3/YAG pegs can result in the initiation of TBC failure as reported by Mumm et al [91], who calculated the localized high levels of stress at the TGO/bondcoat interface. Another site for failure initiation may be defects e.g. the vertical separations between the YSZ lamella in the TBC [92].

A ratcheting phenomenon (Fig 3.6b) was proposed by A.G. Evans et al [93] to explain how the out-of-plane tensile stresses induce the failure of TBC systems with NiPtAl bondcoatings. The stress induced by the initial interface imperfections can locally exceed the yield strength of the bond coat. Plastic deformation of bondcoat under temperature cycling results in the formation of undulations at the TGO/ bondcoat interface. The amplitude of these undulations is increased during cyclic oxidation (repeated cooling) and due to the occurrence of oxide growth stress produced during hot-dwell time. When the amplitude of an undulation is sufficient to induce a critical tensile stress normal to the interface, cracking at the TGO/bondcoat interface occurs. When these cracks are linked up to a defect of sufficient large size, macroscopic scale buckling or edge delamination occurs leading to macroscopic TBC failure.

Surface displacements related to volumetric changes in the NiPtAl coating can induce TGO rumpling [94]. After high temperature oxidation, the flat bond coat was found to rumple which was explained by a phase transformation from β-NiAl to higher density γ′-Ni_3Al, induced by aluminum depletion as a result of oxidation and interdiffusion with substrate. The above phase transformation was claimed to result in a 8% to 38% volume decrease [94], depending on the extent of Al depletion. This contradicts with the observations in Ref. [95] which indicated that the β to γ′ transformation had little effect on the TGO adherence. The β phase can be also transformed into a martensite phase which will result in 2% volume decrease [96-97]. Both γ′ formation and martensitic transformation in the bondcoats are caused by the aluminum depletion and the nickel enrichment from the underlying superalloy. The phase transformation can induce an abrupt change of the CTE for the bondcoat [35], thereby affecting the stress situation and the lifetime of the TBC.

For EB-PVD and APS TBC systems a number of parameters have been identified, which can affect their oxidation behavior and failure. For EB-PVD TBC systems, which form rather flat alumina scales, the parameters which determine the scale adherence are of primary importance for the lifetime. These parameters related to materials and operating conditions are discussed in detail in the next chapters.

The material parameters include the main bondcoat composition. it was, for example, shown [35] for EB-PVD TBC systems the TBC lifetime was longer with Co-base MCrAlY bondcoat compared to Ni-base bondcoats under discontinuous and cyclic conditions. The effect was explained by the coating microstructure which was stabilized by Co addition resulting in a smaller CTE of the bondcoat and consequently in an adherent oxide as compared to that on a Ni-base MCrAlY coating.

As discussed in the chapter 3.2.2, the TGO adherence is critically affected by minor additions of RE's (Y, Zr, Hf, La et al). The RE not only improves the TGO adherence but, if present in large amounts, it is found to increase the TGO growth rate [98]. Therefore an optimum RE-content or reservoir is

required for obtaining long TBC lifetimes. Furthermore, for alumina forming alloys and coatings it was shown that co-doping with several reactive elements may result in improved oxidation resistance compared to that obtained in case of single element doping. However, for TBC systems there are much less data available, which demonstrate a positive effect or a mechanism of co-doping. A recent paper [67] indicates that Zr addition to the bondcoat has a large potential for lifetime extension of EB-PVD TBC systems. However, for APS-TBC systems a negative effect was observed duo to extensive internal oxidation [67].

In addition it should be noted that plasma-sprayed bondcoats contain considerable amounts of impurities, such as O which can tie up the RE's, thereby reducing their reservoir available for being incorporated into the Al_2O_3 scale and exploited a positive effect on the oxide scale properties. It was shown that variations in the MCrAlY-bondcoat oxygen content can result in significant variations of TGO-adherence and, consequently, lifetime of EB-PVD TBC's [67]. The bondcoat oxidation and thus TBC lifetime can be also significantly affected by processing steps after the bondcoat deposition [25].

Recently, developments were initiated by several research groups to improve the oxidation performance and the reproducibility of the oxidation behavior of MCrAlY-bondcoats in EB-PVD-TBC systems by optimization of the pre-treatment procedures. In reference [99] the heat-treatment of EB-PVD MCrAlY bondcoats before TBC deposition was performed at different vacuum pressures (at 1100°C). It was found that the longest TBC-lifetime was obtained by a two stage heat-treatment, i.e. short-term heating in high vacuum to form a β-NiAl rich layer at the coating surface followed by 2 to 4h at "poor" vacuum of 100Pa. In this way, a thin α-Al_2O_3 based scale with a high density of Y-rich oxide pegs formed during oxidation, resulting in superior lifetime compared to that obtained for the standard industrial heat-treatment. A positive effect of the heat-treatment of the bondcoat prior to TBC-deposition in vacuum compared to that in Ar-H_2 on the TBC-lifetime was observed in [100]. The research group at Pittsburgh University [101] also found a significant effect of the pre-treatment procedures on the EB-PVD TBC lifetime. Very smooth bondcoat surfaces were found to provide the longest lifetime, but the lifetime reproducibility was poorer compared to that for bondcoats with moderate roughness. This was attributed to the lower number of nucleation sites for defects but easier crack propagation on very smooth surfaces. One important outcome of all these studies is that the heat-treatment procedure commonly used in industrial applications may not be optimum for achieving extended and reproducible TBC-lifetimes. Another important observation is that the TBC-lifetime depends on the superalloy substrate and the longest lifetimes were observed on specimens were Hf-incorporation from the superalloy occurred during exposure [99, 102]. This was attributed to the positive effect of Hf on the alumina scale adhesion due to the formation of pegs at the scale/ bondcoat interface.

The effect of oxygen partial pressure during plasma spraying and vacuum heat-treatment parameters on the RE-distribution was studied using free-standing Y and Hf containing VPS NiCoCrAlY coatings [30]. In coatings sprayed at high pO_2 the RE's were tied up in form of oxide precipitates during the coating process. Consequently, the alumina scale adherence during oxidation was deteriorated. In contrast, in coatings sprayed at low pO_2 an overdoping effect occurred, resulting in a rapid scale growth and extensive internal oxidation. In order to suppress this negative effect of the low pO_2 coating, an attempt has been made to influence the RE-distribution prior to oxidation via a vacuum heat-treatment in the range of 900 to 1100°C. It was found that such a heat-treatment results in a preferential oxidation of RE. At lower temperatures (900 and 1000°C) of heat-treatment, the oxides formed on the coating surface were discrete particles of hafnia and alumina, whereas at 1100°C the surface oxides were mainly yttria and occasionally yttrium-aluminium pervoskite and hafnia particles. The identification of the different RE-containing oxides was accomplished by fluorescence and Raman spectroscopy. The internal oxide formation (mostly yttria) was found also to be time and temperature dependent. Smaller oxide particles and deeper internal oxidation zones formed when using lower temperature heat-treatment. It was shown that the RE-distribution established during vacuum heat-treatment affected the growth rate of the oxide scales formed during subsequent high-temperature oxidation.

3.3.2 Effect of exposure conditions on TGO formation in the EB-PVD TBC systems

Cooling from oxidation temperature produces a compressive stress in the TGO due to CTE mismatch with the underlying metal components (bondcoat and superalloy). This stress can be calculated using the following equation:

$$\sigma = \frac{E \cdot \Delta\alpha \cdot \Delta T}{1 - \nu} \tag{3.8}$$

where E is Young modulus of the oxide, and ν is the oxide Possion ratio, $\Delta\alpha$ is the CTE difference between the oxide and metal components, and the ΔT is the temperature drop. Stresses in the order of 2-5GPa [93] measured by XRD or Fluorescence Spectroscopy in alumina scales formed in EB-PVD TBC systems with MCrAlY and NiPtAl bondcoat were reported.

Some data are available on the effect of thermal cycle frequency on the scale spallation from alumina forming alloys and coatings but there are much less data available for TBC's. In fact, there is no general agreement in literature on the effect of cycle frequency on the oxide spallation and TBC life. The results show a complex dependence on the alloy/coating type, exposure temperature as well as the total test time. Pint et al [103] found that increasing the thermal cycle frequency had little effect on the rate of oxide spallation of NiPtAl coating, however, a negative (increasing) effect for NiAl and FeCrAlY coatings, depending on a competition between thermal stress and growth stress as well as

defect development at high temperature. The rumpling amplitude of a NiPtAl coating was observed to linearly increase with the number of thermal cycles [104-105].

With the use of hydrogen rich fuels instead of natural gas in the gas turbines to operate in IGCC-power plants with integrated CO_2-capture, the water vapor content of the combustion gas at the turbine inlet will increase from 10% to 60%. The higher H_2O content may reduce performance of the thermal barrier coatings. It was shown as [106] that partially yttria stabilized zirconia can exhibit accelerated transformation from the tetragonal into the monoclinic phase in wet air depending on the Y-content and distribution.

Water vapor effect on bare superalloys, MCrAlY bond coatings, and NiPtAl diffusion aluminides have been studied using a humid atmospheres with a water vapor content ≤10% [107] and the most technologically relevant was an increased tendency to Al_2O_3 spallation [36]. Pint et al [107] found that the amount of oxide scale spallation increased with increasing water vapor content from 10% to 50% for pure NiAl alloy; water vapor reduced the formation of alumina whiskers and ridges at the scale/gas interface.

A number of studies have been performed on the oxidation of alumina forming materials in H_2O containing gases. In high purity FeCrAlY alloys properly doped with reactive elements no effect of a water vapor addition (up to 50 vol.%) to air on the oxidation behavior was observed up to 4000h at 100h cycles [108]. It was shown that in Ni-base alumina forming superalloys [107, 109] the presence of water vapor during cyclic oxidation in air results in an increased amount of scale spallation. The negative influence of water vapor on the scale adherence was attributed to the decrease of the interfacial bonding between the scale and the metal, analogous to the mechanism for hydrogen embrittlement in metals. This mechanism is considered to be the primary reason for the so-called desktop effect, i.e. delayed scale spallation occurring at room temperature after extensive exposure time. This assumption was verified by hydrogen charging experiments using electrochemical cells [110]. A new approach was proposed recently to measure the hydrogen content at the scale/metal interface with resonant nuclear reaction analysis [111]. An important observation was that the adverse effect of water vapor on the alumina scale adherence only occurs if the latter has already been deteriorated e.g. by thermal cycling or impurities such as sulfur [107, 109]. Hence no H_2O effect was found in the case of perfectly adherent oxide/metal interfaces. At high oxidation temperatures and low Al-contents in the materials, the water vapor was shown to extend the transient stage of the oxidation, thus promoting the formation of Ni-rich spinel [112].

Cyclic oxidation experiments performed in Ar-4%H_2-2%H_2O (low pO_2 gas) and air-2%H_2O on an EB-PVD TBC systems with a NiCoCrAlY bondcoat showed longer TBC lifetime in the former

atmosphere [98]. This was related to the slower growth rate of the alumina scale in the low pO_2-environment which had a result that the critical scale thickness to initiate spallation was attained at longer times compared to air oxidation, as also observed previously in studies with FeCrAlY-alloys [108].

Many of the above effects discussed of materials and testing parameters refer to EB-PVD TBC lifetime. In contrast, in modern gas turbines, APS-TBC systems are state-of-the-art coatings. As will be shown in the next chapter the failure mechanisms of APS TBC's are different from those for EB-PVD TBC's.

3.3.3 Failure mechanisms for APS TBC systems

Compared to EB-PVD TBC's, a major difference with respect to TGO formation for APS-TBC's is that in the latter systems the TGO formation locally differs between convex and concave parts of the bondcoat surface. This was demonstrated by Gil et al [46] who found that geometrical factors affected the oxidation of NiCoCrAlY-coatings. Oxide scale morphologies were investigated on flat NiCoCrAlY-surfaces (typical for bondcoats used for EB-PVD TBC's) and rough coating surfaces (typical in case of APS-TBC bondcoats). Whereas on flat MCrAlY surfaces the scales were rather uniform in thickness and composition, on the rough surfaces significant differences in the scale morphology and microstructure occurred between the concave and convex coating surfaces. These differences were explained in terms of geometry-induced inhomogeneous depletion of Y and Al. One of the possible implications of the latter effect could be that variations in the fracture toughness of the oxide-metal interface on rough surfaces occur, which can contribute (in addition to the tensile out-of-plane thermal stresses) to an earlier scale delamination in the convex than in the concave areas, as shown in Fig 3.7.

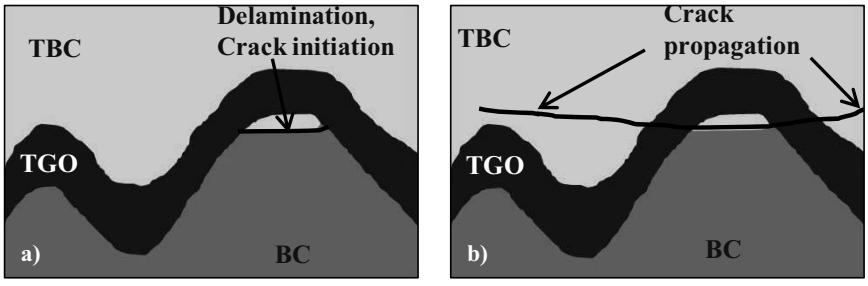

Fig. 3.7 Schematic of APS-TBC failure after long term thermal cycling, showing a) local void/crack formation at the bondcoat/TGO interface and b) subsequent long crack formation through penetrating of the TBC [113]

The out-of-plane stress is mainly generated at the convex parts of the rough bondcoat surfaces, which is believed to be the common site for crack initiation. However, oxide delamination only occurs after the TGO has reached a critical thickness [114], which is similar to the situation prevailing in case of

EB-PVD TBCs. Linkup of micro-cracks within the APS TBC finally results in TBC spallation and failure as proposed by De Masi-Marcin et al [115]. For obtaining crack-linking the cracks should penetrate the TBC in the locations above the concave parts of the bondcoat roughness profile. It was shown by Vaßen et al [116] that at small TGO thickness the residual stress in the TBC in these areas is compressive, which hinders the crack linking. As the TGO grows with time, a conversion of the residual stress from compressive into tensile occurs after a given time, which permits crack linking and failure. This means that the lifetime of APS-TBC systems can be significantly longer than the time for TGO delamination in the convex parts of the bondcoat.

For APS-TBC systems, it was proposed that Al depletion in the bondcoat can result after longer exposure times in formation of non-protective oxides, e.g. spinel, which can provide sites for initiation and propagation of failure relevant cracks [117]. It was observed that TBC systems with MCrAlY bondcoats produced by air plasma spraying are susceptible to spinel formation due to the so-called “diffusion cell” effect [118], resulting from oxidation of individual MCrAlY powder particles during spraying. This leads to a hindering of the Al-flux from the bondcoat bulk towards the surface for alumina scale formation. Each of the solidified MCrAlY powder particles represent a “diffusion cell” which failed after relatively short time by breakaway oxidation involving Ni and Co rich oxide formation resulting in rapid TBC failure.

4 Aims and structure of the present investigations

4.1 Aims of the present investigations

Constantly increasing inlet temperatures of gas turbines related with efficiency increase require extended and more reproducible lifetimes of TBC systems with MCrAlY and NiPtAl bondcoats. In most cases, formation of the TGO is involved in failure initiation in APS-TBC systems and the EB-PVD TBC lifetime can commonly be directly correlated with the TGO spallation. According to literature, TGO formation and failure in TBC systems greatly depend on the main bondcoat composition, and minor bondcoat chemistry such as concentration of reactive elements and impurities as well as coating processing. Increased water vapor content in IGCC power plants with a hydrogen turbine and possibly reduced oxygen partial pressure in the atmosphere can promote earlier failure of EB-PVD TBC systems, however, the effect on APS-TBC systems has, until now, not been extensively studied. With regard to the influence of hot and cold dwell times as well as cooling rates on TBC lifetime only limited data available for EB-PVD TBC systems and virtually no information for APS-TBC systems could be found. In many cases the information from different literature sources is very difficult to compare because of different processing of TBC-systems and/or the testing parameters.

A lot of MCrAlY coatings are presently commercially available, most of them being neither NiCrAlY nor CoCrAlY, but NiCoCrAlY, with different Ni and Co-contents. Over a wide temperature range (800-1100°C), previous studies [25] have shown that CoNiCrAlY coatings have a better phase stability and a lower CTE compared to NiCoCrAlY coatings with low Co content.

The first aim of the presented investigation is therefore to study the effect of bond coat main composition, in particular Co and Ni content, on the lifetime of EB-PVD TBC's under various thermal cycling conditions as well as to verify whether a similar lifetime effect trend with respect to Co-addition to the bondcoat also prevails for APS-TBC system.

The second aim of this investigation is to study the effect of RE additions and impurities in the MCrAlY coatings on the lifetime of TBC systems. Reactive element co-doping by Y+Zr is known to improve oxidation resistance of FeCrAlY-alloys. Preliminary studies of EB-PVD TBC systems with Zr-doped MCrAlY bondcoats indicated a better performance than with conventional MCrAlY bondcoats without Zr [67]. However, no verification of the positive Zr-effect was given under various testing conditions, including temperature cycling at near-operation temperature $T \leq 1000°C$ as well as in different testing atmospheres. For better understanding the Zr-effect on the bondcoat oxidation behavior and the failure of EB-PVD TBC systems, oxidation experiments are necessary with various cycling parameter at 1000°C. Higher O_2-content in MCrAlY coatings resulted in shortening the

lifetime and deteriorating the lifetime reproducibility of EB-PVD TBC systems [67]. On the other hand in APS-TBC systems with Zr doped NiCoCrAlY bondcoat with low O-content showed extremely short lifetimes due to local overdoping. Therefore in the present study APS-TBC systems with MCrAlY bondcoats with and without Zr addition and various O-contents were studied to investigate the effect of this impurity on lifetime. Furthermore in this study, an EB-PVD TBC system with Zr doped MCrAlY bondcoat was oxidized in H_2/H_2O low pO_2 atmosphere, and then compared to traditional MCrAlY coatings to study the effect of oxygen partial pressure on oxidation behavior and failure of TBC with Zr-doped MCrAlY bondcoats. In this way, the possible existence of a critical TGO thickness for the occurrence of TBC failure should be estimated.

The third aim of the present study was to investigate the effect of water vapor on the lifetime of EB-PVD and APS TBC systems. Higher H_2O partial pressures are claimed to increase oxide scale spallation from alumina forming coatings and cause desktop spallation for EB-PVD TBC systems with conventional MCrAlY bondcoats, whereas for APS-TBC systems hardly any data are available. To study the effect of water vapor on the oxidation behavior and lifetime of EB-PVD and APS TBC systems, specimens with four types of MCrAlY bondcoats were oxidized in air with 20%H_2O and the results were compared with data obtained during exposures in laboratory air.

The fourth aim of the current study was to systematically study the effect of temperature cycling parameters, i.e. hot/cold dwell times, heating and cooling rates as well as low dwell temperature, on the life of APS TBC systems with MCrAlY bondcoats. For this purpose, selected TBC-systems were oxidized at three different cooling-rate and five types of thermal cycling parameter sets with different hot/cold dwell time were studied. The specimens with porous TBC and porous bondcoat were tested to study the effect of microstructure of APS TBC and bondcoat on TBC lifetime.

Finally, an assessment of the oxidation behavior and lifetime of EB-PVD TBC systems with NiPtAl bondcoat was performed as an alternative to systems with MCrAlY bondcoats. Two EB-PVD TBC systems, i.e. one with a high and one with a low Al-activity NiPtAl bondcoat, were tested under conditions of varying temperature, atmosphere (dry and wet environments) and cyclic parameters. For better understanding of the effect of the initial oxidation behavior of NiPtAl on the oxide scale formation, short time oxidation experiments followed by analytical characterization were performed on NiPtAl coating surfaces without TBC.

4.2 Outline of the present work

The studies carried out in the present work are divided in three major sections. In the first part investigations related to EB-PVD-TBC systems with MCrAlY-bondcoats will be presented. The

studies will first show a comparison of the oxidation behavior and lifetime related to systems with Ni-base and Co-base MCrAlY-bondcoats under various cycling conditions. Second, the effect of a minor Zr-addition in the bondcoat on the EB-PVD-TBC lifetime will be presented under variation of temperature cycling conditions as well as oxygen partial pressure in the atmosphere. Finally, the studies on the influence of water vapor content in high pO_2 atmospheres on TBC-lifetimes will be presented.

The second part of the thesis concentrates on APS-TBC systems with MCrAlY-bondcoats. The effect of main bondcoat composition is studied using Co-base and Ni-base MCrAlY bondcoats, whereby three TBC-systems with various microstructural parameters (TBC-density, bondcoat-density and roughness profile) are tested in cyclic oxidation experiments. The effect of Zr-addition on APS-TBC lifetime is studied using TBC-systems with deliberately varying O-content in the bondcoat. In addition, the failure mechanisms of the APS-TBC systems under various cycling parameters as well as in wet and dry, high pO_2 atmospheres are studied.

The third part of the thesis concentrates on the oxidation mechanisms and lifetime of EB-PVD-TBC systems with NiPtAl-type bondcoats produced by low and high Al-activity CVD-process. The studies include cyclic oxidation testing under various cycling conditions at 1100 and 1150°C in wet and dry gases and present a comparison of the TGO growth rate, adhesion and failure mechanisms between the NiPtAl and MCrAlY-bondcoats. Finally the effect of the presence of a EB-PVD TBC on the oxidation resistance of NiPtAl-coatings is investigated.

5 Experimental

5.1 Materials and geometry of the specimens

5.1.1 TBC-systems with MCrAlY coatings

Two different specimen geometries were used in this study for TBC-systems with MCrAlY bondcoats, i.e. block and cylinder, as shown in Fig 5.1. The compositions of the studied Ni-base superalloys used as substrates are summarized in Table 5.1.

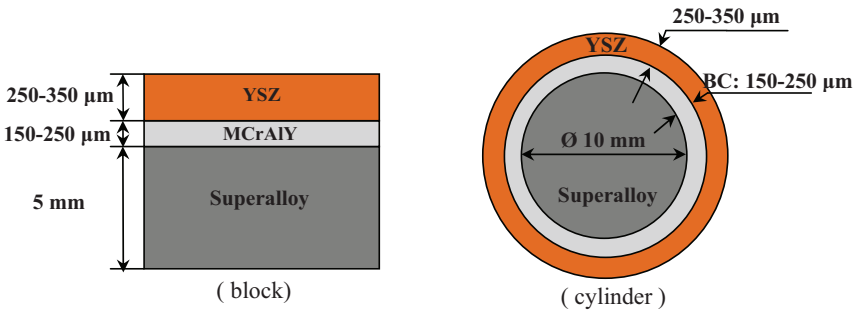

Fig. 5.1 Schematic of the geometries for TBC coated specimens with MCrAlY bondcoats

Table 5.1 Nominal compositions of Ni-base superalloys in wt. % [119]

Alloys	Ni	Co	Cr	Al	Mo	W	Re	Ta	Ti	Hf	Zr
IN738LC	Bal	8.5	16	3.5	1.7	2.5	-	1.7	3.5	-	0.05
CMSX-4	Bal	9	6.5	5.6	0.6	6	3	6.5	1	0.1	-
Rene 80	Bal	9.5	14	3	4	4	-	-	5	-	0.03
CM247LC	Bal	9	8	5.6	0.5	10	-	3.2	0.7	1.4	0.01

A number of conventional and modified MCrAlY coatings were deposited on the superalloy substrates by vacuum plasma spraying (VPS) and high-velocity oxy-fuel (HVOF) techniques. The nominal chemical compositions of the studied bondcoats are presented in Table 5.2.

After the bondcoat deposition the specimens were subjected to a two-stage vacuum heat treatment, according to the specifications for the respective superalloys e.g. for IN738: 1120°C/2h and subsequently 845°C/24h (vacuum base pressure of approximately 10^{-5} mbar). The heat-treated specimens were coated with yttria partially stabilized zirconia by electron-beam physical vapor deposition (EB-PVD) or air plasma spraying (APS) using state-of-the-art manufacturing procedures

[120]. Prior to EB-PVD TBC coating, smoothening of the bondcoat surface was performed by grinding or barrel (media) finishing.

Table 5.2 Nominal chemical composition of the studied bondcoats in wt. %

Bond coat	Ni	Co	Cr	Al	Y	Re	Zr
NiCoCrAlY (low Al)	Bal.	>20	<20	10	0.3	<2	-
NiCoCrAlY (high Al)	Bal.	<15	>20	11	0.4	<2	-
CoNiCrAlY	>25	Bal.	>20	10	0.6	-	-
NiCoCrAlY (low Al)+Zr	Bal.	>20	<20	10	0.3	<2	0.6
CoNiCrAlY+Zr	>25	Bal.	>20	10	0.6	-	0.6
Gamma NiCoCrAlY	Bal.	15	22	6	0.6	-	-
Beta NiCoCrAlY	Bal.	8	-	20	0.6	-	-

5.1.2 NiPtAl coated specimens with/without TBCs

The specimens with NiPtAl coatings were supplied by MTU AERO-Engines GmbH, Germany. The 10×10×2 mm single-crystal superalloy CMSX-4 coupons were electroplated with a thin layer (about 6 µm) of platinum, and subsequently aluminized by a chemical vapor deposition process to produce low activity (low-a_{Al}) aluminum coating and high activity (high-a_{Al}) aluminum coatings. One side of an aluminized specimen was coated with an EB-PVD TBC ceramic top coat as shown in Fig 5.2. A hole (see Fig 5.3) was drilled (before the coating treatment) to suspend the specimens for oxidation testing.

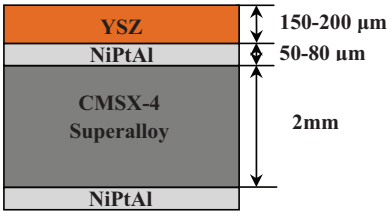

Fig.5.2 Schematic of the specimen geometry with NiPtAl coating partially coated with EB-PVD TBC

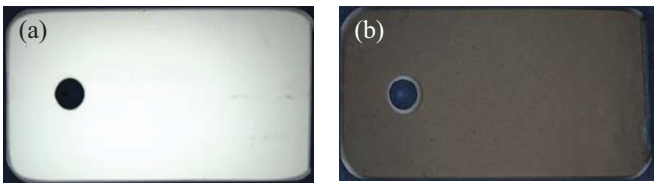

Fig 5.3 Macro-pictures of specimens with NiPtAl coatings, a) side with EB-PVD-TBC coating; b) side without TBC coating

5.2 Oxidation experiments

All specimens were ultrasonically cleaned in acetone and ethanol prior to the oxidation experiments. The TBC systems with MCrAlY and NiPtAl bondcoats were tested in dry or wet atmospheres in the temperature range of 1000°C-1150°C under a total pressure of 1 bar and a gas supply rate of 10 liter/h. The required H_2O partial pressures were produced using a bubble humidifier. Fig 5.4 shows schematically the set-up for discontinuous oxidation experiments. The types of oxidation experiments for the various coating systems are shown in Table 5.3.

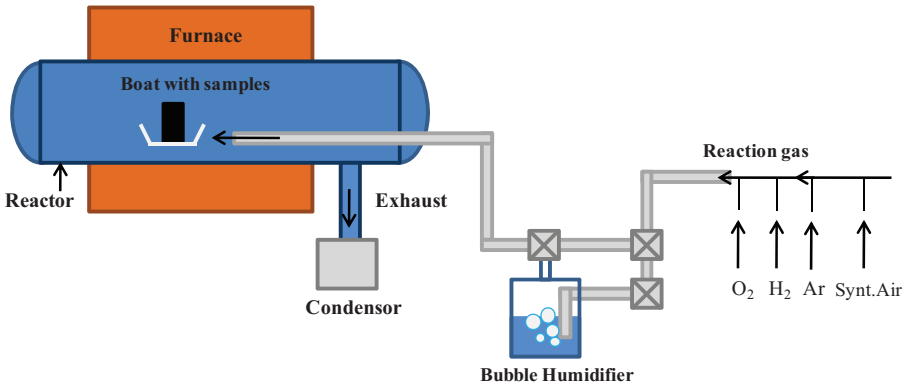

Fig. 5.4 Schematic set-up for discontinuous oxidation testing in wet gases

For the discontinuous oxidation experiments the specimens were exposed in the test gases using 166 hours cycles. At the end of each cycle the samples were cooled down in the furnace to near-room temperature and then manually taken out for inspection.

Table 5.3 Test conditions for various types of coating systems in this study

TBC systems		Thermal cycling Heating/cooling time	T (°C)	Atmosphere composition
TBC	Bondcoats			
EB-PVD	CoNiCrAlY(+Zr)	2h/15min 2h/45min 4h/1h Discontinuous (166h/12h)	1050 1100	Air Air-20%H_2O Ar-4%H_2-2%H_2O
	NiCoCrAlY (low Al) (+Zr)			
	NiCoCrAlY (low Al)			
	Low-a_{Al} NiPtAl	2h/15min 4h/1h Isothermal Discontinuous (166h/12h)	1000 1050 1100	Synt. Air Air-10% H_2O Ar-20%O_2 Ar-4%H_2-2%H_2O
	High-a_{Al} NiPtAl			
APS	CoNiCrAlY	2h/15min 105min/15min 75min/45min 21h/3h 18h/6h Discontinuous (166h/12h)	1050 1100	Air Air-20%H_2O
	NiCoCrAlY			
	NiCoCrAlY (low Al)			

Cyclic oxidation of the TBC specimens was performed in a vertical resistance heated furnace in laboratory air, synthetic (dry) air, and in air with H_2O as well as Ar-H_2-H_2O atmospheres. The specimens were automatically moved into the hot furnace, kept at high temperature for a preset time and then removed from the furnace to cool down to near room temperature with pressurized or still air.

For all experiments in this study, the given oxidation times refer to time at high temperature, which were recorded starting from the time when the specimens were moved in the hot zone of the furnace. The experiments aiming to determine the TBC lifetime were stopped when macroscopic cracking or spallation of the TBC were observed on the surface of the TBC specimens during regular inspections.

5.3 Specimen characterization

To evaluate the TGO morphology and the growth kinetics, metallographic polished cross-sections of the oxidized TBC specimens after various exposure times were prepared using a common specimen preparation method. The specimens for cross-section analysis were mounted in the epoxy resin, then ground and polished to get a mirror-like cross-section for optical metallography and scanning electron microscopy (SEM). For specimens without TBC, a 20-30 μm thick Ni-layer was produced on the sample surface through electroplating in a $NiSO_4$ bath prior to the mounting to minimize the oxide scale damage during grinding and polishing. A thin (nm-range) Pt or Au layer was commonly sputtered on the surface of the oxide scales by physical vapor deposition (PVD) prior to deposition of the Ni layer to increase the electrical conductivity of the oxidized sample surface.

Analysis of the as-received and oxidized materials was performed with optical metallography, scanning electron microscopy (SEM) with energy dispersive X-ray spectroscopy (EDX), and X-ray diffraction (XRD). For measurements of the residual stresses and identification of oxide phases in the TGO, photo-stimulated luminescence spectroscopy (PSLS) was employed according to the commonly used procedure [90, 121]. From selected areas of the oxidized surfaces of the NiPtAl coating thin lamellae were prepared using a focused ion beam (FIB) facility with a Ga ion beam, for analytical studies in a transmission electron microscope (TEM). On oxidized NiPtAl coatings, surface profiles were measured by contact Profilemeter to quantity primarily occurring surface rumpling.

6 Parameters affecting lifetime of EB-PVD TBC systems with MCrAlY bondcoats

6.1 Effect of Co and Ni contents in MCrAlY bondcoats on TBC lifetime

The lifetimes of EB-PVD TBC systems with different Co and Ni contents in MCrAlY bondcoats after 2h/15min cyclic oxidation at 1100°C in air are shown in Fig 6.1. The lifetime of TBC's with NiCoCrAlY (high Al) bondcoat was only about 200h. However, the lifetime of the TBC system with CoNiCrAlY bondcoat was longer by a factor of 4-5 compared to that with the Ni-base bondcoat. The lifetime trend of EB-PVD TBC systems during cyclic oxidation at 1100°C in air was similar to that observed during discontinuous oxidation in Ref. [25].

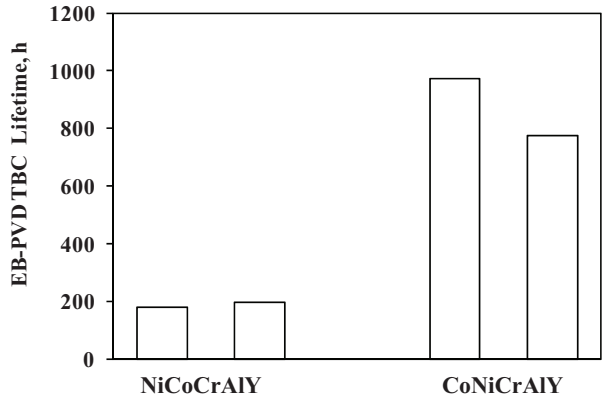

Fig. 6.1 Lifetime of EB-PVD-TBC with MCrAlY bondcoats after cyclic (2h/15min) oxidation in air at 1100°C in air

Fig 6.2 shows the cross-sections of the TBC specimens after 2h/15min cyclic oxidation for 100h at 1100°C in air. The oxide scales at the TBC/bondcoat interface for Ni and Co-base coatings presented similar morphologies and a thickness of approximately 3.0 µm. Precipitates of α-Cr could be found in NiCoCrAlY (high Al) bondcoat as indicated in Fig 6.2a. This can be attributed [25] to the main coating composition, with high Cr, high Al, low Co contents as well as additions of Re. As discussed

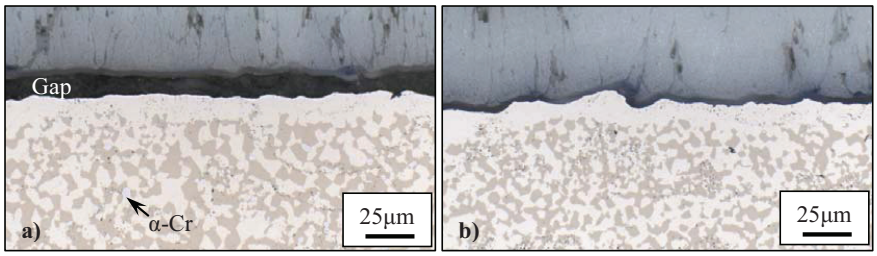

Fig. 6.2 Optical metallographic cross-sections of EB-PVD-TBC systems with MCrAlY bondcoats after cyclic (2h/15min) oxidation for 100h at 1100°C in air, a) NiCoCrAlY (high Al), b) CoNiCrAlY. The gap between TGO and alloy occurred during cross-section preparation

in Ref. [25] and [38] specifically the Re-additions promote the formation α-Cr.

The oxide scale thickness was about 3.5 µm for the Ni-rich MCrAlY coating and 8.0 µm for the Co-rich coating respectively when the TBCs failed as shown in Fig 6.3. The TBC failure in both systems occurred at the TGO/bondcoat interface. In the Co-base bondcoat, a significant β-NiAl depletion occurred in the upper part of the bondcoat due to the oxide scale formation during nearly 1000 h exposure. The Al-depletion after TBC failure was much less pronounced for NiCoCrAlY (high Al) coating due to a significantly shorter TBC lifetime as compared to CoNiCrAlY bondcoat. The longer lifetime of the EB-PVD TBC system with CoNiCrAlY bond coat can be attributed to the fact that the higher Co-content in the CoNiCrAlY coating stabilized the two-phase (γ + β) bondcoat microstructure. In contrast, in the NiCoCrAlY (high Al) bondcoat, the lower Co-content in combination with a higher Al content as well as Re addition of 2% wt resulted in a phase transformation during cooling from oxidation temperature at about 900°C. The phase transformation of the type $\gamma + \beta \rightarrow \gamma' + \alpha$ resulted in a volume change and associated increase in the bondcoat CTE leading to an increase in the thermal mismatch stress in the TGO, which is relaxed by TGO delamination [25]. An additional reason for an increase in the thermally induced residual stress could be increase in creep strength of the NiCoCrAlY coating due to the above phase transformation, which could reduce the amount of TGO stress relaxed by bondcoat creep or plastic deformation [122]. Thereby a TGO delamination and consequently TBC failure were promoted at smaller TGO thickness on the NiCoCrAlY (high Al) bondcoat as compared to the CoNiCrAlY bondcoat.

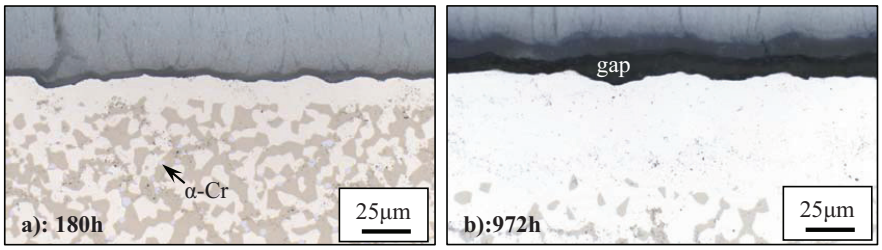

Fig. 6.3 Optical cross-sections of EB-PVD-TBC with MCrAlY bondcoats after cyclic (2h/15min) oxidation till TBC failure at 1100°C in air, a) NiCoCrAlY (high Al), 180h, b) CoNiCrAlY, 972h

In order to find out the relative importance of bondcoat creep relaxation and phase transformations driven CTE mismatch on the TBC lifetime, cyclic oxidation experiments were performed with varying cooling parameters. Thereby in one set of experiments the standard cooling time 15min was extended to 45min. The cooling rate of the 45min cooling by applying a heating shield to reduce the thermal radiation effect from the vertical furnace was slower than the 15min. In addition, the flow rate of the cooling air was reduced. These modifications to the specimen cooling resulted in temperature vs. time curves shown in Fig 6.4.

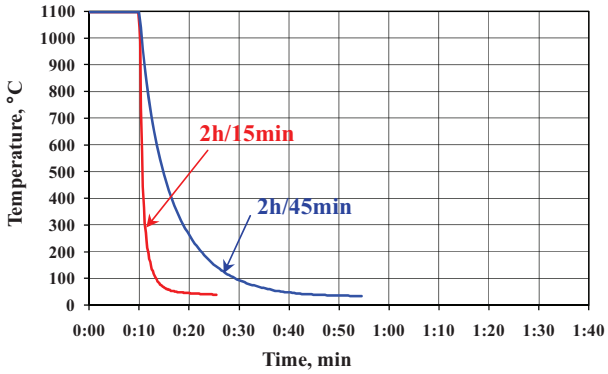

Fig. 6.4 Temperature time curves during cooling in oxidation testing with 2h/15min and 2h/45min cycles

The results of the cyclic oxidation testing with 15min and 45min cooling are shown in Fig 6.5. It can be seen that for the EB-PVD TBC systems with both NiCoCrAlY and CoNiCrAlY types of bondcoats the lifetime is about a factor of two shorter in the test with 45min cooling than in the test with 15min cooling. Cross-sections of the specimens after 2h/45min cycling are presented in Fig 6.6. If the bondcoat creep relaxation would have a major impact on reducing the residual stress in the TGO, longer TBC lifetimes would have been expected with slower cooling rate. This was, however, not observed. Shortening of the TBC lifetimes with slower cooling rate therefore indicates, that phase transformations in the bondcoat during cooling could play a major role in determining the time to failure than bondcoat creep.

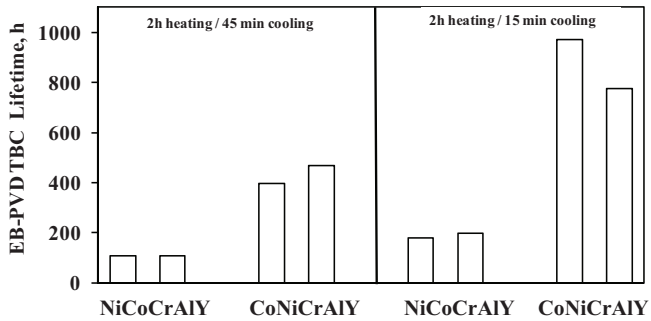

Fig. 6.5 Lifetimes of EB-PVD-TBC with MCrAlY bondcoats after 2h/45min and 2h/15min cyclic oxidation in air at 1100°C (compare cooling curved in Fig 6.4)

The temperature-time curves in Fig 6.4 indicate that an additional parameter might have an effect on the TBC lifetime in both tests, i.e. the time at low temperature. In the test with 15min cooling the specimens are at T<50°C for about 10 minutes, whereas in the test with 45min cooling the temperatures below 50°C are maintained for about 20min per cycle. Therefore, for the same number of

cycles the cold dwell time below 50°C is about twice longer in the test with 45min cooling cycles compared to that in 15min cooling cycles. The longer time at low dwell temperature could promote subcritical crack growth at the TGO/bondcoat interface similar to a desk-top spallation mechanism proposed by Smialek [79], who correlated this effect with the presence of water vapor in the test environment. In chapter 6.3.2 the effect of water vapor on lifetime of EB-PVD-TBC systems with MCrAlY-bondcoats will be studied in more detail.

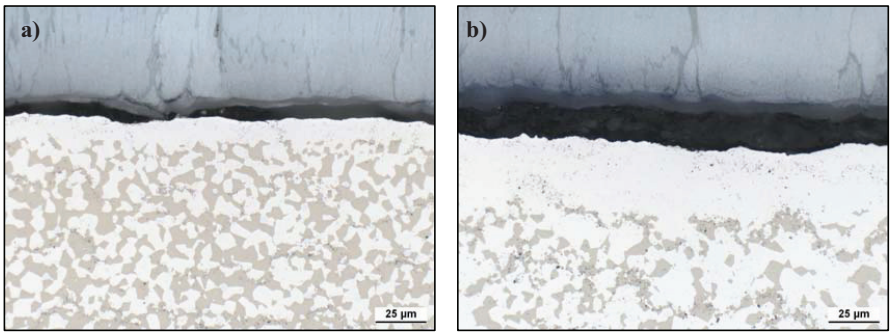

Fig. 6.6 Optical metallographic cross-sections of EB-PVD-TBC with MCrAlY bondcoats after cyclic oxidation 2h/45min till TBC failure at 1100°C in air, a)NiCoCoAlY,108h, b) CoNiCrAlY, 432h

6.2 Effect of exposure conditions on lifetime of EB-PVD TBC systems with conventional and Zr doped MCrAlY bondcoats

The lifetime of EB-PVD-TBC systems with and without a minor Zr-addition to the base NiCoCrAlY (low Al) bondcoat on IN738 cylindrical substrates was studied during oxidation exposures with different heating dwell times, i.e 166h for discontinuous oxidation and 2h for cyclic oxidation.

Figure 6.7 shows the TBC lifetimes after discontinuous and cyclic oxidation testing at 1000°C. During discontinuous testing (166 h cycles) the lifetime of the TBC-system with Y+Zr bondcoat was by approximately a factor of 4 longer than that with the Y bondcoat. In contrast, only a 50% longer lifetime for the system with co-doped bondcoat was obtained during the cyclic (2h cycles) exposure. Thus, for the Y bondcoat both testing procedures delivered similar TBC lifetime results, whereas for the Y+Zr bondcoat the lifetime was significantly shorter under the 2h cycling test.

The cross-sections of the TBC specimens (Figs 6.8 and 6.9) after both types of testing revealed that the specimens with the Y-bondcoat formed compact, flat TGO's. The TBC failure occurred by TGO delamination from the bondcoat in agreement with observations of many other authors (see e.g. references [123-124]). On the contrary, the TBC system with the Y+Zr bondcoat formed inhomogeneous, inwardly growing TGO's with oxide intrusions penetrating into the coating. The TBC

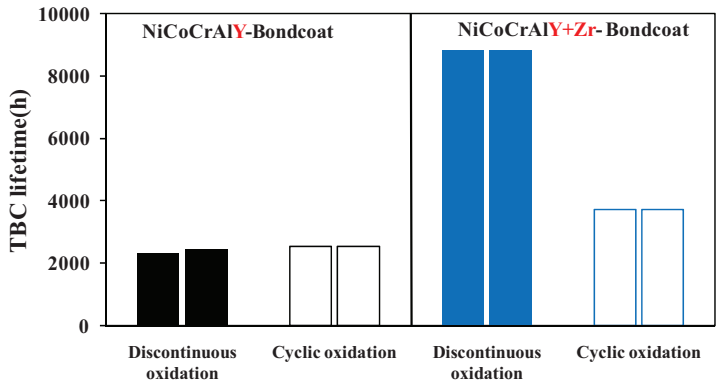

Fig. 6.7 Lifetimes of EB-PVD TBC systems with NiCoCrAlY (low Al) bondcoat with and without minor Zr-addition during discontinuous (166h hot dwell time) and cyclic (2h hot dwell time) oxidation experiments at 1000°C in air

failed under both thermal cycling conditions by cracking at/near the TGO/TBC interface and within the TGO. It is important to note that the TGO thickness after comparable times of exposure was much larger for the Y+Zr than for the Y bondcoat. Obviously, the substantial lifetime dependence on the test procedure for the TBC-system with Y+Zr bondcoat is related to the specific TGO-morphology and the associated failure mechanism, which is discussed below in relation to the Y-bondcoat.

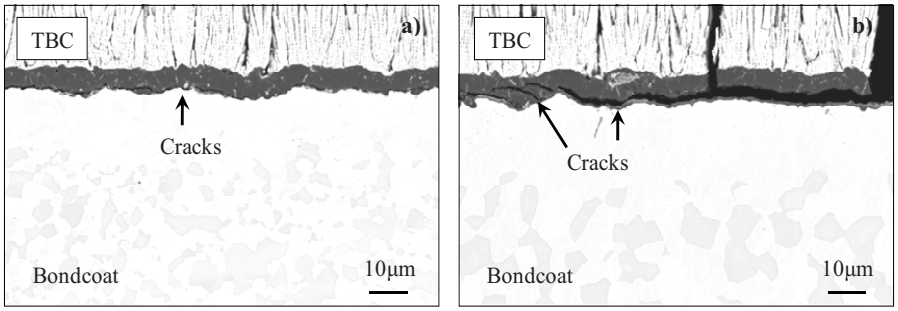

Fig. 6.8 BSE-SEM images of the cross sections of specimens with yttrium bondcoat after failure of the TBC after oxidation in air, a) 2320h discontinuous and b) 2540 cyclic

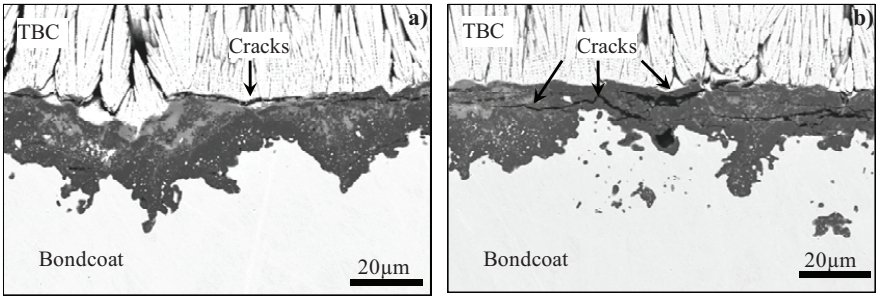

Fig. 6.9 BSE-SEM images of the cross sections of specimens with Y+Zr bondcoat after failure of the TBC a) after 8820h discontinuous oxidation and b) after 3730 cyclic oxidation in air

In the TBC-system with the Y bondcoat the failure occurred at the flat TGO/bondcoat interface, where the delamination cracks, once initiated, could easily propagate. For such flat, compact oxide scales the failure criterion was shown [125] to be the critical thermal strain energy, which for a given coating system is determined by a critical temperature drop and TGO-thickness. The critical temperature drop ΔT for the oxide spallation is given in [125]:

$$\left|\Delta T\right|_{spall} \propto \left[\frac{\gamma_F}{f \cdot X \cdot E_{OX}\left(\Delta\alpha\right)^2\left(1-\nu\right)}\right]^{\frac{1}{2}} \tag{6.1}$$

where, γ_F, fracture energy of the oxide/metal interface; f, fraction of strain energy used in the fracture process; X, the oxide scale thickness; E_{OX}, the Young's modulus of the oxide; $\Delta\alpha=\alpha_{metal}-\alpha_{oxide}$, linear thermal expansion coefficient of metal and oxide respectively; ν, Possion's ratio.

The validity of the critical TGO thickness for failure for EB-PVD-TBC systems with MCrAlY-bondcoats forming flat TGO's was demonstrated recently by Toscano et al. [98], who performed cyclic exposures in test atmospheres with different oxygen partial pressures. The argument of a critical TGO-thickness explains why for the TBC-system with the Y bondcoat comparable lifetimes expressed in hours at the oxidation temperature were found in the discontinuous and cyclic tests. Assuming that the TGO growth rate is not substantially affected by the cycle frequency, the critical TGO thickness for failure of about 6µm was reached after approximately the same accumulated "hot time" in both tests (Fig. 6.8). The relationship between the TGO growth and crack length for the system with Y-bondcoat under both testing conditions are schematically shown in Fig 6.10a.

The crack propagation in the case of the Y+Zr bondcoat at the TGO/bondcoat interface is hindered due to the inhomogeneous TGO morphology. The cracks stop in the regions of TGO-intrusions with a high out-of-plane interfacial compressive stress [93, 122]. Therefore, the thermal mismatch stress in the TGO is mainly relaxed by cracks initiated at defects at the TGO/TBC interface and within the TGO (Fig.6.9). The crack formation was found to be initiated already after relatively short exposure times, because of the rapid growth rate of the TGO on the Y+Zr bondcoat. The reason for this rapid local TGO-growth is incorporation of internal zirconia precipitates in the inwardly growing alumina based scale, as shown previously for alumina forming FeCrAl-base alloys [126]. Consequently, already after relatively short exposure times thick TGO's form on the Y+Zr bondcoat, which can accumulate large amounts of strain energy available for fracture upon cooling.

The strain energy stored in the scale provides the driving force for crack initiation and growth. However, the exact crack paths and the rate of crack propagation also depend on the microstructure and morphology of the TGO. For the uniform, dense alumina scale formed in the TBC-system with Zr-free bondcoat the typically observed crack propagation path is that at the TGO/bondcoat interface.

Therefore, reaching a critical TGO-thickness for this system essentially means that the end of TBC lifetime is reached irrespective of cycle frequency. This is not the case for the TBC system with the Y+Zr-doped bondcoat, where the cracks are initiated at various locations on defects (ZrO_2 precipitates and porosity) within the TGO and at the TBC/TGO interface. It is obvious that linking of cracks formed at various locations is slower than in case of a single, flat interface. Also the CTE mismatch between the TBC and TGO is smaller compared to that between the TGO and the bondcoat [93]. Therefore, formation of thick TGO's in the TBC-system with Zr-containing bondcoat does not result in an immediate failure and the lifetime in the discontinuous test is significantly longer than that with the Zr-free bondcoat.

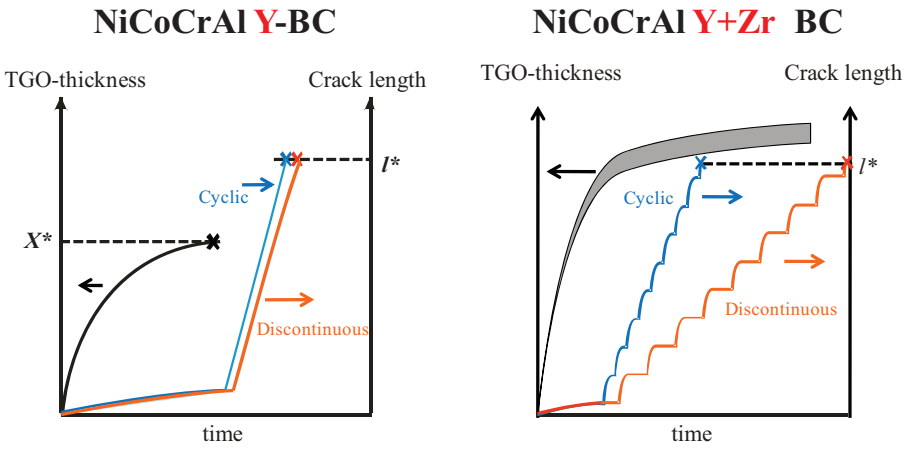

a) Cracks at the TGO/BC-interface

b) Cracks at the TBC/TGO-interface and within TGO

Fig. 6.10 Schematic illustrating effect of cycling conditions on the lifetime of EB-PVD-TBC systems with a) NiCoCrAlY-bondcoat and b) NiCoCrAl Y+Zr containing bondcoat. *X**, critical TGO thickness; *l**, critical crack length for TBC failure

Besides the TGO thickness and microstructure, a third factor determining the rate of crack propagation is the frequency of thermal cycling. In the cyclic oxidation test the specimen is cooled each 2 h, whereas in the discontinuous test it is cooled each 166 h. More rapid propagation of cracks under the former cycling can be expected, as during each cycle the strain energy in the thick TGO is available for crack extension. Consequently, the lifetime of the TBC-system with Y+Zr bondcoat is significantly shorter in the cyclic than in the discontinuous test, although it is still about 50% longer than that of the system with Y bondcoat. Fig 6.10b presents a schematic illustration of the effect of the cycling conditions on the crack formation and lifetime of the TBC-system with Y+Zr bondcoat.

The effect of the TGO defect size and morphology on the failure mechanism and lifetime of EB-PVD-TBC-systems with conventional MCrAlY-bondcoats has been investigated in several studies in the last

decade. Mumm et al. [91] and Evans et al. [93] claimed that presence of Y-rich oxide pegs can initiate TGO-separations in their vicinities. In contrast a more recent analysis by Zhu et al. [124] indicated that such small pegs can even improve the TGO-adherence similar to suggestions made earlier [127] for other alloy systems forming alumina scales. According to the author's knowledge no modeling of crack formation in the TBC-systems forming heterogeneous TGOs, such as that observed for Y+Zr bondcoats in the present study has been performed. Such a modeling is, however, highly desirable to assess the potential benefits of the bondcoat co-doping with Y+Zr under various operation conditions.

It is important to mention that the Y+Zr bondcoat contained rather high amounts of Y and Zr (0.6 mass % of each element) and according to detailed studies published elsewhere [67] a relatively low oxygen content (around 300 ppm). This caused excessive TGO growth in the initial stages of oxidation as a result of "overdoping" by Zr [128-129]. Comparison of the TGO's formed during discontinuous (lifetime of 8820h) and cyclic (lifetime of 3730h) exposure of specimens with the Y+Zr bondcoat reveals only a minor increase in the TGO-thicknesses with time in the late stages of exposure. This indicates that virtually the whole Zr-reservoir in the bondcoat was depleted in the first 3730h of exposure. It has been shown previously that the effective reactive element reservoir not only depends on the RE content of the coating but also on the coating thickness and the exact oxygen content. In high oxygen coatings part of the Zr would be tied up during the manufacturing process into a stable oxide compound thus preventing its incorporation into the TGO. As a consequence much longer TBC-lifetimes observed in the present work with the Y+Zr bondcoat in the discontinuous test can also be achieved in the cyclic test, as indeed verified experimentally (Fig 6.11 and reference [67]). A major challenge in obtaining long, reproducible lifetimes is thus a precise control of the processing parameters, such as vacuum quality during plasma spraying, vacuum quality and temperature regime during subsequent heat-treatment as well as coating thickness. Variations in these processing parameters were shown to affect not only the absolute values of the TBC-lifetime but also the lifetime reproducibility [30].

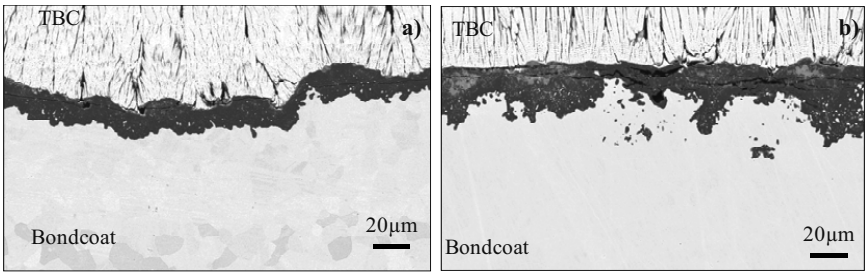

Fig. 6.11 BSE-SEM cross sections images of failed TBC specimens with Y+Zr bondcoats after cyclic oxidation at 1000°C in air: a) Bondcoat with 0.1 wt % Y and 0.2 wt % Zr after 4860h cyclic oxidation, and b) Bondcoat with 0.6 wt % Y and 0.6 wt % Zr after 3730h cyclic oxidation

6.3 Effect of atmosphere composition on lifetime of EB-PVD TBC systems with MCrAlY bondcoats

6.3.1 Effect of oxygen partial pressure on lifetime of EB-PVD TBC systems with conventional and Zr doped MCrAlY bondcoats

It is well known that the growth and adherence of alumina scales on high temperature materials can be affected by the composition of the operating atmosphere. Indications were found that the presence of water vapor in the atmosphere can accelerate scale spallation and promote internal oxidation of Al thereby negatively influencing critical Al-content for transition to external oxidation [112]. These detrimental effects of water vapor might become important in power plants with CO_2-capture where the operating environments of gas turbines will contain higher amounts of H_2O and possibly have lower oxygen partial pressure (pO_2) [2] than in conventional [6] gas turbines.

It is therefore important to study the oxidation behavior and lifetime of TBC systems as a function of bondcoat main and minor composition as well as atmosphere. In the present work the alumina scale formation and associated lifetimes of EB-PVD TBC's have been studied for an Y+Zr co-doped CoNiCrAl, in a high-pO_2 gas and a low-pO_2 gas containing water vapor. The reason for using a low pO_2 gas was to evaluate possible existence of critical TGO-thickness, as observed for an EB-PVD TBC system with Zr-free MCrAlY-bondcoat [67]. In the latter case after the same oxidation time (same number of cycles) a much lower oxidation rate was observed in the low pO_2 gas as compared to high pO_2 gas. These data are used in the present work as a reference for comparison with the Zr-doped bondcoat.

The material used as a substrate was the Ni-base superalloy IN738LC. Two bondcoats of Ni-base MCrAlY, termed NiCoCrAlY (low Al) and Co-base, termed CoNiCrAlY+Zr were deposited on 10mm diameter cylindrical rods of IN738LC by vacuum plasma spraying (VPS). The heat-treated specimens were smoothened and coated with an EB-PVD TBC. Cyclic oxidation of the coated specimens was performed in a vertical resistance heated furnace in laboratory air and in a H_2O-containing low pO_2 model gas Ar-4%H_2-2%H_2O. The specimens were automatically moved into the hot furnace, kept at 1100°C for 4 hours and then removed from the furnace to cool down to near room temperature (about 50°C) for 1 hour per cycle. The cyclic oxidation experiments were terminated when macroscopic cracking or spallation of the TBC were observed.

Fig 6.12 shows TBC-lifetimes during cyclic oxidation at 1100°C in air and in Ar-4%H_2-2%H_2O. For specimens with NiCoCrAlY bondcoat, the TBC lifetime was about 600 hours when exposed to air with an oxygen partial pressure (pO_2) equal to 0.2 bar. The lifetime increased to about 1000 hours when the specimens were exposed in Ar-4%H_2-2%H_2O with an equilibrium pO_2 of 2.2×10^{-14} bar at

1100°C. For the specimens with CoNiCrAlYZr bondcoat the TBC lifetimes were much shorter, i.e. only about 240 hours and there was no significant difference between lifetimes measured in air and Ar-4%H_2-2%H_2O.

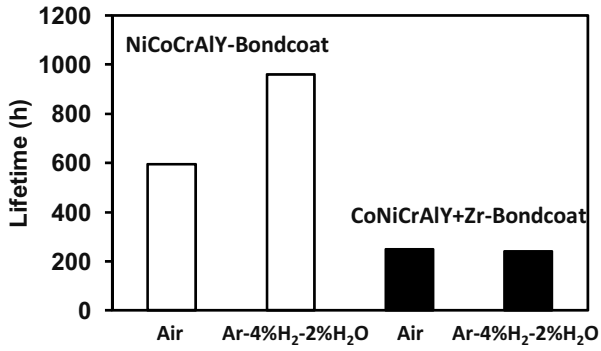

Fig. 6.12 Lifetimes in hours at high temperature of EB-PVD-TBC's on IN738 during cyclic oxidation (4h/1h) at 1100°C as a function of bondcoat composition and atmosphere

Fig 6.13a and b show that in the TBC-system with NiCoCrAlY (low Al) bondcoat homogeneous and uniform alumina-based TGO's formed in both atmospheres. Occasionally, small inclusions of Y-aluminates were found to be incorporated into the scale. Although the scale morphologies in air and Ar-4%H_2-2%H_2O were very similar, the scale thickness being significantly smaller in the latter atmosphere. After 300 hours of cyclic oxidation at 1100°C it was only about 3.5 µm in Ar-4%H_2-2%H_2O compared to about 5 µm in air. Therefore, the difference in the TBC lifetime observed between air and Ar-4%H_2-2%H_2O could be related to differences in the oxide scale growth rate. It is also important to note that in both atmospheres the TBC's with NiCoCrAlY bondcoat failed at the scale/bondcoat interface, similar to the observations made in chapter 6.1.

Fig 6.13c and d shows cross-sections of failed TBC-specimens with CoNiCrAlYZr bondcoat after cyclic oxidation at 1100°C in air and in Ar-4%H_2-2%H_2O. The cross-sections were prepared in the specimen areas, where the TBC was macroscopically still intact. Contrary to the NiCoCrAlY (low Al) bondcoat which formed a flat and uniform TGO, the specimens with CoNiCrAlYZr bondcoat formed much thicker and inhomogeneous scales with oxide intrusions penetrating deep into the coating. The failure mode was also different, i.e. cracks propagating through the scale and at the TBC/TGO interface. Spinel formation on the oxide surface could initiate the crack formation at the TBC/TGO interface. Similar sites of crack formation for the TBC systems with CoNiCrAlYZr bondcoat could be found when the specimens oxidized in air and in Ar-4%H_2-2%H_2O. The oxygen partial pressure did not affect the crack initiation site. The similar morphology and growth rate of the oxide scales on CoNiCrAlYZr-bondcoat in Ar-4%H_2-2%H_2O and in air explain why the measured cyclic lifetimes are virtually independent of the test atmosphere composition.

It can further be argued that the positive effects of high Co-content on the temperature stability of bondcoat microstructure which resulted in extended TBC-life observed earlier with Zr-free CoNiCrAlY-bondcoat (see previous section and references [25, 34]) are overcompensated in the present case by the rapid scale growth due to the minor addition of Zr. The rapid local scale growth resulted in encapsulation of parts of bondcoat by the oxide. After the Al was consumed from the isolated bondcoat parts, they were transformed into spinel, thereby providing ideal sites for crack initiation and propagation (Figs 6.13 c and d).

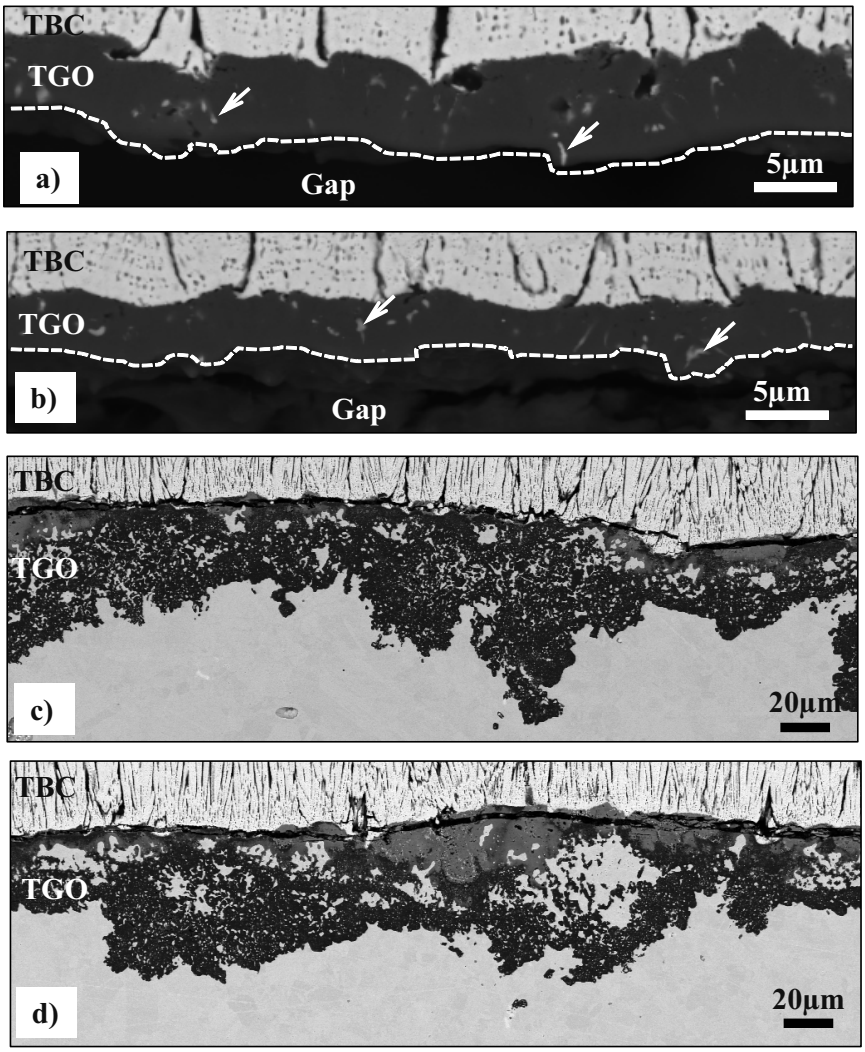

Fig. 6.13 SEM Cross-sections of EB-PVD-TBC specimens with (a, b) NiCoCrAlY and (c, d) CoNiCrAlY+Zr bondcoats after cyclic oxidation at 1100°C in (a, c) air and (b, d) Ar-4%H_2-2%H_2O. The specimens with NiCoCrAlY bondcoats oxidized for 300h, and with CoNiCrAlY+Zr bondcoats for 250h (failure). Gap in a and b formed during mounting and arrows indicate Y-aluminates in TGO

The oxide scale thicknesses measured in cross-sections of specimens with NiCoCrAlY bondcoat after 100 and 300 hours cyclic oxidation were extrapolated to obtain the TGO thickness at TBC-failure, similar as that shown in Fig 6.14. Assuming the common power law time dependence for the thickening rate [2], the estimated TGO thickness at failure was found to be approximately 6 µm in both atmospheres. This value can be considered as the critical scale thickness for the studied EB-PVD-TBC system under the used temperature cycling conditions. It is apparently related to the critical amount of lattice strain energy stored in the oxide upon cooling due to thermal mismatch between the system components, i.e. TBC, alumina scale, bondcoat and superalloy [130]. The reason for the slower TGO-growth rate in the $Ar/H_2/H_2O$ atmosphere is apparently related to the scale microstructure and growth mechanism, which is discussed below.

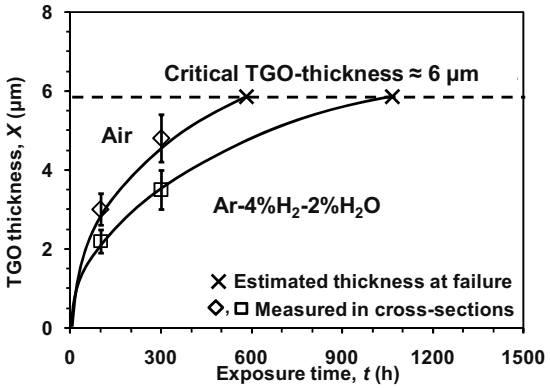

Fig. 6.14 TGO thickness for EB-PVD-TBC specimens with NiCoCrAlY-bondcoat during cyclic oxidation at 1100°C. Extrapolation of measured to TBC-failure times according to common power law time (X=k·t^n)

The oxygen tracer distribution [67] in an alumina scale formed on a free standing NiCoCrAlY coating of similar composition as the bondcoat used in the present work clearly indicates oxygen diffusion along short-circuit paths as the predominant scale growth mechanism [131]. These short-circuit paths are most likely the oxide grain boundaries, similar to the observations made previously for FeCrAl-base oxide dispersion strengthened (ODS) alloys [73] and FeCrAlY-type materials [132].

Fig 6.15 showed an SEM In-Lens [29] image with a typical TGO-microstructure formed on the NiCoCrAlY bondcoat after 100 hours cyclic air oxidation at 1100°C. The grain size of the scale is seen to increase with increasing distance from the oxide/TBC interface. This scale microstructure is similar to that observed for FeCrAlY-alloys [132] and other EB-PVD TBC systems [133] and can be attributed to a competitive grain growth process.

According to reference [132] the flux of oxygen J_O across the scale can be written as:

$$J_O = -\frac{C \cdot D_{eff}}{RT} \cdot \frac{\partial \mu_O}{\partial x} \tag{6.2}$$

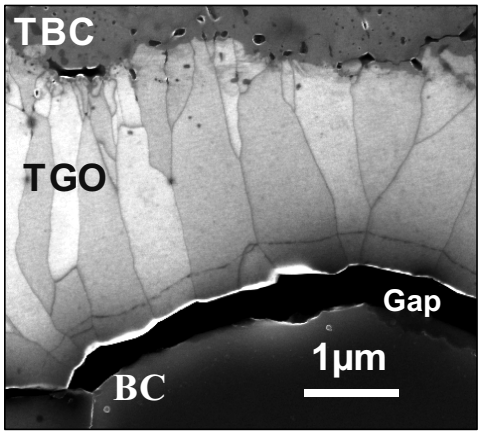

Fig. 6.15 SEM In-lens image of typical TGO-microstructure on NiCoCrAlY-bondcoat after 100 hours air oxidation at 1100° C. (Gap formed during mounting)

where C is the concentration of the diffusing species; μ_o, the oxygen chemical potential; x, the distance from the scale/gas interface; R, the gas constant; and T, the oxidation temperature in Kelvin. Assuming grain boundary oxygen diffusion to control the oxide scale growth, the effective diffusion coefficient D_{eff} can be written as [134]:

$$D_{eff} = \frac{2D_{GB} \cdot \delta_{GB}}{r(x)} \tag{6.3}$$

and the oxygen chemical potential is given by

$$\mu_o = \mu_o^0 + RT \ln pO_2 \tag{6.4}$$

where D_{GB} is the grain boundary diffusion coefficient; δ_{GB} and r, the grain boundary width and grain size respectively; x is the distance from the scale/gas interface, $\mu_O{}^0$ is the chemical potential of pure oxygen and pO_2 is the oxygen partial pressure.

The oxygen flux J_O depends on the gradient in oxygen chemical potential (μ_o) according to equation (6.2). Due to very similar oxide scale morphologies on the NiCoCrAlY coating oxidized in air and Ar-H_2-H_2O (Fig 6.13) as well as observations made for FeCrAlY-alloys [132] it is likely to assume that the growth mechanism is the same in both used atmospheres (i.e. inward grain boundary oxygen diffusion). The equation for the relationship between oxide scale thickness and oxygen potential gradient derived for FeCrAlY alloys is as follows [132]:

$$\frac{r_0 X^2}{2} + \frac{aX^3}{3} = -\frac{2D_{GB}\delta_{GB}}{RT} \cdot \Delta\mu \cdot t \tag{6.5}$$

In the Ar-H_2-H_2O atmosphere the oxygen potential μ_o is much lower than that in air due to much lower oxygen partial pressure, in others words, the oxygen potential gradient $\Delta\mu$ within the oxide is lower in Ar-H_2-H_2O than in air. This results in a smaller oxygen flux across the scale and a slower TGO growth in Ar-H_2-H_2O than in air. The diffusivity of oxygen (D_{GB}) along the grain boundaries in the alumina scale was shown to be for FeCrAlY alloys also lower in H_2/H_2O gas than in air. This was attributed to some less mobiles species, e.g. hydroxyl groups and/or water molecules as well as oxygen and hydrogen ions in the former atmosphere [132]. Fig 6.16a shows schematically the mechanism of scale formation with NiCoCrAlY-bondcoats in both atmospheres.

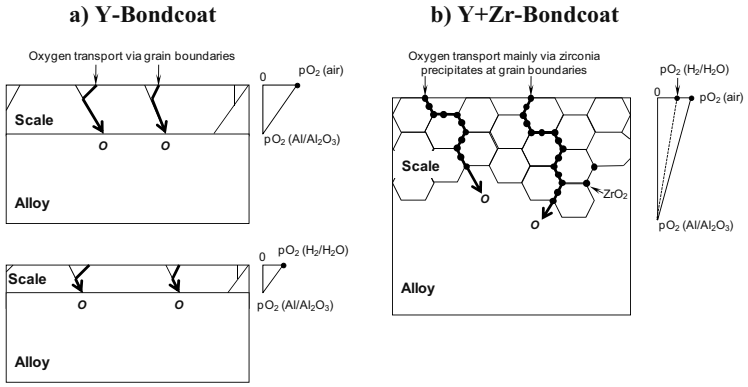

Fig.6.16 Schematic of oxide scale formation on a) Y and/or b) Y+Zr doped MCrAlY-bondcoats in different atmospheres. Presence of TBC is neglected

For the Zr-doped CoNiCrAlY bondcoat, comparing with the NiCoCrAlY-bondcot, a different oxide scale microstructure and apparently a different scale growth mechanism are effective. The locally rapid scale growth on CoNiCrAlYZr coatings was manifested by the fact that frequently metal inclusions were observed in the oxide scale (Fig 6.17). Close to the original bondcoat surface, where the oxygen partial pressure was sufficiently high, these metal inclusions were found to transform gradually into spinel type oxide. These spinels could facilitate crack initiation and/or propagation in the TBC-system during cyclic oxidation [135].

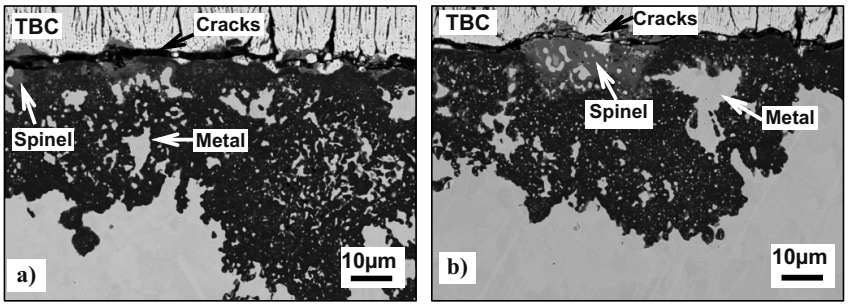

Fig. 6.17 SEM cross-sections of EB-PVD-TBC specimens with CoNiCrAlY+Zr bondcoat after cyclic oxidation till failure for 250 h at 1100°C in a) air and b) Ar-4%H_2-2%H_2O

The high magnification SEM image in Fig 6.18 reveals that the alumina scales on the CoNiCrAlYZr-bondcoat contained a large volume fraction of fine ZrO_2-precipitates. Assuming the ZrO_2 precipitates to be located at the alumina grain boundaries, the resulting scale microstructure is seen to be extremely fine-grained. The scale grain size in the inner part of the scale on the CoNiCrAlYZr-bondcoat estimated from Fig 6.18 is far less than 1 μm, contrary to the columnar grain microstructure observed on the NiCoCrAlY-bondcoat in Fig 6.15. Apparently the presence of finely distributed ZrO_2 in the oxide scale on the CoNiCrAlYZr-bondcoat promotes rapid inward oxygen transport through the scale. This effect is partly due to the fine scale grain size, but mainly due to fast oxygen lattice diffusion in zirconia [136]. The rapid oxygen inward transport via a non-uniform network of short circuit paths can explain the waviness of the scale/metal interface and inclusion of metal particles into the scale.

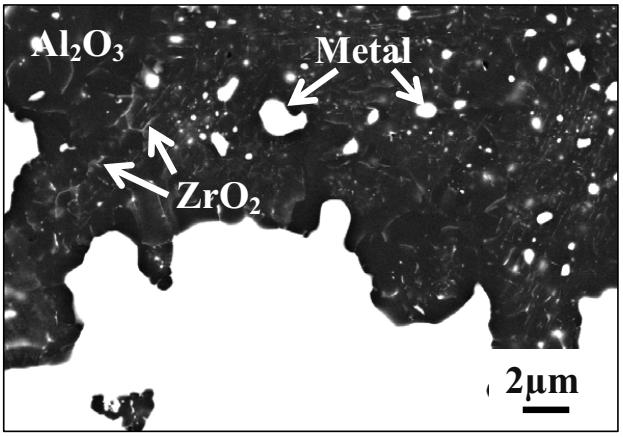

Fig.6.18 SEM cross-section of EB-PVD-TBC specimen with CoNiCrAlY+Zr bondcoat after cyclic oxidation till failure at 1100°C in air for 250h. Arrows indicate metal particles and ZrO_2

The observed scale microstructure would qualitatively explain why no significant difference in the scale thickness and morphology is seen on the CoNiCrAlYZr-bondcoat between Ar-4%H_2-2%H_2O and air exposures. The lower pO_2 in the former atmosphere should lead to reduction in alumina growth rate, as it was the case for the NiCoCrAlY-coating. For the CoNiCrAlYZr-bondcoat, however, this effect is probably of only minor importance, since the oxygen transport in the scale does not occur via alumina grain boundaries but rather via virtually continuous zirconia pathways (Fig 6.18). The oxygen diffusivity in zirconia is much larger than that in alumina and the major point defects are considered to be oxygen vacancies [136-137]. The process of oxygen vacancy formation is represented by the equation:

$$O_o^{\times} = V_o^{\bullet\bullet} + 2e' + \frac{1}{2}O_2(g) \qquad (6.6)$$

in which $O_o^{\times}$ is an oxygen ion on a regular lattice site, $V_o^{\bullet\bullet}$ is an oxygen vacancy, e' is a negatively charged electron.

Considering oxygen vacancies in zirconia being the predominant defects, the corresponding expression for the oxidation rate k_p is :

$$k_p = const. \cdot \left[\left(\frac{1}{p_{O_2}^{Scale/metal}} \right)^{1/6} - \left(\frac{1}{p_{O_2}^{Scale/gas}} \right)^{1/6} \right] \tag{6.7}$$

The values of oxygen partial pressure at the scale/gases interface equal 0.2 bar for Ar-O_2, and 10^{-14} bar for Ar/H_2/H_2O, respectively. The pO_2 at the scale/metal interface can be estimated from thermodynamic equilibrium of the reaction:

$$2Al + \frac{3}{2}O_2 = Al_2O_3 \tag{6.8}$$

For unit Al-activity pO_2 can be calculated [5] at 1100°C to be 10^{-28} bar. Even if the Al-activity is much lower the resulting scale/metal interface pO_2 is still very low, e.g. $pO_2 \approx 10^{-23}$ bar for $a_{Al}=10^{-4}$. It can be seen that for ideal example pO_2(scale/metal) is much smaller than pO_2(scale/gas). Then, according to equation (6.7), the oxide scale growth rate k_p is in a large range of oxygen partial pressures independent of the pO_2 in the environment.

Of a particular interest is the mechanism of Zr-incorporation into the alumina scale. Considering similar thermodynamic stabilities of zirconia and alumina, as well as high Zr-diffusivity and low oxygen permeability for FeCrAl Y+Zr co-doped alloys it was proposed [138] that zirconia precipitates are nucleated at or just below the scale/metal interface, which become almost immediately embedded into the inward growing scale. It is important to note that for the Zr-doped FeCrAlY-alloy studied in [138] slower oxidation rate was observed in H_2/H_2O atmosphere compared to Ar-O_2. In contrast in the present work the oxide scale thickness on the Zr-doped CoNiCrAlY bondcoat are very similar in both atmospheres. The reason for this effect can be much higher Zr-content in the latter material (0.6 wt%) compared to only 0.03 wt% in the FeCrAlYZr-alloy. Other possibilities indicate faster diffusion of Zr and/or O in the CoNiCrAlY compared to FeCrAlY, but the exact values are not available in literature.

It should be noted that the effect of minor Zr-additions on the bondcoat performance cannot in general be considered as negative. The short TBC-lifetime observed in the present investigation is a result of so-called “scale overdoping” with Zr [139]. This is due to a high Zr-content (0.6 mass %) in the presently studied bondcoat, resulting in a large Zr-reservoir, i.e. a large amount of Zr available for incorporation into the oxide scale. It is shown in section chapter 6.2 that for bondcoats with an optimized, smaller Zr-reservoir, e.g. due to a lower Zr-content, the TBC-lifetime can be extended

compared to Zr-free bondcoats. The latter observation was related to the fact that the location for initiation of TBC-failure was shifted from the scale/metal to the TBC/scale interface. It is recognized, however, that an optimum Zr-reservoir, which depends not only on the Zr-content but also on the oxygen and carbon contents, as well as bondcoat thickness [34], might be difficult to control in a large scale coating manufacturing process because of inevitable variations in the processing parameters, such as vacuum quality during VPS and heat-treatment, extent of coating smoothening, etc.

Furthermore, comparison of the latter results with those above presented in chapter 6.2 indicates that the effect of Zr on oxide scale formation and associated TBC-lifetime strongly depends on the operating (testing) conditions, such as oxidation temperature and temperature cycling. At higher temperatures, e.g. 1100°C as used in the present study, the Zr-incorporation into the scale is rather rapid. In contrast, at 1000°C, which is closer to the real bondcoat operation temperature, the Zr-diffusion in direction of the scale from the bondcoat bulk is more sluggish. Consequently, at 1000°C the lifetime of TBC's on Zr-doped MCrAlY-bondcoats was found to be extended compared to a system with Zr-free bondcoat of similar main composition, whereas no significant life extension was observed at 1100°C. The degree of TBC-lifetime extension by Zr-doping of the bondcoat at lower temperatures was, however, found to depend on the temperature cycling parameters which were discussed in chapter 6.2. The improvement was less pronounced for testing with 2 hour high-temperature dwells, due to faster crack propagation and coalescence in the scale compared to long (166 hour) high temperature dwells.

6.3.2 Effect of water vapor on lifetime of EBPVD-TBC systems with NiCoCrAlY bondcoats in atmospheres with high oxygen partial pressure

In the previous chapter the oxidation behavior of EB-PVD TBC systems in H_2O-containing, low pO_2 environments was studied. However, real gas turbine service environments typically have a high oxygen partial pressure because the combustion occurs with excess oxygen. Furthermore, as mentioned in the introduction, gas turbines in IGCC power plants will be operating using H_2-rich fuels, with a consequence that the combustion products will have much higher H_2O-contents. Therefore in the present work a comparison of lifetime for EB-PVD TBC systems with MCrAlY bondcoat in air and air+20%H_2O during discontinuous oxidation at 1050°C was performed. Fig 6.19 shows that higher water vapor content in the atmosphere significantly shortened the lifetime of the studied EB-PVD TBC systems.

Cross-sections of the failed specimens are presented in Fig 6.20 and 6.21 for laboratory air and laboratory air+20%H_2O exposures, respectively. It can be seen that in all cases failure occurred by crack propagation at the TGO/bondcoat interfaces observed commonly for EB-PVD TBC systems with MCrAlY bondcoats [91].

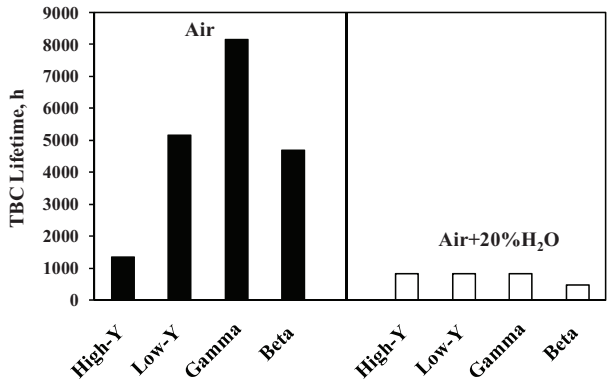

Fig. 6.19 Lifetime of EB-PVD TBC systems with NiCoCrAlY BC after discontinuous oxidation (167h/cycle) at 1050°C in air and air+20%H_2O. High-Y BC: NiCoCrAlY (low Al) with 0.6 wt% Y; Low-Y BC: NiCoCrAlY (low Al) with 0.3 wt% Y; Gamma BC: NiCoCrAlY (low Al) bottom layer + Gamma NiCoCrAl (upper) layer ; Beta BC: NiCoCrAlY (low Al) bottom layer + Beta upper layer

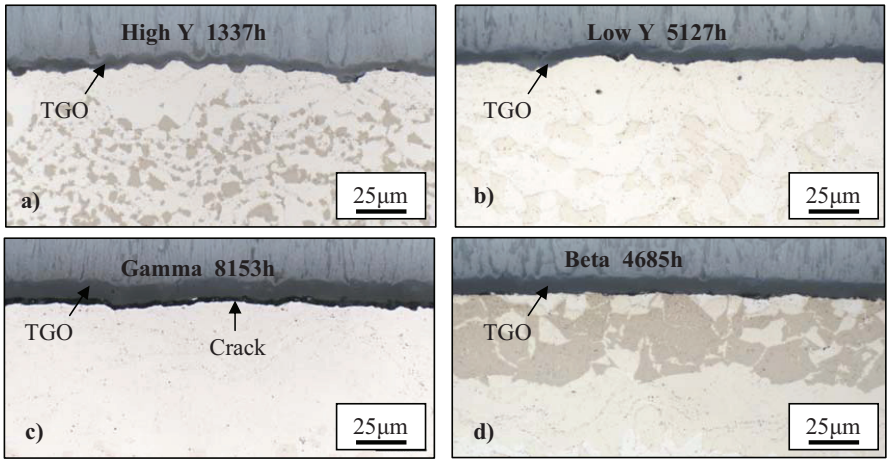

Fig. 6.20 Cross-sections of EB-PVD TBC systems with NiCoCrAlY BC after discontinous oxidation till failure in air at 1050°C, and a) NiCoCrAlY (high Y), b) NiCoCrAlY (low Y), c) NiCoCrAlY+ Gamma, d)NiCoCrAlY+Beta

For the air exposures the absolute values of the lifetimes are different for the various bondcoats and no obvious correlation with the bondcoat composition can be made. One of the possible reasons for the large lifetime variations can be the variation in the RE-reservoir and consequently of the TGO-adherence. It was found in previous work [67] that the lifetime of the EB-PVD TBC systems with the studied bondcoats exhibited significant variations even within one specimen batch. This was attributed to a varying RE-reservoir established by conventional bondcoat-processing, i.e. vacuum plasma spraying of the bondcoat followed by high temperature vacuum heat-treatment and smoothening of the sample surfaces by a media finishing process. Each of the processing steps could in principle change

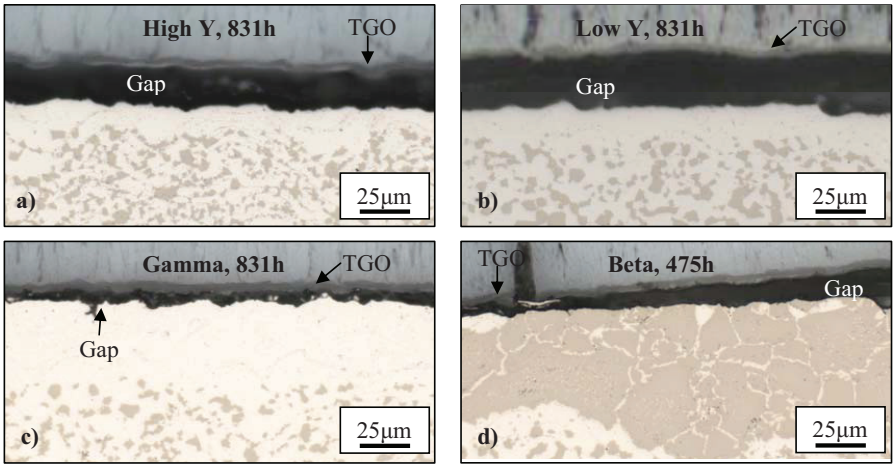

Fig. 6.21 Cross-sections of EB-PVD TBC systems with NiCoCrAlY BC after discontinous oxidation till failure in air+20%H_2O at 1050°C, and a) NiCoCrAlY (high Y), b) NiCoCrAlY (low Y), c) NiCoCrAlY+ Gamma, d)NiCoCrAlY+Beta

the distribution of RE. The RE addition, e.g. Y can be oxidized during the VPS coating process as well as on the coating surface during vacuum heat-treatment. The surface smoothening not only removes the Y-rich oxides formed during vacuum heat-treatment but also reduces the coating thickness, resulting in a further reduction of the RE-reservoir. The difference in the RE-reservoir can result as a consequence in significant differences in the oxide scale adhesion between different samples, which might explain why the TBC failure occurred at very different TGO-thicknesses.

In spite of significant lifetime variations of EB-PVD TBC systems with different bondcoats, the absolute lifetime values for all systems studied are much longer when tests are performed in laboratory air as compared to laboratory air with 20%H_2O. This result indicates that water vapor promoted TBC failure to occur at a much smaller critical TGO thickness as compared to a drier environment. A possible reason for this effect is likely enhanced spallation of the alumina scales in presence of moisture, as proposed by other authors [110, 112]. It is important to note that the mechanism proposed in reference [110, 112] to explain the H_2O-effect on scale spallation (hydrogen embrittlement of the TGO/bondcoat interface, H being produced by reaction between H_2O and Al) implies H_2O access to a poorly intact scale/metal interface. It was observed that the extent of the H_2O effect on the alumina scale spallation from Ni-base superalloys was much stronger for alloys with higher S-content, which exhibited a more extensive scale spalling, than alloys with low sulfur in the dry atmosphere [112]. Combing the observation from [112] with those in the present work it can be speculated that the oxide scale adherence in the studied TBC-systems was not optimum probably due to significant and non-uniform RE-reservoir depletion from the bondcoats during processing as described above.

6.4 General discussion of findings with EB-PVD TBC systems with MCrAlY bondcoats

The lifetime of EB-PVD TBC specimens with CoNiCrAlY bondcoat was longer than that with NiCoCrAlY (high Al) bondcoat during cyclic oxidation in air at 1100°C. This can be attributed to a lower CTE for the Co-rich bondcoat. Slower cooling rates and longer dwell times at low temperature with the same hot dwell time were found to shorten the lifetime of EB-PVD TBCs with Co-rich as well as Ni-rich bondcoat.

The lifetime of EB-PVD TBC systems with conventional NiCoCrAlY bondcoats was comparable after cyclic and discontinuous oxidation in air. The critical TGO thickness played a critical role in determining the crack propagation at the TGO/ bondcoat interface. This could be illustrated by experiments in a low-pO_2 gas. The growth rate of TGO's formed in TBC systems with conventional MCrAlY bondcoat was slower in low pO_2 environments due to a smaller oxygen flux across the scale induced by the lower oxygen chemical potential in the atmosphere as compared to high pO_2 gas. Therefore, the TBC life was longer in H_2/H_2O atmosphere with a low oxygen partial pressure than in air because a longer time was required to reach the critical oxide scale thickness for TBC-failure. The EB-PVD TBC lifetime was mainly controlled by the time for reaching a critical oxide thickness and was not significantly affected by the temperature cycling frequency.

The TBC systems with Zr-doped MCrAlY bondcoat exhibited a longer lifetime after discontinuous oxidation compared to cyclic oxidation. The life of the TBC on Zr-doped MCrAlY bondcoat during the discontinuous test was also longer than that with the Zr-free bondcoat. Oxygen diffusion through short-circuit paths (ZrO_2 precipitates) in the TGO promoted internal oxidation and formed an inhomogeneous TGO/bondcoat interface. Therefore, it was impossible to define a critical TGO thickness related to TBC failure as in the above case of the conventional MCrAlY bondcoat. The low pO_2 in H_2/H_2O gas had no clear effect on the TGO growth rate and TBC lifetime because the O-diffusivity in ZrO_2 appeared to be virtually independent of pO_2.

The lifetime of TBC's with Zr-containing bondcoat strongly depended on exposure conditions e.g. temperature and cyclic frequency. The crack formation and propagation for the case of the Zr-doped bondcoat occurred within the thick TGO as well as at the TBC/TGO interface. In spite of formation of a thick TGO in the TBC system at high temperature an immediate TBC failure did not occur during the oxidation. However, the lifetime of the TBC-system with Y+Zr bondcoat was significantly shorter in the cyclic than in the discontinuous test, although it was still about 50% longer than that of the system with conventional Zr-free bondcoat. The latter effect can be related to a more rapid propagation of cracks in the TGO and at the TGO/TBC interface with using high frequency thermal cycling.

The water vapor rich atmosphere with high oxygen partial pressure appeared to be detrimental for the lifetime of EB-PVD TBC with NiCoCrAlY bondcoats. The moisture-induced delayed spallation [110] could be an operating mechanism negatively affecting the Al_2O_3 scale adhesion.

7 Parameters affecting lifetime of APS TBC systems with MCrAlY bondcoats

7.1 General Remarks

Although EB-PVD TBC systems show high resistance against temperature cycling, one of the drawbacks for their more extensive use is the relatively high manufacturing cost. APS-TBC systems are nowadays used by most of the OEM's producing industrial gas-turbines. The advantages of APS-TBC's include lower manufacturing costs and lower thermal conductivity than EB-PVD TBCs. The APS-TBC systems are also claimed to be more resistant against penetration and attack of corrosive species such as calcium–magnesium–aluminum-silicate (CMAS). Therefore, in this section the parameters affecting the TGO formation and lifetime of APS-TBC systems with MCrAlY bondcoats are presented

7.2 Effect of Co and Ni contents in MCrAlY bondcoats on lifetime of APS TBC systems

Previous studies with EB-PVD TBC systems [25] as well as those in the present investigation in

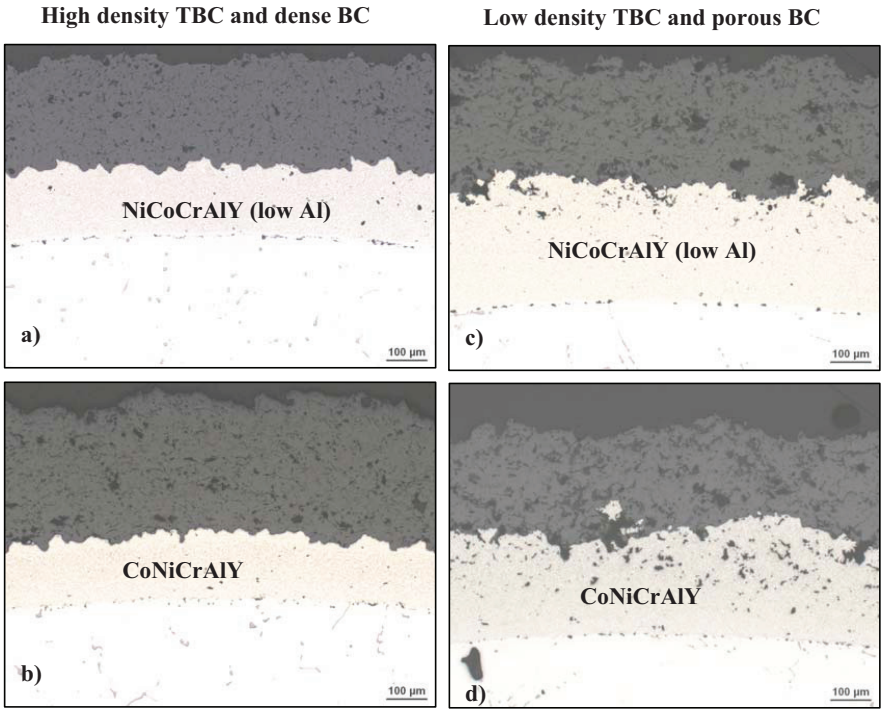

Fig.7.1 Optical metallographic cross-sections of as-received APS-TBC's with MCrAlY bond coats on IN738 alloy: a) and c) NiCoCrAlY (low Al) BC; b) and d) CoNiCrAlY BC; a) and b) show systems with high density TBC and dense BC; c) and d) the systems with low density TBC and porous BC

chapter 6.1 have shown that their lifetime is longer when using CoNiCrAlY bondcoats compared to NiCoCrAlY bondcoats. This difference was attributed to the stabilization of two-phase γ + β coating microstructure by Co, resulting in reduction of the CTE of the coatings. Therefore, in the present investigation a study has been undertaken to check whether a similar positive effect of Co additions to the bondcoat on the lifetime also occurs in the case of APS-TBC systems. It is well known from literature that the measured cyclic oxidation lifetimes of APS-TBC systems are significantly affected by the microstructure of the bondcoat as well as topcoat [34]. Consequently, TBC systems were produced with substantial differences in the coatings microstructures as shown in Fig 7.1. The parameters varied were bondcoat roughness profile and porosities of TBC and bondcoat. In this experiment, the NiCoCrAlY (low Al) and CoNiCrAlY bondcoats deposited on IN738 superalloy were used to investigate the effect of the parameters on lifetime of APS-TBC's. For proprietary reasons the TBC-lifetimes in this chapter are given as relative values in arbitrary units (a.u.). These relative lifetimes were calculated by dividing the measured TBC-lifetimes in hours at high temperature by a constant.

7.2.1 Coating systems with high density APS TBC and dense bondcoats

Fig. 7.2 shows the lifetime data of studied APS-TBC systems after 2h/15min cyclic oxidation in air at 1100°C and 1050°C. At 1100°C the lifetimes of systems with CoNiCrAlY bondcoat was approximately twice as long as those with NiCoCrAlY (low Al) bondcoat. At 1050°C the average lifetime of the specimens with CoNiCrAlY bondcoat was about 1500h, which was longer by a factor of three than that with the NiCoCrAlY (low Al) bondcoat.

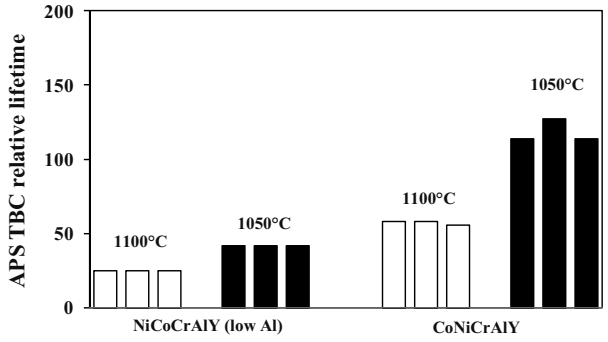

Fig.7.2 Lifetime of high density APS-TBC's with dense MCrAlY bond coats on IN738 alloy after 2h/15min cyclic oxidation in air at 1100°C and 1050°C

After cyclic oxidation in air at 1100°C the failure modes were similar for the TBC systems with NiCoCrAlY (low Al) and CoNiCrAlY bondcoats (Fig 7.3). In both conditional cases, the cracks could be found within the TBC close to the interface with the bondcoat. Apparently, the cracks initially formed at the peaks of the bondcoats surface, and then the cracks propagated through the TBC (Fig

7.4). Finally, crack coalescence occurred, which could lead to macroscopic TBC failure. Based on the similarities in failure mode between the two TBC systems it can be argued that lower CTE of the CoNiCrAlY bondcoat compared to NiCoCrAlY (low Al) bondcoat was one of major factors that determined the longer lifetime of the system with the former bondcoat.

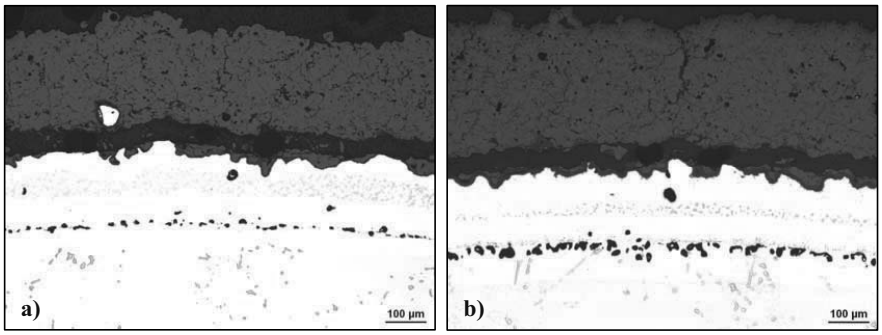

Fig.7.3 Optical metallographic cross-sections of failed APS-TBC's with MCrAlY BCs on IN738 alloy after 2h/15min cyclic oxidation at 1100°C in air, a): NiCoCrAlY BC, 324h , b): CoNiCrAlY BC, 720h

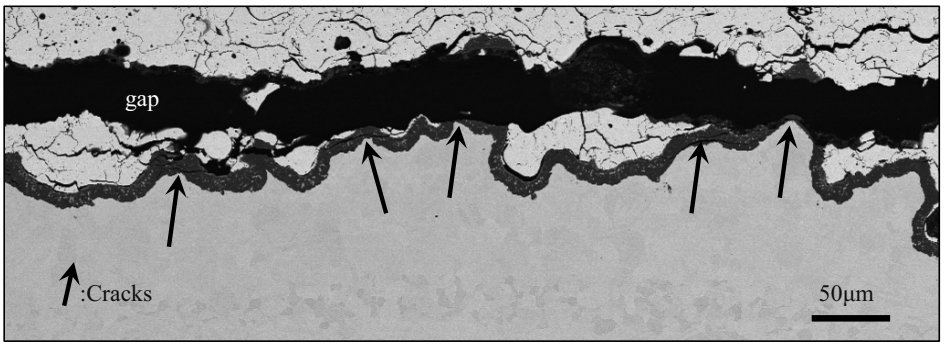

Fig 7.4 SEM image of APS-TBC system with CoNiCrAlY BCs on IN738 alloy after 2h/15min cyclic oxidation at 1100°C in air till TBC failure for 720h. The arrows point out the cracks formed at peaks of the bondcoat system

Fig 7.5a shows the SEM cross-section of APS-TBC systems with NiCoCrAlY (low Al) bondcoat after

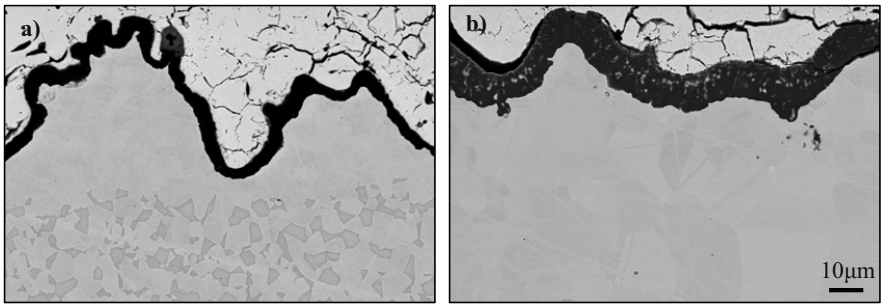

Fig.7.5 Cross-sections of APS-TBC's with MCrAlY BCs on IN738 alloy after 2h/15min cyclic oxidation at 1100°C in air, a) NiCoCrAlY (low Al), 100h and b) CoNiCrAlY, 720h

100h cyclic oxidation at 1100°C in air. The oxide scale on the bondcoat mainly consists of alumina. There were virtually no Y-rich oxides in the scale on NiCoCrAlY (low Al) bondcoat due to a relatively small Y reservoir in the coating (the Y-content in NiCoCrAlY (low Al) is about 0.3%). However, the Y-rich oxides could be found in the specimens with CoNiCrAlY bondcoat (Fig 7.5b). The high Y-content (about 0.6% Y) in the CoNiCrAlY bondcoat caused the formation of Y-aluminates in the TGO. The Y-rich oxides are found only in the outer part of TGO on the CoNiCrAlY bondcoat. The absence of the Y-aluminates in the inner part of the TGO is apparently due to depletion of Y from the bondcoat after the extended oxidation time for the formation of Y-aluminates, as described elsewhere [98]. The TGO located at the convex parts of the bondcoat contained less Y-rich oxides than the concave parts. This effect was shown by Gil et al. [46] to be related to faster Y-depletion underneath convex bondcoat surfaces with a large volume to surface ratio compared to the concave surfaces. It should be noted that the high Y-content in the CoNiCrAlY bondcoat alone can not explain a longer TBC lifetime compared to that on the NiCoCrAlY bondcoat. It is evident from Fig 7.4 and 7.5b that the TBC-failure occurred after the Y had been largely depleted from the bondcoat. This argument is also supported by the observation of M.Subanovic [67] who found that the Y content in VPS MCrAlY bondcoats had no major effect on the thermal cyclic lifetime of APS TBC's. Therefore it is believed that a lower CTE of the CoNiCrAlY bondcoat compared to that of the NiCoCrAlY (low Al) bondcoat made the most significant contribution to the longer lifetime of the TBC, which is supported by the previous discussion on EB-PVD TBC systems in chapter 6.1.

7.2.2 Coating systems with low density APS TBC's and porous bondcoats

The low density APS TBC systems with porous NiCoCrAlY (low Al) and CoNiCrAlY bondcoats on IN738 superalloy were tested under 2h/15min cycles at 1100°C and 1050°C in air. The lifetime data are shown in Fig 7.6. Contrary to the lifetime of high density TBC's shown in Fig 7.2, the lifetime of the TBC system with porous NiCoCrAlY bondcoat exhibited a lifetime which was by about 20% at 1100°C and 15% at 1050°C, than observed for the CoNiCrAlY bondcoat.

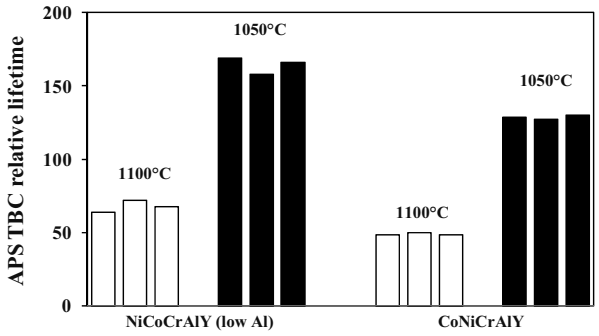

Fig. 7.6 Lifetime of low density APS-TBC's with porous MCrAlY bond coats on alloy IN738 after 2h/15min cyclic oxidation in air at 1100°C and 1050°C

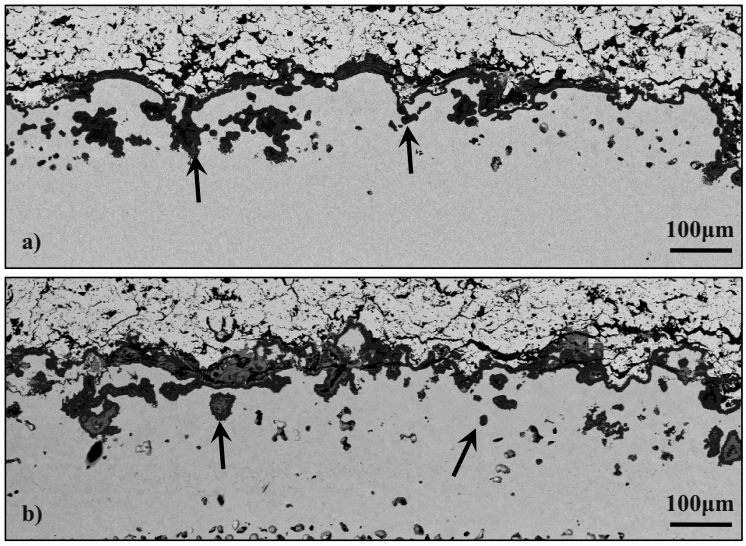

Fig. 7.7 SEM images of failed APS-TBC's with MCrAlY bond coats on alloy IN738 after 2h/15min cyclic oxidation at 1100°C in air, a): NiCoCrAlY (low Al), 828h , b): CoNiCrAlY, 594h. The arrows point to the internal oxides formed in the pores near the coating surface

The oxide scale morphologies can be observed in Fig 7.7 showing the cross-sections of the low-density TBC with the two porous bondcoats. It can be noted that the surfaces of pores in the upper part of the bondcoats were oxidized. Apparently, the pores which were present in the as-received bondcoats (Fig 7.1) had partly a direct contact to the bondcoat surface allowing rapid oxygen penetration. Fig 7.8 shows the high magnification pictures of cross-sections of the specimens with the two studied bondcoats. Repeated cracking within the oxide scale could be observed in Fig 7.8a for the specimens with NiCoCrAlY (low Al) bondcoats which is a different crack morphology compared to the dense bondcoat in the chapter in 7.2.1 (Fig 7.4). In the convex parts of the bondcoat roughness profile the TGO is very thick, consisting of several layers, whereas cracks run parallel to each other

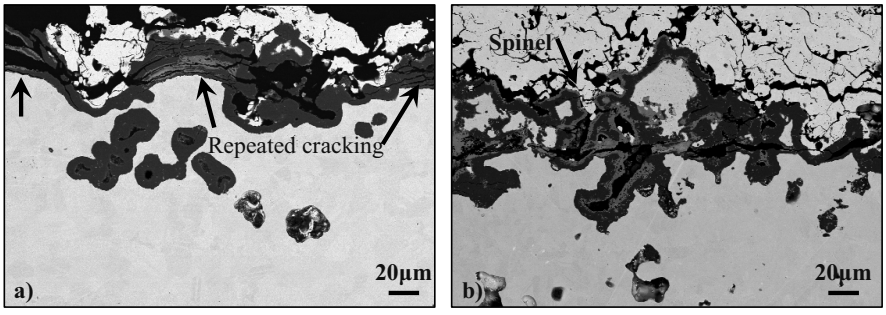

Fig. 7.8 SEM images of failed APS-TBC's with MCrAlY bond coats on alloy IN738 after 2h/15min cyclic oxidation at 1100°C in air, a): NiCoCrAlY (low Al), 828h, showing repeated cracking within the TGO; b): CoNiCrAlY, 594h, showing spinel formation and cracking in the outer part of BC

within the TGO. Such repeated cracking morphology can be an indication of the extended TBC lifetime as will be discussed in the next chapter. For the system with CoNiCrAlY bondcoat in Fig 7.7b and 7.8b, spinel phase oxidation could be found on the surface of the alumina scale, which could be one of the reasons for a relatively short TBC lifetime shown in Fig 7.6. The detailed reason for such morphologies, e.g. repeated cracking for NiCoCrAlY (low Al) and spinel formation for CoNiCrAlY bondcoat, will be discussed in the next chapter.

Porosity formation at bondcoat/alloy interfaces for both MCrAlY coatings, is shown in Fig 7.9. There are more pores formed at the CoNiCrAlY/alloy interface after nearly 600 h exposure than at the NiCoCrAlY/alloy interface after more than 800 h oxidation. In the as-received condition (Fig 7.10a and b), some alumina particles can be observed at the bondcoat/alloy interface. These particles apparently originate from the specimen alloy surface preparation (grit blasting) prior to bondcoat deposition. The porosity (Fig 7.10 c and d) at the bondcoat/alloy interface increased for both coatings during oxidation for 300h at 1050°C. The Kirkendall effect probably played an important role for the formation of pores due to non-equal fluxes of diffusing elements e.g. Ni, Co, Cr, and Al. However, much more pores formed at the CoNiCrAlY bondcoat/alloy interface could be observed after shorter time in Fig 7.9b. The latter phemonon is probably related to the formation of β-NiAl and carbides precipitates next to the pores on the side of superalloy (Fig 7.10d). Much more Cr and Co could diffuse into the base superalloy due to higher Cr and Co contents in case of the CoNiCrAlY compared to the NiCoCrAlY (low Al) bondcoat (see Table 5.2) during high temperature exposure. The higher Cr-content in the case of the CoNiCrAlY bondcoat is likely to promote the Cr-carbide formation (in Fig 7.10d) and also increases the Al activity in the coating thereby promoting its diffusion into the base alloy. The most important effect of Co is believed to be the stabilization of the β-phase in the

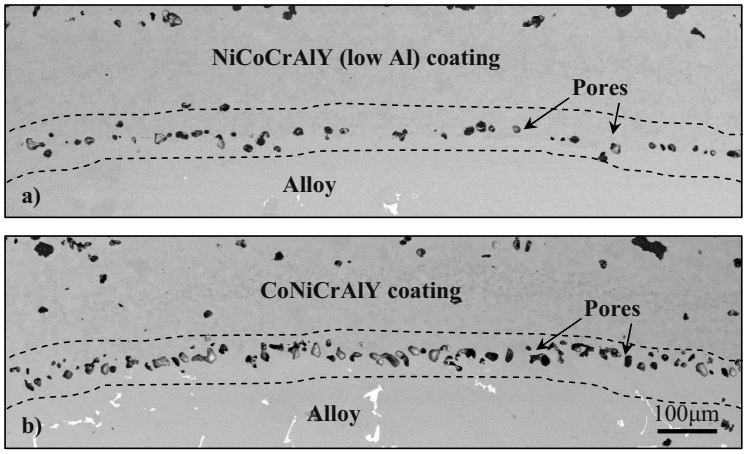

Fig. 7.9 SEM images of the porosity at the MCrAlY BC/IN738 alloy interface, failed APS TBC after 2h/15min cyclic oxidation at 1100°C in air, a): NiCoCrAlY (low Al), 828h ; b): CoNiCrAlY, 594h

interdiffusion zone formed between IN738 and the CoNiCrAlY bondcoat. Formation of β-NiAl and the carbide phase apparently induced a considerable volume change in the interdiffusion zone [35] which finally resulted in enhanced formation of porosity at the bondcoat/alloy interface. It should be pointed out that the reverse β to γ phase transformation occurred after extended time due to continuous elements interdiffusion, whereby no β phase precipitates could be found for the failed TBC system after nearly 600h oxidation at 1100°C (Fig 7.9b).

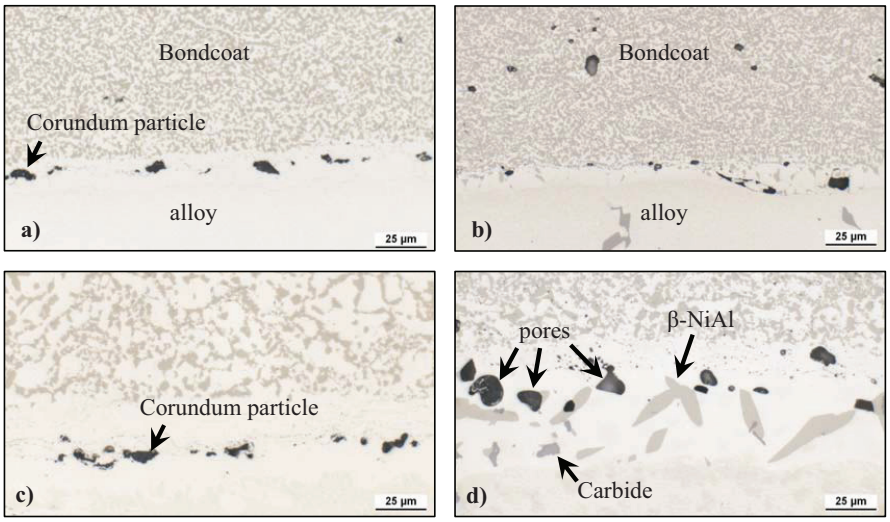

Fig 7.10 Metallographic cross-sections of as-received a) NiCoCrAlY (low Al) BC and b) CoNiCrAlY BC/superalloy interface as well as after oxidation at 1050°C in air for 300h, c) NiCoCrAlY (low Al); d) CoNiCrAlY

7.2.3 Effect of bondcoat and TBC microstructure on lifetime of APS TBC systems

The above presented results indicate that significant TBC-lifetime extension was obtained with CoNiCrAlY bondcoat compared to NiCoCrAlY in the TBC-systems with dense TBC and bondcoat. In contrast, with low density TBC and porous bondcoat the TBC lifetime was even slightly shorter with the CoNiCrAlY compared to the NiCoCrAlY coating. It is clear, therefore, that the TBC and bondcoat microstructures play a crucial role in governing the TBC-system lifetime. To evaluate the effect of TBC and bondcoat microstructure on the lifetime of the TBC system, detailed analytical studies of the samples were performed in the as-received condition as well as after oxidation. In addition, a TBC-system was studied, which had a dense NiCoCrAlY (low Al) and a porous TBC to separate the effects of TBC and bondcoat microstructures on the system lifetime.

7.2.3.1 NiCoCrAlY(low Al) bondcoat

The lifetimes of the APS TBC-systems with NiCoCrAlY (low Al) bondcoats at 1050°C and 1100°C are summarized in Fig 7.11. At 1050°C the system with dense TBC and dense bondcoat showed the

shortest lifetime among the TBC systems studied. The system with porous TBC and porous bondcoat showed a nearly 4 times longer lifetime than that of the specimens with dense coatings. The system with porous TBC and dense bondcoat showed a lifetime which was longer only by a factor of two compared to the TBC system with dense coatings. A qualitatively similar lifetime trend for the above three TBC systems could be also observed at 1100°C.

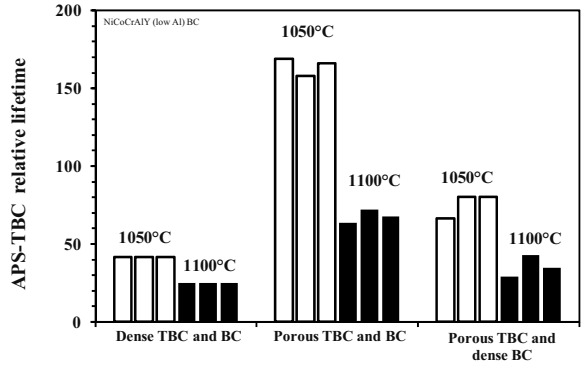

Fig 7.11 Lifetimes of the TBC systems with NiCoCrAlY (low Al) bondcoats after 2h/15min cyclic oxidation in air at 1050°C and 1100°C

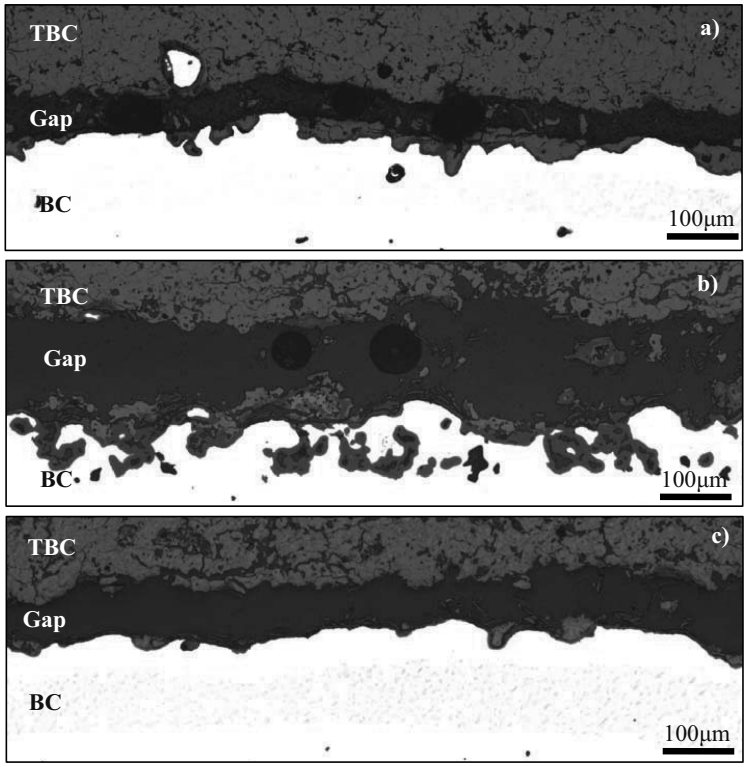

Fig. 7.12 Optical metallographic cross-sections for the three different TBC systems with NiCoCrAlY (low Al) bondcoat after failure (2h/15min cyclic oxidation in lab air at 1100°C): a) dense TBC and BC, b) porous TBC and BC, and c) porous TBC and dense BC

In Fig 7.12, the metallographic cross-sections illustrating the TBC failure modes of the three above mentioned TBC systems are summarized. For the system with dense TBC and bondcoat, a “classical” failure mode can be observed [111] i.e. the cracks form at the TGO/bondcoat interface, on hill at the bondcoat surface and then grow in the TBC until occurrence of macroscopic failure. In contrast in the system with low density TBC’s and porous bondcoat the crack path is substantially more complex than that in the dense TBC system. In many places a very thick and severely cracked TGO is observed, which is, however, still in contact with the bondcoat surface. For the specimen of porous TBC with porous bondcoat, the outer part of the bondcoat included some voids with oxidized surfaces. The systems with porous TBC and dense bondcoat exhibited a similar TGO morphology compared to the dense TBC system (Fig 7.12c). Fig 7.12 also shows that β-NiAl phase still could be found at the center of the bond coatings after TBC lifetime indicating that in all cases Al-depletion was not the reason for TBC-failure. According to the lifetime data in Fig 7.11, the microstructure of the porous NiCoCrAlY bondcoat provided a beneficial effect on the TBC life; the possible mechanisms responsible for this effect will be discussed below.

The dense NiCoCrAlY bondcoat formed a uniform alumina scale on its surface (Fig 7.13a). The cracks initiated in the convex parts of the coating surface (Fig 7.13a and c).

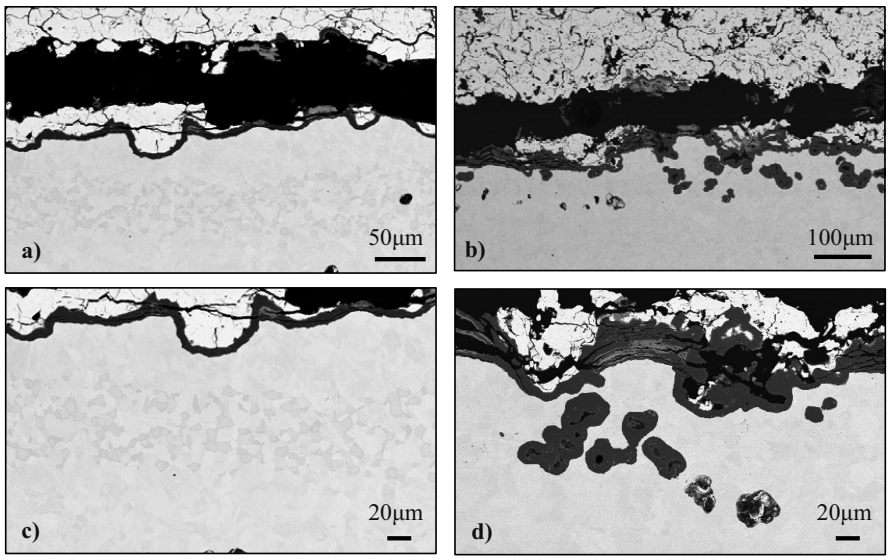

Fig 7.13 Cross-sections of failed APS-TBC’s with NiCoCrAlY (low Al) bond coats on IN738 alloy after 2h/15min cyclic oxidation at 1100°C in air, a) and c): dense TBC and BC, 324h , b) and d): porous TBC and BC, 828h

During cooling of an APS-TBC system exposed to high-temperature oxidizing environment, high compressive out-of-plane stresses are generated at the TGO/bondcoat interface concave parts of the rough bondcoat surface, which prevents TGO spallation. In the convex parts of the rough surface,

however, tensile out-of-plane stresses will build up the TGO/bondcoat interface. The TGO thickness and the radius of curvature govern the stress value. These tensile stresses promote crack initiation at the TGO/bondcoat interface, as shown in Fig 7.14a. The resistance of the interface to TGO delamination depends on the TGO adhesion and the stress value. When the cracks at the hill of the coating propagate along the roughness profile, the shear stress in the TGO would increase with the tensile stress decreasing. The alumina scale fracture occurs when the shear stress reaches a critical value which depends on the TGO mechanical properties. Subsequently, the crack penetrates the TGO and enters the TBC. The rate of crack propagation through the TBC depends strongly on its microstructural properties. In the case of the dense TBC system, the rate of crack growth is higher than in the other two systems, since there are less microstructural defects in the TBC, such as pores or microcracks to dissipate the energy available for fracture at the crack tip.

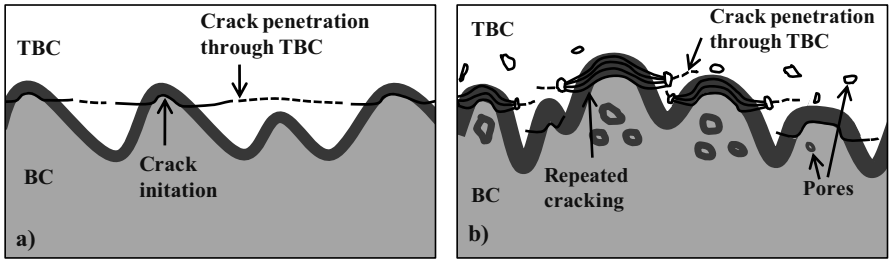

Fig 7.14 Schematic illustrating different crack growth and propagation modes in different APS TBC systems, a) dense TBC and BC; b) porous TBC and BC

The system with dense bondcoat and porous TBC is more “strain-tolerant” than the dense TBC system because the TBC contains a larger number of defects, thereby effectively reducing the crack growth rate. As a consequence, a longer lifetime is measured with the former system in a thermal cyclic test. For the system with porous TBC and porous bondcoat, however, the situation is different. One significant difference compared to the other two systems is the observed layered morphology of the TGO at bondcoat “hill”. The mechanism of the formation of the layers can be derived from Fig 7.15. The columnar oxide microstructure, which is a typical characteristic for the inward growth of the alumina scale, could be observed for each of the separate TGO layers. This observation indicates that the formation of separate TGO-layers occurred independently and each layer formed on a fresh metal surface, rather than parallel cracks were initiated in the TBC and then propagated via defects in the thick alumina scale.

It is therefore obvious, that the bondcoat surface morphology and/or micro-structure have a substantial impact on the TBC-lifetime. To understand the effect of microstructures of dense and porous coating systems on the TBC life, some coating parameters are summarized in Table 7.1, which were derived using image analysis of the TBC system cross-sections. The root-mean-square (*RMS*) roughness is defined as the average height of the bond coating surface relative to the mid-section, and the tortuosity

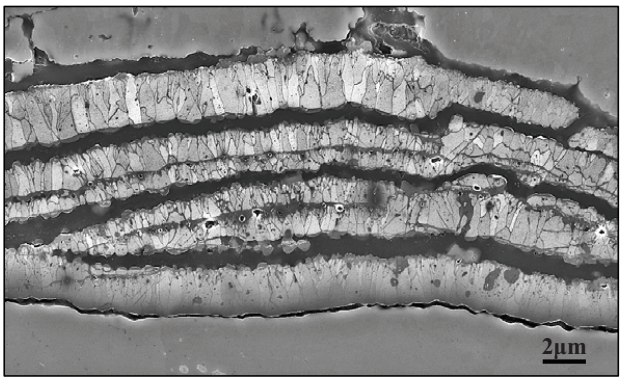

Fig 7.15 In-Lens SEM-image of the repeated TGO cracking during cyclic oxidation at 1050°C in APS-TBC system with NiCoCrAlY (low Al) bondcoat

(L/L_0) is the length of the digitized profile (L) of the bondcoat rough surface divided by the length of the cross-section window. Fig 7.16 shows the profiles of the dense and porous bondcoats. It can be clearly seen that the roughness of the porous bondcoat is significantly higher than that of the dense bondcoat.

Table 7.1 Microstructural parameters of studied TBC systems derived from metallographic cross-sections using image analysis software analySIS®

Types	Porosity of TBC	Bondcoat surface roughness (*RMS*), µm	Bondcoat surface tortuosity (L/L_0)
Dense TBC and BC	7-8%	13	1.43
Porous TBC and BC	9-14%	22	1.98

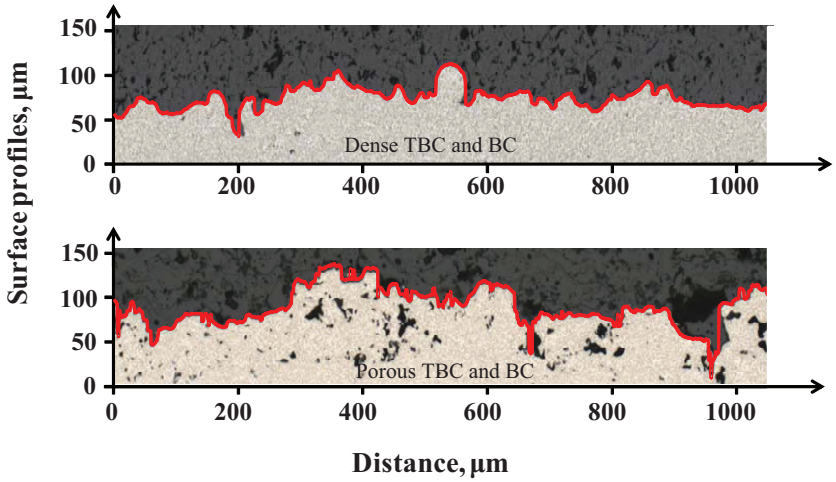

Fig. 7.16 Bondcoat surface roughness profiles digitalized for as-received dense and porous TBC systems

Based on the comparison of roughness profiles it can be argued that the bondcoat surface of the porous bondcoat exhibits a more convoluted morphology than the dense bondcoat. This micro-roughness results in crack initiation in locations at different heights with respect to the mid-section. Consequently, the coalescence of these growing cracks is a slower process, as compared to a more uniform roughness profile. This in turn allows formation of the observed repeated cracking of the TGO (Fig 7.8). These considerations are illustrated schematically in Fig 7.14b. Another possible reason for the slow crack growth in the TBC and repeated cracking of TGO can be bondcoat porosity. The outer bondcoat areas with oxidized pores can perhaps serve as a graded layer having a lower CTE compared to the bulk of the coating resulting in a reduction of stress generated by CTE-mismatch between BC and TBC.

Fig 7.17 summarizes schematically the effect of various microstructural parameters on the crack propagation and lifetime of the APS-TBC systems The time dependence of crack length is substantiated by experimental results previously published by Trunova et al [140]. The porous TBC systems show a slower crack growth rate resulting in lifetime extension as compared to the dense TBC system. The porous bondcoat could further extend the TBC life by modifying the crack initiation pattern in the TBC and/or by reducing the effective bondcoat coefficient of thermal expansion as discussed above.

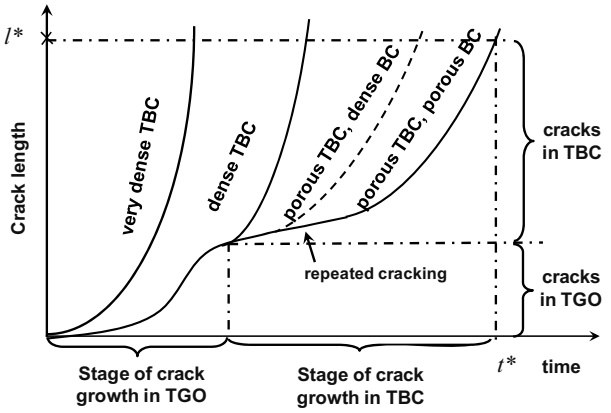

Fig. 7.17 Schematic of the rates of crack formation and propagation for the APS-TBC systems with NiCoCrAlY BC during cyclic oxidation in air, *l**: critical crack length leading to occurrence of macroscopic TBC-failure after time *t**

It should be noted that very-dense TBC's (porosity below 7%) with compact bondcoat exhibited at 1100°C a shorter lifetime, about 100h, compared to the above three TBC systems after 2h/15min cyclic oxidation in air. Fig 7.18a shows the cross-sections of the as-received specimens, of which the TBC exhibited a very high density that was even higher than that of the discussed above dense TBC system. In Fig 7.18b, the parallel and vertical cracks within the APS TBC could be found when the specimen failed, whereas the TGO showed a good adherence to the bondcoat/TGO/TBC interface.

These observations point out that the failure of very-dense TBC's was not directly associated with bondcoat oxidation. The crack formation in the TBC is mainly associated with the strain energy accumulated within the ceramic top coat during cyclic oxidation, especially during cooling. The early TBC failure which occurs in the ceramic top coat above the bondcoat is an indication of an extremely low strain-compliance of the very dense TBC although there were perhaps some small cracks also formed in the TGO.

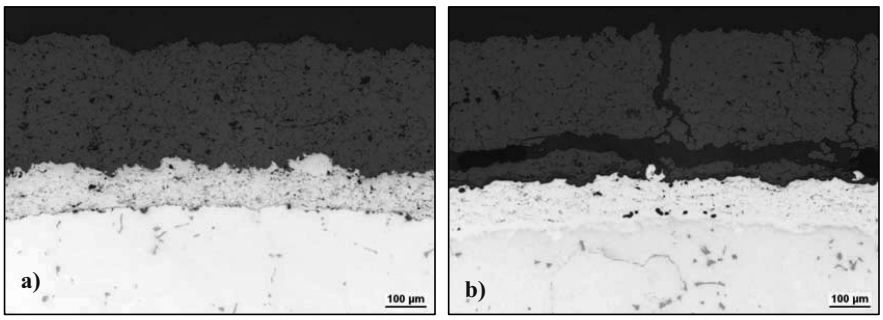

Fig. 7.18 Optical metallographic images of very-dense APS-TBC system with NiCoCrAlY (low Al) BC on IN738LC, a) as-received; b) after 2h/15min cyclic oxidation for 100h at 1100°C in air

7.2.3.2 CoNiCrAlY bondcoat

The lifetime data of the APS TBC with CoNiCrAlY bondcoats after cyclic oxidation are summarized in Fig 7.19. The lifetime of the dense TBC systems with dense bondcoat was about 1500h, which is comparable with that of porous TBC and bondcoat systems at 1050°C. The lifetime of both TBC systems was about 700h at 1100°C, which is only half of that at 1050°C. These lifetime data illustrate that the porous TBC with CoNiCrAlY bondcoat are not longer than the TBC lifetimes observed in the case of NiCoCrAlY (low Al) coating.

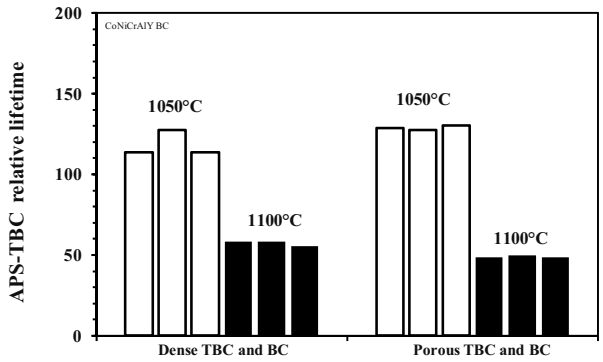

Fig 7.19 Lifetime of TBC systems with CoNiCrAlY bondcoats after 2h/15min cyclic oxidation in air at 1050°C and 1100°C

SEM Cross-sections of the system with dense TBC and dense CoNiCrAlY bondcoat (Fig 7.20a) showed that cracks formed in the convex parts of TGO/ bondcoat interface while then penetrated into the TBC. The failure mechanism is similar to that discussed for dense NiCoCrAlY bondcoat (see Fig 7.14a). Internal oxidation and cracks can be found at the surface of the porous bondcoat in Fig 7.20b. The typical repeated cracking, which was observed for the porous NiCoCrAlY (low Al) bondcoat in Fig 7.13, can only rarely be found for the porous CoNiCrAlY bondcoat in Fig 7.20d. The spinel formation and crack propagation through this mixed oxide dominated the degradation of the TBC system with porous coatings, which prevented a lifetime extension compared to the dense TBC system.

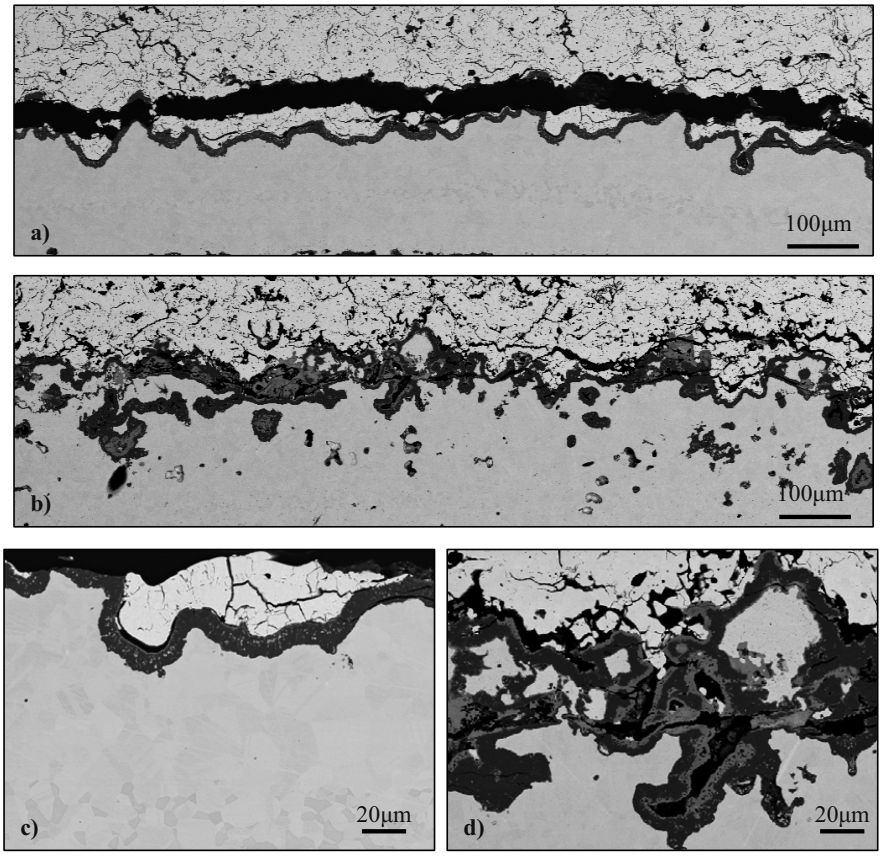

Fig. 7.20 SEM cross-sections of failed APS-TBC's with CoNiCrAlY bondcoats on alloy IN738 after 2h/15min cyclic oxidation at 1100°C in air, a) and c): dense TBC and BC, 720h , b) and d): porous TBC and BC, 630h

To summarize, for CoNiCrAlY bondcoat the extensive spinel formation is observed only in the case of porous coatings. In contrast, on dense CoNiCrAlY bondcoat and on porous and dense NiCoCrAlY bondcoats the spinel formation is insignificant. These observations can be explained as follows:

In the beginning of the bondcoat oxidation process the oxides of all main elements are formed (Ni, Co, Cr, Al), and only after this transient oxidation process a continuous α-Al_2O_3 is established. The duration of the transient oxidation depends on a number of factors, including temperature, alloy (coating) composition and microstructure. It is known from literature [136] that the growth rate of Co-base oxides is significantly faster that that of the Ni-base oxides, due to a much larger concentration of cationic defects in the former oxide. Faster growing transient oxide delays the time before which slowly growing α-Al_2O_3 to be formed as a continuous scale rather than a Co/Al (Ni/Al respectively) mixed oxide (spinel) is formed. This explains why spinel formation is stronger in case of the CoNiCrAlY bondcoat (higher Co-content) compared to the NiCoCrAlY- bondcoat.

The above arguments can, however, not explain why the spinel formation occurs on the porous CoNiCrAlY bondcoat, whereas it cannot be seen on the dense bondcoat. Studies of the as-received materials in Fig 7.21 indicate that the porous bondcoat has a higher roughness and a more convoluted surface and it exhibits more substantial porosity in the outer part of the bondcoat compared to the dense coating. The former microstructure results in much faster Al-depletion due to a much higher layer surface to volume ratio, then rapidly consuming the Al from the bondcoat. As a consequence, the transient oxidation stage will be longer for the porous bondcoat. Fig 7.20b shows that due to the specific morphology of the porous bondcoat and the internal bondcoat-porosity some parts of the coating can become separated from the rest of the bondcoat by the growing oxides. After longer exposure times, this effect results in local breakaway oxidation of the separated parts which become “blocks” of spinel oxides. These spinel “blocks” represent sites for easy crack initiation and/or propagation during thermal cycling, then contributing to shortening of the TBC lifetime.

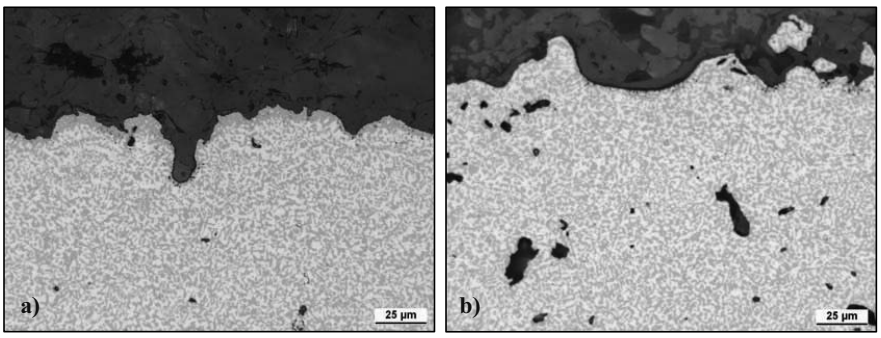

Fig.7.21 Optical metallographic cross-sections of as-received APS-TBC’s with CoNiCrAlY bond coats on IN738 alloy, a): dense BC, b): porous BC

Based on the considerations presented above, one would expect at least some minor amounts of transient oxide (spinel) to be present in the outer part of the TGO formed on the dense CoNiCrAlY bondcoat. This could, however, not be observed in the SEM images (Fig 7.20c). In order to find the reasons for this difference, as-received TBC-systems with dense and porous CoNiCrAlY bondcoat

were studied in more detail. As can be seen in Fig 7.21 the system with dense bondcoat exhibits a thin layer of β-NiAl at the very bondcoat surface, which cannot be observed on the surface of the porous bondcoat.

This thin β-NiAl layer on the dense bondcoat formed during the vacuum heat treatment prior to TBC-deposition as a result of Cr-evaporation. According to the Thermo-calc® calculation in Fig 7.22, the γ and β phases in the coating could transform to β when the Cr-content decreases during the heat treatment. This thin Al-rich β-NiAl layer could suppress the spinel formation due to a high Al-content and a lower Co-content on the coating surface in the dense coatings.

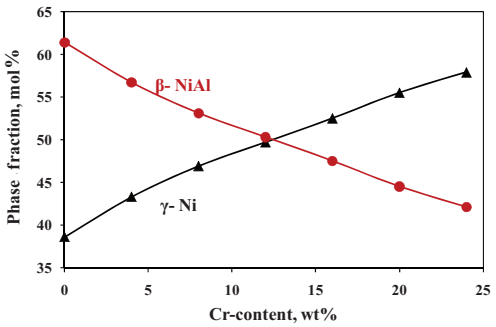

Fig.7.22 Equilibrium Beta-NiAl fraction as a function of Cr-content calculated by Thermo-calc® for the composition of the studied CoNiCrAlY coating at 1120°C

Since different vacuum furnaces were used for the heat-treatment of the dense and porous bondcoats it is believed that the difference in Cr-evaporation can be related to different vacuum qualities prevailing in two equipments. In both cases the vacuum quality during heat-treatment was better than 10^{-4}mbar. Based on recent studies [141] it can be argued that the rate of Cr-evaporation increases with increasing vacuum quality, i.e. decreasing the residual pressure in the vacuum chamber.

According to the above results, a high Co-content in the MCrAlY bondcoat can promote spinel formation. During high temperature air exposure the effect can be accelerated by a high surface roughness and a high porosity of the bondcoat. The spinel formation was shown to be detrimental for the APS TBC lifetime. The formation of spinel could be suppressed by a thin layer of β-NiAl phase formed on the bondcoat surface of one of the TBC-systems during vacuum heat-treatment. These results imply that in the case of APS TBC systems the bondcoat surface roughness and composition are of great importance for obtaining a long and reproducible TBC life.

7.3 Effect of O content on the lifetime of APS TBC systems with MCrAlY and MCrAlY+Zr bondcoats

In chapter 6.2, it was shown that minor Zr additions to the NiCoCrAlY bondcoats can result in lifetime extension of the EB-PVD TBC systems. The magnitude of the extension was, however, strongly dependent on the Zr-reservoir in the bondcoat. In contrast to EB-PVD TBC systems, however, a high Zr-content (0.6 wt %) in the bondcoat resulted in a shorter TBC lifetime in case of the APS TBC's [67]. The reason for this negative effect was claimed to be a excessive non-uniform incorporation of Zr into the TGO resulting in local over-doping on the rough bondcoat surfaces. Accumulation of Zr-rich oxides in the concave parts of the bondcoat occurred, which provided short-circuit paths for oxygen diffusion thus promoting scale growth. Rapid growth of the TGO in the neighboring concave areas finally led to encapsulation of the convex bondcoat areas by oxides. The encapsulated areas failed by breakaway oxidation due to the formation of voluminous Ni/Co-rich oxides, which initiated the macroscopic TBC failure.

In section 6.1.1 it was shown for EB-PVD TBC systems that TGO-overdoping can be suppressed and TBC-lifetime substantially extended by reducing the reservoir of free Zr in the coating through decreasing the zirconium content. Another possibility could be to increase the O-content in the coating. In this way, Y and/or Zr could be partly tied-up in the bond coatings and the incorporation of the reactive elements into the TGO could be reduced, thereby reducing the scale growth rate and internal oxidation.

In this study, the effect of O content on the life of APS TBC's has been investigated for the NiCoCrAlY bondcoat with and without Zr-addition. The O-content in the coating was varied by varying the vacuum quality during the VPS process. The oxygen content in the bondcoats was measured using free-standing MCrAlY coatings. The free-standing coatings were produced using the same VPS-process as applied for the bondcoats for the TBC-systems, by spraying 2 mm thick coatings on 20×20 mm steel plates. The free standing coatings were removed from the steel plates by spark-erosion, and then ground and cleaned in ethanol prior to the combustion analysis of the oxygen content. The analysis of the Y, Zr and O contents are presented in Table 7.2.

Table 7.2 Y, Zr, O-contents in the free-standing MCrAlY (low Al) BC, mass %

	Y	Zr	Low O-content	High O-content
NiCoCrAlY (low Al), low Y	0.28	-	0.05	0.2
NiCoCrAlY (low Al), Zr-mod.	0.28	0.6	0.05	0.2

Lifetime cyclic oxidation testing on APS-TBC systems with NiCoCrAlY (low Al) bondcoat with two different O-contents, with and without Zr addition were performed at 1100°C in air (Fig 7.23). The

average TBC lifetime with NiCoCrAlY+Zr bondcoat with a high O-content was about 300h, which was by a factor of two longer compared to that formed for a bondcoat with a low O-content. Furthermore, the average values of lifetime of the TBC system with Zr-doped, high-O bondcoat are similar to those of Zr-free bondcoats with low as well as high O-contents.

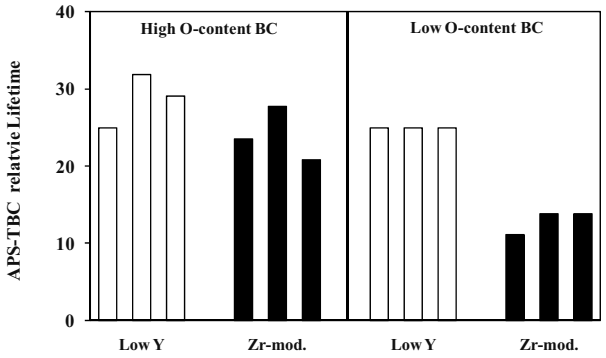

Fig. 7.23 Lifetime of cylindrical APS-TBC with NiCoCrAlY (low Al) BC with various Y, Zr and O contents tested in 2h/15min cyclic oxidation experiment at 1100°C in air. Low Y: NiCoCrAlY (low Al), low Y BC; Zr-mod.: NiCoCrAlY (low Al), Zr-mod. BC. Concentration of Y, Zr, O are given in Table 7.2

Fig 7.24 shows metallographic cross-sections of the studied TBC systems after oxidation until failure at 1100°C. It can be seen that the TGO morphologies and failure modes are similar between all systems except the one with Zr-doping and low O-content, in agreement with the lifetime data in Fig 7.23. In the three first mentioned systems rather uniform TGO's formed and the crack propagation path is similar as described in the previous section for NiCoCrAlY bondcoat, i.e. cracks initiated at the TGO/bondcoat interfaces of the convex surfaces propagating through the TBC. The system with Zr-doped bondcoat and low O-content shows excessive oxidation in the concave parts of the bondcoat. The two systems with the high O-content show numerous oxide inclusions throughout the bondcoat, which were identified by EDX-analysis to be Y/Al-rich oxides, in agreement with previous observations [25].

As discussed in the introduction to the present work, additions of reactive elements, such as Y are of significant importance for the oxide scale adherence on alumina forming alloys and coatings. Furthermore, it has been shown that the positive RE-effect depends on the RE-reservoir and RE-distribution in the alloy/coating prior to the high-temperature oxidation. It was found [65] that during cyclic oxidation of NiCrAl alloys the resistance of the oxide scale to spallation increased with increasing Y to S and Hf to C ratio. The results with EB-PVD TBC systems with Y+Zr co-doped MCrAlY bondcoats with low Y, Zr contents also suggested [67] that the TGO adherence and the TBC lifetime can be shortened and become less reproducible due to impurities in the bondcoat introduced during processing. This is, because for flat TGO/bondcoat interfaces loss of scale adherence results in

a rapid crack propagation and failure of TGO and TBC. The results in the current chapter, however, indicate that for APS-TBC systems the increasing O-content does not have a negative effect on the TBC life. The reason is that a different failure mechanism prevailing in the case of APS-TBC systems, as discussed in the previous chapter (Fig 7.17). Apparently, the time representing crack formation and growth at the TGO/bondcoat interface represents only a relatively small fraction of the APS-TBC lifetime, which is mainly determined by the crack propagation rate in the TBC.

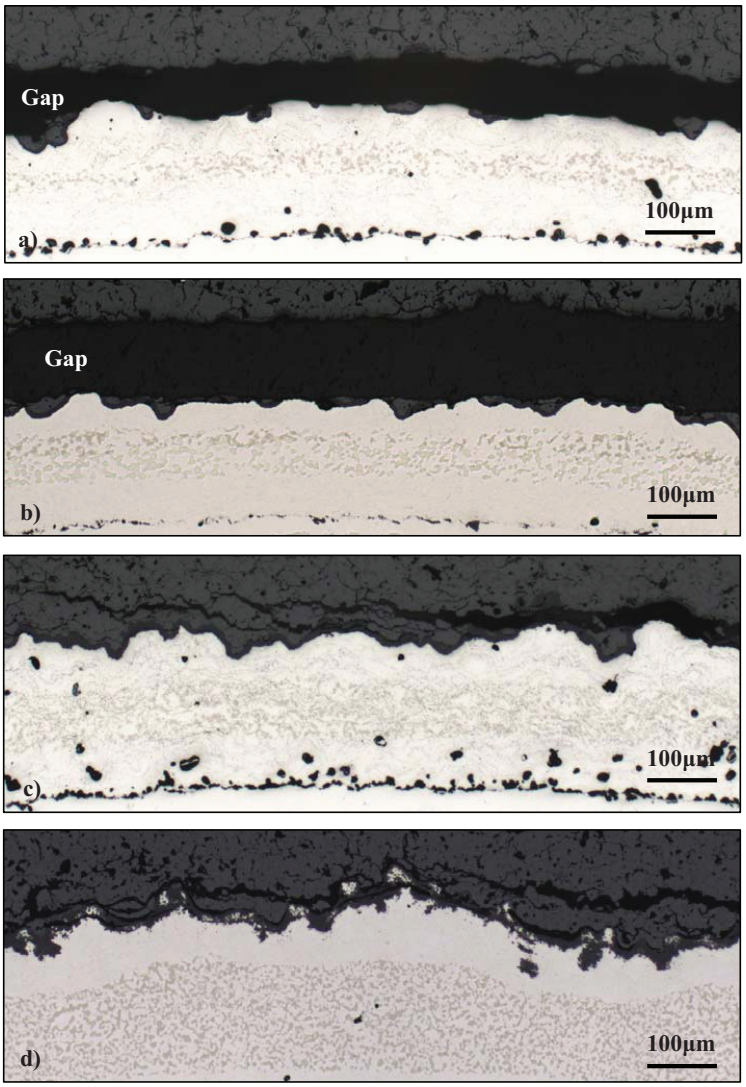

Fig. 7.24 Optical metallographic images for APS-TBC with NiCoCrAlY (+Zr) BC specimen after 2h/15min cyclic oxidation till TBC failure at 1100°C in air, a),Y high-O (324h); b) Y, low-O (324h); c) Y+Zr, High-O (306h); d)Y+Zr, Low-O (144h)

7.4 Effect of atmosphere composition on lifetime of APS-TBC systems with MCrAlY bondcoats

The presence of a higher water vapor content in the atmosphere exhibited a detrimental effect on the lifetime of EB-PVD TBC systems with MCrAlY bondcoats as discussed in chapter 6.3.2. This was explained by hydrogen embrittlement of the oxide scale/bondcoat interface; hydrogen being produced by reaction between H_2O and Al from the bondcoat. Therefore, tests were performed with APS-TBC systems, which had the same bondcoats compositions as those used in the EB-PVD TBC systems in chapter 6.3.2. In this case, it should be checked to see whether a similar detrimental effect of H_2O also occurs in case of APS-TBC systems. The results of the tests show that the water vapor in the atmosphere does not have a significant effect on the APS TBC lifetime in high oxygen partial pressure environment (Fig 7.25). The lifetime of APS TBC systems with MCrAlY bondcoats are comparable when oxidized in air and air + 20%H_2O. It should be noted that the lifetime of the APS-TBC systems with NiCoCrAlY+Beta bondcoat was more than two times longer than the lifetimes of TBC-systems with other bondcoats. This can be probably related to a lower thermal expansion coefficient of the β-phase compared to that of the γ and γ + β MCrAlY-coatings. The lower CTE results in a lower thermal mismatch stress in the TGO and/or the TBC upon cooling, as described previously in chapter 7.2.1.

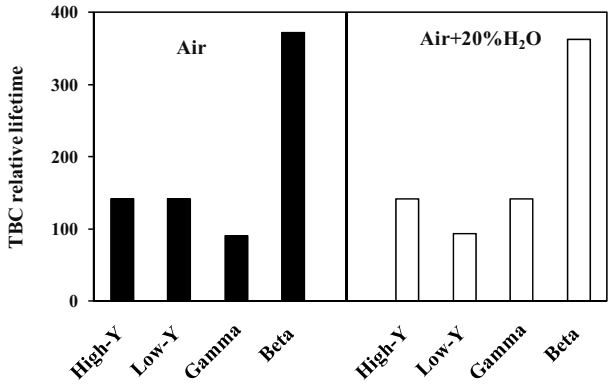

Fig. 7.25 Lifetime of APS TBC systems with different bondcoat after discontinuous oxidation (167h) at 1050°C in air and air + 20% H_2O. High-Y BC: NiCoCrAlY (low Al) with 0.6 wt% Y; Low-Y BC: NiCoCrAlY (low Al) with 0.3 wt% Y; Gamma BC: NiCoCrAlY (low Al) bottom layer + Gamma NiCoCrAl (upper) layer ; Beta BC: NiCoCrAlY (low Al) bottom layer + Beta upper layer

Fig 7.26 shows metallographic cross-sections of the studied APS-TBC-systems after exposure untill failure in laboratory air and laboratory air + 20% H_2O. It can be seen that the crack propagation paths in the TBC are very similar in both atmospheres indicating very similar failure modes. As shown in chapter 7.2.3 and reference [113] the TBC-failure is initially TGO-delaminations from the bondcoat-hills followed by crack extension through the TGO into the TBC until a critical size for macroscopic damage is reached.

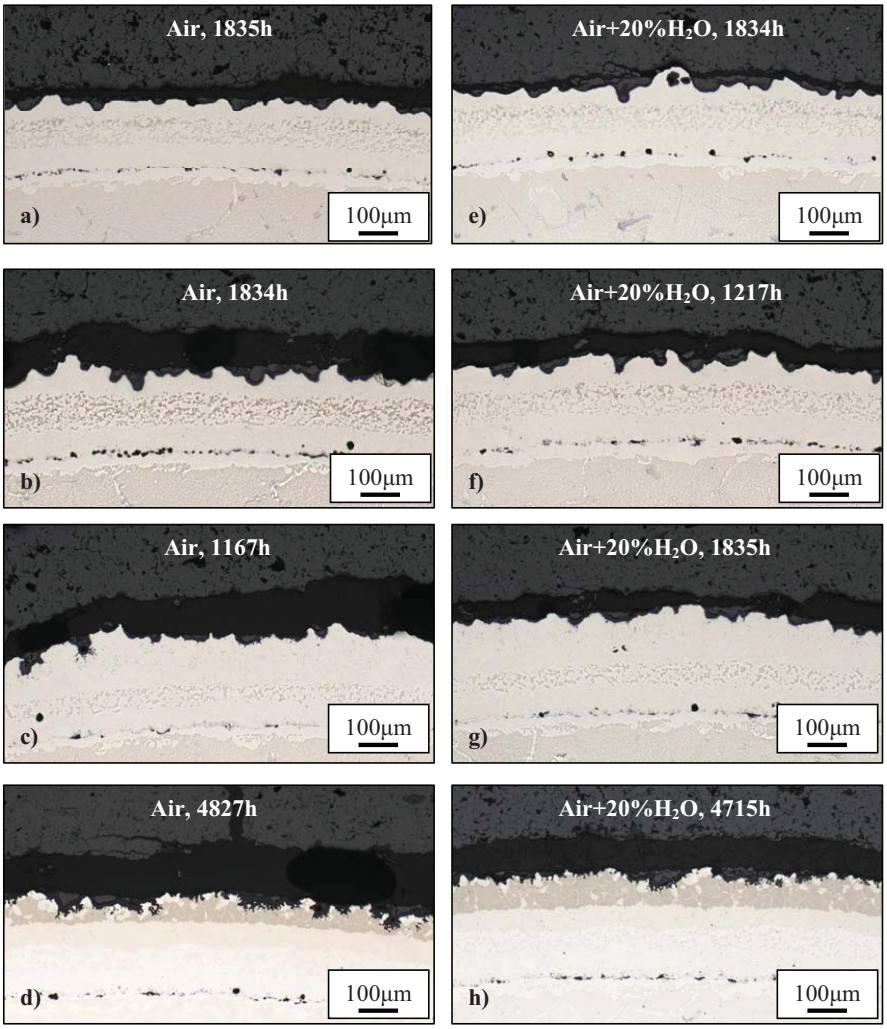

Fig. 7.26 Optical metallographic cross-sections of failed APS-TBC systems with NiCoCrAlY BCs after discontinuous oxidation (167h cycles) at 1050°C in air and air+20%H_2O, a) and e): NiCoCrAlY (low Y); b) and f): NiCoCrAlY (high Y); c) and g): NiCoCrAlY + Gamma; d) and h): NiCoCrAlY + Beta

Investigation of the morphologies and thickness of the TGO's formed in the dry and wet atmospheres reveals a very similar oxidation behavior of the studied TBC-systems in the two environments (Fig 7.27). It is worth emphasizing that similar lifetimes of APS-TBC systems with MCrAlY bondcoats in wet and dry air contrast with the observations made with EB-PVD TBC systems where a large effect of the water vapor on lifetimes was observed. The difference in behavior of the two types of TBC-systems is related to different failure mechanisms. Whereas in the case of EB-PVD TBC systems the presence of water vapor can affect the TGO adherence by H-embrittlement, in the APS-TBC systems it can affect only the early stages of failure, i.e. the delaminations at the scale/metal interface of the

bondcoat-hills. The stage of crack propagation through the TBC seems to be much less affected by the presence of H_2O in the test environment. One of the possible reasons for this finding can be that no reactive metal, such as Al is available for a chemical reaction to produce hydrogen. Another reason is

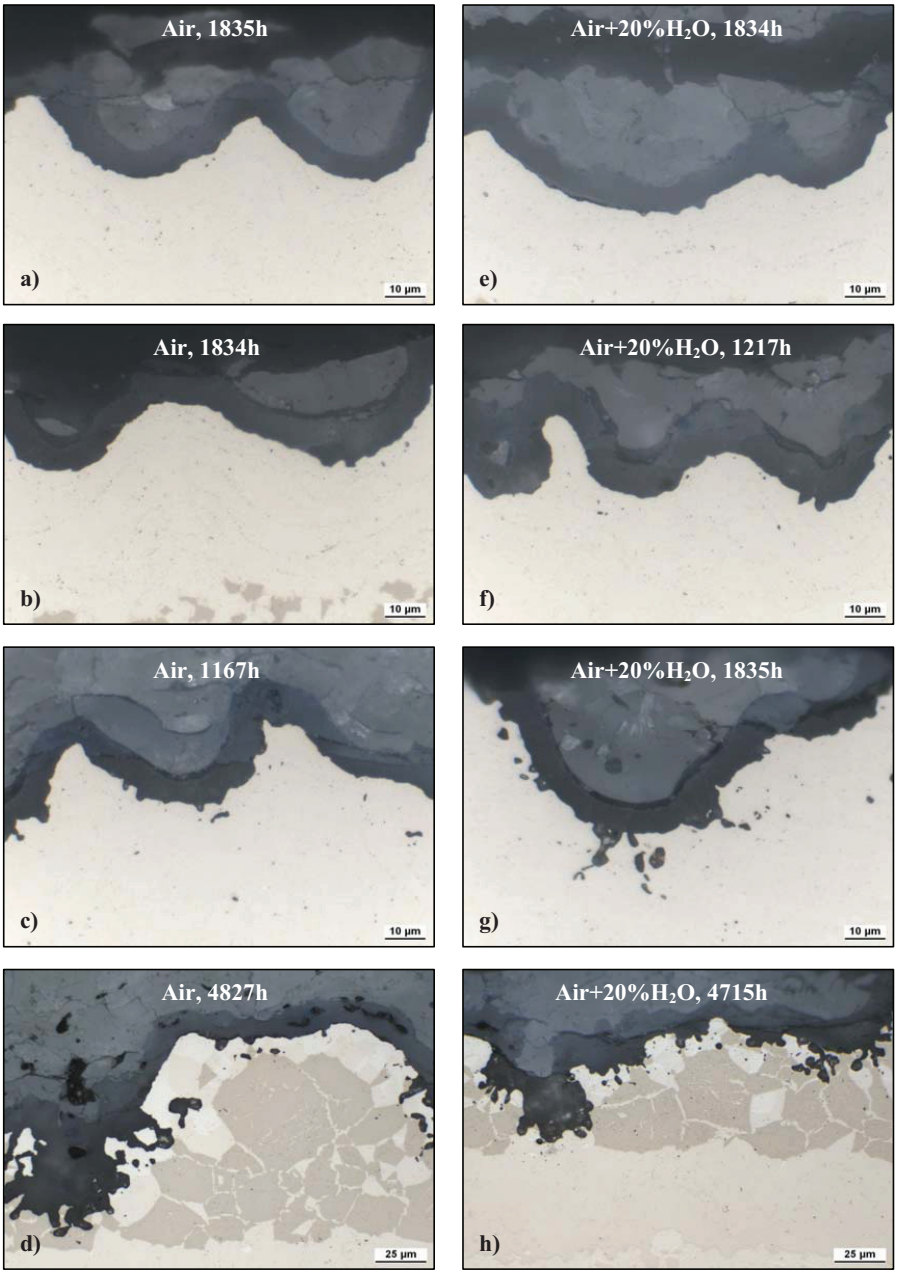

Fig. 7.27 Optical metallographic cross-sections of failed APS-TBC systems with NiCoCrAlY BCs after discontinuous oxidation (167h cycles) at 1050°C in air and air+20%H_2O, a) and e): NiCoCrAlY (low Y); b) and f): NiCoCrAlY (high Y); c) and g): NiCoCrAlY + Gamma; d) and h): NiCoCrAlY + Beta

that single phase YSZ ceramics with 6-8% Y_2O_3 seem to be stable in the presence of H_2O [142]. This contrasts to many other oxide systems, such as glasses, where the presence of moisture was claimed to induce premature mechanical failure of the material by a chemical reaction involving H_2O at the crack tip, a mechanism known as "static fatigue" [143].

Fig 7.28 shows XRD patterns of the APS-TBC systems in the as-received condition as well as after exposure for about 4800h in dry and wet air. It can be seen that the phase composition of the TBC has hardly been changed during the exposure at 1050°C in test gas with H_2O addition. This confirms the above considerations that only a minor effect of H_2O on the phase composition of the TBC occurs.

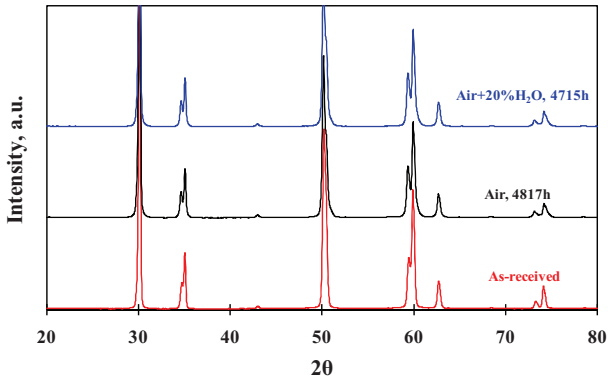

Fig. 7.28 XRD analysis of the as-received APS TBC as well as after oxidation for 4817h and 4715h in air and air+20%H_2O, respectively

7.5 Effect of temperature cycling parameters on lifetime of APS-TBC systems with MCrAlY bondcoats

7.5.1 Effect of cycling frequency on lifetime of APS-TBC with NiCoCrAlY bondcoat

It is well known that APS-TBC lifetime is affected by temperature cyclic conditions. However so far no standardized procedures exist, for the cyclic furnace tests to assess the TBC-lifetime. This makes it difficult to compare the results from different laboratories. Some laboratories are using short cycles of 1-2h hot dwells with cooling periods of 10-20min [103]. In this case forced air cooling is essential to reach near room temperatures within the short cooling time. Other laboratories operate with long cycles, whereby the hot dwell times are in the order of 24-200h and use significantly longer cold dwell times (typically a few hours) with still air cooling. The above differences in test procedure can have a big effect on the measured TBC-lifetime. Since during each temperature cycle stresses are generated in the components of the TBC system due to the differences in CTE, high cycle frequencies can result in more extensive damage and shorter TBC lifetimes.

It was demonstrated for alumina forming alloys and coatings [103] that higher cycle frequencies result in accelerated scale spallation. Another important parameter is the cooling/heating rates. It was shown [122] that alumina scale adhesion can be affected by the creep of the substrate metal. Therefore, slower cooling rates, which can promote metal (or coating) creep can result in a lower residual stress in the TGO/TBC and consequently a longer TBC life. Finally, cold dwell times in EB-PVD TBC systems were shown to be important for TBC lifetime [144] since alumina scale spallation at room temperature is promoted by moisture. Thus, EB-PVD TBC systems were shown to be susceptible to the so-called "desk-top" effect, i.e. delayed spallation of an initially intact TBC during exposure at room temperature. In contrast, for APS-TBC there were no definite conclusions on the desk-top effect. Therefore, in the present project the effect of temperature cycling parameters on the lifetime of APS-TBC systems with NiCoCrAlY (low Al) bondcoat has been investigated.

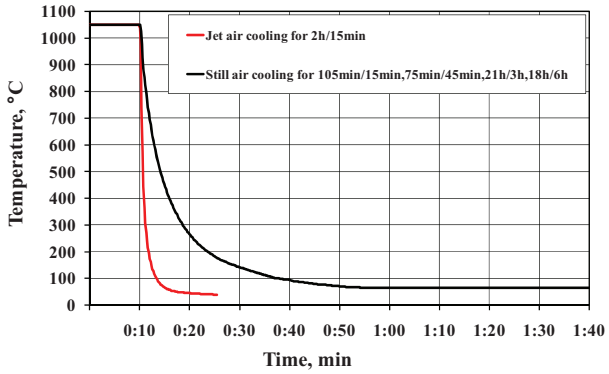

Fig. 7.29 Cooling curves for the different cycling: 105min/15min, 75min/45min, 21h/3h, 18h/6h, and 2h/15min with jet air cooling

Different hot/cold time cycling e.g. 105min/15min, 75min/45min, 21h/3h, 18h/6h, and 2h/15min were carried out for the porous and dense APS TBCs systems at 1050°C in laboratory air. Fig 7.29 showed the different cooling curves. In the first four cycles the specimens were cooled down using still laboratory air. The details of the cycling are shown in Table 7.3.

Table 7.3 Details of the cycling parameters for studied APS-TBC systems

Total cycle length, h	**Hot time, relative length (%)**	**Cold time, relative length (%)**	**Final temperature at the end of cold time, °C**
2h	75min, 62.5%	45min, 37.5%	65°C
	105min, 87.5%	15min, 12.5%	140°C
24h	18h, 62.5%	6h, 37.5%	65°C
	21h, 87.5%	3h, 12.5%	65°C
2.25h	2h, 88.9%	15min, 11.1%	35°C

Fig 7.30 shows the lifetime (time at high temperature) of the porous and dense APS-TBC systems with NiCoCrAlY (low Al) bondcoat under different cyclic conditions at 1050°C. The lifetime of the porous TBC systems was longer than that of the dense TBC system under each of the five cycling conditions, confirming the outcome of the lifetime tests in chapter 7.2.3.1. The data in Fig 7.30 also point out that the average lifetime of the porous TBC systems after 24h-cycle oxidation seemed to be longer, i.e. about 4000h, than that after 2h-cycling. For 24h-cycle oxidation, the life of the porous TBC's showed a larger scatter than the 2h-cycle exposure. For 2h-cycle, a shorter lifetime of the porous TBC's could be observed after 75min/45min cycling compared to 105min/45min cyclic oxidation.

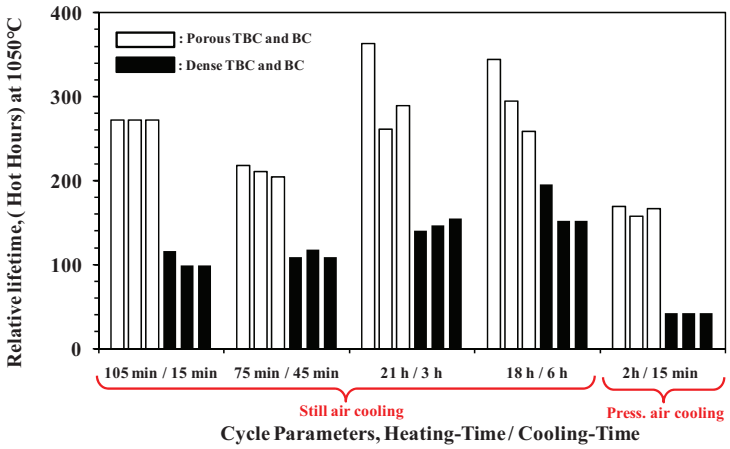

Fig. 7.30 Lifetime expressed in hot hours for porous and dense TBC systems after different hot/cold time cyclic oxidation at 1050°C in air

For the dense TBC system, a similar dependence on cycling parameters was observed as for porous TBC systems, i.e. for the 24h-cycling exposure the lifetime was longer than for the 2h-cycling. The TBC life was again shorter when the specimens were cooled in 2h/15min cycles at a fast rate to a lower final temperature. It should be noted that the reproducibility of the lifetime data for the dense TBC-system after 24h-cycling oxidation was better than that of the porous TBC systems. During 2h-cycling exposures with still air cooling the lifetimes of the dense TBC-systems were very similar contrary to the observation with the porous TBC systems.

Fig 7.31 shows the lifetimes of the TBC systems presented as the number of cycles for the above five cycling oxidation tests. The porous TBC specimens under 2h-cycle oxidation survived about 2000 cycles till the TBC failure, which is about a factor of 10 longer than that after 24h-cycling. Compared to the life data after 2h/15min cyclic oxidation, it can be concluded that in addition to the cycle frequency, the final cooling temperature as well as cooling rate can be important factors for the TBC lifetime. The above presented lifetime data indicate that the different relative cold time fractions of

12.5% and 37.5% had no significant effect on the lifetime of APS-TBC systems. More likely, the lifetimes were dependent on the final cooling temperature and/or cooling rate.

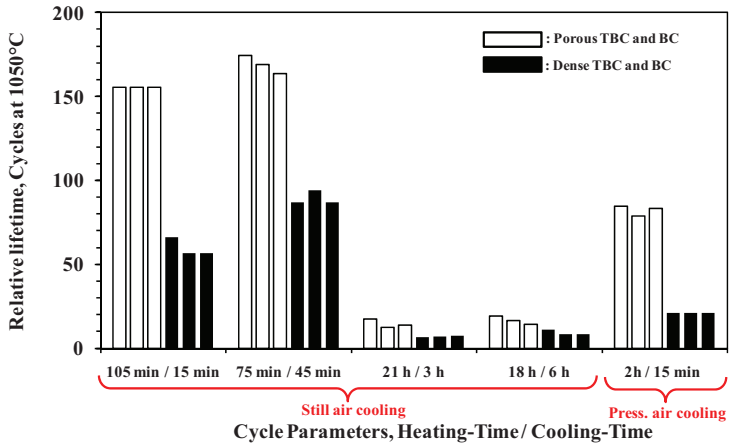

Fig. 7.31 Cycles to failure of porous and dense TBC systems after different hot/cold time cyclic oxidation at 1050°C in air

Metallographic cross-sections were prepared from the TBC specimens after different cyclic exposure conditions. Since for a given system the TGO morphologies and crack propagation patterns were similar under all the cycling conditions, here, only the cross-sections of the failed TBC systems after 21h/3h cyclic oxidation are shown in Fig 7.32. Internal oxidation was found for the porous TBC systems (Fig 7.32a) due to the porous microstructure of the bondcoat, as previously discussed in chapter 7.2.3. The high magnification SEM images in Fig 7.33a shows that the repeated cracking of the TGO is a typical characteristic of the porous TBC systems. The cracks form on the convex surfaces of the dense bondcoat, and then penetrate through the TBC, which is typical for the dense TBC systems as shown in Fig 7.32b and 7.33b.

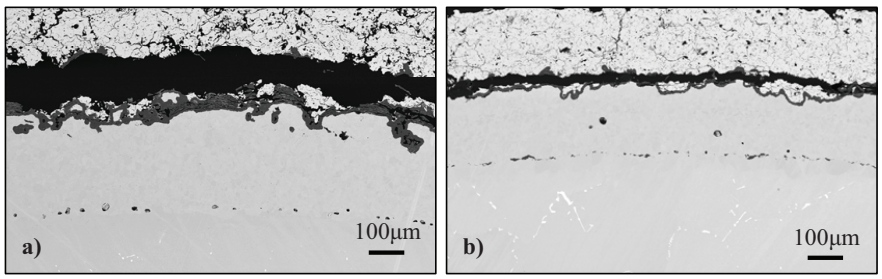

Fig. 7.32 SEM cross-sections of failed APS-TBC systems with NiCoCrAlY bond coats on IN738 after 21h/3h cyclic oxidation at 1050°C in lab. air, a) 4725 h, porous TBC system , b) 2016 h, dense TBC system

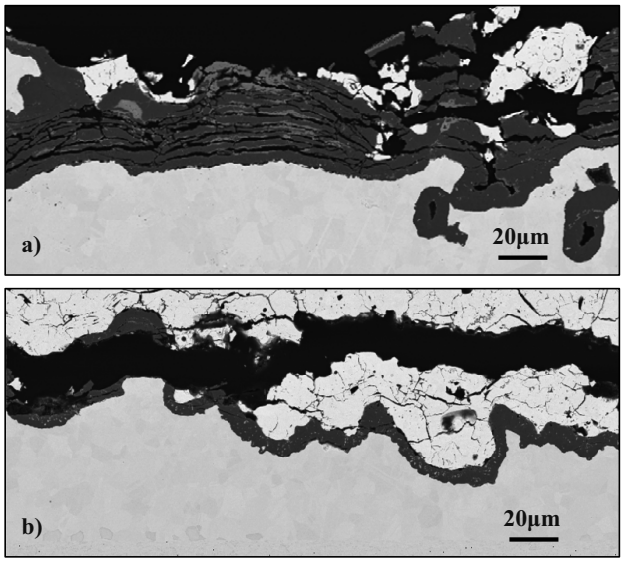

Fig. 7.33 Cross-sections of failed APS TBC systems after 21h/3h cyclic oxidation showing, a) repeated cracking of the TGO in porous TBC system, b) typical crack propagation for the dense TBC system

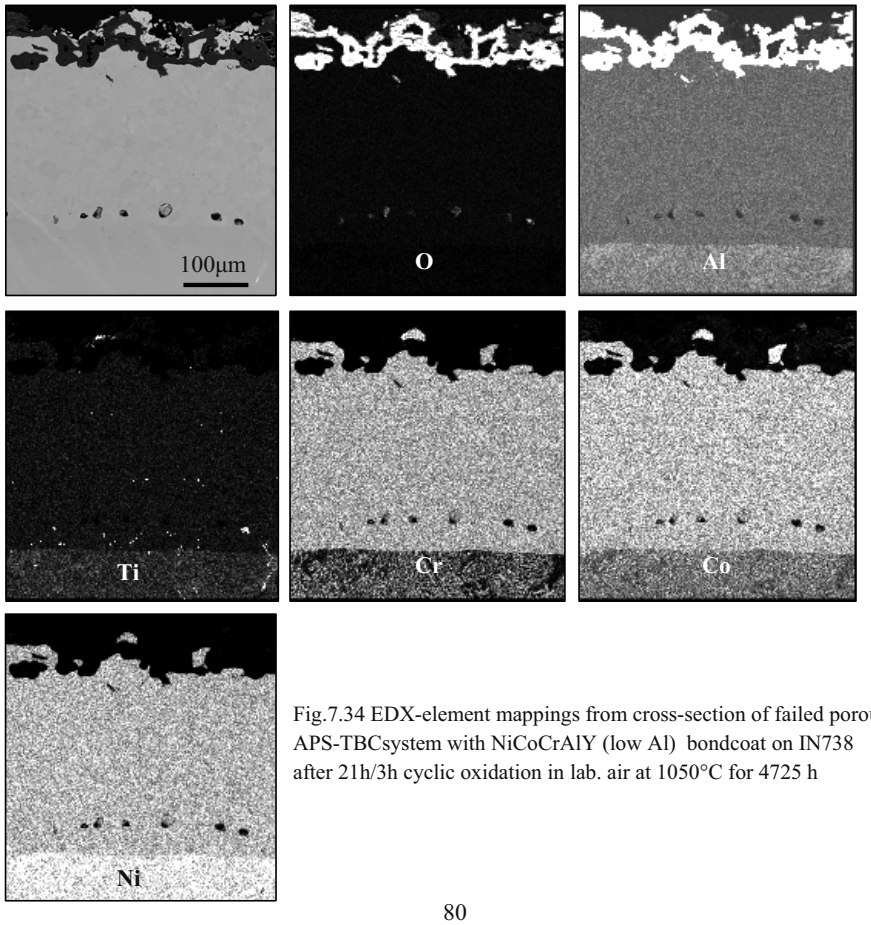

Fig.7.34 EDX-element mappings from cross-section of failed porous APS-TBCsystem with NiCoCrAlY (low Al) bondcoat on IN738 after 21h/3h cyclic oxidation in lab. air at 1050°C for 4725 h

For investigating the composition of the TGO and the bondcoat, EDX elemental mappings were obtained from the cross-sections of the APS-TBC systems. Fig 7.34 shows the elemental mapping for failed porous APS-TBC systems with NiCoCrAlY (low Al) bondcoat. The O and Al elemental mappings confirmed that the oxide was mainly alumina. The elemental mappings of the major bondcoat elements Ni, Cr, Co and Al clearly show that the bondcoat is single phase (γ-Ni). Metal particles containing Ni, Cr, Co and virtually no Al were observed in the outer part of the bondcoat. Non-protective oxide (spinel) formation due to Al depletion, however, was in general not found. Randomly, very small Ti-rich precipitates could be checked in the bondcoat, which are, however, believed not to have any significant effect on the TGO formation.

The elemental mappings for the dense APS-TBC system with NiCoCrAlY (low Al) bondcoat are shown in Fig 7.35. The O and Al mappings present a relatively uniform alumina based TGO. In the center of the bondcoat γ′ precipitates were found as indicated by their high Ti-content. The morphology of these particles indicates that γ′ formed from the β phase, possibly due to Ti diffusion from the superalloy into the bondcoat. Why the γ′-formation was not observed in the case of the

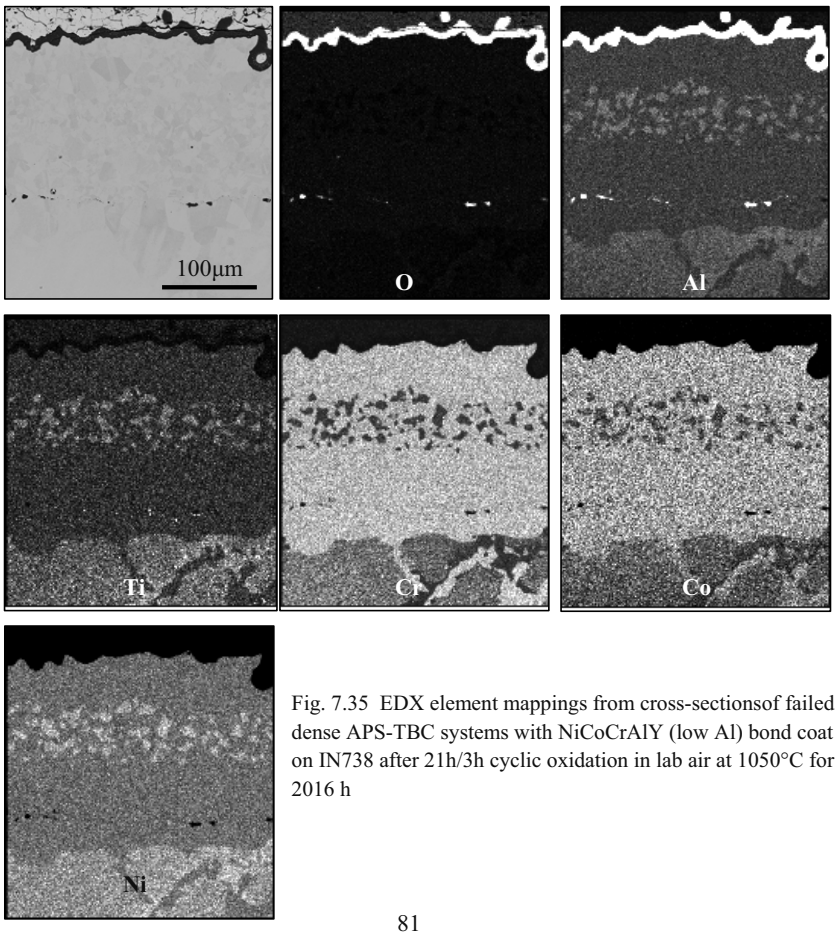

Fig. 7.35 EDX element mappings from cross-sectionsof failed dense APS-TBC systems with NiCoCrAlY (low Al) bond coat on IN738 after 21h/3h cyclic oxidation in lab air at 1050°C for 2016 h

porous TBC system, which has normally the same bondcoat and superally, is not fully understood. Perhaps it is related to the factor of two longer exposure time, whereby more Al would be consumed for the scale formation resulting in destabilization of the γ′ phase.

7.5.2 Effect of cooling rate to TBC-systems with NiCoCrAlY bondcoat

An important result in the previous chapter was that the TBC lifetime of the specimens in the 2h cyclic test was shorter in the case of pressurized air cooling than formed for the still air cooling. The reason for this effect can be either a faster cooling rate (Fig 7.29) or a lower cold dwell temperature (Table 7.3) in the former cycle. In order to clarify, which of the two testing parameters causes the difference in lifetime of TBC's, a set of cyclic oxidation experiments was performed with deliberately varied cooling rate but essentially the same cold dwell temperature, as discussed in this section.

Failure of TBC systems is normally associated with stresses in the TGO, which mainly develop during cooling from oxidation to room temperature. The reduction of TGO stress does not automatically mean an improvement of oxide adherence, however, the slow cooling rate could promote stress relaxation [145] due to alloy/ bondcoat creep and plastic deformation. On the other hand, a lower cold dwell temperature can promote strain energy relaxation through crack propagation [117]. In the present study, two different cooling rates were generated through adjustment of the air flow rate, whereas both cycling parameters sets had the same final cold dwell temperature. The cooling curves for both experiments are shown in Fig 7.36. The porous and dense TBC systems with NiCoCrAlY (low Al) bondcoat were investigated in these tests. For the dense TBC system the base material was IN738, whereas for the porous TBC-system it was CM247. It is important to note that other batches of samples were used in Chapter 7.2.3.1 for the effect of bondcoat main composition. Hence, the absolute lifetime values obtained in these two tests cannot be directly compared.

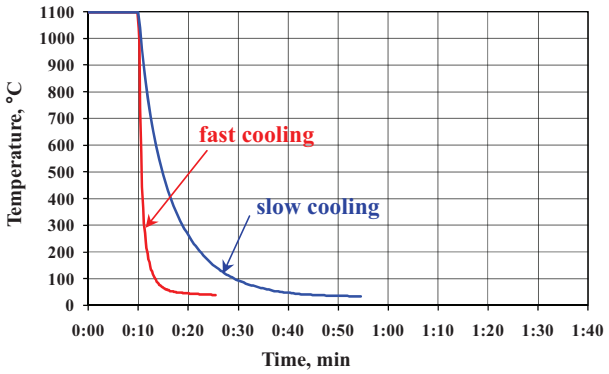

Fig. 7.36 Cooling curves for the 2h/15min and 2h/45min cycling test with the same cold dwell temperature of 35°C

Fig 7.37 shows the lifetimes of APS TBC systems after 2h/15min and 2h/45min cyclic oxidation at 1100°C in air. The average lifetime of dense TBC systems after 2h/15min cyclic oxidation at 1100°C was similar to that after 2h/45min cyclic exposure. However, the 2h/45min cycle with slow cooling rate resulted in a slightly larger scatter of lifetime for the dense TBC system. The porous TBC systems exhibited similar lifetimes after 2h/15min and 2h/45min cyclic oxidation. It can be seen that for a given TBC system the cooling rate did not have a substantial effect on the TBC lifetime.

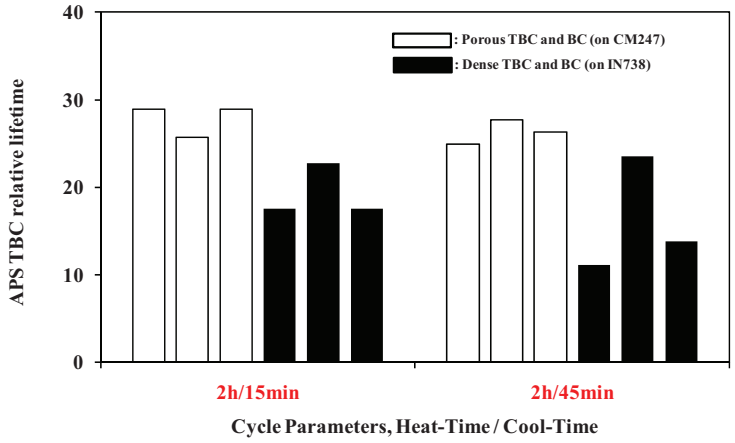

Fig. 7.37 Lifetime of the porous and dense APS-TBC systems with NiCoCrAlY(low Al) BCs after 2h/15min (fast cooling) and 2h/45min (slow cooling) cyclic oxidation at 1100°C in air

The cross-sections of the failed APS-TBC systems are shown in Fig 7.38. The different test parameters did substantially not affect the morphologies of the TGO for both TBC systems. The microstructure of the bondcoat induced different TGO morphologies between dense and porous TBC systems as already observed previously (Chapter 7.2.3). Oxidation of pore surfaces in the TBC system with porous bondcoat induced a rapid Al-depletion from the bondcoat, which resulted in a complete transformation of β-NiAl into γ-Ni phase.

According to the results presented in this chapter, the APS-TBC lifetimes were similar after different cooling rates with similar cold dwell temperature. Therefore, the exact value of low cold dwell temperature could play a role in determining APS-TBC lifetime. The reason for this effect is not understood at the moment. Acoustic emission data [146] indicated that cracking in an APS system greatly increased by changing the cold dwell temperature from 350°C to 60°C, resulting in significant shortening of the TBC lifetime.

It is remarkable that the relatively small difference between the two cold dwell temperatures, i.e. 65°C vs. 35°C, could have a significant effect on the TBC lifetime. Such an effect cannot be related to elastic thermal stress generated due to CTE mismatch between the metallic (bondcoat and superalloy)

and ceramic (TGO and TBC) constituents of the system. Further studies are required in order to explain the above effect of cold dwell temperature on the lifetime of TBC's.

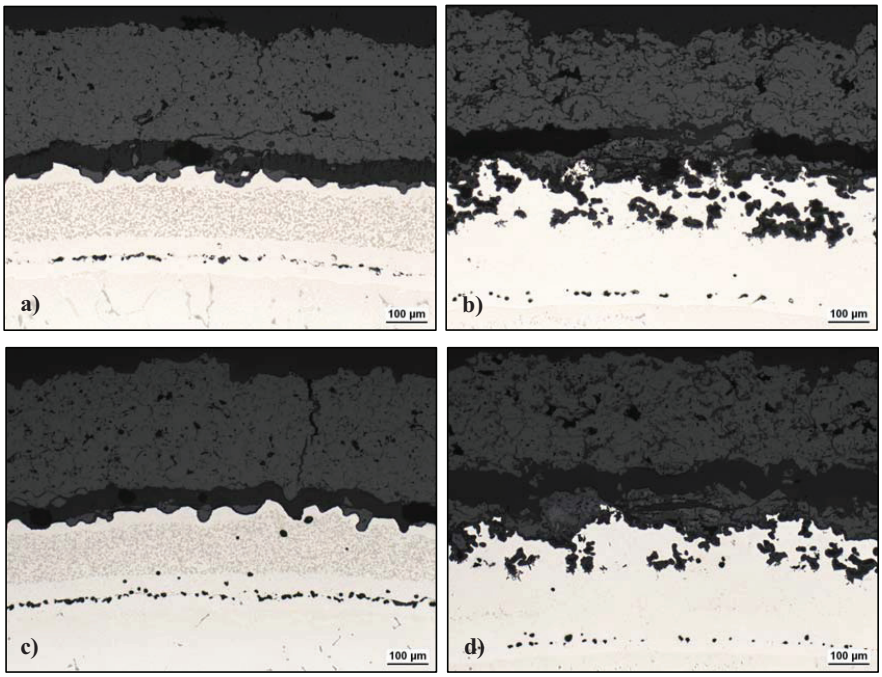

Fig. 7.38 Optical metallographic cross-sections for failed APS TBC's with NiCoCrAlY BC after cyclic oxidation in air at 1100°C, a) and b): 2h/15min; c) and d): 2h/45min; a) and c): systems with dense BC and TBC; b) and d): systems with porous BC and TBC

7.6 Discussion of findings related to APS-TBC systems with MCrAlY bondcoats

The studies on APS-TBC systems with MCrAlY bondcoats revealed that their lifetime is affected by the main bondcoat composition, minor addition of Zr in the bondcoat, TBC and bondcoat microstructure as well as testing conditions. With respect to the main bondcoat composition, it was observed that for a dense bondcoat the TBC lifetime was longer when using a Co-base MCrAlY compared to a Ni-base MCrAlY coating. This could be explained by a higher microstructure stability (less phase transformations) as a function of temperature in Co-base bondcoats, similar to the observations made earlier with EB-PVD TBC systems.

In the case of TBC-systems with porous bondcoat the positive effect of Co was lost due to enhanced bondcoat-oxidation. The latter occurred because of locally prevailing higher surface to volume ratio of the rough and porous bondcoat thus promoting formation of non-protective spinel oxides, rather than alumina observed in the case of a dense bondcoat. An additional reason for formation of an alumina

scale on the dense Co-base bondcoat could be β-NiAl enrichment at the bondcoat surface as a result of Cr evaporation during vacuum heat-treatment of this batch of specimens.

The lifetime of APS-TBC systems was observed to be affected by the TBC porosity and the outer roughness profile of the bondcoat. These microstructure parameters appeared to determine the crack propagation rates in the TBC. It could be demonstrated that for porous, strain-tolerant TBC's the lifetime can be extended by a factor of 2 to 3 by a favorable ('microrough') bondcoat surface topography with respect to a simple "sinusoidal" type one.

Minor additions of Zr to an MCrAlY bondcoat, which were shown to be beneficial for the lifetime of EB-PVD TBC systems, appear to have no positive, but rather a negative effect on the lifetime of APS-TBC systems. This was due to "overdoping" of the TGO's with Zr, whereby ZrO_2 precipitates formed, which served as short circuit paths for inward oxygen diffusion, resulting in rapid oxidation of bondcoat concave surfaces. In the present work it was shown that the negative Zr effect could be suppressed by higher O-content in the bondcoat. Thereby the lifetime became similar to the system with Zr free NiCoCrAlY bondcoat. Furthermore, it was shown that for NiCoCrAlY bondcoat the exact O-content does not have a substantial effect on the TBC lifetime, contrary to what was observed in EB-PVD TBC systems. This is because in APS TBC systems the failure is determined mainly by crack propagation through the TBC and not primarily by the oxide scale adherence as in the case of EB-PVD TBC systems.

Presence of water vapor in the atmosphere appeared to have no significant effect on the APS TBC lifetime contrary to the observations made with EB-PVD TBC. This finding indicates that the crack penetration rate within YSZ is insensitive to the presence of water vapor and perhaps is related to YSZ phase stability in high temperature water vapor containing environment.

Finally, studies related to variation of temperature cycling parameters have shown that the lifetime of APS-TBC systems can be affected by the cyclic frequency and cold dwell temperature. More frequent cycling and lower cold dwell temperature shorten the lifetime, whereas cooling rate and duration of the cold dwell appeared to have no significant effect.

It should be noted that the absolute values of the lifetimes of the studied APS-TBC's as well as the EB-PVD TBC systems with MCrAlY bondcoats determined in a cyclic oxidation test at 1000°C or extrapolated to this temperature from higher temperatures (1100°C and 1150°C) appear to be rather short as compared to the lifetime requirement of 25000 h operating hours (Fig 8.16). Although the TBC lifetimes determined in a cyclic oxidation test on laboratory samples cannot be compared directly with the TBC lifetimes of the turbine hardware under real operating conditions, the results of the

above tests indicate that the lifetimes of TBC systems with MCrAlY bondcoats may not be sufficiently long for the above lifetime requirement at 1000°C. Therefore, alternative TBC systems with other types of bondcoats should be considered. NiPtAl bondcoats are commonly used in EB-PVD TBC systems for protection of aircraft engine components made of single crystal Ni-base superalloys. Therefore in the next chapter EB-PVD TBC systems with NiPtAl bondcoat will be studied and the lifetimes and oxidation behavior will be compared with those of the TBC systems with MCrAlY bondcoat.

8 Factors affecting lifetime of EB-PVD TBC-systems with NiPtAl bondcoats

8.1 General Remarks

Pt-modified nickel aluminide as oxidation resistant coatings or as a bondcoat for thermal barrier coating (TBC) have been commonly used for protection of jet-engine components. The application of NiPtAl coatings in industrial gas turbines is, however, less common than use of MCrAlY bondcoats. The Pt-modified aluminide bondcoat forms an alumina scale, which is similar to involved MCrAlY-coatings, in TBC failure although the failure mechanisms can be different. For MCrAlY-type bondcoats numerous compositions are available commercially. Furthermore it is easy to produce a coating with a modified composition. In contrast, for NiPtAl-coatings and bondcoats the coating chemistry depends largely on the used aluminizing process and to some extent on the composition of the substrate alloy, from which elements such as Cr, W etc are incorporated into the aluminized layer. With respect to the aluminizing process, the NiPtAl coatings can be divided into two groups: high and low Al-activity (a_{Al}), respectively. There are plenty of data in the literature on the oxidation behavior and lifetime of TBC systems with NiPtAl bondcoats. However, a direct comparison of high and low-a_{Al} bondcoats with respect to TBC lifetime has not yet been shown. Therefore, in the present studies the lifetime of EB-PVD TBC systems with high and low-a_{Al} NiPtAl bondcoats will be measured in a cyclic oxidation test in the air with and without water vapour and compared to the systems with MCrAlY bondcoats. The TBC failure mechanism will be also investigated in this work.

8.2 Effect of NiPtAl bondcoats manufacturing on lifetime of EB-PVD TBC

The lifetimes of EB-PVD-TBC with low-a_{Al} or high-a_{Al} NiPtAl bond coatings after 2h/15min cyclic

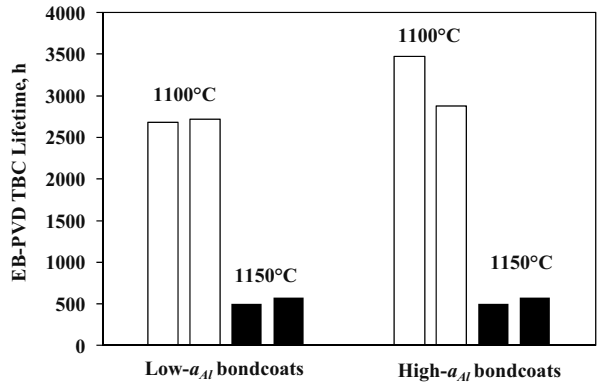

Fig. 8.1 Lifetime of EB-PVD-TBC with NiPtAl coatings on CMSX-4 alloy after 2h/15min cyclic oxidation at 1100°C in air

oxidation at 1100°C and 1150°C in air are summarized in Fig 8.1. The EB-PVD TBC lifetimes at 1150°C were approximately 500 h, which was only 15 to 20% from the values measured at 1100°C. This could be related to the fast TGO growth rate at the higher temperature; a detailed discussion will be given in the following chapter. No clear difference of the TBC lifetime at 1100°C and 1150°C was found between the low-a_{Al} and high-a_{Al} coatings. The lifetime for the TBC specimens with these bond coatings exhibited a quite good reproducibility.

8.2.1 Characterization of as-received TBC systems with NiPtAl coatings

To understand the TBC failure mechanism, the characterizations of as-received EB-PVD TBC with NiPtAl coatings were performed to have a reference for analyses of the oxidized materials. Fig 8.2 shows SEM cross-sections of EB-PVD-TBCs with low-a_{Al} and high-a_{Al} bondcoats deposited on the single crystal superalloy CMSX-4. The low-a_{Al} bondcoat was found to be slightly thinner and the interdiffusion zone slightly thicker compared to the high-a_{Al}. The high-a_{Al} coating consists of two phases, i.e. β-NiAl and $PtAl_2$ whereas the low-a_{Al} coating was single phase β-NiAl, which was confirmed by XRD analysis performed on specimen parts, which had not been coated with TBC, in Fig 8.3.

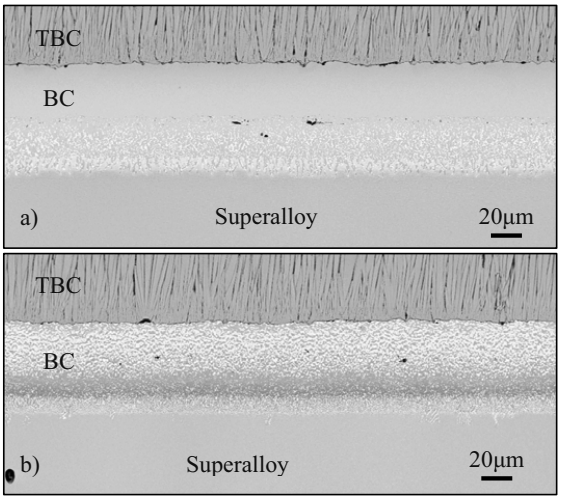

Fig. 8.2 SEM cross-sections of as-received EB-PVD-TBC systems on CMSX-4 with NiPtAl bondcoats, a) low-a_{Al}, b) high-a_{Al} coatings

The XRD patterns are in good agreement with the SEM-images in Fig 8.4 revealing that the low-a_{Al} bondcoat only consisted of Pt-containing β-NiAl phase, however, β-NiAl and $PtAl_2$ appeared for the high-a_{Al} bondcoat. According to the literature [147] the low-a_{Al} coating grows by Ni outward diffusion from the superalloy. In contrast, the high-a_{Al} NiPtAl coating grows by Al inward diffusion into the

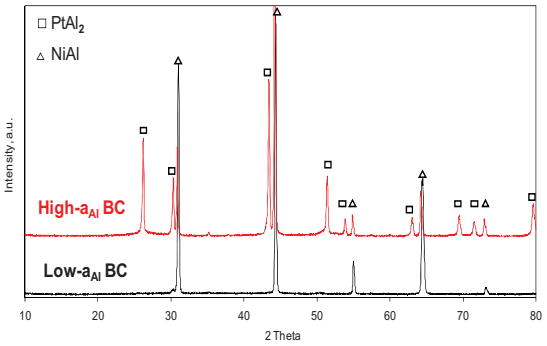

Fig. 8.3 XRD analysis for (TBC free) NiPtAl coatings at room temperature

superalloy. Fig 8.4 also points out that the interdiffusion zones, which are located between bondcoat and superalloy, consisted of β-NiAl phase together with a number of Cr/Ti/Ta/W-rich precipitates. In the cross-section of the low-a_{Al} coating, occasionally some small pores could be observed between the bondcoat and the interdiffusion zone. For the high-a_{Al} coating, no such defects could be found in the bondcoat near the superalloy.

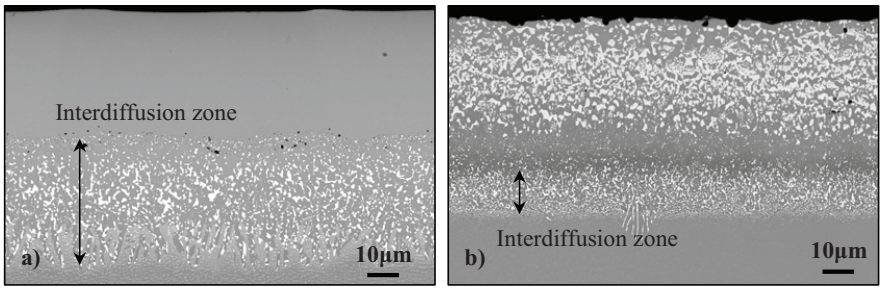

Fig. 8.4 SEM images for as-received NiPtAl coating without TBC, a) low-a_{Al}, b) high-a_{Al} coatings

The chemical compositions of the as-received NiPtAl coatings were analysed by EDX, as shown in Fig 8.5. In the as-received condition, the Ni-content was about 30 at% for the high-a_{Al} coating and nearly 50 at% for the low-a_{Al} coating. In contrast, the Al content was 40 at% in the low-a_{Al} and over 52 at% for the high-a_{Al} coating. The Pt-content in the high-a_{Al} coating was about 10 at% and approximately 5 at% in the low-a_{Al} coating. Other elements, e.g. Co and Cr resulting from outward diffusion from the CMSX-4 superalloy during the coating processes were also observed. Using these measured element concentrations for the low-a_{Al} and high-a_{Al} coating, both coating composition are plotted in the ternary Ni-Pt-Al phase diagram at 1100°C/1150°C in Fig 8.6.

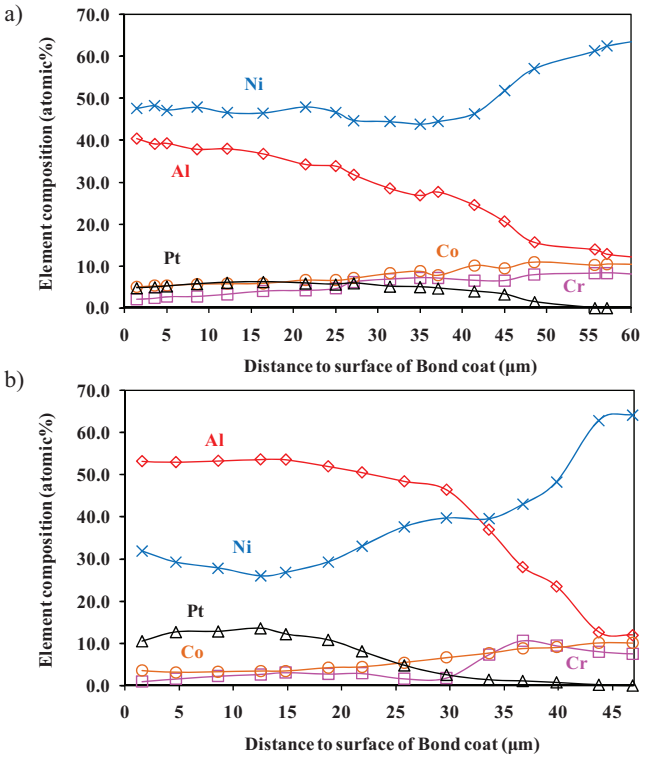

Fig. 8.5 EDX elemental profiles for as-received NiPtAl coatings measured in metallographic cross-sections, a) low-a_{Al}, b) high-a_{Al} coatings

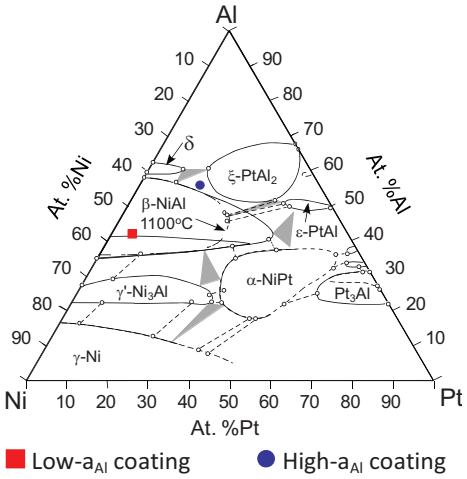

Fig. 8.6 Indication of measured composition for both NiPtAl coatings in tenary Ni-Al-Pt Phase diagram at 1100°C [148-149]

8.2.2 Characterization of oxidized TBC systems with NiPtAl bondcoats

Fig 8.7 shows the composition profiles of the bondcoat and interdiffusion zone for low-a_{Al} coating after 20h cyclic oxidation at 900°C and 1100°C. Comparison of the concentration profiles with in the as-received condition (Fig 8.5) revealed the Ni and Al concentration in the low-a_{Al} coating almost did not changed after 20h oxidation at 900°C.

The Al and Ni concentration profiles for the low-a_{Al} coating after 20 h oxidation at 1100°C shown in Fig 8.7b, were clearly different from those in the as-received coating and after exposure for 20 h at 900°C. The Al concentration in the bondcoat decreased from 40 at% in the as-received to about 30 at% after 1100°C exposure for 20h. The decreased Al content is caused by the fast interdiffusion with the superalloy substrate at high temperature and by alumina scale formation. It should be noted that the Pt content in the outer part of bondcoat does not seem to change significantly, however, the Pt profile after 20 h oxidation indicated that inward diffusion of Pt into the superalloy substrate was stronger at 1100°C than at 900°C. The concentration profiles of other elements, e.g. Co and Cr, also changed only slightly with increasing oxidation temperature.

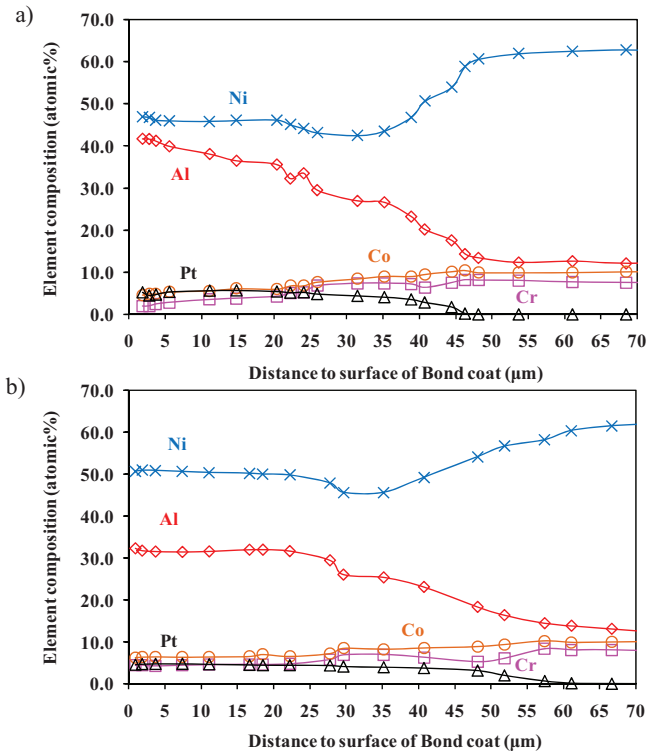

Fig 8.7 EDX elemental profiles for low-a_{Al} NiPtAl coating after 20 h cyclic oxidation in air , a) at 900°C, b) at 1100°C

Fig 8.8 shows the elemental concentration profiles for the high-a_{Al} coating after 20 h exposure at 900°C and 1100°C. The high-a_{Al} coating exhibited drastic compositional changes after 20 h exposure at 1100°C compared to those at 900°C. The average concentrations of elements e.g. Ni, Al and Pt in the coatings hardly changed during 20 h oxidation at 900°C. The Ni and Al concentration profiles in the outer part of high-a_{Al} bondcoat presented similar elemental diffusion trends compared to those of the low-a_{Al} coating.

The Al content dropped from over 52 at% to about 35 at% and the Pt content from 12 to 6 at% when the high-a_{Al} coating was exposed for 20h at 1100°C. The Ni content increased from 25 at% to 50 at%, and Cr from 1 to 5 at%, respectively. These Ni, Al and Pt concentration profiles after 20h oxidation indicated that significant phase transformation and/or interdiffusion processes occurred for this coating at 1100°C. The Ni-Pt-Al phase diagram (Fig 8.6) indicated that the as manufactured composition of the high-a_{Al} coating was located in the two-phase area, and near to the boundary of the single-phase β-NiAl field. A small decrease in the Al-content would result in $PtAl_2$ dissolution.

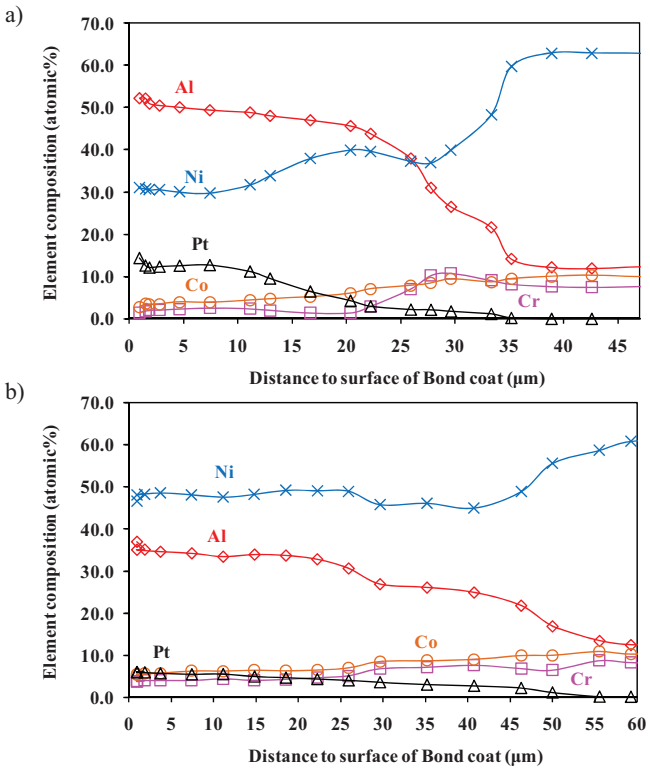

Fig 8.8 EDX elemental profiles for high-a_{Al} NiPtAl coating after 20 h cyclic oxidation in air , a) at 900°C, b) at 1100°C

To understand the changes in the coating compositions, Fig 8.9 shows the cross-sections of the specimens after 20 h cyclic oxidation at 900°C and 1100°C. The interdiffusion zone (IZ) became larger due to the elements interdiffusion compared to the as-received condition. The $PtAl_2$ particles in the high-a_{Al} coating were stable after 20 h exposure at 900°C, however, these Pt-aluminide precipitates decomposed after 20 h exposure at 1100°C. Fig 8.9c and d point out that the coating microstructure and the depth of the interdiffusion zone for the high-a_{Al} coating are comparable with those for the low-a_{Al} coating after 20 h oxidation at 1100°C.

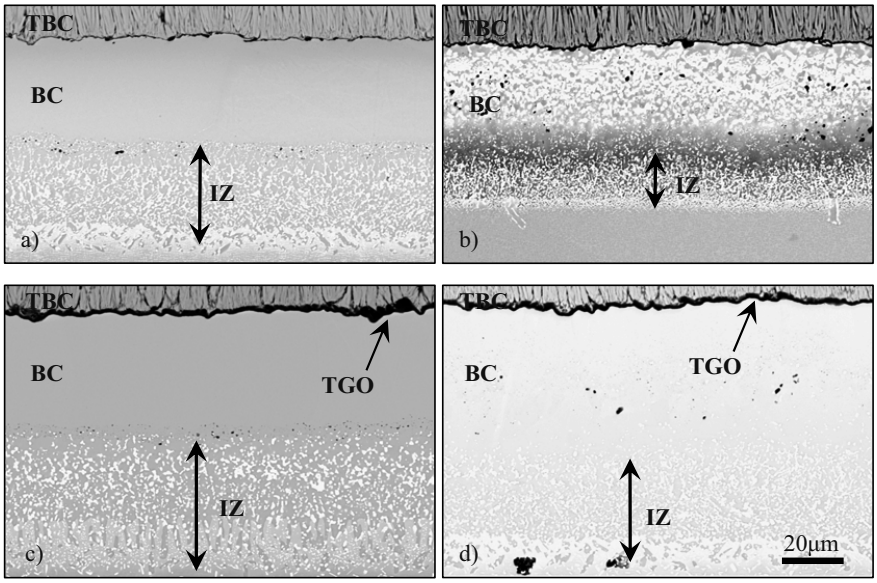

Fig. 8.9 SEM images of cross-sections for EB-PVD-TBC with NiPtAl coating after 2h/15min cyclic oxidation for 20 h, a): low-a_{Al}, 900°C, b): high-a_{Al}, 900°C, c): low-a_{Al}, 1100°C, and d): high-a_{Al}, 1100°C

Dissolution of the $PtAl_2$ phase in the high-a_{Al} coating during exposure at 1100°C observed in Fig 8.9 is in agreement with the EDX data in Fig 8.8. An explanation of this effect can be given using the ternary Ni-Pt-Al phase diagram in Fig 8.6. The single β-NiAl phase field in Fig 8.6 can be easily expanded due to presence of other elements such as e.g. Co, Cr, and W incorporated from the superalloy. Thereby the two-phase microstructure of the high-a_{Al} coating which is stable at 900°C, becomes unstable and $PtAl_2$ dissolves simply upon heating to 1100°C.

Fig 8.10 a and b show SEM-images of the studied TBC systems with the low and high-a_{Al} coatings after 300 h oxidation at 1100°C. The TGO morphology and thickness are very similar for both bondcoat systems. Fig 8.11shows that in a number of locations cracks were performed at the TBC/TGO interface as well as at the TGO/ bondcoat interface.

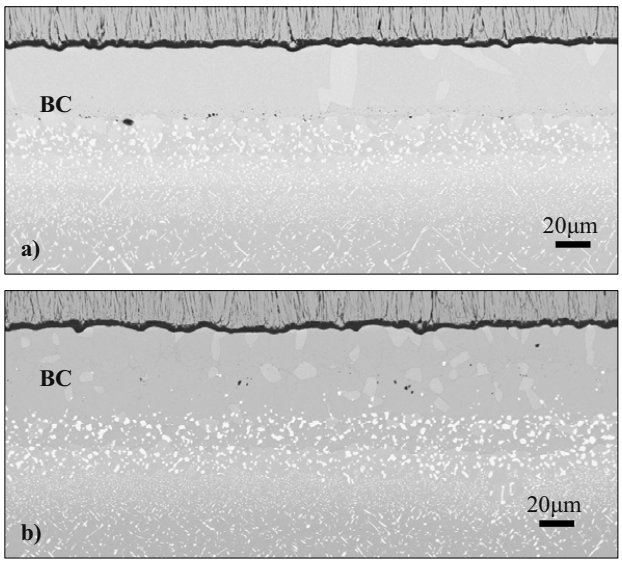

Fig.8.10 SEM images of cross-sections forEB-PVD TBC with NiPtAl coatings after oxidation for 300h at 1100°C, a): low-a_{Al}; b): high-a_{Al} bondcoat, respectively

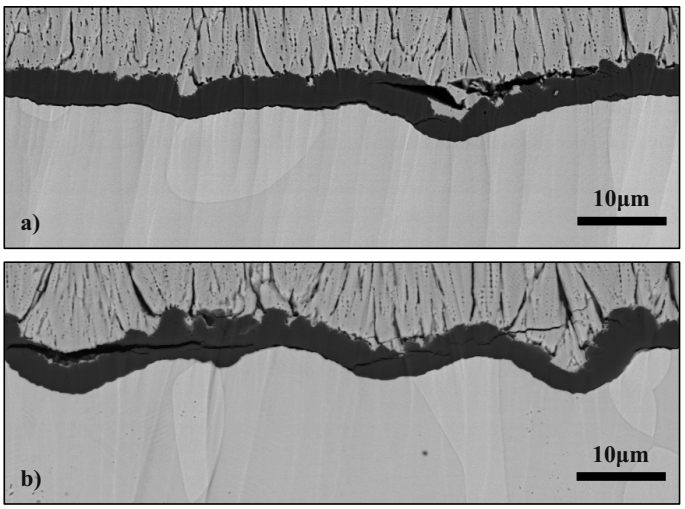

Fig.8.11 SEM images of cross-sections for EB-PVD-TBC systems with NiPtAl bondcoats after 2h/15min cyclic oxidation for 300 h at 1100°C in air, a) low-a_{Al}, b) high-a_{Al} NiPtAl coatings

Metallographic cross-sections in Fig 8.12 show that after extended exposure time at 1100°C, the microstructure of the coatings changed from β-NiAl to β-NiAl + γ´-Ni_3Al. The formation of the γ´-phase occurred mainly at the coating grain boundaries. A more uniform distribution of γ´ in the high-a_{Al} coating is probably related to a smaller grain size of this coating. (Such microstructure probably originated from transformation of β-NiAl + $PtAl_2$ with a very fine grain size into single phase β-NiAl).

The transformation of β-NiAl to γ′-Ni_3Al is induced by Al-depletion from the bondcoat as a result of TGO-formation and interdiffusion with the base material.

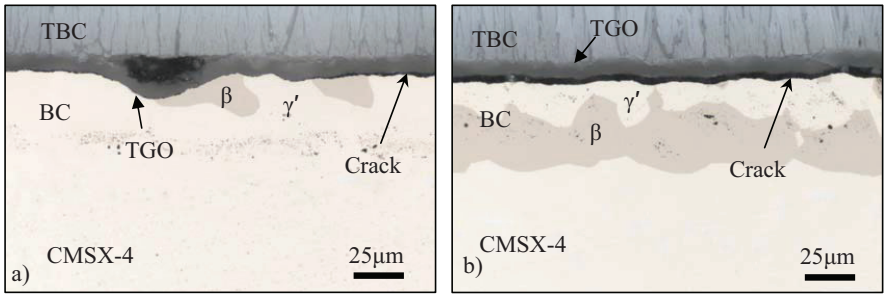

Fig.8.12 Metallographic cross-sections of TBC systems with NiPtAl coatings after cyclic oxidation to failure at 1100°C in air, a): low-a_{Al}, 2718 h, b):high-a_{Al}, 2880 h

Fig 8.13 shows macro-pictures of the EB-PVD-TBC specimens with NiPtAl-bondcoats exhibiting failure after cyclic oxidation at 1100°C. The figures indicate macroscopic TBC buckling originating from the middle of the samples. The images in Fig 8.14 indicate that failure occurred at the TGO/ bondcoat interface, which was rather flat. Thereby the failure mode was similar to that observed for EB-PVD TBC systems with MCrAlY bondcoats (chapter 6.1). This observation is different to that made by other authors [94], who found for similar systems bondcoat rumpling and delamination at the TGO/bondcoat interface to be the main degradation failure mode. The TGO thickness upon occurrence of failure was very similar (7-8 µm) in both studied systems with NiPtAl bondcoats.

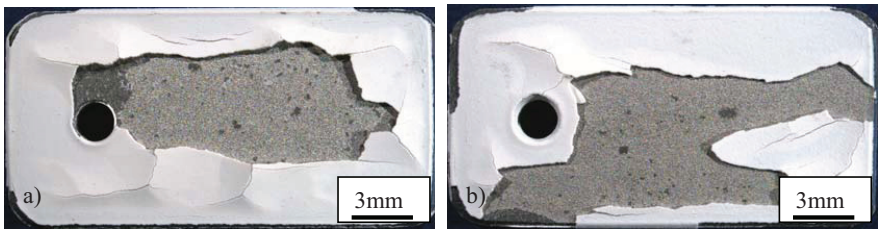

Fig.8.13 Macro-photographs for TBC-coated sides after cyclic oxidation to failure at 1100°C in air, a): low-a_{Al}, 2718 h, b):high-a_{Al}, 2880 h

The thickness of the thermally grown oxide was measured in SEM cross-sections after different exposure times. Fig 8.15 summarizes the TGO thickness measurements for the EB-PVD-TBC systems with both types of NiPtAl bondcoats as a function of time at 900°C, 1000°C, 1100°C, and 1150°C. For similar exposure times the TGO thickness increased with increasing exposure temperature, as expected from the common Arrhenius type temperature dependence of the oxidation rate. At 1100°C and 1150°C, the TGO thickness was approximately 7~8µm for failed TBC systems with both NiPtAl coatings. The TGO thickness measurement of the samples exposed at 1100°C allowed a meaningful fit with a power law time dependence of the TGO thickness (Fig 8.15). Within the measurement error,

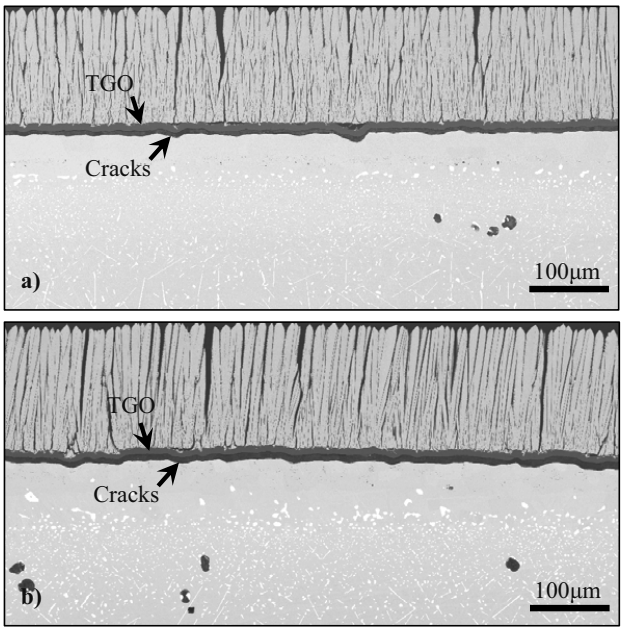

Fig.8.14 SEM images of cross-sections for TBC-coated sides after 2h/15min cyclic oxidation to failure at 1100°C, a): low-a_{Al}, 2682 h, b): high-a_{Al}, 3474 h

the TGO growth kinetics could be described using a sub-parablic, near cubic law. Such growth kinetics were observed for compact alumina scales formed on RE-doped FeCrAlY and MCrAlY-alloys [29]. It should be noted that the TGO thickness between the low-a_{Al} and high-a_{Al} coatings were very similar after the same oxidation time at certain temperature.

Based on the presented results it can be stated that the aluminizing process used for the NiPtAl-bondcoat manufacturing (high or low-a_{Al}) has no major effect on the TBC lifetime at 1100°C and 1150°C. The failure is apparently determined by a critical TGO thickness, which is very similar in case of both bond coatings and at both studied temperatures (Fig 8.15).

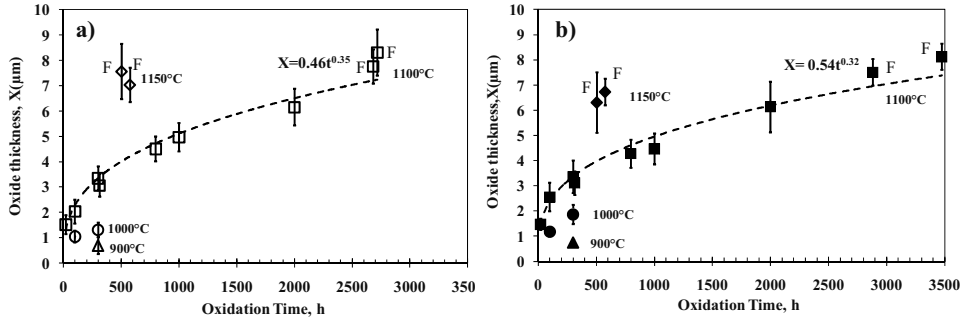

Fig. 8.15 TGO thickness (X) as a function of time (t) during cyclic oxidation of TBC coating specimens at different temperature in air, a) low-a_{Al} coating, and b) high-a_{Al} coating. 'F' indicates macroscopic TBC failure

8.2.3 Comparison of oxidation behavior and failure modes of EB-PVD TBC systems with NiPtAl and MCrAlY bondcoats

The lifetime of EB-PVD-TBC systems with NiPtAl coatings during cyclic oxidation at 1100°C reached approximately 2000 h after, which is significantly longer than that obtained for conventional MCrAlY coatings, as shown in Fig 8.16. The lifetime of EB-PVD TBC system with MCrAlY bondcoat can be extended by optimization of the reactive element (Y and Zr) contents in the coatings or by using a platinized NiCoCrAlY bondcoat [86], or by using a CoNiCrAlY bondcoat (due to a lower CTE than NiCoCrAlY bondcoat), as illustrated in chapters 6 and 7. Assuming the same lifetime trend as observed at 1150°C and 1100°C prevails also at low temperatures, Fig 8.16 shows that the EB-PVD TBC systems with NiPtAl bondcoats offer a large potential to fulfill the TBC lifetime requirement of 25000h at temperatures as high as 1000°C.

It should be noted that the lifetimes of the various systems presented in Fig 8.16 can not be unequivocally compared due to differences in base materials, sample geometries and processing steps. For the specimens with the NiPtAl bondcoats, the substrate alloy is a single crystal Ni-base superally CMSX-4, compared to the conventionally cast Ni-base alloy IN738 used for MCrAlY bondcoats. Other differences include sample processing, such as coating thickness and sample geometry. For the NiPtAl coating on CMSX-4, flat specimens of about 2mm thickness were used, contrary to cylinder type specimens with 10mm diameter for most of the MCrAlY bondcoat. However, the previous discussion illustrated that in all cases the TBC failure was linked to the TGO formation at the

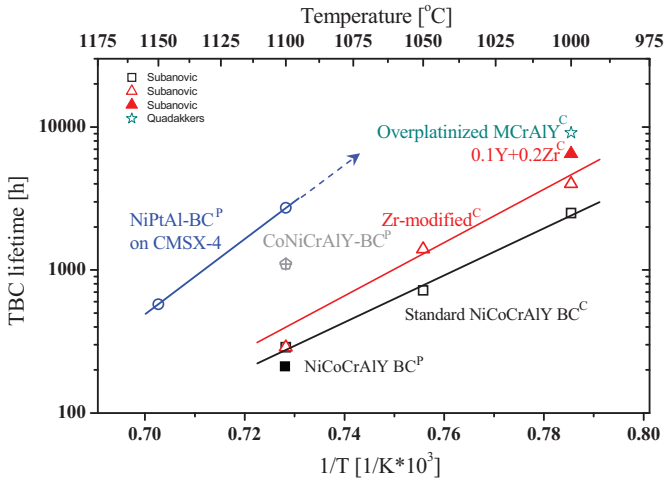

Fig. 8.16 Average lifetime of EB-PVD TBC with different bondcoats as a function of temperature after 2h/15min cyclic oxidation in air. Part of data was taken from Subanovic [67] and Quadakkers et al. [86]. The base material for systems with MCrAlY-bondcoats was IN738 whereas for those with NiPtAl-bondcoats CMSX-4 was used. 'P'- indicates plate and 'C'- cylinder specimen geometry, respectively

TBC/bondcoat interface. Therefore, analysis of differences in the TGO growth rate and adhesion among these coatings can help to understand intrinsic mechanisms, which determine the lifetime of TBC's with NiPtAl bondcoats as compared to those with conventional MCrAlY bondcoats.

In Fig 8.17, the time dependence of TGO thickness and the critical oxide thickness in EB-PVD TBC systems with NiPtAl and MCrAlY coatings are compared. In terms of bondcoat oxidation, there were two clear differences between the two coating systems, which may affect the TBC lifetime. First, the critical TGO thickness for the NiPtAl coatings was approximately 7-8 µm, which was slightly higher than the 5-6 µm formed for a typical MCrAlY bondcoat (see chapter 6.3). Since the alumina scale growth rate obeys a near-cubic time dependence, this difference, which is not very large in absolute values, can have a substantial effect on the TBC-lifetime. For example, increasing the critical alumina scale thickness from 6 to 8 µm should for a given scale growth rate result in a factor of 2.4 increase in lifetime. Second, the TGO growth rate on the NiPtAl bondcoats appears to be slower than that on the MCrAlY coatings when comparing under the same exposure conditions. The combination of a slower TGO growth rate and larger critical TGO thickness for the NiPtAl bondcoats could make a substantial contribution to the longer lifetime of the TBC compared with that found in case of MCrAlY bondcoats.

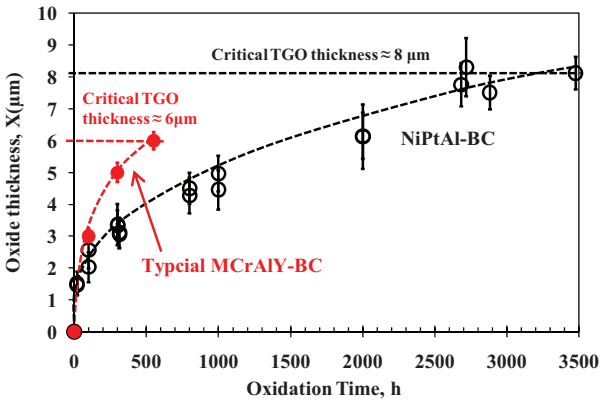

Fig .8.17 Alumina oxide thickness as function of time and critical TGO thickness for failure of EB-PVD-TBC systems with NiPtAl and MCrAlY bondcoats during cyclic oxidation at 1100°C in air

The critical TGO thickness for the onset of spallation of the NiPtAl coatings is higher than ones of typical MCrAlY coatings. One of the possible reasons for this effect can be an improvement of oxide scale adhesion by Pt as claimed by many other authors [42]. The TGO growth rate on the NiPtAl coatings is significantly slower than that on the typical NiCoCrAlY (low Al) coatings. One of the reasons for this effect could be the oxide microstructure. It was shown for many alumina forming alloys (e.g. FeCrAl and MCrAlY) that the scale growth mainly occurs via oxide grain boundary transport [132, 150], and the same is likely also to the case for NiPtAl coatings [151]. Therefore, if the

alumina scale microstructure on NiPtAl bondcoats is much more coarse grained compared to that on MCrAlY bondcoats, it will result in a slower scale growth. The effect of the oxide grain size on the oxidation kinetics was demonstrated recentely for FeCrAl alloys [152]. The TGO on the NiPtAl coatings was found to consist of two layers: an outer equiaxed and inner columnar alumina layer (Fig 8.18a). The equiaxed small grains in the outer part of the TGO of the NiPtAl coating (Fig 8.18b) may originate from the initial stages of oxidation or they are the result of an outward scale growth process. The Pt particles and other defects, e.g. pores, were found within the equiaxed alumina layer. In fact, the grain size of the TGO on the typical MCrAlY coatings was similar or even slightly larger than that of the oxide on the NiPtAl coatings, even in the columnar alumina zone (Fig 8.18c). Therefore the alumina scale grain size cannot fully explain the slower oxide growth rate on NiPtAl compared to that of MCrAlY bondcoats.

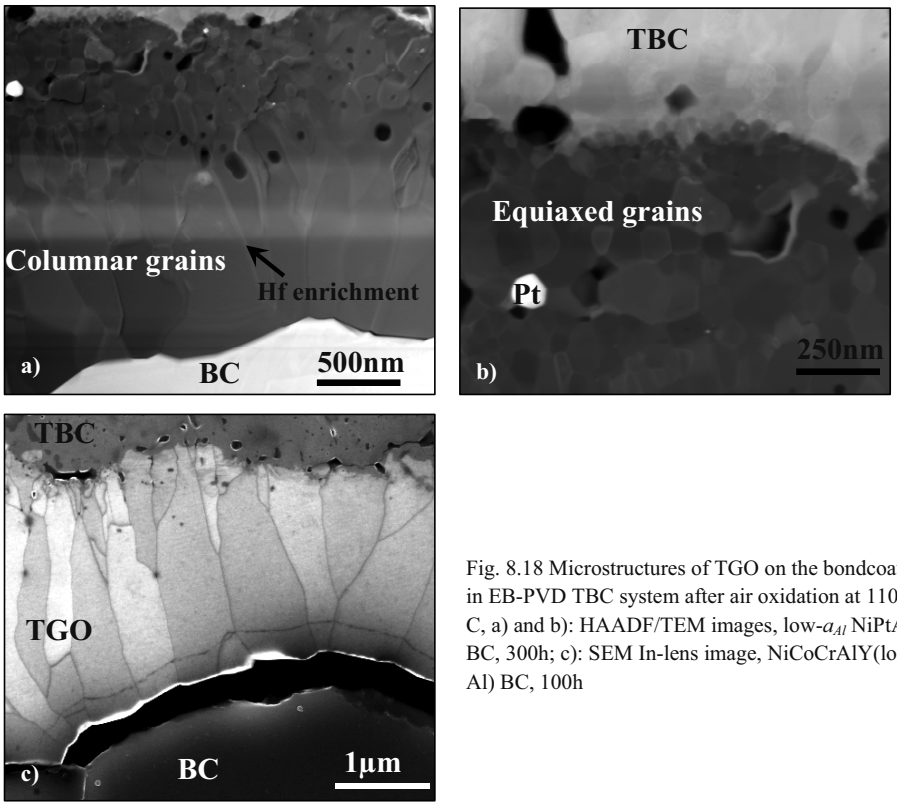

Fig. 8.18 Microstructures of TGO on the bondcoats in EB-PVD TBC system after air oxidation at 1100° C, a) and b): HAADF/TEM images, low-a_{Al} NiPtAl BC, 300h; c): SEM In-lens image, NiCoCrAlY(low Al) BC, 100h

Another possible reason for the slower TGO growth on NiPtAl bondcoat can be Hf-segregation which was observed at the alumina grain boundaries within the columnar oxide area in Fig 8.18a. On the other sample side, which was not coated with the TBC, HfO_2 formation after longer exposure times was observed even on top of the alumina scale, as shown in Fig 8.19. The BSE image in Fig 8.19b shows the distribution of these HfO_2 particles. The source of Hf for the formation of Hf-segregation

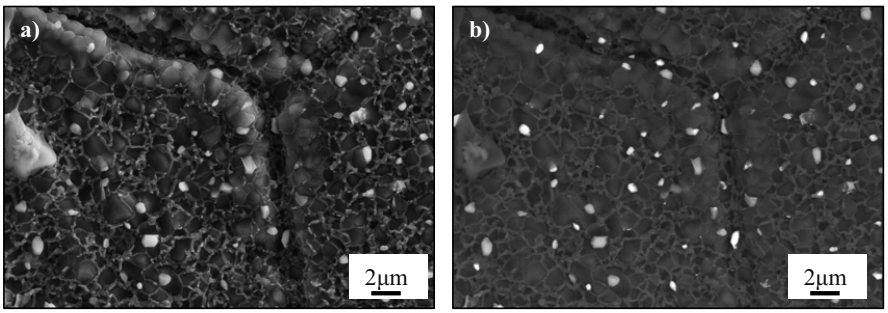

Fig. 8.19 SEM images for the low-a_{Al} coatings without TBC topcoat after 1000 h isothermal oxidation at 1100°C in air, a): SE signal; and b): BSE image

and formation of the HfO_2 particles is Hf diffusing from the CMSX-4 base alloy. This is in agreement with observation from other authors [153]. Hf segregation to the TGO grain boundaries claimed to significantly reduces the scale growth rate, as was observed for FeCrAlY alloys [154] and MCrAlY-alloys [76] as well as for NiPtAl-alloys. Comparison of the studied EB-PVD TBC systems with MCrAlY and NiPtAl bondcoats revealed similarities in failure modes (delamination at the TGO/ bondcoat interface) upon reaching a certain TGO thickness. However, the exact mechanism for TGO growth and adhesion can be quite different between the two studied systems.

8.3 Parameters affecting oxidation behavior of NiPtAl-coatings

8.3.1 Effect of TBC top coat on rumpling of NiPtAl coatings

The EB-PVD TBC ceramic top coat was observed to suppress surface rumpling of the NiPtAl bondcoats. A flat and homogeneous alumina layer was found to form at the TBC/bondcoat interface, whereas coating rumpling could be observed on the side without TBC (Fig 8.20). The rumpling is probably related to the microstructures of the NiPtAl bondcoat, especially the γ′-Ni_3Al distribution within the coatings. It is obvious that the TBC suppresses bondcoat rumpling as also found by other researchers [155]. The strength of γ′ is significantly higher than that of β, as confirmed by nano-indentation testing [156]. Therefore, the phase transformation from β to β + γ′ changes the overall mechanical properties of the coatings with increasing exposure time. Thus γ′-Ni_3Al formation in the NiPtAl coating could affect the rumpling of the NiPtAl coatings by just increasing the bondcoat strength.

The rumpling process is related to cyclic plastic strains in the bond coat driven by the growth strains in the oxide combined with thermal expansion mismatch between oxide, bond coating, and substrate [93, 157-158]. The thickness of the NiPtAl coating also was shown to have an effect on the occurrence of rumpling [159], although the exact mechanism was not completely clarified. It may be related to

mechanical as well as chemical factors. The chemical composition affects the coating mechanical properties, such as the thermal expansion coefficient, creep and plastic strength. Others researchers [50] proposed that neither the alumina scale formation nor the difference in CTE between the bondcoat and superalloy have an influence on the rumpling. Rather the volume changed associated with phase transformation in the bondcoat is claimed to promote the rumpling [51].

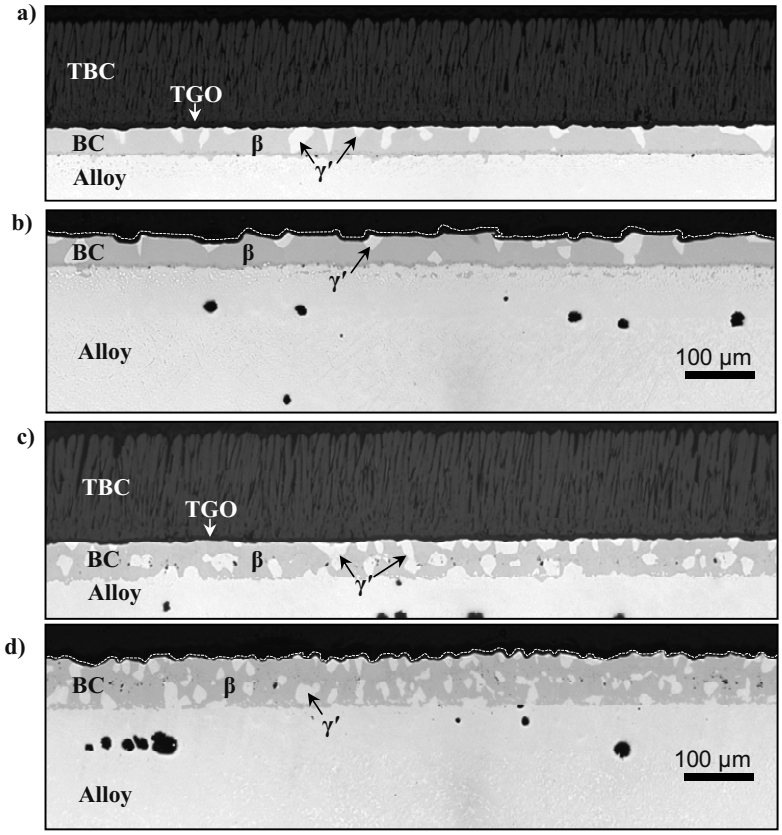

Fig.8.20 Metallographic cross-section images of the NiPtAl coatings with TBC a), c) and without TBC b), d) after 772h discontinuous oxidation at 1100°C in air. a) and b):low-a_{Al}, c) and d):high-a_{Al} coatings

As already shown in the previous chapter, bondcoat rumpling was not observed on the TBC-coated sides of the CMSX-4 samples with NiPtAl coatings. However, substantial rumpling was observed on the sides of the same samples without TBC (Fig 8.20). In the metallographic cross-sections it can be seen that the rumpling is different between the high-a_{Al} and low-a_{Al} coatings and probably has a correlation with the coating microstructures. The white phase seen in both coating cross-sections is γ′, which formed at the coating grain boundaries due to rapid Al-depletion as a result of the TGO growth and Al-diffusion into the base alloy [94].

In order to explain the observed differences in rumpling between the two coatings, detailed studies of specimen sides without TBC were performed using Profilometer, PSLS and SEM after various exposure conditions. Figs 8.21 and 8.22 show profiles of the low-a_{Al} and the high-a_{Al} coatings respectively after various cyclic oxidation times at 1100°C. The amplitude of the rumpling obviously increases with increasing time and/or the number of cycles.

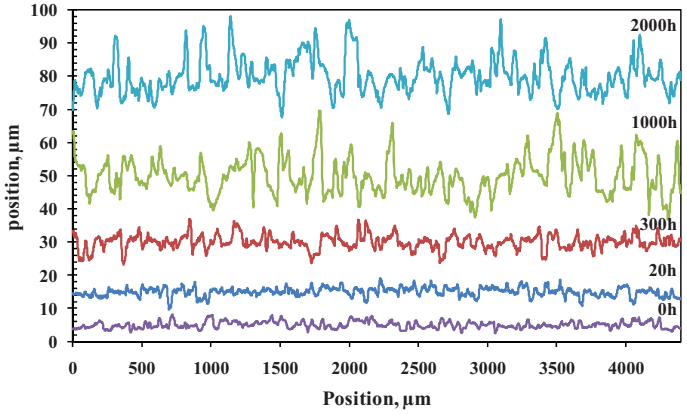

Fig.8.21 Oxide/ coating interface profiles of the as-received low-a_{Al} NiPtAl coating (without TBC top coat) after 2h/15min cyclic oxidation for 20h, 300h, 1000h, and 2000h at 1100°C in air

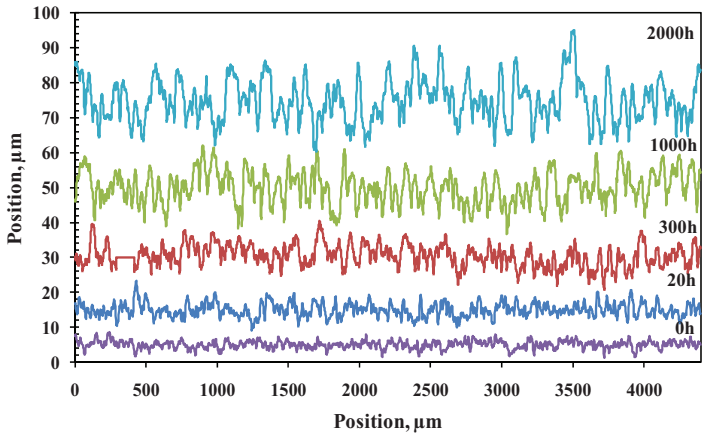

Fig.8.22 Oxide/ coating interface profiles of the as-received high-a_{Al} NiPtAl coating (without TBC top coat) after 2h/15min cyclic oxidation for 20h, 300h, 1000h, and 2000h at 1100°C in air

The profile data presented in Figs 8.21 and 8.22 were used to calculate various parameters of the rough surface according to the procedure proposed by [51]. To suppress the effect of minor manufacturing related surface irregularities, the measured data points were smoothened using a standard procedure of averaging 7 measured neighboring points. Although the length, L, along the surface of the oxide is in general sensitive to the algorithm of smoothening, the curve in Fig 8.23 is reasonably accurate when the smoothening window is much smaller than the size of undulations.

Utilizing the ratio of the length L for the oxide surface profile and the projected length L_0 of the measured profiles, L/L_0, it is possible to assess the surface tortuosity. The amplitude of undulations in normal direction was calculated as the Root-Mean-Square (*RMS*) of the measured coordinates of the oxide surface relative to the mid-line (in Fig 8.23).

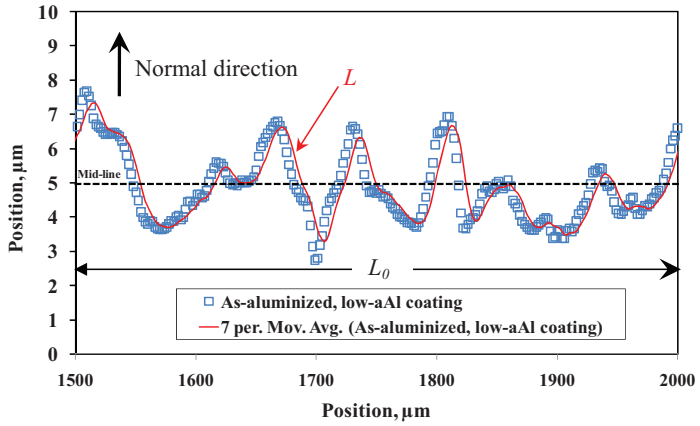

Fig.8.23 Procedure for calculating the BC profile used in the present study. Smoothening by averaging of 7 points to obtain a curve (red line), and L calculated as sum of distances between the neighboring averaged points

Due to the configuration of the coating surface was assumed to be represented by a simple sinusoidal periodic function. The roughness parameters *RMS* and L_0 could be measured from the actual measured profiles. The equivalent rumpling wavelengths for the specimens could be compared using the formulation [159]:

$$W \approx \frac{\pi\sqrt{2}\cdot RMS}{\sqrt{\frac{L}{L_0}-1}} \tag{8.1}$$

Analysis of the rumpling parameters in Fig 8.24 indicates that the average roughness (*RMS*) is similar on both bondcoats (i.e. low and high-a_{Al} coatings) and it increases with increasing exposure time. L/L_0 also increases with exposure time, but the values are different for the two bondcoats. For a given exposure time L/L_0 is larger for the high-a_{Al} than for the low-a_{Al} bondcoat. Also it should be noted that the wavelength in both cases exhibits only a minor increase with increasing exposure time. The wavelengths are much lager for low-a_{Al} than for the high-a_{Al} bondcoat, as is clearly appeared from the metallographic cross-sections in Fig 8.20.

A similar effect as obtained by presence of TBC in respect to suppression of rumpling is exhibited by bondcoat polishing prior to oxidation (Figs 8.24 and 8.25). The *RMS* and L/L_0 is much smaller in case of the pre-polished specimens than in case of specimen oxidation in the as-received conditions.

However, this polishing treatment does not show a clear effect on the wavelength of the coating surface. In Fig 8.25, the residual oxide stress on the polished surfaces is shown to be significantly higher than that on the non-treated NiPtAl coating surfaces. These observations indicate that the primary reason for rumpling is not the γ′ precipitation at the coating grain boundaries, since this is not expected to be affected by the surface polishing. Apparently the surface polishing suppresses the

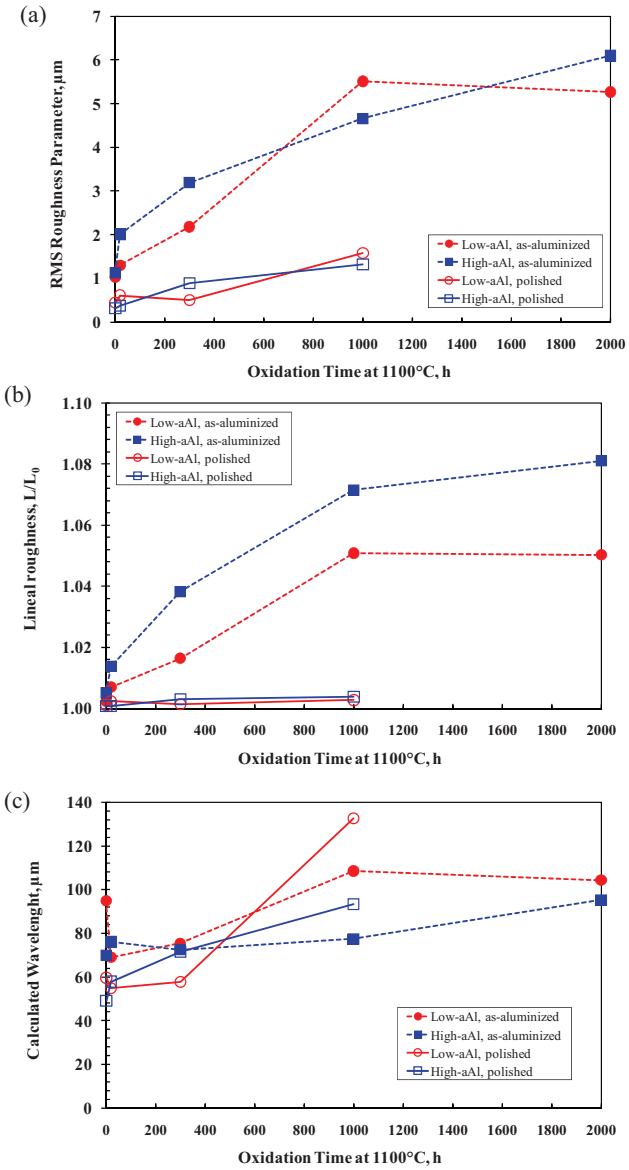

Fig.8.24 Rumpling parameters of the oxide/NiPtAl coatings (with TBC top coat) as a function of time during cyclic oxidation at 1100°C, a): *RMS*; b):L/L_0; c): *W*. The values for oxidized coatings in the as-aluminized state shown by solid marks, and the coatings which ware polished prior to oxidation by empty marks

initiation of rumpling (see Fig 8.24), since initial undulations for rumpling to start with a smaller grain size on the polished coating surfaces than that in as-received condition.

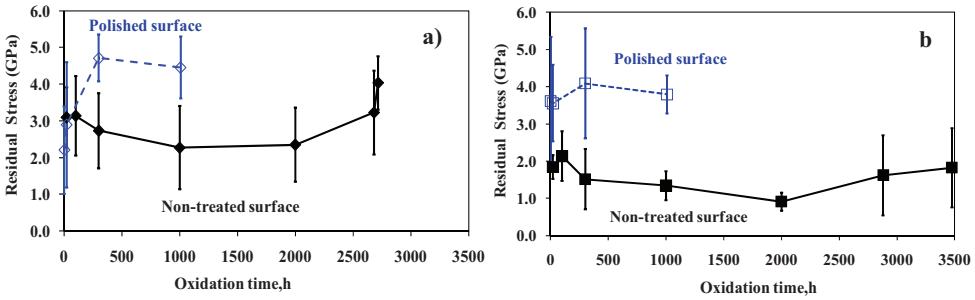

Fig.8.25 Effect of polishing treatment prior to oxidation on the residual compressive stress in the oxide scale formed on the NiPtAl coatings (without TBC topcoat) after cyclic oxidation at 1100°C in air, a):low-a_{Al}, b): high-a_{Al} coatings

It may be argued that the major difference in rumpling behavior between the two coatings is related to substantial differences in the coating grain size. The latter is apparent from the SEM-images presented in Fig 8.26, in which ridges are clearly seen to be associated with the coating grain boundaries for the low-a_{Al} NiPtAl coating, whereas the center of the grains are more or less flat. Oxide spallation occurs from the ridges after longer times of cyclic oxidation (Fig 8.27).

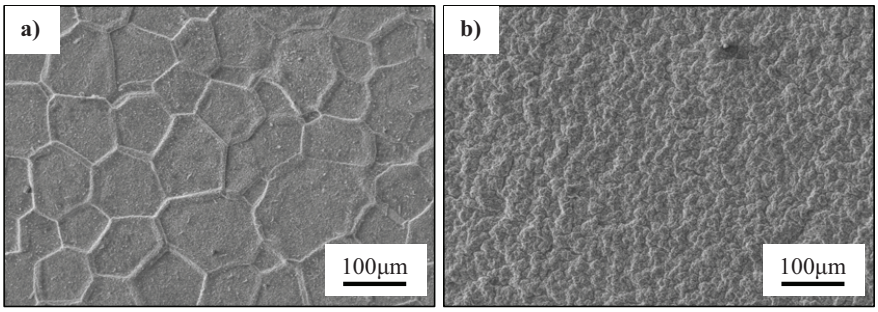

Fig.8.26 SEM images of the oxide surfaces for as-received NiPtAl coatings (without TBC top coat) after 2h/15min cyclic oxidation for 100h at 1100°C in air, a): low-a_{Al}, and b): high-a_{Al} coatings

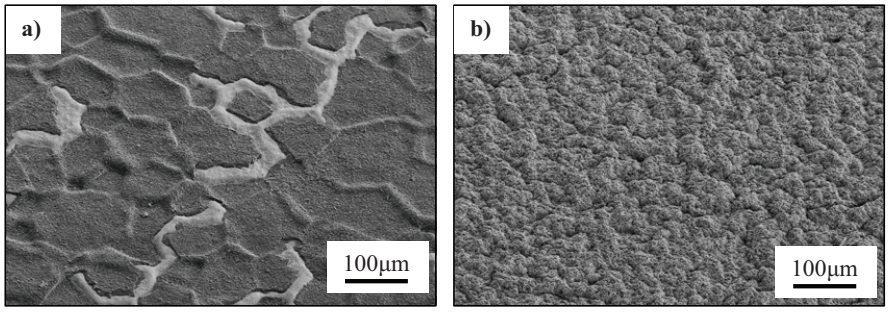

Fig.8.27 SEM images of the oxide surface for as-received NiPtAl coatings (without TBC top coat) after 2h/15min cyclic oxidation for 1000h at 1100°C in air, a): low-a_{Al}, and b): high-a_{Al} coatings

Fig 8.28 shows PSLS oxide stress measurements in the vicinity of the coating grain boundary for the oxidized low-a_{Al} NiPtAl coating. The stress in the center of the coating grain is significantly higher and the scatter is much less compared to that on the ridges. This observation can explain why a much lower stress is measured on the non-treated NiPtAl surfaces after oxidation, than for the TBC-coated sides (following shown in Fig 8.29) and polished surfaces. In the former case the stress is partly relaxed by out-of-plane deformation, whereas in the latter case the oxide is under a more uniform, biaxial compression. As the surface of the high-a_{Al} NiPtAl coating is significantly more convoluted than that on the low-a_{Al} coating, statistically random locations for stress measurements should provide more "relaxed" stress values resulting in a lower average stress in case of the high-a_{Al} bondcoat, which is indeed experimentally observed.

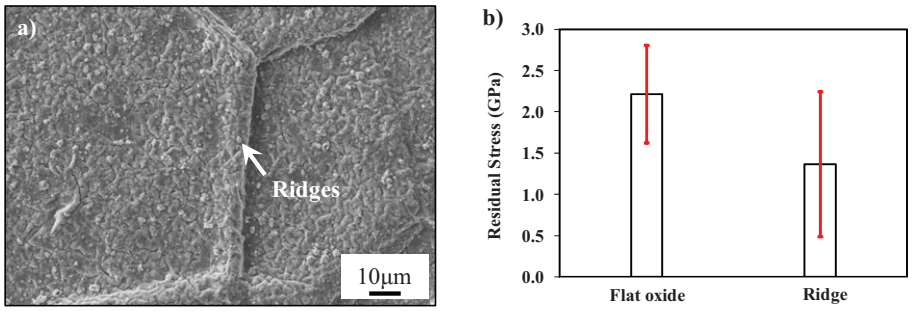

Fig.8.28 Effect of ridges on residual stress in oxide on low-a_{Al} coating (without TBC top coat) exposed in the as-aluminized condition after 2h/15min cyclic oxidation for 100h at 1100°C in air, a): SEM images of ridges, b): stress in oxide on the ridge and on flat oxide scale. Red line indicates measurement data range

The reason for higher residual stress on the "flat" TBC coated sides of the high-a_{Al} bondcoat than that on the low-a_{Al} bondcoat might be related to a larger volume fraction and/or to a more homogeneous distribution of the γ′-phase in the high-a_{Al} coating. These factors could effectively strengthen the coating thereby reducing the overall stress relaxation in the oxide by coating creep during cooling, a mechanism which was suggested in [89] to be important for metallic coatings, such as MCrAlY.

Fig 8.29 presents the residual stress in the oxide for the low and high-a_{Al} NiPtAl bondcoats with and without TBC after discontinuous oxidation at 1100°C in air. For the low-a_{Al} coating (Fig 8.29a) on the side with TBC, the stress after 1h oxidation was about 3.0GPa, and increased to a peak value of 3.3 GPa, then slowly decreasing to 3.0GPa. A small deviation for the stress in the oxide on the side with TBC could be observed. In contrast, the oxide stress on the side without TBC had a large scatter up to 2.0GPa. The average oxide stress on the side without TBC was by about 0.5GPa smaller than that on the side with TBC. Comparing oxide stress measurement with metallographic cross-sections in Fig 8.20 these observations can be explained by the fact that the TBC top coat suppressed the rumpling of the bondcoat, which resulted in a build up of a higher stress compared to the sides without TBC, where

the oxide stress was partly relaxed by the bondcoat deformation (rumpling). These arguments are the same as suggested by other authors [94].

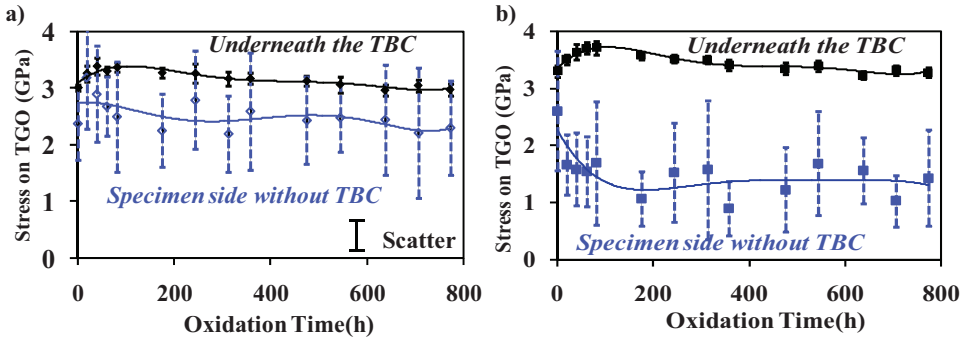

Fig.8.29 Residual compressive stress measured by PSLS in alumina scales formed on NiPtAl coating with and without TBC after discontinuous oxidation at 1100°C in air, a):low-a_{Al}, b): high-a_{Al} coatings

Microstructures of the low-a_{Al} and high-a_{Al} NiPtAl coatings were analysed using EBSD on the specimen sides without TBC. Fig 8.30 shows the top view of polished NiPtAl coatings prior to oxidation. The low-a_{Al} coating (Fig 8.30a) was single-phase β-NiAl with an average grain size of approximately 100 ± 50 µm. The high-a_{Al} coatings were two-phase (β-NiAl and $PtAl_2$) in agreement with the XRD data in Fig 8. 3.

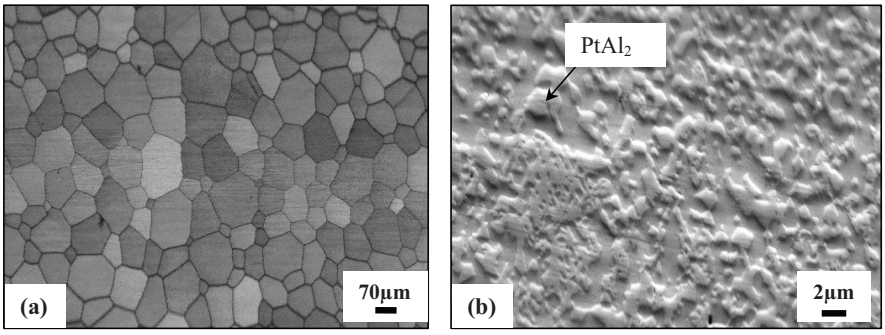

Fig. 8.30 SEM pattern of polished coatings prior to oxidation, a): low-a_{Al}, EBSD-map , b): high-a_{Al}, secondary electron (SE) image

Fig 8.31 shows an EBSD pattern of the low-a_{Al} coating in normal direction which shows a random grain orientation. The β-NiAl orientation could affect oxide scale formation especially in the early stages of exposure. For example, scales formed on (111) of the β-NiAl orientation were found to be thicker than scales on (001) orientation specimens after equal oxidation times [160]. Fig 8.32 shows the EBSD patterns for NiAl and $PtAl_2$ phases in the high-a_{Al} coating. The two-phase grain orientation in the high-a_{Al} coating is random.

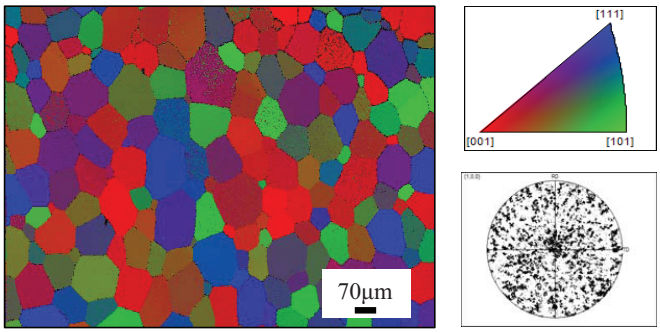

Fig.8.31 EBSD pattern for low-a_{Al} NiPtAl coating (normal direction to the coating surface)

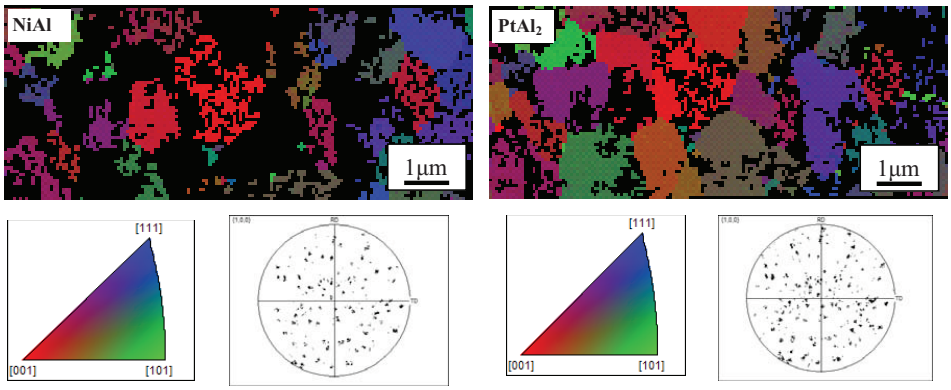

Fig.8.32 EBSD for high-a_{Al} NiPtAl coating (normal direction to the coating surface)

To investigate the intrinsic oxidation behavior of NiPtAl coatings, specimens were polished to 1μm before oxidation. Fig 8.33 shows the SEM images for the surfaces of NiPtAl coatings after 8h oxidation in Ar-20%O_2. Tensile cracks in the oxide and local oxide spallation as well as oxide re-growth could be observed for the low-a_{Al} coating (Fig 8.33a). Void formation underneath the oxide scale was seen in the places where the oxides had spalled. The formation of radial cracks (Fig 8.33c) in the oxide scales on Ni-aluminides was attributed to the oxide volume shrinkage due to the transformation of metastable θ-Al_2O_3 to α-Al_2O_3 phase [151]. The high-a_{Al} coating exhibited another oxide surface morphology, showing a "network" of oxide ridges and no oxide spallation could be found.

Comparison of the surface morphologies in Fig 8.33 indicates that the transformation of θ to α-Al_2O_3 occurred earlier for the high-a_{Al} than for the low-a_{Al} coating, although only α-Al_2O_3 was found with PSLS on both coatings after 8 h exposure at 1100°C. Fig 8.34 shows that differences in oxide morphologies on the polished surfaces remained after much longer exposure times (1000h). The

specimen surface of the low-a_{Al} coating shows local oxide spallation and voids (Fig 8.35), which cannot be observed on the high-a_{Al} coating.

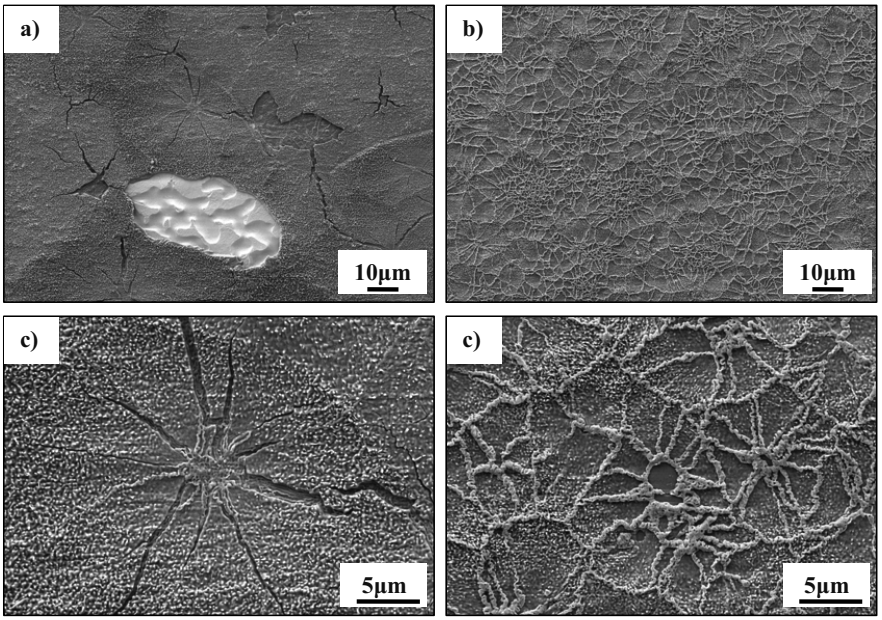

Fig. 8.33 SEM images for the surface of NiPtAl coatings after 8h oxidation at 1100°C in Ar-20%O_2, a) and c): low-a_{Al}; b) and d): high-a_{Al} coatings

The oxide morphologies for the low-a_{Al} and high-a_{Al} NiPtAl coatings after isothermal oxidation at 1100°C for 1000h in air are shown in Fig 8.34. Pieces of locally spalled alumina scale were found on the low-a_{Al} coating. White particles on the top of the oxide can be observed (Fig 8.34c), which were (Ta,Ti,Hf)-rich oxides confirmed by EDX analysis. Apparently Ta, Ti and Hf diffused from the CMSX-4 base alloy into the coating and became incorporated into the TGO. The flat and homogenous oxide scale on the high-a_{Al} coating is presented in Figs 8.34b and d. With increasing the oxidation time to 1000h, the ridges observed after 8 h (Fig 8.33) disappeared. The TGO outward growth probably resulted in overgrowth of the initially formed ridges. Whisker-like alumina could be observed on the top of oxide scale in Fig 8.34d, which illustrated significantly different oxide morphologies between low-a_{Al} and high-a_{Al} coatings.

An interesting observation for the low-a_{Al} coating was that large voids were observed locally underneath the oxide scale even after long time exposure (1000h at 1100°C) as shown in Fig 8.35. The oxide scale above the voids tended to spall during the cooling stages. This type of voids was already observed in similar coatings systems by other researchers [161-162]. The reasons for the void formation at the oxide/metal interface during oxidation are still in debate. One hypotheses based on diffusion phenomena was proposed in references [79, 163], whereby the alumina scale formation

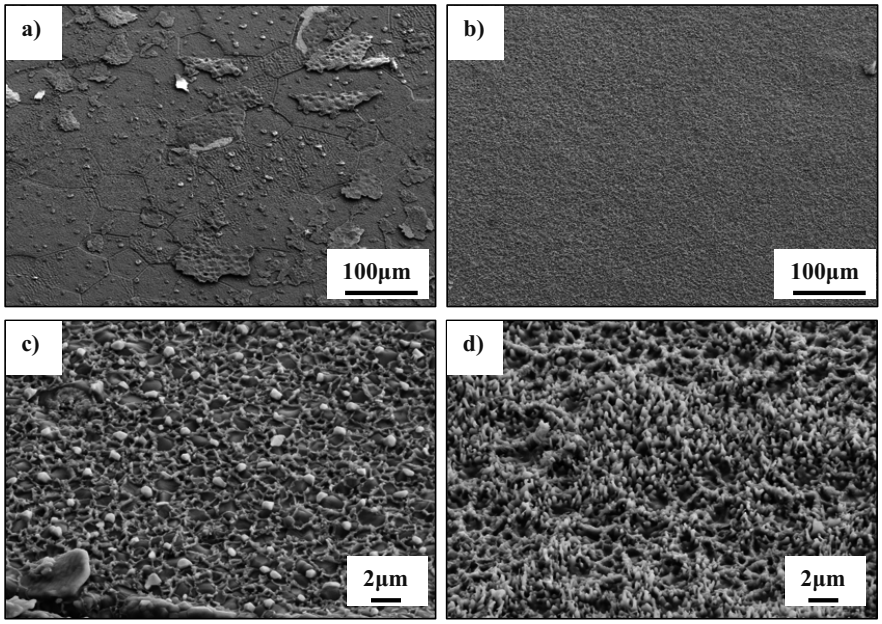

Fig 8.34 SEM images for the oxide on the polished NiPtAl coatings after 1000h isothermal oxidation at 1100°C in air, a) and c): low-a_{Al}, b) and d): high-a_{Al} coatings

was assumed to induce the Al and Ni concentration gradients in the coating. The difference in the Ni and Al diffusion fluxes might be compensated by vacancies. These vacancies could coalesce and form interfacial voids according to Kirkendall mechanism [163]. The Al consumption from β-NiAl might simply create Al vacancies, which can coalesce to form interfacial voids [77, 164]. Some authors considered that these voids could be associated with a very high frequency of thermal cycling [165]. Tolpygo et al [94] found that the transformation of β-NiAl to the γ′-Ni_3Al phase could lead to a volume reduction of 16~38%, which depended on the used calculation procedure. The volume reduction could contribute not only to the surface rumpling but also to the formation of interfacial voids. In the present study, thermal cycling did not prevail. Comparison of Fig 8.35 with 8.33

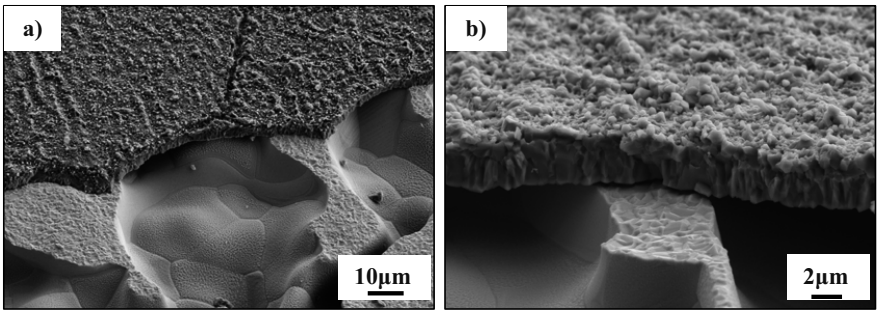

Fig 8.35 SEM images for the low-a_{Al} coatings after 1000h isothermal oxidation at 1100°C in air, a): low and b): high magnification

indicates that void formation can be associated with metastable alumina formation in the initial stages of exposure. Outward growing metastable θ-Al_2O_3 could result in vacancy injection to the oxide/bondcoat interface, as suggested by other authors for NiAl oxidation [166]. Increase in the void size with increasing exposure time can be explained e.g. by S-segregation to the void surface, which was proposed to accelerate void growth [167]. These voids can be filled up again by stable α-alumina during oxidation.

8.3.2 Effect of temperature cycling conditions and water vapor on the lifetimes of TBC's with the NiPtAl coatings

Fig 8.36 shows lifetimes of EB-PVD TBC systems with low-a_{Al} and high-a_{Al} NiPtAl bondcoats during cyclic oxidation at 1150°C in various atmospheres. It can be seen that changes in the atmosphere with respect to water vapor content have no significant effect on the lifetimes of both studied TBC systems.

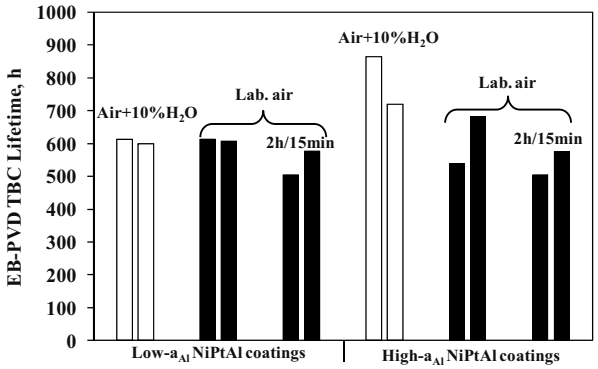

Fig.8.36 Lifetime for EB-PVD-TBC with the NiPtAl coatings after 4h/1h cyclic oxidation at 1150°C in air+10%H_2O and laboratory air. Also included the lifetime data after 2h/15min cyclic oxidation

Fig 8.37 presents the cross-sections of the failed TBC systems with NiPtAl coatings after cyclic oxidation at 1150°C using 2h/15min and 4h/1h cycles. The delamination for the TBC systems in all cases occurred at the TGO/ bondcoat interface. A high fraction of β-NiAl phase could still be found in the cross-sections of the low-a_{Al} as well as high-a_{Al} coatings. The TGO thickness was about 7~8μm when the TBC occurred failure after the two different cyclic oxidation parameters. Comparison with the cross-sections at 1100°C shown in Fig 8.12, showed that more β-phase was presented in the coating after oxidation until failure at 1150°C than at 1100°C. Because of the similar TGO thickness at occurrence of failure at 1100°C and 1150°C, the Al consumption induced by oxide scale formation should be similar at high temperature. Therefore, the more extensive β transformation to γ′ at 1100°C is due to more extensive Al-diffusion into the base alloy after a longer exposure time.

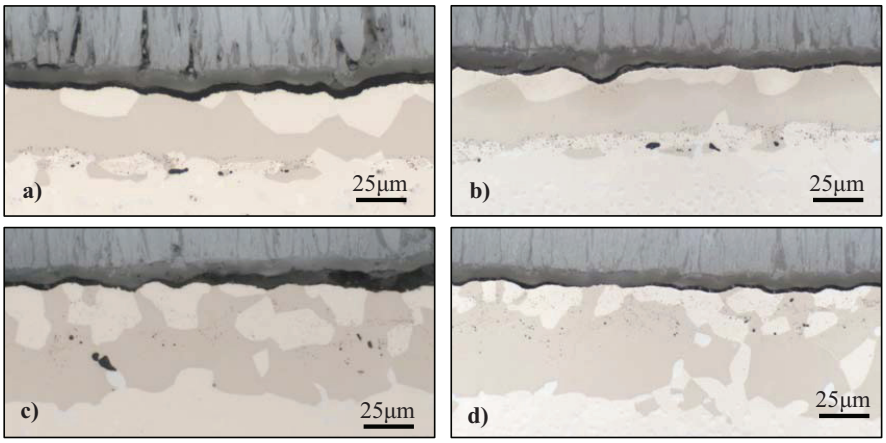

Fig.8.37 Optical cross-section of EB-PVD-TBC with NiPtAl coatings after 2h/15min (a and c) and 4h/1h (b and d) cyclic oxidation till TBC failure at 1150°C in air, a) and b): low-a_{Al} coating: c) and d): high-a_{Al} coating

Fig 8.38 shows similar TGO morphologies and thicknesses for the TBC systems with NiPtAl coatings after exposure in laboratory air and in air+10%H_2O. The similar TGO morphologies and thickness for TBC failure under different cyclic conditions, H_2O content as well as at 1100°C and 1150°C could be observed. These above changes of conditions did not result in a change of lifetime of the TBC systems (Fig 8.36), which indicated that the critical TGO thickness plays a major role in determining the lifetime of TBC systems with NiPtAl-bondcoats.

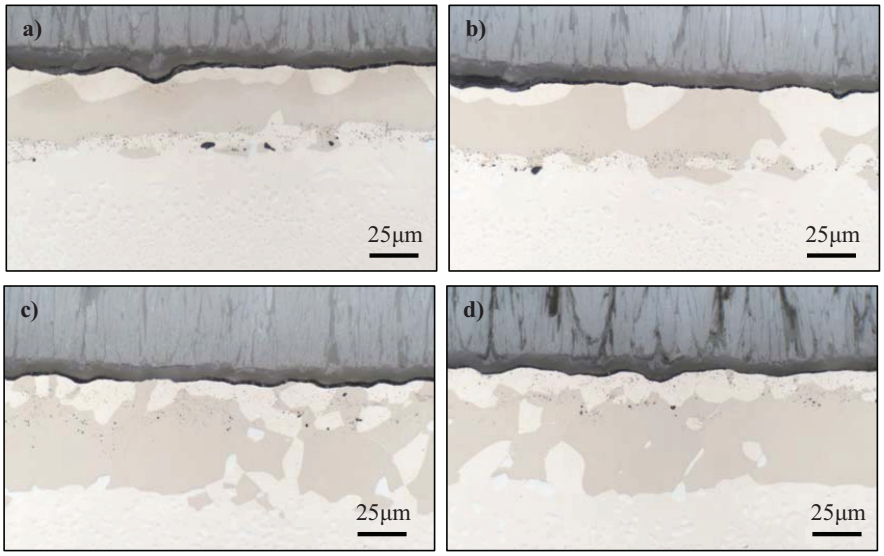

Fig.8.38 Optical images for EB-PVD TBC with low-a_{Al} (a, b) and high-a_{Al} (c, d) BC after 4h/1h cyclic oxidation till TBC failure at 1150°C, a) and c): Synthetic air; b) and d): Air+10%H_2O

It should be noted that in the 4h heating/1h cooling test the specimens were exposed in a quartz recipient in order to have a direct comparison between the dry and wet air. This resulted in significantly lower heating/cooling rates of the speciemens as compared to the 2h heating /15min cooling cycles, where no quartz recipient was used and the cooling was performed using pressurized air.

Nevertheless, considering the statistical nature of TBC failure, the more severe cyclic conditions in the 2h/15min test have not resulted in significant shortening of the TBC lifetime. TBC life appears to be mainly governed by the time at temperature. The absence of a water vapor effect on the lifetime of EB-PVD TBC systems with NiPtAl coating differs from EB-PVD TBC systems with MCrAlY bondcoats (chapter 6.3.2). For the latter system, a significant detrimental effect was observed.

In reference [107] it was argued that deterioration of scale adherence by water vapor is more strongly pronounced for systems with a poorer oxide scale adherence. Therefore it is possible that NiPtAl bondcoats, which are known to possess a superior scale adherence in the cyclic oxidation test, are less sensitive to the adverse influence of water vapor than MCrAlY bondcoats. It was shown [67] that in the latter coatings the scale adherence crucially depends on the interaction of Y with impurities such as oxygen introduced during coating manufacturing and, in addition, Y is subjected to depletion during the oxidation process. In NiPtAl coatings the Pt content is significantly higher that that of Y. Therefore, even though Pt is depleted due to diffusion into the superalloy, this process is significantly slower than that of Y-depletion due to a much larger Pt reservoir. Therefore the positive effect of Pt on Al_2O_3-scale adherence is retained up to much longer times than that of Y.

9 Summary

In the present project the oxidation behavior and lifetime of different TBC-systems based on yttria stabilized zirconia (YSZ) under varying exposure conditions has been studied. The range of investigated materials included EB-PVD-TBC systems with MCrAlY and NiPtAl bondcoats as well as APS-TBC systems with MCrAlY bondcoats. For systems with MCrAlY-bondcoats the effects of major bondcoat composition (Co-content), minor addition (Zr and O contents) and for those with NiPtAl bondcoats the effects of aluminizing parameters (low Al activity vs. high Al activity process) have been investigated. The variation of testing parameters comprised high temperature and low temperature dwell times, cooling rate, water vapor content and, for selected systems, also the oxygen partial pressure (pO_2) in the atmosphere.

The results of the first part of the study on EB-PVD TBC systems with MCrAlY-type bondcoats showed that the lifetime in cyclic oxidation test is significantly affected by the main bondcoat-composition, in particular the Co-content. The lifetime was significantly longer in case of CoNiCrAlY bondcoats than with NiCoCrAlY bondcoats. This was attributed to a more stable coating microstructure, resulting in a lower CTE of CoNiCrAlY bondcoat resulting in lower thermal mismatch stresses generated in the oxide scale upon cooling.

The positive effect of co-doping MCrAlY bondcoats with Zr on the EB-PVD TBC lifetime observed in previous studies [67] was found to strongly depend on the used cycling parameters. This was related to the specific mechanisms of the oxide scale formation: locally enhanced inward growth due to incorporation of ZrO_2 precipitates into the alumina scale resulting in a convoluted scale/bondcoat interface. Consequently, during cyclic oxidation the failure of the TBC system with Y/Zr-doped bondcoat was initiated by crack formation within the oxide scale and at the scale/TBC interface. Due to the fact that the cracks formed at different locations with respect to out of plane direction, the TBC-lifetime was mainly limited by the growth rate of individual cracks. Crack growth was higher in a test with a high cycling frequency (2 h-cycle) compared to that in a low frequency (166 h-cycle) test. As a result, the lifetime of TBC-system with Zr-doped bondcoat was a factor of two shorter in the test with 2 h than in that with 166 h-cycle. It is important to note that even under 2 h-cycle tests, the lifetime of the TBC with a Zr-doped bondcoat was about 50% longer than that of the system with NiCoCrAlY-bondcoat of the same composition, however, without Zr-addition. In the latter case the failure occurred at the flat oxide scale/bondcoat interface upon reaching a critical oxide scale thickness whereby the time to failure was independent of the cycling parameters.

Studies of an EB-PVD-TBC system with Y/Zr-doped bondcoat revealed that the lifetime is not extended in an atmosphere with a low pO_2 (H_2/H_2O-mixture) compared to that in a high pO_2 gas (e.g.

air), as was observed previously [25] in the system with conventional MCrAlY-bondcoat without Zr. This observation could be attributed to a different scale growth mechanism (mainly oxygen diffusion in zirconia precipitates) on the former, Y/Zr-codoped bondcoat as compared to oxygen grain boundary diffusion in a rather pure alumina scale on the Zr-free bondcoat. Accordingly, the scale growth rate on the Zr-doped bondcoat appeared to be initially determined by oxygen diffusion via oxygen vacancies in zirconia, which was shown to be virtually independent of pO_2 in the atmosphere. The situation was different in the case of the Zr-free bondcoat, where the scale growth was reduced in the low PO_2 gas mainly due to reduction of the oxygen potential gradient, i.e. the driving force for oxygen diffusion along alumina grain boundaries.

Increase of water vapor content in the high pO_2 test atmosphere from about 2 to 20 % was detrimental for the lifetime of EB-PVD TBC systems with MCrAlY-type bondcoats. Moisture-induced spallation could be an operating mechanism adversely affecting the Al_2O_3 scale adhesion. This result indicates that the lifetimes of EB-PVD TBC systems with MCrAlY-type bondcoats in hydrogen gas-turbines in IGCC power plants operating with a significantly higher water vapor content in the exhaust gas may be significantly reduced compared to conventional turbines burning natural gas.

Studies of APS-TBC systems revealed that, similar to the observation made for the EB-PVD TBC systems, CoNiCrAlY-bondcoats can provide a longer lifetime due to a more stable bondcoat microstructure as compared to NiCoCrAlY bondcoats. It was, however, found that the rough bondcoat surfaces of Co-base MCrAlY coatings are more susceptible to non-protective oxidation with formation of Co-rich spinel oxides, which can serve as sites for crack initiation during temperature cycling leading to significant shortening of the APS-TBC lifetime. This adverse effect can be suppressed by a minor (few micrometers) Al-enrichment at the bondcoat surface resulting from Cr-evaporation, which occurs during coating heat-treatment in high vacuum.

The lifetime of APS-TBC systems with Ni-base MCrAlY bondcoats, which tend to form rather pure alumina scales, is significantly longer with porous TBC and a porous bondcoat which exhibits high roughness and convoluted morphology than that with a dense TBC and dense bondcoat featuring a “sinusoidal” roughness profile. For the former system repeated oxide scale delamination and re-growth was observed in the convex parts of the bondcoat surface, indicating that occurrence of oxide delamination on bondcoat hills did not lead to immediate TBC-failure. The repeated oxide delamination /re-growth was not observed in systems with dense TBC and bondcoat. Using the TBC system with dense bondcoat and porous TBC it could be demonstrated that the bondcoat roughness and surface profile play, in addition to the TBC properties, an important role in governing the time to failure of an APS-TBC system.

A higher water vapor content in the test atmosphere appeared to have no significant effect on the lifetime of APS-TBC systems, contrary to the observations made with EB-PVD TBC systems. This could be attributed to differences in the failure mechanisms between the two system types. The crack propagation rate through the ceramic YSZ topcoat, which determines the failure of APS-TBC systems, seems to be not significantly affected by the presence of water vapor in the test gas.

Variation of temperature cycling parameters showed that the lifetime of APS-TBC systems can be affected by the cyclic frequency. Shorter cycles result in more rapid crack initiation and propagation resulting in a shortening of the TBC-lifetime. In contrast, the cooling rate within the range studied seems to have no significant effect on the system lifetime.

In general, it could be concluded that, contrary to EB-PVD TBC systems, for APS-TBC's no critical TGO-thickness for failure can be defined, since the lifetime depends to a large extent on the crack propagation rate in the TBC. As shown above, the rate of crack growth depends substantially on the microstructural properties of the systems, which in turn are determined by the coating spraying parameters.

Cyclic oxidation lifetimes of EB-PVD TBC systems with Ni(Pt)Al bondcoats on a single crystal superalloy appeared to be significantly longer than those of commonly TBC systems with MCrAlY-bondcoats on polycrystalline superalloys. Although the difference in lifetime can be partly related to the different base materials used, it can be argued that the growth rate of the alumina scale is lower and the critical scale thickness for failure is larger for Ni(Pt)Al coatings than for MCrAlY-coatings. The latter observation might be attributed to the positive effect of Pt on the alumina scale adherence and makes the EB-PVD-TBC systems with NiPtAl bondcoats potentially attractive for application in gas-turbines in spite of the high cost of Pt. The above most important effects of various parameters on the crack formation and lifetime of various TBC-systems are summarized schematically in Fig 9.1.

Studies of EB-PVD TBC systems with two types of NiPtAl bondcoats produced by low and high Al-activity aluminizing processes revealed very similar oxidation behavior and lifetime. The lifetimes of the TBC systems with NiPtAl bondcoat were not significantly affected by changing the cycling frequency or by higher water vapor content in the test atmosphere.

Finally, the presence of the TBC was observed to suppress the differences in metastable alumina formation and the frequently observed rumpling of the NiPtAl coatings in thermal cyclic test, which were clearly pronounced for low and high Al activity coatings on the sides without TBC. If the TBC was absent the low Al-activity coating was shown to have a longer time to transformation from theta into alpha alumina. The rumpling parameters, such as wavelength and surface tortuosity were clearly

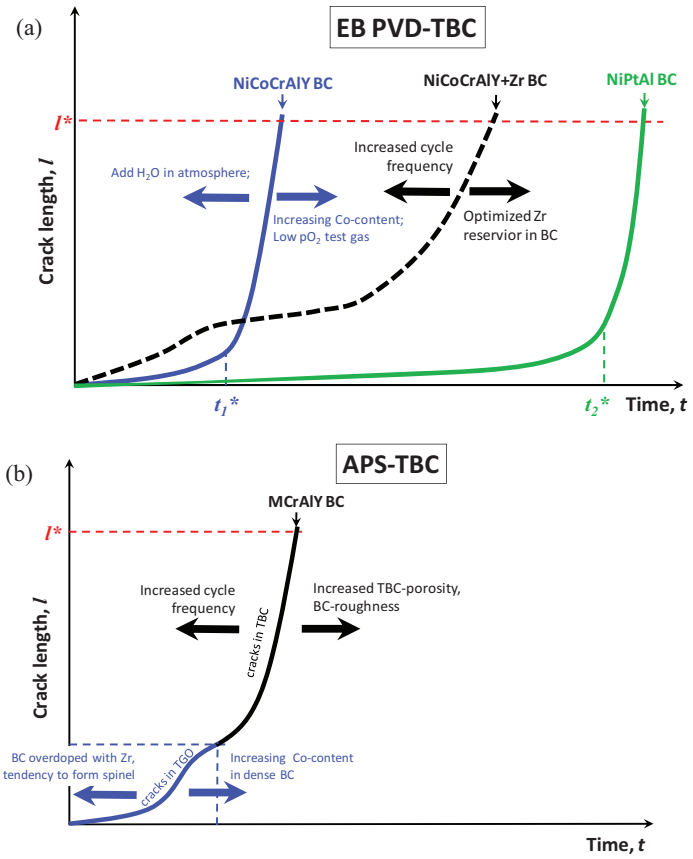

Fig 9.1 Schematic influence of material and testing parameters on crack formation and lifetime of a) EB-PVD and b) APS TBC lifetime; t_1^*, t_2^*- times to reach critical TGO thickness for failure which occurs at critical crack length of l^*

different between the two studied aluminized coating types. The rumpling was, however, not observed on the specimen sides coated with the TBC, which failed on both bondcoats by delamination at the scale/bondcoat interface at a similar critical TGO thickness.

10 References

1. IEA, *World Energy Outlook 2009, International Energy Agency*,Paris, France, **2009**.
2. IPCC, *Special report on carbon dioxide capture and storage*,Cambridge Univeristy Press, England, **2005**.
3. *VGB Facts and Figures - Electricity Generation,*www.vgb.org,VGB PowerTech e.V., **2010/2011**.
4. R.C. Reed, *The superalloys fundamentals and applications*. Cambridge, UK: Cambridge University Press, **2006**.
5. D.J. Young, *High Temperature Oxidation and Corrosion of Metals*. Elsevier: Cambridge,UK, **2008**.
6. C. Lechner and J.Seume, *Stationäre Gasturbinen*, Springer Press, Berlin, **2003**.
7. G.W. Goward, *Progress in coatings for gas turbine airfoils*, Surface and Coatings Technology, **1998**. 108-109: p. 73-79.
8. N.P. Padture, M. Gell, and E.H. Jordan, *Thermal Barrier Coatings for Gas-Turbine Engine Applications*, Science, **2002**. 296: p. 280-284.
9. R. Vassen, A. Stuke, and D. Stöver, *Recent Developments in the Field of Thermal Barrier Coatings*, Journal of Thermal Spray Technology, **2009**. 18(2): p. 181-186.
10. U. Schulz, C. Leyens, K. Fritscher, M. Peters, B. Saruhan-Brings, O. Lavigne, J.-M. Dorvaux, M. Poulain, R. Mévrel, and M. Caliez, *Some recent trends in research and technology of advanced thermal barrier coatings*, Aerospace Science and Technology, **2003**. 7: p. 73-80.
11. X.Q.Cao, R.Vaßen, and D.Stöver, *Ceramic materials for thermal barrier coatings*, Journal of the European Ceramic Society, **2004**. 24(1): p. 1-10.
12. Z. Xu, L. He, X. Zhong, R. Mu, S. He, and X. Cao, *Thermal barrier coating of lanthanum–zirconium–cerium composite oxide made by electron beam-physical vapor deposition*, Journal of Alloys and Compounds, **2009**. 478(1-2): p. 168-172.
13. R. Vassen, X. Cao, F. Tietz, D. Basu, and D. Stöver, *Zirconates as New Materials for Thermal Barrier Coatings*, Journal of the American Ceramic Society, **2000**. 83(8): p. 2023-2028.
14. W. Ma, S. Gong, H. Xu, and X. Cao, *The thermal cycling behavior of Lanthanum–Cerium Oxide thermal barrier coating prepared by EB–PVD*, Surface & Coatings Technology, **2006**. 200(16-17): p. 5113-5118.
15. R. Vaßen, M.O. Jarligo, T. Steinke, D.E. Mack, and D. Stöver, *Overview on advanced thermal barrier coatings*, Surface & Coatings Technology, **2010**. 205(4): p. 938-942.
16. R.A.Miller, *Current status of thermal barrier coatings — An overview*, Surface & Coatings Technology, **1987**. 30(1): p. 1-11.
17. R.G. Wellman and J.R. Nicholls, *A review of the erosion of thermal barrier coatings*, Journal of Physics D: Applied Physics, **2007**. 40(16): p. 293-305.
18. D. Chen, M. Gell, E.H. Jordan, E. Cao, and X. Ma, *Thermal Stability of Air Plasma Spray and Solution Precursor Plasma Spray Thermal Barrier Coatings*, Journal of the American Ceramic Society, **2007**. 90(10): p. 3160-3165.
19. J.H.Zaat, *A Quarter of a Century of Plasma Spraying*, Annual Review of Materials Science, **1983**. 13: p. 9-42.
20. T.E. Strangman, *Thermal barrier coatings for turbine airfoils*, Thin Solid Films, **1985**. 127(1-2): p. 93-106.
21. H. Guo, H. Xu, X. Bi, and S. Gong, *Preparation of Al_2O_3–YSZ composite coating by EB-PVD*, Materials Science and Engineering A, **2002**. 325: p. 389-393.
22. J.R. Nicholls, K.J. Lawson, A. Johnstone, and D. Rickerby, *Low Thermal Conductivity EB-PVD Thermal Barrier Coatings*, Materials Science Forum, **2001**. 369-372: p. 595-606.
23. H.-J. Rätzer-Scheibe and U. Schulz, *The effects of heat treatment and gas atmosphere on the thermal conductivity of APS and EB-PVD PYSZ thermal barrier coatings*, Surface & Coatings Technology, **2007**. 201: p. 7880-7888.
24. J.R. Nicholls, K.J. Lawson, A. Johnstone, and D.S. Rickerby, *Methods to reduce the thermal conductivity of EB-PVD TBCs*, Surface and Coatings Technology, **2002**. 151-152: p. 383-391.
25. J.P. Toscano, *Influence of composition and processing on the oxidation behavior of MCrAlY-coating for TBC applications (Ph.D thesis)*, RWTH-AACHEN, **2008**.

26. T.S. Sidhu, S. Prakash, and R.D. Agrawal, *Hot corrosion and performance of nickel-based coatings*, Current science, **2006**. 90(1): p. 41-47.
27. P.Hancock, *Vanadic and chloride attack of superalloys*, Materials Science and Technology, **1987**. 3(7): p. 536-544.
28. B.Gleeson, *Thermal barrier coatings for aeroengine applications*, Journal of propulsion and power, **2006**. 22(2): p. 375-383.
29. D. Naumenko, B. Gleeson, E. Wessel, L. Singheiser, and W.J. Quadakkers, *Correlation between the Microstructure, Growth Mechanism, and Growth Kinetics of Alumina Scales on a FeCrAlY Alloy*, Metallurgical and Materials Transactions A, **2007**. 38: p. 2974-2983.
30. M. Subanovic, D. Sebold, R. Vassen, E. Wessel, D. Naumenko, L. Singheiser, and W.J. Quadakkers, *Effect of manufacturing related parameters on oxidation properties of MCrAlY-bondcoats*, Materials and Corrosion, **2008**. 59(6): p. 463-470.
31. B.A. Pint, J.R. Distefano, and I.G. Wright, *Oxidation resistance: One barrier to moving beyond Ni-base superalloys*, Materials Science and Engineering A, **2006**. 415: p. 255-263.
32. J.A. Haynes, B.A. Pint, Y. Zhang, and I.G. Wright, *Comparison of the cyclic oxidation behavior of β-NiAl, β-NiPtAl and γ–γ′ NiPtAl coatings on various superalloys*, Surface & Coatings Technology, **2007**. 202: p. 730-734.
33. N. Vialas and D. Monceau, *Effect of Pt and Al content on the long-term, high temperature oxidation behavior and interdiffusion of a Pt-modified aluminide coating deposited on Ni-base superalloys*, Surface & Coatings Technology, **2006**(201): p. 3846-3851.
34. D.Naumenko, V.Shemet, L.Singheiser, and W.J.Quadakkers, *Failure mechanisms of thermal barrier coatings on MCrAlY-type bondcoats associated with the formation of the thermally grown oxide*, Journal of Materials Science, **2009**. 44: p. 1687–1703.
35. J. Toscano, A. Gil, T. Hüttel, E. Wessel, D. Naumenko, L. Singheiser, and W.J. Quadakkers, *Temperature dependence of phase relationships in different types of MCrAlY-coatings*, Surface & Coatings Technology, **2007**. 202: p. 603-607.
36. N.Birks, G.H.Meier, and F.S.Pettit, *High-temperature oxidation of metals (2nd Edition)*, Cambridge Univeristy Press, England, **2006**.
37. J.R. Nicholls, *Designing Oxidation-Resistant Coatings*,Journal of Materials **2000**. 1: p. 28-35.
38. D.R.G. Achar, R. Munoz-Arroyo, L. Singheiser, and W.J. Quadakkers, *Modelling of phase equilibria in MCrAlY coating systems*, Surface and Coatings Technology, **2004**. 187(2-3): p. 272-283.
39. N. Czech, F. Schmitz, and W. Stamm, *Improvement of MCrA1Y coatings by addition of rhenium*, Surface and Coatings Technology, **1994**. 68/69: p. 17-21.
40. T.A. Taylor and D.F. Bettridge, *Development of alloyed and dispersion-strengthened MCrAlY coatings*, Surface & Coatings Technology, **1996**. 86-87: p. 9-14.
41. K. Ogawa, K. Ito, T. Shoji, D.W. Seo, H. Tezuka, and H. Kato, *Effects of Ce and Si Additions to CoNiCrAlY Bond Coat Materials on Oxidation Behavior and Crack Propagation of Thermal Barrier Coatings*, Journal of Thermal Spray Technology, **2006**. 15(4): p. 640-651.
42. J.A. Haynes, B.A. Pint, K.L. More, Y. Zhang, and I.G. Wright, *Influence of Sulfur, Platinum, and Hafnium on the Oxidation Behavior of CVD NiAl Bond Coatings*, Oxidation of metals, **2002**. 58(5/6): p. 513-544.
43. A. Hesnawi, H. Li, Z. Zhou, S. Gong, and H. Xu, *Isothermal oxidation behaviour of EB-PVD MCrAlY bond coat*, Surface & Coatings Technology, **2007**. 81(8): p. 947-952.
44. B.K. Pant, V. Arya, and B.S. Mann, *Development of Low-Oxide MCrAlY Coatings for Gas Turbine Applications*, Journal of Thermal Spray Technology, **2007**. 16(2): p. 275-280.
45. P. Richer, M. Yandouzi, L. Beauvais, and B. Jodoin, *Oxidation behaviour of CoNiCrAlY bond coats produced by plasma, HVOF and cold gas dynamic spraying*, Surface & Coatings Technology, **2010**. 204(24): p. 3962-3974.
46. A. Gil, V. Shemet, R. Vassen, M. Subanovic, J. Toscano, D. Naumenko, L. Singheiser, and W.J. Quadakkers, *Effect of surface condition on the oxidation behaviour of MCrAlY coatings*, Surface & Coatings Technology, **2006**. 201(7): p. 3824-3828.
47. W.R. Chen, X. Wu, B.R. Marple, D.R. Nagy, and P.C. Patnaik, *TGO growth behaviour in TBCs with APS and HVOF bond coats*, Surface & Coatings Technology, **2008**. 202: p. 2677-2683.

48. G.W.Goward and D.H.Boone, *Mechanism of formation of diffusion aluminide coatings on Nickel-base superalloys*, Oxidation of metals, **1971**. 3(5): p. 475-495.
49. G. Lehnert and H. Meinhardt, *Present state and trend of development of surface coating methods against oxidation and corrosion at high temperatures*, Electrodeposition and Surface Treatment, **1972**. 1(1): p. 71-76.
50. V.K. Tolpygo and D.R. Clarke, *On the rumpling mechanism in nickel-aluminide coatings Part I: an experimental assessment*, Acta Materialia, **2004**. 52: p. 5115-5127.
51. V.K. Tolpygo and D.R. Clarke, *On the rumpling mechanism in nickel-aluminide coatings Part II: characterization of surface undulations and bond coat*, Acta Materialia, **2004**. 52: p. 5129-5141.
52. M.W. Chen, M.L. Glynn, R.T. Ott, T.C. Hufnagel, and K.J. Hemker, *Characterization and modeling of a martensitic transformation in a platinum modified diffusion aluminide bond coat for thermal barrier coatings*, Acta Materialia, **2003**. 51: p. 4279-4294.
53. B. Gleeson, D. Sordelet, and W.Wang, *US Patent No. 20040229075A1*. 2003.
54. Y. Zhang, B.A. Pint, J.A. Haynes, and I.G. Wrig, *A platinum-enriched γ+γ'two-phase bond coat on Ni-based superalloys*, Surface & Coatings Technology, **2005**. 200(5/6): p. 1259-1263.
55. J.A. Haynes, B.A. Pint, Y. Zhang, and I.G. Wright, *Comparison of the oxidation behavior of β and γ-γ'NiPtAl coatings*, Surface & Coatings Technology, **2009**. 204(6-7): p. 816-819.
56. W.J. Quadakkers, *Growth mechanisms of oxide scales on ODS alloys in the temperature range 1000–1100°C*, Materials and Corrosion, **1990**. 41(12): p. 659-668.
57. K.P.R. Reddy, J.L. Smialek, and A.R. Cooper, *^{18}O Tracer Studies of $A1_20_3$ Scale Formation on NiCrAI Alloys*, Oxidation of metals, **1982**. 17(5/6): p. 429-449.
58. W.J. Quadakkers, D. Naumenko, E. Wessel, V. Kochubey, and L. Singheiser, *Growth Rates of Alumina Scales on Fe–Cr–Al Alloys*, Oxidation of Metals, **2004**. 61(1/2): p. 17-37.
59. P.Berthod, *Kinetics of High Temperature Oxidation and Chromia Volatilization for a Binary Ni–Cr Alloy*, Oxidation of metals, **2005**. 64(3/4): p. 235-252.
60. S. Hayashi and B. Gleeson, *Early-Stage Oxidation Behavior of Pt-Modified gamma prime-Ni3Al-Based Alloys with and without Hf Addition*, Oxidation of metals, **2009**. 71: p. 5-19.
61. H.J.Grabke, *Oxidation of NiAl and FeAl*, Intermetallics, **1999**. 7(10): p. 1153-1158.
62. R. Anton, *Untersuchungen zu den Versagensmechanismen von Wärmedämmschicht-Systemen im Temperaturbereich von 900°C bis 1050°C bei zyklischer Temperaturbelastung (Ph.D thesis)*. RWTH-Aachen, **2003**.
63. B. Tryon, T.M. Pollock, M.F.X. Gigliotti, and K. Hemker, *Thermal expansion behavior of ruthenium aluminides*, Scripta Materialia, **2004**. 50: p. 845-848.
64. M.A. Helminiak, N.M. Yanara, F.S. Pettit, T.A. Taylor, and G.H. Meier, *The behavior of high-purity, low-density air plasma sprayed thermal barrier coatings*, Surface & Coatings Technology, **2009**. 204(6-7): p. 793-796.
65. B.A. Pint, *Optimization of Reactive-Element Additions to Improve Oxidation Performance of Alumina-Forming Alloys*, Journal of the American Ceramic Society, **2003**. 86(4): p. 686-695.
66. W.J.Quadakkers, K.Schmidt, H.Grübmeier, and E.Wallura, *Composition,structure and protective properties of alumina scales on iron-based oxide dispersion strengthened alloys*, Materials at High Temperatures, **1992**. 10(1): p. 23-32.
67. M. Subanovic, *Einfluss der Bondcoatzusammensetzung und Herstellungsparameter auf die Lebensdauer von Wärmedämmschichten bei zyklischer Temperaturbelastung*, in *Fakultät für Maschinenwesen (Ph.D thesis)*. RWTH-Aachen, **2009**.
68. B. Gudmundsson and B.E. Jacobson, *Yttrium oxides in vacuum-plasma-sprayed CoNiCrAlY coatings*, Thin Solid Films, **1989**. 173(1): p. 99-107.
69. W. Braue, K. Fritscher, U. Schulz, C. Leyens, and R. Wirth, *Nucleation and Growth of Oxide Constituents on NiCoCrAlY Bond Coats During the Different Stages of EB-PVD TBC Deposition and Upon Thermal Loading*, Materials Science Forum, **2004**. 461-464: p. 899-906.
70. T.J. Nijdama and W.G. Sloof, *Effect of reactive element oxide inclusions on the growth kinetics of protective oxide scales*, Acta Materialia, **2007**. 55(17): p. 5980-5987.
71. R. Cueff, H. Buscail, E. Caudron, C. Issartel, and F. Riffard, *Influence of Yttrium-Alloying Addition on the Oxidation of Alumina Formers at 1173 K*, Oxidation of Metals, **2002**. 58(5/6): p. 439-455.

72. B.A.Pint, *Experimental observations in support of the dynamic-segregation theory to explain the reactive-element effect*, Oxidation of metals, **1996**. 45(1-2): p. 1-37.
73. W.J. Quadakkers, Holzbrecher, K.G. Briefs, and H. Beske, *Differences in growth mechanisms of oxide scales formed on ODS and conventional wrought alloys*, Oxidation of metals, **1989**. 32(1-2): p. 67-88.
74. W.J.Quadakkers, *Growth mechanisms of oxide scales on ODS alloys in the temperature range 1000–1100°C*, Materials and Corrosion, **1990**. 41(12): p. 659-668.
75. P.Y. Hou, *Segregation Phenomena at Thermally Grown Al_2O_3/Alloy Interfaces*, Annu. Rev. Mater. Res., **2008**. 38: p. 275-298.
76. B.A. Pint, I.G. Wright, W.Y. Lee, Y. Zhang, K. Prüßner, and K.B. Alexander, *Substrate and bond coat compositions: factors affecting alumina scale adhesion*, Materials Science and Engineering A, **1998**. 245: p. 201-211.
77. L. Rivoaland, V. Maurice, P. Josso, M.-P. Bacos, and P. Marcus, *The Effect of Sulfur Segregation on the Adherence of the Thermally-Grown Oxide on NiAl—II: The Oxidation Behavior at 900°C of Standard, Desulfurized or Sulfur-Doped NiAl(001) Single-Crystals*, Oxidation of metals, **2003**. 60(1-2): p. 159-178.
78. V.K.Tolpygo, *The Morphology of Thermally Grown α-Al_2O_3 Scales on Fe-Cr-Al Alloys*, Oxidation of metals, **1999**. 51(5/6): p. 449-477.
79. J.L. Smialek, *Oxide morphology and spalling model for NiAl*, Oxidation of metals, **1978**. 9(3): p. 309-320.
80. P.Y. Hou, T. Izumi, and B. Gleeson, *Sulfur Segregation at Al_2O_3/γ-Ni + γ'-Ni_3Al Interfaces: Effects of Pt, Cr and Hf Additions*, Oxidation of metals, **2009**. 752: p. 109-124.
81. P.Y.Hou and V.K.Tolpygo, *Examination of the platinum effect on the oxidation behavior of nickel-aluminide coatings*, Surface & Coatings Technology, **2007**. 202: p. 623-627.
82. H. Svensson, M. Christensen, P. Knutsson, G. Wahnström, and K. Stiller, *Influence of Pt on the metal-oxide interface during high temperature oxidation of NiAl bulk materials*, Corrosion Science, **2009**. 51(3): p. 539-546.
83. F.Qin, J.W.Anderegg, and C.J.Jenks, *The effect of Pt on Ni_3Al surface oxidation at low-pressures*, Surface Science, **2007**(601): p. 146-154.
84. H.M. Tawancy, A. UI-Hamid, N.M. Abbas, and M.O. Aboelfotoh, *Effect of platinum on the oxide-to-metal adhesion in thermal barrier coating systems*, Journal of Materials Science, **2008**. 43: p. 2978–2989.
85. M.Chieux, R.Molins, L.Rémy, C.Duhamel, M.Sennour, and Y.Cadoret, *Effect of material and environmental parameters on the microstructure evolution and oxidation behavior of a Ni-based superalloy coated with a Pt-modified Ni-aluminide*, Materials Science Forum, **2008**. 595-598: p. 33-40.
86. W.J. Quadakkers, V. Shemet, D. Sebold, R. Anton, E. Wessel, and L. Singheiser, *Oxidation characteristics of a platinized MCrAlY bond coat for TBC systems during cyclic oxidation at 1000 8C*, Surface & Coatings Technology, **2005**. 199: p. 77-82.
87. D.R.Carke and C.G.Levi, *Materials design for the next generation thermal barrier coatings*, Annu. Rev. Mater. Res., **2003**. 33: p. 383-417.
88. R.G. Wellman and J.R. Nicholls, *A mechanism for the erosion of EB PVD TBCS*, Materials Science Forum, **2001**. 369-372: p. 531-538.
89. H.E. Evans, *Stress effects in high temperature oxidationi of metals*, International Materials Reviews, **1995**. 40(1): p. 1-40.
90. J.A. Nychka and D.R. Clarke, *Damage quantification in TBCs by photo-stimulated luminescence spectroscopy*, Surface and Coatings Technology, **2001**. 146-147: p. 110-116.
91. D.R. Mumm and A.G. Evans, *On the role of imperfections in the failure of a thermal barrier coating made by electron beam deposition*, Acta Materialia, **2000**. 48(8): p. 1815-1827.
92. N.M. Yanar, *The failure of thermal barrier coatings at elevated temperatures (Ph.D thesis)*. University of Pittsburgh, **2004**.
93. A.G. Evans, D.R. Mumm, J.W. Hutchinson, G.H. Meier, and F.S. Pettit, *Mechanisms controlling the durability of thermal barrier coatings*, Progress in materials science, **2001**. 46(5): p. 505-553.
94. V.K. Tolpygo and D.R. Clarke, *Surface rumpling of a (Ni,Pt)Al bond coat induced by cyclic oxidation*, Acta Materialia, **2000**. 48: p. 3283-3293.

95. M. Reid, M.J. Pomeroy, and J.S. Robinson, *Microstructural Transformations in Platinum Aluminide Coated CMSX-4 Superalloy*, Materials Science Forum, **2004**. 461-464: p. 343-350.
96. M.W. Chen, T. Ottb, T.C. Hufnagel, P.K. Wright, and K.J. Hemker, *Microstructural evolution of platinum modified nickel aluminide bond coat during thermal cycling*, Surface & Coatings Technology, **2003**. 163-164: p. 25-30.
97. Y. Zhang, J.A. Haynes, B.A. Pint, I.G. Wright, and W.Y. Lee, *Martensitic transformation in CVD NiAl and (Ni,Pt)Al bond coatings*, Surface & Coatings Technology, **2003**. 163-164: p. 19-24.
98. J. Toscano, D. Naumenko, A. Gil, L. Singheiser, and W.J. Quadakkers, *Parameters affecting TGO growth rate and the lifetime of TBC systems with MCrAlY-bondcoats*, Materials and Corrosion, **2008**. 59(6): p. 501-507.
99. T. Nijdam, *Promoting alpha-Al_2O_3 growth upon high-temperature oxidation of NiCoCrAlY-alloys (PhD thesis)*. Technical University of Delft, **2005**.
100. H. Lau, C. Leyens, U. Schulz, and C. Friedrich, *Influence of bondcoat pre-treatment and surface topology on the lifetime of EB-PVD TBCs*, Surface and Coatings Technology, **2003**. 165: p. 217-223.
101. N.M. Yanar, F.S. Pettit, and G.H. Meier, *Failure characteristics during cyclic oxidation of yttria stabilized zirconia thermal barrier coatings deposited via electron beam physical vapor deposition on platinum aluminide and on NiCoCrAlY bond coats with processing modifications for improved performances*, Metallurgical and Materials Transactions A, **2006**. 37(5): p. 1563-1580.
102. U. Schulz, M. Menzebach, C. Leyens, and Y.Q. Yang, *Influence of substrate material on oxidation behavior and cyclic lifetime of EB-PVD TBC systems*, Surface & Coatings Technology, **2001**. 146-147: p. 117-123.
103. B.A. Pint, P.F. Tortorelli, and I.G. Wright, *Effect of Cycle Frequency on High-Temperature Oxidation Behavior of Alumina-Forming Alloys*,Oxidation of metals, **2002**. 58(1/2): p. 73-101.
104. V.K. Tolpygo and D.R. Clarke, *Temperature and cycle-time dependence of rumpling in platinum-modified diffusion aluminide coatings*, Scripta Materialia, **2007**. 57: p. 563-566.
105. N.M. Yanar, G.M. Kim, F.S. Pettit, and G.H. Meier. *Degradation of EBPVD YSZ Thermal Barrier Coatings on Platinum Aluminide and NiCoCrAlY Bond Coats During High Temperature Exposure*. in *Proc. Of the Turbine Forum: Advanced Coatings for High Temperatures. Forum of Technology*. Dorsten, Germany, **2002**.
106. K. Yasuda, Y. Goto, and H. Takeda, *Influence of Tetragonality on Tetragonal-to-Monoclinic Phase Transformation during Hydrothermal Aging in Plasma-Sprayed Yttria-Stabilized Zirconia Coatings*, Journal of the American Ceramic Society, **2001**. 84(5): p. 1037-1042.
107. B.A. Pint, H. J.A, Y. Zhang, K.L. More, and I.G. Wright, *The effect of water vapor on the oxiation behavior of Ni-Pt-Al coatings and alloys*, Surface & Coatings Technology, **2006**. 201: p. 3852-3856.
108. G.J. Tatlock, H. Al-Badairy, R. Bachorczyk-Nagy, and R. Fordham, *The effect of gas composition and contaminants on the lifetime of surface-treated FeCrAlRE alloys*, Materials and Corrosion, **2005**. 56(12): p. 867-873.
109. R. Janakiraman, G.H. Meier, and F.S. Pettit, *The effect of water vapor on the oxidation of alloys that develop alumina scales for protection*, Metallurgical and materials transactions A, **1999**. 30(11): p. 2905-2913.
110. J.L. Smialek, *Moisture-induced delayed spallation and interfacial hydrogen embrittlement of alumina scales*,Journal of the Minerals, Metals and Materials Society **2006**. 58(1): p. 29-35.
111. H.-E. Zschau, M. Dietricha, D. Renusch, M. Schütze, J. Meijer, and H.-W. Becker, *Detection of hydrogen in hidden and spalled layers of turbine blade coatings*, Nuclear Instruments and Methods in Physics Research Section B, **2006**. 249(1-2): p. 381-383.
112. M.C. Maris-Sida, G.H. Meier, and F.S. Pettit, *Some water vapor effects during the oxidation of alloys that are α-Al2O3 formers*, Metallurgical and materials transactions A, **2003**. 34(11): p. 2609-2619.
113. W.J. Quadakkers, A.K. Tyagi, D. Clemens, R. Anton, and L. Singheiser. *The significance of bond-coat oxidation for the life of TBC coatings*. in *Elevated temperature coatings: science and technology 3, ICMCTF-conference*. Warrendale PA: TMS, **1999**.

114. A. Rabiei and A.G. Evans, *Failure mechanisms associated with the thermally grown oxide in plasma-sprayed thermal barrier coatings*, Acta Materialia, **2000**. 48(15): p. 3963-3976.
115. J.T. DeMasi-Marcin, K.D. Sheffler, and S. Bose, *Mechanisms of Degradation and Failure in a Plasma-Deposited Thermal Barrier Coating*, Journal of Engineering for Gas Turbines and Power, **1990**. 112(4): p. 521-526.
116. R. Vaßen, G. Kerkhoff, and D. Sto¨ver, *Development of a micromechanical life prediction model for plasma sprayed thermal barrier coatings*, Materials Science and Engineering A, **2001**. 303: p. 100-109.
117. D.Renusch, H.Echsler, and M.Schütze, *Progress in life time modeling of APS-TBC Part one: residual, thermal and growth stresses including the role of thermal fatigue*, Materials at High Temperatures, **2004**. 21(2): p. 65-76.
118. H.E. Evans and M.P. Taylor, *Diffusion Cells and Chemical Failure of MCrAlY Bond Coats in Thermal-Barrier Coating Systems*, Oxidation of metals, **2001**. 55(1-2): p. 17-34.
119. http://www.c-mgroup.com/vacuum_melt_index.htm.
120. Y.Tamarin, *Protective Coatings for Turbine Blades*, ASM International,Ohio, **2002**.
121. A.Secluk and A.Atkinson, *Analysis of Cr^{3+} luminescence spectra from thermally grown oxide in thermal barrier coatings*, Materials Science and Engineering A, **2002**. 335: p. 147-156.
122. H.E. Evans and M.P. Taylor, *Creep relaxation and the spallation of oxide layers*, Surface & Coatings Technology, **1997**. 94-95: p. 27-33.
123. T. Xu, S. Faulhaber, C. Mercer, M. Maloney, and A. Evans, *Observations and analyses of failure mechanisms in thermal barrier systems with two phase bond coats based on NiCoCrAlY*, Acta Materialia, **2004**. 52(6): p. 1439-1450.
124. H.X. Zhu, N.A. Fleck, A.C.F. Cocks, and A.G. Evans, *Numerical simulations of crack formation from pegs in thermal barrier systems with NiCoCrAlY bond coats*, Materials Science and Engineering A, **2005**. 404(1-2): p. 26-32.
125. H.E. Evans and R.C. Lobb, *Conditions for the initiation of oxide-scale cracking and spallation*, Corrosion Science, **1984**. 24(3): p. 209-222.
126. E. Wessel, V. Kochubey, D. Naumenko, L. Niewolak, L. Singheiser, and W.J. Quadakkers, *Effect of Zr addition on the microstructure of the alumina scales on FeCrAlY-alloys*, Scripta Materialia, **2004**. 51(10): p. 987-992.
127. D.P. Whittle and P. J. Stringer, *Improvements in High Temperature Oxidation Resistance by Additions of Reactive Elements or Oxide Dispersions*, Phil. Trans. R. Soc. Lond. A, **1980**. 295(1413): p. 309-329.
128. R. Pendse and J. Stringer, *The influence of alloy microstructure on the oxide peg morphologies in a Co-10%Cr-11%Al alloy with and without reactive element additions*, Oxidation of metals, **1985**. 23(1-2): p. 1-16.
129. B.A. Pint and K.B. Alexander, *Grain Boundary Segregation of Cation Dopants in α-Al_2O_3 Scales*, J. Electrochem. Soc., **1998**. 145(6): p. 1819-1829.
130. A.G.Evans, M.Y.He, and J.W.Hutchinson, *Mechanics-based scaling laws for the durability of thermal barrier coatings*, Progress in materials science, **2001**. 46: p. 249-271.
131. S.N. Basu and J.W. Halloran, *Tracer isotope distribution in growing oxide scales*, Oxidation of metals, **1987**. 27(3-4): p. 143-155.
132. D.J. Young, D. Naumenko, L. Niewolak, E. Wessel, L. Singheiser, and W.J. Quadakkers, *Oxidation kinetics of Y-doped FeCrAl-alloys in low and high pO_2 gases*, Materials and Corrosion, **2010**. 61(10): p. 838-844.
133. M. Karadge, X. Zhao, M. Preuss, and P. Xiao, *Microtexture of the thermally grown alumina in commerical thermal barrier coatings*, Scripta Materialia, **2006**. 54: p. 639-644.
134. A. Atkinson, *Transport processes during the growth of oxide films at elevated temperature*, Reviews of Modern Physics **1985**. 57(2): p. 437-470.
135. E.A.G. Shillington and D.R. Clarke, *Spalling failure of a thermal barrier coating associated with aluminum depletion in the bond-coat*, Acta Materialia, **1999**. 47(4): p. 1297-1305.
136. P. Kofstad, *High temperature corrosion*, Elsevier, London, **1988**.
137. F.J. Keneshea and D.L. Douglass, *The diffusion of oxygen in Zirconia as a function of oxygen pressure*, Oxidation of metals, **1971**. 3(1): p. 1-14.

138. D.J. Young, D. Naumenko, E. Wessel, L. Singheiser, and W.J. Quadakkers, *Effect of Zr Additions on the Oxidation Kinetics of FeCrAlY Alloys in Low and High pO_2 Gases*, Metallurgical and Materials Transactions A, **2011**. 42(5): p. 1173-1183.
139. J. Klöwer, *Factors affecting the oxidation behaviour of thin Fe-Cr-Al foils Part II: The effect of alloying elements: Overdoping*, Materials and Corrosion, **2000**. 51(5): p. 373-385.
140. O. Trunova, T. Beck, R. Herzog, R.W. Steinbrech, and L. Singheiser, *Damage mechanisms and lifetime behavior of plasma sprayed thermal barrier coating systems for gas turbines—Part I: Experiments*, Surface & Coatings Technology, **2008**. 202(20): p. 5027-5032.
141. I. Keller and D. Naumenko, *unpublished research*.
142. K. Yasuda, M. Itoh, S. Arai, T. Suzuki, and M. Nakahashi, *Phase transformation of yttria-stabilized zirconia plasma-sprayed coatings in a humid atmosphere*, Journal of Materials Science, **1997**. 32: p. 6291-6297.
143. W.J. Plumbridge, *Review: Fatigue-crack propagation in metallic and polymeric materials*, Journal of Materials science, **1972**. 7(8): p. 939-962.
144. J.L. Simalek, J.A. Nesbitt, C.A. Barrett, and C.E. Lowell, *Cyclic oxidaiton testing and modelling: a NASA lewis perspective*, in *Proceedings of an EFC workshop*, M. Schütze and W.J. Quadakkers, Editors. IOM Communications Ltd: Frankfurt am Main. **1999**, p. 148-168.
145. V.K. Tolpygo and D.R. Clarke, *Spalling failure of a-alumina films grown by oxidation: I. Dependence on cooling rate and metal thickness*, Materials Science and Engineering A, **2000**. 278: p. 142-150.
146. O. Trunova, P. Bednarz, R. Herzong, T. Beck, and L. Singheiser, *Microstructural and acoustic damage analysis and finite element stress simulation of air plasma-sprayed thermal barrier coatings under thermal cycling*, International Journal of Materials Research, **2008**(10): p. 1129-1135.
147. B.M. Warnes and D.C. Punola, *Clean diffusion coatings by chemical vapor depostion*, Surface and Coatings Technology, **1997**. 94/95: p. 1-6.
148. S. Hayashi, S.I. Ford, D.J. Young, D.J. Sordelet, M.F. Besser, and B. Gleeson, *a-NiPt(Al) and phase equilibria in the Ni–Al–Pt system at 1150°C*, Acta Materialia, **2005**. 53: p. 3319-3328.
149. B. Gleeson, W. Wang, S. Hayashi, and D. Sordelet, *Effects of Platinum on the Interdiffusion and Oxidation Behavior of Ni-Al-Based Alloys*, Materials Science Forum, **2004**. 461-464: p. 213-222.
150. K.A. Unocic and B.A. Pint, *Characterization of the alumina scale formed on a commercial MCrAlYHfSi coating*, Surface & Coatings Technology, **2010**. 205(5): p. 1178-1182.
151. V.K. Tolpygo and D.R. Clarke, *Microstructural study of the theta-alpha transformation in alumia scales formed on nickel-aluminides*, Materials at High Temperatures, **2000**. 17(1): p. 59-70.
152. H. Hattendorf, R. Hojda, D. Naumenko, and A. Kolb-Telieps, *A new austenitic alumina forming alloy: an aluminium-coated FeNi32Cr20*, Materials and Corrosion, **2008**. 59(6): p. 449-454.
153. V.K. Tolpygo, K.S. Murphy, and D.R. Carke, *Effect of Hf, Y and C in the underlying superalloy on the rumpling of diffusion aluminide coatings*, Acta Materialia, **2008**. 56(3): p. 489-499.
154. D. Naumenko, V. Kochubey, L. Niewolak, A. Dymiati, J. Mayer, L. Singheiser, and W.J. Quadakkers, *Modification of alumina scale formation on FeCrAlY alloys by minor additions of group IVa elements*, Journal of materials science, **2008**. 43: p. 4550-4560.
155. V.K. Tolpygo, D.R. Clarke, and K.S. Murphy, *Oxidation-induced failure of EB-PVD thermal barrier coatings*, Surface & Coatings Technology, **2001**. 146-147: p. 124-131.
156. J.C. Zhao, *A combinatorial approach for structural materials*, Advanced engineering materials, **2001**. 3: p. 143-147.
157. M.Y. He, A.G. Evans, and J.W. Hutchinson, *The ratcheting of compressed thermally grown thin films on ductile substrates*, Acta materialia, **2000**. 48: p. 2593-2601.
158. D.R. Mumm, A.G. Evans, and I.T. Spitsberg, *Characterization of a cyclic displacement instability for a thermally grown oxide in a thermal barrier system*, Acta Materialia, **2001**. 49(12): p. 2329-2340.
159. V.K. Tolpygo and D.R. Clarke, *Rumpling induced by thermal cycling of an overlay coating:the effect of coating thickness*, Acta Materialia, **2004**. 52: p. 615-621.

160. J.Doychak, J.L.Smialek, and T.E.Mitchell, *Transient oxidation of single-crystal beta-NiAl*, Metallurgical Transactions A, **1989**. 20A: p. 499-518.
161. N. Vialas and D. Monceau, *Substrate Effect on the High Temperature Oxidation Behavior of a Pt-modified Aluminide Coating. Part II:Long-term Cyclic-oxidation Tests at 1050°C*, Oxidation of metals, **2007**. 68: p. 223-242.
162. J. Angenete, K. Stiller, and V. Langer, *Oxidation of Simple and Pt-Modified Aluminide Diffusion Coatings on Ni-Base Superalloys—I. Oxide Scale Microstructure*, Oxidation of metals, **2003**. 60(1/2): p. 47-82.
163. J.D. Kuenzly and D.L. Douglass, *The oxidation mechanism of Ni_3Al containing yttrium*, Oxidation of metals, **1974**. 8(3): p. 139-178.
164. J. Angenete and K. Stiller, *Oxidation of Simple and Pt-Modified Aluminide Diffusion Coatings on Ni-Base Superalloys—II. Oxide Scale Failure*, Oxidation of metals, **2003**. 60(1/2): p. 83-100.
165. G.M. Kim, N.M. Yanar, E.N. Hewitt, F.S. Pettit, and G.H. Meier, *The effect of the type of thermal exposure on the durability of thermal barrier coatings*, Scripta Materialia, **2002**. 46(7): p. 489-495.
166. H. Svensson, P. Knutsson, and K. Stiller, *Formation and Healing of Voids at the Metal–Oxide Interface in NiAl Alloys*, Oxidation of metals, **2009**. 71: p. 143-156.
167. P.Y. Hou, *Segregation behavior at TGO/bondcoat interfaces*, Journal of materials Science, **2009**. 44: p. 1711-1725.

Acknowledgements

Many thanks to Dr. D. Naumenko and Prof. W.J. Quadakkers. I greatly appreciate theirs guidance, discussions, and continued support of this work. I feel very lucky to work together with them. I also very much appreciate their patience and understanding during this time.

I wish to thank Prof. L. Singhersier, for his great leadership to form excellent research atmosphere within the IEK-2, FZJ and support of this work as well as for co-advising my thesis.

I would like to express my gratitude to Prof. J. M. Schneider, for the valuable referee comments on my thesis as my supervisor at the RWTH-Aachen University.

I am grateful to my colleagues in the Institute for Energy and Climate Research (IEK) of the Forschungszentrum Jülich GmbH, for materials manufacturing (R. Vaßen and K.H. Rauwald), carrying out the oxidation experiments (H. Cosler, R. Mahnke and A. Kick), SEM analysis (E. Wessel), SNMS-depth profiling (L. Niewolak), Raman (P. Huczkowski), metallographic investigations (V. Gutzeit, J. Bartsch and M. Felden).

I also express my thanks to Dr. W. Braue in the German Aerospace Center (DLR), Materials Research Institute, for the TEM analysis and valuable discussions, as well as to Dr. E. Affeldt in the MTU Aero Engines GmbH, for the supply of TBC specimens with NiPtAl bondcoats.

To all the colleagues in high temperature corrosion group, Joanna Zurek; Vladimir Shemet; Leszek Niewolak; Pawel Huczkowski; Thomas Hüttel; Tomasz Olszewski; Anton Chyrkin; Sayee Ganesh Gopalakrishnan; Cristina Asensio Jimenez; Laura Garcia Fresnillo; Aleksandra Jalowicka,; Isabelle Keller; Wojciech Nowak, for the great time and their great help during my staying about 5 years in Juelich.

Funding by German Research Foundation (DFG; GrantNo. NA 615-2) is gratefully acknowledged.

To my family, especially my wife and daughter as well as friends for their constant support and help during this time.

1. **Einsatz von multispektralen Satellitenbilddaten in der Wasserhaushalts- und Stoffstrommodellierung – dargestellt am Beispiel des Rureinzugsgebietes**
   von C. Montzka (2008), XX, 238 Seiten
   ISBN: 978-3-89336-508-1

2. **Ozone Production in the Atmosphere Simulation Chamber SAPHIR**
   by C. A. Richter (2008), XIV, 147 pages
   ISBN: 978-3-89336-513-5

3. **Entwicklung neuer Schutz- und Kontaktierungsschichten für Hochtemperatur-Brennstoffzellen**
   von T. Kiefer (2008), 138 Seiten
   ISBN: 978-3-89336-514-2

4. **Optimierung der Reflektivität keramischer Wärmedämmschichten aus Yttrium-teilstabilisiertem Zirkoniumdioxid für den Einsatz auf metallischen Komponenten in Gasturbinen**
   von A. Stuke (2008), X, 201 Seiten
   ISBN: 978-3-89336-515-9

5. **Lichtstreuende Oberflächen, Schichten und Schichtsysteme zur Verbesserung der Lichteinkopplung in Silizium-Dünnschichtsolarzellen**
   von M. Berginski (2008), XV, 171 Seiten
   ISBN: 978-3-89336-516-6

6. **Politikszenarien für den Klimaschutz IV – Szenarien bis 2030**
   hrsg.von P. Markewitz, F. Chr. Matthes (2008), 376 Seiten
   ISBN 978-3-89336-518-0

7. **Untersuchungen zum Verschmutzungsverhalten rheinischer Braunkohlen in Kohledampferzeugern**
   von A. Schlüter (2008), 164 Seiten
   ISBN 978-3-89336-524-1

8. **Inorganic Microporous Membranes for Gas Separation in Fossil Fuel Power Plants**
   by G. van der Donk (2008), VI, 120 pages
   ISBN: 978-3-89336-525-8

9. **Sinterung von Zirkoniumdioxid-Elektrolyten im Mehrlagenverbund der oxidkeramischen Brennstoffzelle (SOFC)**
   von R. Mücke (2008), VI, 165 Seiten
   ISBN: 978-3-89336-529-6

10. **Safety Considerations on Liquid Hydrogen**
    by K. Verfondern (2008), VIII, 167 pages
    ISBN: 978-3-89336-530-2

11. **Kerosinreformierung für Luftfahrtanwendungen**
von R. C. Samsun (2008), VII, 218 Seiten
ISBN: 978-3-89336-531-9

12. **Der 4. Deutsche Wasserstoff Congress 2008 – Tagungsband**
hrsg. von D. Stolten, B. Emonts, Th. Grube (2008), 269 Seiten
ISBN: 978-3-89336-533-3

13. **Organic matter in Late Devonian sediments as an indicator for environmental changes**
by M. Kloppisch (2008), XII, 188 pages
ISBN: 978-3-89336-534-0

14. **Entschwefelung von Mitteldestillaten für die Anwendung in mobilen Brennstoffzellen-Systemen**
von J. Latz (2008), XII, 215 Seiten
ISBN: 978-3-89336-535-7

15. **RED-IMPACT**
Impact of Partitioning, Transmutation and Waste Reduction Technologies on the Final Nuclear Waste Disposal
SYNTHESIS REPORT
ed. by W. von Lensa, R. Nabbi, M. Rossbach (2008), 178 pages
ISBN 978-3-89336-538-8

16. **Ferritic Steel Interconnectors and their Interactions with Ni Base Anodes in Solid Oxide Fuel Cells (SOFC)**
by J. H. Froitzheim (2008), 169 pages
ISBN: 978-3-89336-540-1

17. **Integrated Modelling of Nutrients in Selected River Basins of Turkey**
Results of a bilateral German-Turkish Research Project
project coord. M. Karpuzcu, F. Wendland (2008), XVI, 183 pages
ISBN: 978-3-89336-541-8

18. **Isotopengeochemische Studien zur klimatischen Ausprägung der Jüngeren Dryas in terrestrischen Archiven Eurasiens**
von J. Parplies (2008), XI, 155 Seiten, Anh.
ISBN: 978-3-89336-542-5

19. **Untersuchungen zur Klimavariabilität auf dem Tibetischen Plateau - Ein Beitrag auf der Basis stabiler Kohlenstoff- und Sauerstoffisotope in Jahrringen von Bäumen waldgrenznaher Standorte**
von J. Griessinger (2008), XIII, 172 Seiten
ISBN: 978-3-89336-544-9

20. **Neutron-Irradiation + Helium Hardening & Embrittlement Modeling of 9%Cr-Steels in an Engineering Perspective (HELENA)**
by R. Chaouadi (2008), VIII, 139 pages
ISBN: 978-3-89336-545-6

21. **in Bearbeitung**

22. **Verbundvorhaben APAWAGS (AOEV und Wassergenerierung) – Teilprojekt: Brennstoffreformierung – Schlussbericht**
von R. Peters, R. C. Samsun, J. Pasel, Z. Porš, D. Stolten (2008), VI, 106 Seiten
ISBN: 978-3-89336-547-0

23. **FREEVAL**
Evaluation of a Fire Radiative Power Product derived from Meteosat 8/9 and Identification of Operational User Needs
Final Report
project coord. M. Schultz, M. Wooster (2008), 139 pages
ISBN: 978-3-89336-549-4

24. **Untersuchungen zum Alkaliverhalten unter Oxycoal-Bedingungen**
von C. Weber (2008), VII, 143, XII Seiten
ISBN: 978-3-89336-551-7

25. **Grundlegende Untersuchungen zur Freisetzung von Spurstoffen, Heißgaschemie, Korrosionsbeständigkeit keramischer Werkstoffe und Alkalirückhaltung in der Druckkohlenstaubfeuerung**
von M. Müller (2008), 207 Seiten
ISBN: 978-3-89336-552-4

26. **Analytik von ozoninduzierten phenolischen Sekundärmetaboliten in *Nicotiana tabacum* L. cv Bel W3 mittels LC-MS**
von I. Koch (2008), III, V, 153 Seiten
ISBN 978-3-89336-553-1

27. **IEF-3 Report 2009. Grundlagenforschung für die Anwendung**
(2009), ca. 230 Seiten
ISBN: 978-3-89336-554-8

28. **Influence of Composition and Processing in the Oxidation Behavior of MCrAlY-Coatings for TBC Applications**
by J. Toscano (2009), 168 pages
ISBN: 978-3-89336-556-2

29. **Modellgestützte Analyse signifikanter Phosphorbelastungen in hessischen Oberflächengewässern aus diffusen und punktuellen Quellen**
von B. Tetzlaff (2009), 149 Seiten
ISBN: 978-3-89336-557-9

30. **Nickelreaktivlot / Oxidkeramik – Fügungen als elektrisch isolierende Dichtungskonzepte für Hochtemperatur-Brennstoffzellen-Stacks**
von S. Zügner (2009), 136 Seiten
ISBN: 978-3-89336-558-6

31. **Langzeitbeobachtung der Dosisbelastung der Bevölkerung in radioaktiv kontaminierten Gebieten Weißrusslands – Korma-Studie**
von H. Dederichs, J. Pillath, B. Heuel-Fabianek, P. Hill, R. Lennartz (2009), Getr. Pag.
ISBN: 978-3-89336-532-3

32. **Herstellung von Hochtemperatur-Brennstoffzellen über physikalische Gasphasenabscheidung**
von N. Jordán Escalona (2009), 148 Seiten
ISBN: 978-3-89336-532-3

33. **Real-time Digital Control of Plasma Position and Shape on the TEXTOR Tokamak**
by M. Mitri (2009), IV, 128 pages
ISBN: 978-3-89336-567-8

34. **Freisetzung und Einbindung von Alkalimetallverbindungen in kohlebefeuerten Kombikraftwerken**
von M. Müller (2009), 155 Seiten
ISBN: 978-3-89336-568-5

35. **Kosten von Brennstoffzellensystemen auf Massenbasis in Abhängigkeit von der Absatzmenge**
von J. Werhahn (2009), 242 Seiten
ISBN: 978-3-89336-569-2

36. **Einfluss von Reoxidationszyklen auf die Betriebsfestigkeit von anodengestützten Festoxid-Brennstoffzellen**
von M. Ettler (2009), 138 Seiten
ISBN: 978-3-89336-570-8

37. **Großflächige Plasmaabscheidung von mikrokristallinem Silizium für mikromorphe Dünnschichtsolarmodule**
von T. Kilper (2009), XVII, 154 Seiten
ISBN: 978-3-89336-572-2

38. **Generalized detailed balance theory of solar cells**
by T. Kirchartz (2009), IV, 198 pages
ISBN: 978-3-89336-573-9

39. **The Influence of the Dynamic Ergodic Divertor on the Radial Electric Field at the Tokamak TEXTOR**
von J. W. Coenen (2009), xii, 122, XXVI pages
ISBN: 978-3-89336-574-6

40. **Sicherheitstechnik im Wandel Nuklearer Systeme**
von K. Nünighoff (2009), viii, 215 Seiten
ISBN: 978-3-89336-578-4

41. **Pulvermetallurgie hochporöser NiTi-Legierungen für Implanat- und Dämpfungsanwendungen**
von M. Köhl (2009), XVII, 199 Seiten
ISBN: 978-3-89336-580-7

42. **Einfluss der Bondcoatzusammensetzung und Herstellungsparameter auf die Lebensdauer von Wärmedämmschichten bei zyklischer Temperaturbelastung**
von M. Subanovic (2009), 188, VI Seiten
ISBN: 978-3-89336-582-1

43. **Oxygen Permeation and Thermo-Chemical Stability of Oxygen Permeation Membrane Materials for the Oxyfuel Process**
by A. J. Ellett (2009), 176 pages
ISBN: 978-3-89336-581-4

44. **Korrosion von polykristallinem Aluminiumoxid (PCA) durch Metalljodidschmelzen sowie deren Benetzungseigenschaften**
von S. C. Fischer (2009), 148 Seiten
ISBN: 978-3-89336-584-5

45. **IEF-3 Report 2009. Basic Research for Applications**
(2009), 217 Seiten
ISBN: 978-3-89336-585-2

46. **Verbundvorhaben ELBASYS (Elektrische Basissysteme in einem CFK-Rumpf) - Teilprojekt: Brennstoffzellenabgase zur Tankinertisierung - Schlussbericht**
von R. Peters, J. Latz, J. Pasel, R. C. Samsun, D. Stolten
(2009), xi, 202 Seiten
ISBN: 978-3-89336-587-6

47. **Aging of ^{14}C-labeled Atrazine Residues in Soil: Location, Characterization and Biological Accessibility**
by N. D. Jablonowski (2009), IX, 104 pages
ISBN: 978-3-89336-588-3

48. **Entwicklung eines energetischen Sanierungsmodells für den europäischen Wohngebäudesektor unter dem Aspekt der Erstellung von Szenarien für Energie- und CO_2 - Einsparpotenziale bis 2030**
von P. Hansen (2009), XXII, 281 Seiten
ISBN: 978-3-89336-590-6

49. **Reduktion der Chromfreisetzung aus metallischen Interkonnektoren für Hochtemperaturbrennstofzellen durch Schutzschichtsysteme**
von R. Trebbels (2009), iii, 135 Seiten
ISBN: 978-3-89336-591-3

50. **Bruchmechanische Untersuchung von Metall / Keramik-Verbundsystemen für die Anwendung in der Hochtemperaturbrennstoffzelle**
von B. Kuhn (2009), 118 Seiten
ISBN: 978-3-89336-592-0

51. **Wasserstoff-Emissionen und ihre Auswirkungen auf den arktischen Ozonverlust**
Risikoanalyse einer globalen Wasserstoffwirtschaft
von T. Feck (2009), 180 Seiten
ISBN: 978-3-89336-593-7

52. **Development of a new Online Method for Compound Specific Measurements of Organic Aerosols**
by T. Hohaus (2009), 156 pages
ISBN: 978-3-89336-596-8

53. **Entwicklung einer FPGA basierten Ansteuerungselektronik für Justageeinheiten im Michelson Interferometer**
von H. Nöldgen (2009), 121 Seiten
ISBN: 978-3-89336-599-9

54. **Observation – and model – based study of the extratropical UT/LS**
by A. Kunz (2010), xii, 120, xii pages
ISBN: 978-3-89336-603-3

55. **Herstellung polykristalliner Szintillatoren für die Positronen-Emissions-Tomographie (PET)**
von S. K. Karim (2010), VIII, 154 Seiten
ISBN: 978-3-89336-610-1

56. **Kombination eines Gebäudekondensators mit H2-Rekombinatorelementen in Leichwasserreaktoren**
von S. Kelm (2010), vii, 119 Seiten
ISBN: 978-3-89336-611-8

57. **Plant Leaf Motion Estimation Using A 5D Affine Optical Flow Model**
by T. Schuchert (2010), X, 143 pages
ISBN: 978-3-89336-613-2

58. **Tracer-tracer relations as a tool for research on polar ozone loss**
by R. Müller (2010), 116 pages
ISBN: 978-3-89336-614-9

59. **Sorption of polycyclic aromatic hydrocarbon (PAH) to Yangtze River sediments and their components**
by J. Zhang (2010), X, 109 pages
ISBN: 978-3-89336-616-3

60. **Weltweite Innovationen bei der Entwicklung von CCS-Technologien und Möglichkeiten der Nutzung und des Recyclings von CO_2**
Studie im Auftrag des BMWi
von W. Kuckshinrichs et al. (2010), X, 139 Seiten
ISBN: 978-3-89336-617-0

61. **Herstellung und Charakterisierung von sauerstoffionenleitenden Dünnschichtmembranstrukturen**
von M. Betz (2010), XII, 112 Seiten
ISBN: 978-3-89336-618-7

62. **Politikszenarien für den Klimaschutz V – auf dem Weg zum Strukturwandel, Treibhausgas-Emissionsszenarien bis zum Jahr 2030**
hrsg. von P. Hansen, F. Chr. Matthes (2010), 276 Seiten
ISBN: 978-3-89336-619-4

63. **Charakterisierung Biogener Sekundärer Organischer Aerosole mit Statistischen Methoden**
von C. Spindler (2010), iv, 163 Seiten
ISBN: 978-3-89336-622-4

64. **Stabile Algorithmen für die Magnetotomographie an Brennstoffzellen**
von M. Wannert (2010), ix, 119 Seiten
ISBN: 978-3-89336-623-1

65. **Sauerstofftransport und Degradationsverhalten von Hochtemperaturmembranen für CO2-freie Kraftwerke**
von D. Schlehuber (2010), VII, 139 Seiten
ISBN: 978-3-89336-630-9

66. **Entwicklung und Herstellung von foliengegossenen, anodengestützten Festoxidbrennstoffzellen**
von W. Schafbauer (2010), VI, 164 Seiten
ISBN: 978-3-89336-631-6

67. **Disposal strategy of proton irradiated mercury from high power spallation sources**
by S. Chiriki (2010), xiv, 124 pages
ISBN: 978-3-89336-632-3

68. **Oxides with polyatomic anions considered as new electrolyte materials for solid oxide fuel cells (SOFCs)**
by O. H. Bin Hassan (2010), vii, 121 pages
ISBN: 978-3-89336-633-0

69. **Von der Komponente zum Stack: Entwicklung und Auslegung von HT-PEFC-Stacks der 5 kW-Klasse**
von A. Bendzulla (2010), IX, 203 Seiten
ISBN: 978-3-89336-634-7

70. **Satellitengestützte Schwerewellenmessungen in der Atmosphäre und Perspektiven einer zukünftigen ESA Mission (PREMIER)**
von S. Höfer (2010), 81 Seiten
ISBN: 978-3-89336-637-8

71. **Untersuchungen der Verhältnisse stabiler Kohlenstoffisotope in atmosphärisch relevanten VOC in Simulations- und Feldexperimenten**
von H. Spahn (2010), IV, 210 Seiten
ISBN: 978-3-89336-638-5

72. **Entwicklung und Charakterisierung eines metallischen Substrats für nanostrukturierte keramische Gastrennmembranen**
von K. Brands (2010), vii, 137 Seiten
ISBN: 978-3-89336-640-8

73. **Hybridisierung und Regelung eines mobilen Direktmethanol-Brennstoffzellen-Systems**
von J. Chr. Wilhelm (2010), 220 Seiten
ISBN: 978-3-89336-642-2

74. **Charakterisierung perowskitischer Hochtemperaturmembranen zur Sauerstoffbereitstellung für fossil gefeuerte Kraftwerksprozesse**
von S.A. Möbius (2010) III, 208 Seiten
ISBN: 978-3-89336-643-9

75. **Characterization of natural porous media by NMR and MRI techniques: High and low magnetic field studies for estimation of hydraulic properties**
by L.-R. Stingaciu (2010), 96 pages
ISBN: 978-3-89336-645-3

76. **Hydrological Characterization of a Forest Soil Using Electrical Resistivity Tomography**
by Chr. Oberdörster (2010), XXI, 151 pages
ISBN: 978-3-89336-647-7

77. **Ableitung von atomarem Sauerstoff und Wasserstoff aus Satellitendaten und deren Abhängigkeit vom solaren Zyklus**
von C. Lehmann (2010), 127 Seiten
ISBN: 978-3-89336-649-1

78. **18th World Hydrogen Energy Conference 2010 – WHEC2010 Proceedings**
Speeches and Plenary Talks
ed. by D. Stolten, B. Emonts (2012)
ISBN: 978-3-89336-658-3

78-1. **18th World Hydrogen Energy Conference 2010 – WHEC2010 Proceedings**
Parallel Sessions Book 1:
Fuel Cell Basics / Fuel Infrastructures
ed. by D. Stolten, T. Grube (2010), ca. 460 pages
ISBN: 978-3-89336-651-4

78-2. **18th World Hydrogen Energy Conference 2010 – WHEC2010 Proceedings**
Parallel Sessions Book 2:
Hydrogen Production Technologies – Part 1
ed. by D. Stolten, T. Grube (2010), ca. 400 pages
ISBN: 978-3-89336-652-1

78-3. **18th World Hydrogen Energy Conference 2010 – WHEC2010 Proceedings**
Parallel Sessions Book 3:
Hydrogen Production Technologies – Part 2
ed. by D. Stolten, T. Grube (2010), ca. 640 pages
ISBN: 978-3-89336-653-8

78-4. **18th World Hydrogen Energy Conference 2010 – WHEC2010 Proceedings**
Parallel Sessions Book 4:
Storage Systems / Policy Perspectives, Initiatives and Cooperations
ed. by D. Stolten, T. Grube (2010), ca. 500 pages
ISBN: 978-3-89336-654-5

78-5. **18th World Hydrogen Energy Conference 2010 – WHEC2010 Proceedings**
Parallel Sessions Book 5:
Stategic Analysis / Safety Issues / Existing and Emerging Markets
ed. by D. Stolten, T. Grube (2010), ca. 530 pages
ISBN: 978-3-89336-655-2

78-6. **18th World Hydrogen Energy Conference 2010 – WHEC2010 Proceedings**
Parallel Sessions Book 6:
Stationary Applications / Transportation Applications
ed. by D. Stolten, T. Grube (2010), ca. 330 pages
ISBN: 978-3-89336-656-9

78 Set (complete book series)

18th World Hydrogen Energy Conference 2010 – WHEC2010 Proceedings
ed. by D. Stolten, T. Grube, B. Emonts (2010)
ISBN: 978-3-89336-657-6

79. **Ultrafast voltex core dynamics investigated by finite-element micromagnetic simulations**
by S. Gliga (2010), vi, 144 pages
ISBN: 978-3-89336-660-6

80. **Herstellung und Charakterisierung von keramik- und metallgestützten Membranschichten für die CO_2-Abtrennung in fossilen Kraftwerken**
von F. Hauler (2010), XVIII, 178 Seiten
ISBN: 978-3-89336-662-0

81. **Experiments and numerical studies on transport of sulfadiazine in soil columns**
by M. Unold (2010), xvi, 115 pages
ISBN: 978-3-89336-663-7

82. **Prompt-Gamma-Neutronen-Aktivierungs-Analyse zur zerstörungsfreien Charakterisierung radioaktiver Abfälle**
von J.P.H. Kettler (2010), iv, 205 Seiten
ISBN: 978-3-89336-665-1

83. **Transportparameter dünner geträgerter Kathodenschichten der oxidkeramischen Brennstoffzelle**
von C. Wedershoven (2010), vi, 137 Seiten
ISBN: 978-3-89336-666-8

84. **Charakterisierung der Quellverteilung von Feinstaub und Stickoxiden in ländlichem und städtischem Gebiet**
von S. Urban (2010), vi, 211 Seiten
ISBN: 978-3-89336-669-9

85. **Optics of Nanostructured Thin-Film Silicon Solar Cells**
by C. Haase (2010), 150 pages
ISBN: 978-3-89336-671-2

86. **Entwicklung einer Isolationsschicht für einen Leichtbau-SOFC-Stack**
von R. Berhane (2010), X, 162 Seiten
ISBN: 978-3-89336-672-9

87. **Hydrogen recycling and transport in the helical divertor of TEXTOR**
by M. Clever (2010), x, 172 pages
ISBN: 978-3-89336-673-6

88. **Räumlich differenzierte Quantifizierung der N- und P-Einträge in Grundwasser und Oberflächengewässer in Nordrhein-Westfalen unter besonderer Berücksichtigung diffuser landwirtschaftlicher Quellen**
von F. Wendland et. al. (2010), xii, 216 Seiten
ISBN: 978-3-89336-674-3

89. **Oxidationskinetik innovativer Kohlenstoffmaterialien hinsichtlich schwerer Lufteinbruchstörfälle in HTR´s und Graphitentsorgung oder Aufarbeitung**
von B. Schlögl (2010), ix, 117 Seiten
ISBN: 978-3-89336-676-7

90. **Chemische Heißgasreinigung bei Biomassenvergasungsprozessen**
von M. Stemmler (2010), xv, 196 Seiten
ISBN: 978-3-89336-678-1

91. **Untersuchung und Optimierung der Serienverschaltung von Silizium-Dünnschicht-Solarmodulen**
von S. Haas (2010), ii, 202 Seiten
ISBN: 978-3-89336-680-4

92. **Non-invasive monitoring of water and solute fluxes in a cropped soil**
by S. Garré (2010), xxiv, 133 pages
ISBN: 978-3-89336-681-1

93. **Improved hydrogen sorption kinetics in wet ball milled Mg hydrides**
by L. Meng (2011), II, 119 pages
ISBN: 978-3-89336-687-3

94. **Materials for Advanced Power Engineering 2010**
ed. by J. Lecomte-Beckers, Q. Contrepois, T. Beck and B. Kuhn
(2010), 1327 pages
ISBN: 978-3-89336-685-9

95. **2D cross-hole MMR – Survey design and sensitivity analysis for cross-hole applications of the magnetometric resistivity**
by D. Fielitz (2011), xvi, 123 pages
ISBN: 978-3-89336-689-7

96. **Untersuchungen zur Oberflächenspannung von Kohleschlacken unter Vergasungsbedingungen**
von T. Melchior (2011), xvii, 270 Seiten
ISBN: 978-3-89336-690-3

97. **Secondary Organic Aerosols: Chemical Aging, Hygroscopicity, and Cloud Droplet Activation**
by A. Buchholz (2011), xiv, 134 pages
ISBN: 978-3-89336-691-0

98. **Chrom-bezogene Degradation von Festoxid-Brennstoffzellen**
von A. Neumann (2011), xvi, 218 Seiten
ISBN: 978-3-89336-692-7

99. **Amorphous and microcrystalline silicon applied in very thin tandem solar cells**
by S. Schicho (2011), XII, 190 pages
ISBN: 978-3-89336-693-4

100. **Sol-gel and nano-suspension electrolyte layers for high performance solid oxide fuel cells**
by F. Han (2011), iv, 131 pages
ISBN: 978-3-89336-694-1

101. **Impact of different vertical transport representations on simulating processes in the tropical tropopause layer (TTL)**
by F. Plöger (2011), vi, 104 pages
ISBN: 978-3-89336-695-8

102. **Untersuchung optischer Nanostrukturen für die Photovoltaik mit Nahfeldmikroskopie**
von T. Beckers (2011), xiii, 128 Seiten
ISBN: 978-3-89336-696-5

103. **Impact of contamination on hydrogenated amorphous silicon thin films & solar cells**
by J. Wördenweber (2011), XIV, 138 pages
ISBN: 978-3-89336-697-2

104. **Water and Organic Nitrate Detection in an AMS: Laboratory Characterization and Application to Ambient Measurements**
by A. Mensah (2011), XI, 111 pages
ISBN: 978-3-89336-698-9

105. **Entwicklung eines neuen Konzepts zur Steuerung der thermischen Ausdehnung von glaskeramischen Verbundwerkstoffen mit angepasster Fließfähigkeit am Beispiel der Hochtemperatur-Brennstoffzelle**
von E. Wanko (2011), xi, 134 Seiten
ISBN: 978-3-89336-705-4

106. **Tomographic reconstruction of atmospheric volumes from infrared limb-imager measurements**
by J. Ungermann (2011), xiv, 153 pages
ISBN: 978-3-89336-708-5

107. **Synthese und Identifizierung von substituierten Mg-Al-Cl Doppelhydroxidverbindungen mit Schwerpunkt IR-Spektroskopie**
von B. Hansen (2011), XII, 121 Seiten
ISBN: 978-3-89336-709-2

108. **Analysis of spatial soil moisture dynamics using wireless sensor networks**
by U. Rosenbaum (2011), xxii, 120 pages
ISBN: 978-3-89336-710-8

109. **Optimierung von APS-ZrO2-Wärmedämmschichten durch Variation der Kriechfestigkeit und der Grenzflächenrauhigkeit**
von M. E. Schweda (2011), 168 Seiten
ISBN: 978-3-89336-711-5

110. **Sorption of a branched nonylphenol isomer and perfluorooctanoic acid on geosorbents and carbon nanotubes**
by C. Li (2011), X, 102 pages
ISBN: 978-3-89336-716-0

111. **Electron Transport in the Plasma Edge with Rotating Resonant Magnetic Perturbations at the TEXTOR Tokamak**
by H. Stoschus (2011), iv, 113 pages
ISBN: 978-3-89336-718-4

112. **Diffusion and Flow Investigations in Natural Porous Media by Nuclear Magnetic Resonance**
by N. Spindler (2011), viii, 144 pages
ISBN: 978-3-89336-719-1

113. **Entwicklung und Erprobung des Hygrometer for Atmospheric Investigations**
von T. Klostermann (2011), IV, 118 Seiten
ISBN: 978-3-89336-723-8

114. **Application of functional gene arrays for monitoring influences of plant/seasons on bacterial functions and community structures in constructed wetlands (Bitterfeld, Germany)**
by J. Ning (2011), xiv, 157 pages
ISBN: 978-3-89336-724-5

115. **Wasseraustrag aus den Kathodenkanälen von Direkt-Methanol-Brennstoffzellen**
von A. Schröder (2011), VII, 228 Seiten
ISBN: 978-3-89336-727-6

116. **CITYZEN Climate Impact Studies**
ed. by M. Schultz (2011), 45 pages
ISBN: 978-3-89336-729-0

117. **Software Tools zum interoperablen Austausch und zur Visualisierung von Geodatensätzen über das Internet**
von M. Schultz, M. Decker, S. Lührs (2011), iv, 156 Seiten
ISBN: 978-3-89336-730-6

118. **Optimierung eines Leichtbaudesigns für ein SOFC-Brennstoffzellenstack**
von T. Nguyen-Xuan (2011), III, 154 Seiten
ISBN: 978-3-89336-732-0

119. **Institute of Energy and Climate Research IEK-6:**
Nuclear Waste Management & Reactor Safety Report 2009/2010
Material Science for Nuclear Waste Management
ed. by M. Klinkenberg, S. Neumeier, D. Bosbach (2011), 242 pages
ISBN: 978-3-89336-735-1

120. **Fate of the Antibiotic Sulfadiazine in Yangtze River Sediments: Transformation, Sorption and Transport**
by N. Meng (2011), XII, 111 pages
ISBN: 978-3-89336-736-8

121. **Thermodynamische Eigenschaften gasförmiger und kondensierter Verbindungen für Hochtemperaturanwendungen**
von T. Markus (2011), II, 131 Seiten
ISBN: 978-3-89336-728-3

122. **Ein neues LIF-Instrument für flugzeug- und bodengebundene Messungen von OH- und HO_2-Radikalen in der Troposphäre**
von S. Broch (2011), IV, 160 Seiten
ISBN: 978-3-89336-742-9

123. **Processes in the Yangtze River System - Experiences and Perspectives**
Workshop-Proceedings
ed. by S. Küpper, G. Subklew, R.-D. Wilken (2011), 83 pages
ISBN: 978-3-89336-744-3

124. **Thermo-Mechanical Properties of Mixed Ion-Electron Conducting Membrane Materials**
by B. Huang (2011), 130 pages
ISBN: 978-3-89336-746-7

125. **Growth, Etching, and Stability of Sputtered ZnO:Al for Thin-Film Silicon Solar Cells**
by J. I. Owen (2011), xv, 192 pages
ISBN: 978-3-89336-749-8

126. **Entwicklung geträgerter $Ba_{0,5}Sr_{0,5}Co_{0,8}Fe_{0,2}O_{3-\delta}$ Sauerstoff-Permeationsmembranen**
von F. Schulze-Küppers (2011), ii, 119 Seiten
ISBN: 978-3-89336-752-8

127. **Development of the 2-Component-Injection Moulding for Metal Powders**
by A. P. Cysne Barbosa (2011), XIV, 150 pages
ISBN: 978-3-89336-753-5

128. **Performance of Tungsten-Based Materials and Components under ITER and DEMO Relevant Steady-State Thermal Loads**
by G. H. Ritz (2011), X, 128 pages
ISBN: 978-3-89336-755-9

129. **Experimentelle Bestimmung und numerische Simulation von Viskositäten in Schlackesystemen unter Vergasungsbedingungen**
von T. Nentwig (2011), 156 Seiten
ISBN: 978-3-89336-756-6

130. **Development of Thin Film Oxygen Transport Membranes on Metallic Supports**
by Y. Xing (2012), iv, 117 pages
ISBN: 978-3-89336-765-8

131. **Release of Inorganic Trace Elements from High-Temperature Gasification of Coal**
by M. Bläsing (2012), XVIII, 145 pages
ISBN: 978-3-89336-772-6

132. **Rauchgasseitige Korrosion von Nickelbasislegierungen für zukünftige 700°C-Dampfkraftwerke**
von F. Lüttschwager (2012), 145 Seiten
ISBN: 978-3-89336-773-3

133. **In-Situ Raman Spectroscopy: A Method to Study and Control the Growth of Microcrystalline Silicon for Thin-Film Solar Cells**
by S. Muthmann (2012), x, 134 pages
ISBN: 978-3-89336-774-0

134. **Remote sensing of sun-induced fluorescence for improved modeling of gross primary productivity in a heterogeneous agricultural area**
by A. Schickling (2012), xvi, 135 pages
ISBN: 978-3-89336-775-7

135. **Untersuchung der Ladungsträgerkonzentration und -beweglichkeit in mikrokristallinen Siliziumlegierungen mit Hall-Effekt undThermokraft**
von C. Sellmer (2012), 159 Seiten
ISBN: 978-3-89336-778-8

136. **Development of thin film inorganic membranes for oxygen separation**
by H. J. Moon (2012), XII, 118 pages
ISBN: 978-3-89336-781-8

137. **Influence of Material and Testing Parameters on the Lifetime of TBC Systems with MCrAlY and NiPtAl Bondcoats**
by P. Song (2012), V, 126 pages
ISBN: 978-3-89336-783-2

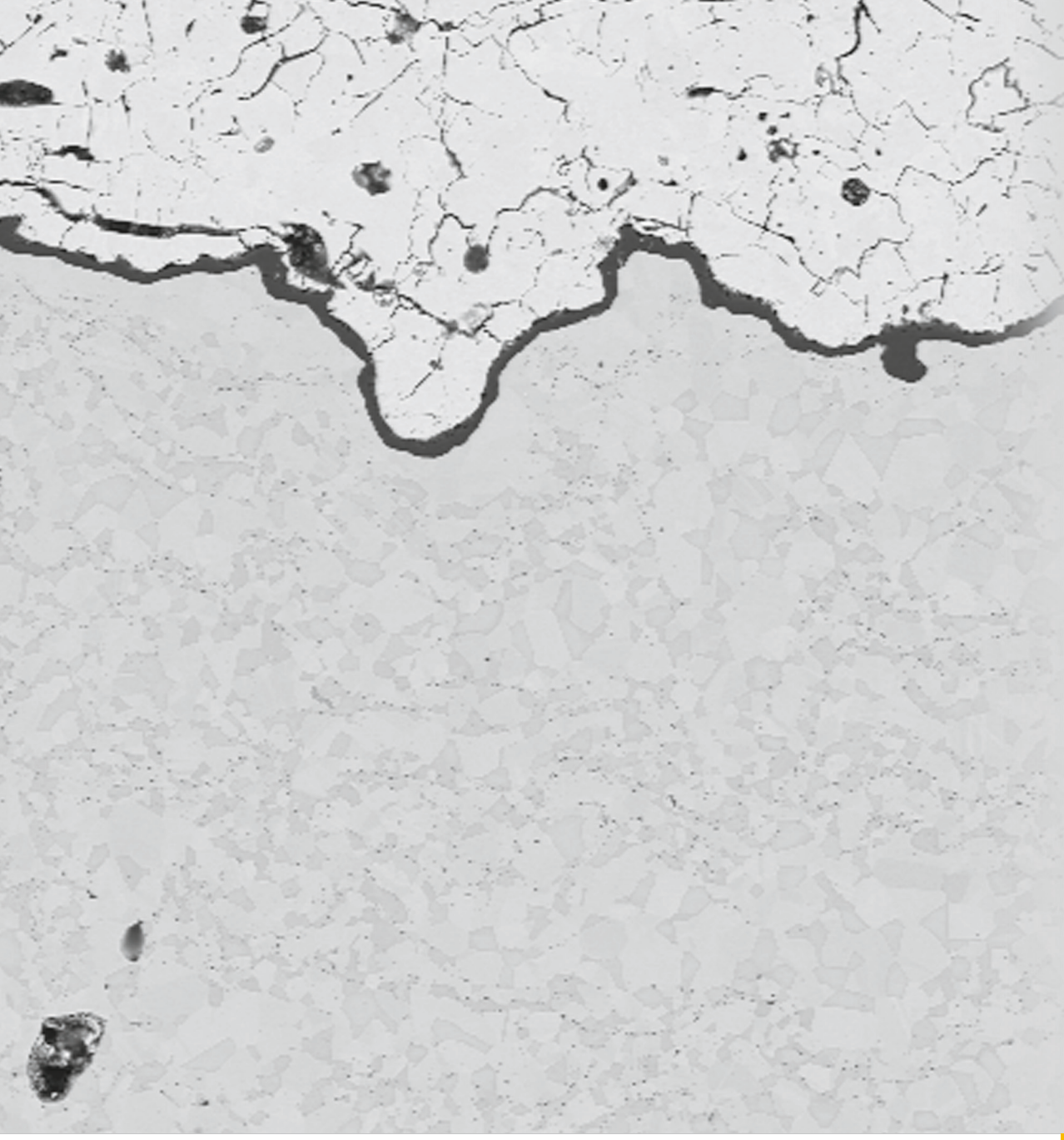

Energie & Umwelt / Energy & Environment
Band / Volume 137
ISBN 978-3-89336-783-2

JÜLICH
FORSCHUNGSZENTRUM